

FABRICATION OF ADVANCED ORGANIC-INORGANIC NANOCOMPOSITE  
COATINGS FOR BIOMEDICAL APPLICATIONS BY ELECTRODEPOSITION

By

XIN PANG, B.S., M.S.

A Thesis

Submitted to the School of Graduate Studies

In Partial Fulfillment of the Requirements

for the Degree

Doctor of Philosophy

McMaster University

© Copyright by Xin Pang, March 2008

DOCTOR OF PHILOSOPHY (2008)

McMaster University

(Materials Science and Engineering)

Hamilton, Ontario

TITLE:           Fabrication of Advanced Organic-Inorganic Nanocomposite Coatings  
                    for Biomedical Applications by Electrodeposition

AUTHOR:       Xin Pang, B.S. (Central-South University of Technology, China)

                    M.S. (Central-South University of Technology, China)

                    M.S. (University of Alberta)

SUPERVISOR:    Dr. Igor Zhitomirsky

NUMBER OF PAGES: XX, 217

## Abstract

Novel electrodeposition strategies have been developed for the fabrication of thick adherent zirconia ceramic and composite coatings for biomedical applications. The new method is based on the electrophoretic deposition (EPD) of polyelectrolyte additives combined with the cathodic precipitation of zirconia. The method enables the room-temperature electrosynthesis of crystalline zirconia nanoparticles in the polymer matrix. Adherent crack-free coatings up to several microns thick were obtained. The deposits were studied by thermogravimetric and differential thermal analysis, X-ray diffraction analysis, scanning and transmission electron microscopy, and atomic force microscopy. Obtained results pave the way for electrodeposition of other ceramic-polymer composites.

Novel advanced nanocomposite coatings based on bioceramic hydroxyapatite (HA) have been developed for the surface modification of orthopaedic and dental implant metals. HA nanoparticles prepared by a chemical precipitation method were used for the fabrication of novel HA-chitosan nanocomposite coatings. The use of chitosan enables room-temperature fabrication of the composite coatings. The problems related to the sintering of HA can be avoided. A new electrodeposition strategy, based on the EPD of HA nanoparticles and electrochemical deposition of chitosan macromolecules, has been developed. The method enabled the formation of dense, adherent and uniform coatings of various thicknesses in the range of up to 60

$\mu\text{m}$ . Bioactive composite coatings containing 40.9–89.8 wt% HA were obtained. The deposit composition and microstructure can be tailored by varying the chitosan and HA concentrations in the deposition bath. A mathematical model describing the formation of the HA-chitosan composite deposit has been developed. X-ray studies revealed preferred orientation of HA nanoparticles in the nanocomposites. Obtained coatings provide corrosion protection of the substrates and can be utilized for the fabrication of advanced biomedical implants.

For further functionalization of the HA-chitosan composite coating, Ag and  $\text{CaSiO}_3$  have been incorporated into the coating. Novel HA–Ag–chitosan and HA– $\text{CaSiO}_3$ –chitosan nanocomposite coatings have been deposited as monolayers, laminates, and coatings of graded composition. The obtained results can be used for the development of biocompatible antimicrobial coatings with controlled  $\text{Ag}^+$  release rate, and nanocomposite coatings with enhanced bioactivity.

## Acknowledgements

I hereby sincerely acknowledge the support of many people without whom I would never have been able to complete this thesis.

First, I am greatly indebted to my supervisor, Dr. Igor Zhitomirsky, who has gone beyond a mere thesis supervisor by providing me with intellectual challenges, constant encouragements, and an appropriate research environment.

Sincere thanks to my supervisory committee members, Dr. Gianluigi Botton and Dr. Marek Niewczas, who have generously offered constant support and invaluable instructions through the whole journey of my studies and thesis writing.

I would also thank all my groupmates in the lab, for their friendship and for rescuing me whenever I needed help.

Last but not least, I thank my love husband, Chao Shi. I gratefully thank him for his unconditional trust in me, and for putting up with me during stressful times.

I am very thankful for the financial support from the Natural Science and Engineering Research Council of Canada (NSERC).

## Table of Contents

Abstract.....	iii
Acknowledgements .....	v
Table of Contents .....	vi
List of Figures .....	xi
List of Tables .....	xx
Chapter 1 Introduction.....	1
Chapter 2 Literature Review and Research Objectives.....	5
2.1 Metals and alloys for orthopaedic and dental implant applications.....	5
2.1.1 Stainless steels .....	5
2.1.2 Ti and Ti alloys .....	7
2.2 Bioceramic materials for orthopaedic and dental implant applications.....	9
2.2.1 Alumina and zirconia .....	10
2.2.2 Bioglasses and calcium silicates .....	12
2.2.3 Hydroxyapatite and other calcium phosphates .....	14
2.2.3.1 Calcium phosphates.....	14
2.2.3.2 Hydroxyapatite.....	18
2.3 Electrodeposition techniques.....	20
2.3.1 Electrolytic deposition.....	22
2.3.2 Electrophoretic deposition.....	23
2.3.3 Particle interactions and suspension stability .....	25

2.3.3.1	The DLVO theory .....	25
2.3.3.2	Other interparticle forces .....	28
2.3.4	Particle charging .....	31
2.3.4.1	Aqueous suspensions.....	32
2.3.4.2	Non-aqueous suspensions.....	34
2.3.4.3	Additives for particle charging .....	35
2.3.5	Solvents .....	36
2.3.6	Binders.....	38
2.3.7	The electrical double layer and electrophoretic mobility.....	41
2.3.8	Kinetics of electrophoretic deposition.....	47
2.4	Electrodeposition of bioceramic and composite coatings on implant metals and alloys.....	50
2.4.1	Electrolytic deposition of zirconia coatings .....	50
2.4.2	Electrophoretic deposition of hydroxyapatite coatings.....	54
2.4.3	Electrodeposition of organic-inorganic composite coatings .....	58
2.5	Research objectives.....	59
Chapter 3	Experimental Procedures.....	61
3.1	Materials.....	61
3.1.1	Materials purchased from commercial suppliers .....	61
3.1.2	Synthesis of hydroxyapatite nanoparticles .....	62
3.2	Coating by electrodeposition methods.....	62
3.2.1	Experimental setups for electrodeposition .....	62
3.2.2	Preparation of solutions and suspensions for electrodeposition .....	63

3.2.3	Electrodeposition procedures.....	65
3.3	Characterization of the coatings .....	66
3.3.1	Materials characterization methods.....	66
3.3.1.1	Investigation of deposition yield.....	66
3.3.1.2	X-ray diffraction analysis .....	66
3.3.1.3	Thermogravimetric and differential thermal analysis .....	67
3.3.1.4	Scanning and transmission electron microscopy .....	68
3.3.1.5	Atomic force microscopy .....	69
3.3.1.6	Inductively coupled plasma spectrometry .....	69
3.3.2	Electrochemical methods.....	70
3.3.2.1	Corrosion cell setup.....	70
3.3.2.2	Testing solution.....	70
3.3.2.3	Testing methods .....	71
3.3.2.3.1	Tafel plot.....	71
3.3.2.3.2	Electrochemical impedance spectroscopy .....	72
Chapter 4	Experimental Results and Discussion .....	74
4.1	Coating systems investigated.....	74
4.2	Cathodic electrodeposition of zirconia coatings.....	75
4.2.1	Fabrication of ZrO <sub>2</sub> coatings with weak polyelectrolyte additives.....	75
4.2.1.1	Experimental results .....	75
4.2.1.2	Discussion.....	86
4.2.2	Fabrication of ZrO <sub>2</sub> coatings with a strong polyelectrolyte additive ....	94
4.2.2.1	Experimental results .....	94
4.2.2.2	Discussion.....	103
4.3	Electrodeposition of hydroxyapatite-chitosan nanocomposite coatings ....	110
4.3.1	Experimental results.....	110
4.3.1.1	TEM studies of the synthesized hydroxyapatite nanoparticles.....	110
4.3.1.2	XRD analysis of the hydroxyapatite nanoparticles and chitosan....	112
4.3.1.3	TG/DTA investigations of the hydroxyapatite nanoparticles and chitosan.....	113
4.3.1.4	TG/DTA investigations of the composite deposits .....	115

4.3.1.5	XRD investigations of the composite deposits .....	121
4.3.1.6	Deposition yield .....	125
4.3.1.7	SEM/TEM investigations of the coatings.....	128
4.3.1.8	Electrochemical characterization of the coatings.....	135
4.3.2	Discussion.....	141
4.3.2.1	Codeposition of hydroxyapatite and chitosan.....	141
4.3.2.2	Chemical composition of the composite coatings.....	145
4.3.2.3	Microstructure of the composite coatings.....	147
4.3.2.4	Deposition yield .....	148
4.3.2.5	Corrosion protection properties of the composite coatings .....	150
4.3.3	Modelling of the formation of the composite deposits .....	151
4.4	Electrodeposition of hydroxyapatite-Ag-chitosan nanocomposite coatings .....	161
4.4.1	Codeposition of hydroxyapatite, silver, and chitosan .....	162
4.4.2	Chemical composition of the composite deposits.....	164
4.4.3	Microstructure of the composite monolayer coatings.....	167
4.4.4	Microstructure of the composite multilayer coatings.....	171
4.4.5	Ag <sup>+</sup> release rate of the composite coatings.....	173
4.4.6	Corrosion protective properties of the composite coatings .....	175
4.5	Electrodeposition of functionally graded hydroxyapatite-CaSiO <sub>3</sub> -chitosan nanocomposite coatings .....	177
4.5.1	Codeposition of hydroxyapatite, CaSiO <sub>3</sub> , and chitosan .....	177
4.5.2	SEM studies of microstructure of the obtained composite coatings...	180
4.5.3	Preparation of the composite coatings of graded composition and lamine structure.....	183

4.5.4	Corrosion protection properties of the composite coatings .....	186
4.6	Summary .....	189
Chapter 5	Conclusions and Future Work .....	192
5.1	Conclusions .....	192
5.2	Suggestions for future work .....	195
References	.....	197

## List of Figures

Figure 2-1	Thickness of coatings deposited using ELD and EPD. ....	21
Figure 2-2	Total interaction energy between spherical particles as a function of interparticle separation according to the DLVO theory. ....	27
Figure 2-3	Schematic of the double layer surrounding a charged particle and evolution of the electric potential from the surface potential, $\psi_0$ , to zero far from the particle. The potential at the surface of shear, the limit between the liquid moving with the particle and the liquid, which does not move with the particle, is termed the $\zeta$ potential ( $\psi_\zeta$ ) and is the main parameter determining the electrokinetic behavior of the particle. ....	32
Figure 2-4	$\zeta$ potential of ceramic particles versus pH of suspension. ....	33
Figure 2-5	Schematic representation of the double layer and potential drop across the double layer: (a) surface charge, (b) Stern layer, (c) diffuse layers of counter-ions. ....	42
Figure 2-6	Deposition yield as a function of suspension concentration $C_s$ . ....	47
Figure 3-1	A schematic of the setup of the deposition cell. ....	63
Figure 3-2	A schematic of the corrosion cell setup for the electrochemical measurement. ....	71
Figure 4-1	Deposit weight versus deposition time for the deposits prepared from the 5mM $ZrOCl_2$ + 0.4 g/l PEI solutions on a Pt substrate at a current density of 5 mA/cm <sup>2</sup> . ....	76
Figure 4-2	TG data for the deposits obtained from the 5 mM $ZrOCl_2$ solutions at a current density of 5 mA/cm <sup>2</sup> (heating rate = 5 °C/min). ....	76
Figure 4-3	TG data for the deposits obtained from the 5 mM $ZrOCl_2$ solutions containing (a) 0.4 g/l PEI and (b) 1.0 g/l PEI at a current density of 5 mA/cm <sup>2</sup> (heating rate = 5 °C/min). ....	77
Figure 4-4	XRD patterns for the deposits obtained from the 5 mM $ZrOCl_2$ solutions containing 0.4 g/l PEI (a) as prepared and after annealing for 1	

	hr at (b) 200, (c) 400, (d) 600, and (e) 800 °C (▲ = tetragonal zirconia, ● = monoclinic zirconia).....	78
Figure 4-5	XRD pattern of a composite coating prepared from the 5 mM ZrOCl <sub>2</sub> solutions containing 1.0 g/l PEI and 4.0 g/l YSZ (● = YSZ, ▲ = Ni substrate).....	79
Figure 4-6	TG data for the deposits obtained from the 5 mM ZrOCl <sub>2</sub> solutions containing (a) 0.75 g/l PAH and (b) 1.5 g/l PAH at a current density of 5 mA/cm <sup>2</sup> (heating rate = 5 °C/min). ....	79
Figure 4-7	XRD patterns for the deposits obtained from the 5 mM ZrOCl <sub>2</sub> solutions containing 0.75 g/l PAH (a) as prepared and after annealing for 1 hr at (b) 200, (c) 400, (d) 600, and (e) 800 °C (▲ = tetragonal zirconia, ● = monoclinic zirconia).....	80
Figure 4-8	SEM picture of the sectioned deposit obtained from a 5 mM ZrOCl <sub>2</sub> + 0.4 g/l PEI solution on a graphite substrate (bar = 10 μm).....	81
Figure 4-9	SEM picture of the composite deposit prepared from a 5 mM ZrOCl <sub>2</sub> + 0.4 g/l PEI solution on a carbon felt (bar = 10 μm). ....	81
Figure 4-10	SEM pictures of the composite deposits on individual carbon fibres, obtained from the 5 mM ZrOCl <sub>2</sub> solutions containing (a) 0.4 g/l PEI and (b and c) 1.0 g/l PEI (bar=10 μm).....	84
Figure 4-11	AFM images of the coatings prepared from the 5 mM ZrOCl <sub>2</sub> solutions containing (a) 0.4 and (b and c) 1.0 g/l PEI at a current density of (a and b) 1.5 and (c) 3 mA/cm <sup>2</sup> , with a deposition time of (a and c) 3 and (b) 5 min.....	85
Figure 4-12	Deposit weight versus deposition time for the deposits prepared from the 5 mM ZrOCl <sub>2</sub> solutions (a) without additives, and containing (b) 0.5 g/l and (c) 1.0 g/l PDDA on a stainless steel substrate at a current density of 3 mA/cm <sup>2</sup> . ....	94
Figure 4-13	TG data for the deposits prepared from the 5 mM ZrOCl <sub>2</sub> solutions (a) without additives and containing (b) 0.5 g/l and (c) 1.0 g/l PDDA. ....	96

Figure 4-14	XRD patterns of the deposits prepared from the 5 mM ZrOCl <sub>2</sub> solutions (a) without PDDA and (b) containing 0.5 g/l PDDA.....	97
Figure 4-15	AFM images of the composite coatings prepared from the 5 mM ZrOCl <sub>2</sub> + 1.0 g/l PDDA solution at current densities of (a) 3 mA/cm <sup>2</sup> and (b) 5 mA/cm <sup>2</sup> , deposition time 3 min. ....	98
Figure 4-16	SEM pictures of the deposits on stainless steel substrates prepared from the pure 5 mM ZrOCl <sub>2</sub> solution (a,b,c) without additives and (d,e,f) containing 0.5 g/l PDDA: deposition time (a,d) 1, (b,e) 2 and (c,f) 5 min. ....	99
Figure 4-17	SEM pictures of the deposits on stainless steel substrates prepared from the pure 5 mM ZrOCl <sub>2</sub> solution (a,b,c) without additives and (d,e,f) containing 0.5 g/l PDDA: deposition time (a,d) 1, (b,e) 2 and (c,f) 5 min after sintering at 600 °C for 1 hr. ....	100
Figure 4-18	XRD patterns for the deposits obtained from the 5 mM ZrOCl <sub>2</sub> solutions, containing 0.5 g/l PDDA: after annealing during 1 hr at (a) 200, (b) 400, (c) 600, (d) 800, and (e) 1000 °C. ▲ – tetragonal zirconia, ● – monoclinic zirconia. ....	101
Figure 4-19	XRD patterns for the deposits prepared from the 5 mM ZrOCl <sub>2</sub> + 0.5 g/l PDDA solution at a current density of 3 mA/cm <sup>2</sup> after annealing at 600 °C during 1 hr: deposition time (a) 22 min and (b) 30 min. ▲ – tetragonal zirconia, ● – Fe <sub>2</sub> O <sub>3</sub> , and ■ – substrate. ....	102
Figure 4-20	TEM images of the HA nanoparticles.....	111
Figure 4-21	XRD pattern of as-prepared HA nanoparticles.....	112
Figure 4-22	XRD pattern of (a) as received chitosan, and (b) the deposit prepared from the 0.5 g/l chitosan solution in the mixed ethanol-water solvent (17% water), deposition time of 20 min. ....	112
Figure 4-23	(a) TG and (b) DTA data for the HA powders, prepared by the chemical precipitation method.....	114
Figure 4-24	(a,b) TG and (c,d) DTA data for (a,c) as-received chitosan powders and	

(b,d) the pure chitosan deposit obtained from a 0.5 g/l chitosan solution. .....	114
Figure 4-25 (a) TG and (b) DTA data for the composite HA-chitosan deposit prepared from the 1.0 g/l HA suspension in the mixed ethanol-water solvent (17% water) containing 0.5 g/l chitosan, deposition time of 20 min.....	116
Figure 4-26 (a) TG and (b) DTA data for the composite HA-chitosan deposit prepared from the 8.0 g/l HA suspension in the mixed ethanol-water solvent (17% water) containing 0.5 g/l chitosan, deposition time of 20 min.....	116
Figure 4-27 TG (a) and DTA (d) data for as-prepared HA powders, compared to (b,c) TG and (e,f) DTA data for the composite HA-chitosan deposits obtained from the (b,e) 2.0 g/l and (c,f) 4.0 g/l HA suspensions in the mixed ethanol-water solvent (17% water) containing 0.5 g/l chitosan at a constant current density of 0.1 mA/cm <sup>2</sup> . .....	117
Figure 4-28 (a,b) TG and (c,d) DTA data for (a,c) as-prepared HA powders and (b,d) the composite HA-chitosan deposits obtained from a 0.5 g/l chitosan solution containing 3.0 g/l HA.....	118
Figure 4-29 (a,b,c,d) TG and (e,f,g,h) DTA data for (a,e) as-prepared HA powders, and the composite HA-chitosan deposits obtained from the 3.0 g/l HA suspensions containing (b,f) 0.1 g/l, (c,g) 0.5 g/l, and (d,h) 0.7 g/l chitosan.....	119
Figure 4-30 The variation of the HA content in the composite coatings as a function of the HA concentration in the 0.5 g/l chitosan solutions used for EPD. .....	121
Figure 4-31 XRD pattern of the composite HA-chitosan deposit prepared from the 8.0 g/l HA suspension in the mixed ethanol-water solvent (17% water) containing 0.5 g/l chitosan, deposition time of 20 min. • – HA (JCPDS 09-0432).....	122
Figure 4-32 XRD patterns for (a) as-prepared HA particles, (b) the pure HA deposit on 316L stainless steel obtained from a 3.0 g/l HA suspension, and the composite deposits on 316L stainless steel prepared from the 0.5 g/l chitosan solutions containing (c) 0.5 g/l, (d) 1.0 g/l, and (e) 3.0 g/l HA,	

- and (f) the same composite deposit as in (e) scraped from the substrate.  
 (▼ — HA • — substrate). ..... 123
- Figure 4-33 The variation of the XRD intensity ratio  $I(300)/I(211)$  of the HA peaks for the same coatings as a function of the HA concentration in the 0.5 g/l chitosan solutions used for EPD. .... 124
- Figure 4-34 XRD patterns for (a) as-prepared HA powders, and a composite deposit (b) on the Ti substrate and (c) scraped from the Ti substrate. The composite deposit was prepared from the 4 g/l HA suspension in the mixed ethanol-water solvent (17% water) containing 0.5 g/l chitosan at a constant current density of  $0.1 \text{ mA/cm}^2$  (▼ — HA). ..... 125
- Figure 4-35 Deposit weight versus deposition time for the deposits prepared from the (a) 4.0 g/l HA and (b) 8.0 g/l HA suspensions in the mixed ethanol-water solvent (17 wt% water) containing 0.5 g/l chitosan, at a current density of  $0.1 \text{ mA/cm}^2$ . ..... 126
- Figure 4-36 Deposit weight versus HA concentration in the suspensions in the mixed ethanol-water solvent (17 % water) containing 0.5 g/l chitosan, at constant current densities of (a) 0.1 and (b)  $0.2 \text{ mA/cm}^2$ , and deposition time of 3 min. .... 126
- Figure 4-37 Deposit weight versus chitosan concentration in 3.0 g/l HA suspensions, at a current density of  $0.1 \text{ mA/cm}^2$  and deposition time of 5 min. The concentration of acetic acid in all the suspensions was 1.9 mM. .... 127
- Figure 4-38 SEM pictures of sectioned HA-chitosan composite deposits on graphite substrate obtained from the 8.0 g/l HA suspension in the mixed ethanol-water solvent (17% water) containing 0.5 g/l chitosan at a current density of  $0.1 \text{ mA/cm}^2$  and deposition time: (a) 1 min, (b) 3 min, (c) 5 min, and (d) 7 min. .... 129
- Figure 4-39 The variation of deposit thickness with the deposition time for the HA-chitosan composite deposits prepared from the 0.5 g/l chitosan solutions containing (a) 4 g/l and (b) 8 g/l HA. .... 130
- Figure 4-40 SEM pictures of the HA-chitosan composite deposit on stainless steel wire obtained from the 8.0 g/l HA suspension in the mixed ethanol-water solvent (17% water) containing 0.5 g/l chitosan at a current density of 0.1

- mA/cm<sup>2</sup> and deposition time 3 min: (a) A — uncoated area, and B — coated area at low magnification; (b) coated area at a higher magnification. .... 131
- Figure 4-41 SEM pictures of HA-chitosan composite deposits obtained from the 4 g/l HA suspension in the mixed ethanol-water solvent (17% water) containing 0.5 g/l chitosan: on Ti wire substrate, (a) at a constant voltage of 8 V and deposition time of 3 min and (b) at a constant voltage of 12 V and deposition time of 7 min; and on Ti gauze substrate (c,d - different magnifications) at a constant voltage of 12 V and deposition time of 20 min..... 132
- Figure 4-42 SEM images of the HA–chitosan composite deposits on 316L stainless-steel wire prepared from the 0.5 g/l chitosan solutions containing 3.0 g/l HA, with a deposition time of (a) 3 min, (b) 5 min (A — uncoated area, B — coated area), and (c) 10 min. (d) the coated area B at a higher magnification..... 133
- Figure 4-43 SEM pictures of the HA–chitosan composite coatings prepared from the 0.5 g/l chitosan solutions containing (a) 8.0 g/l, and (b) 0.5 g/l HA..... 134
- Figure 4-44 High-resolution TEM image of the lattice fringes of a HA crystal in a chitosan matrix for the composite deposit prepared from a 0.5 g/l chitosan solution containing 0.5 g/l HA. .... 135
- Figure 4-45 Bode plots in Ringer's solution for (a) uncoated stainless steel, and (b) coated stainless steel samples prepared from the 4.0 g/l HA suspension in the mixed ethanol-water solvent (17% water) containing 0.5 g/l chitosan at a current density of 0.1 mA/cm<sup>2</sup> and a deposition time of 20 min.... 136
- Figure 4-46 Tafel plots in Ringer's solution for (a) uncoated stainless steel, and (b) coated stainless steel samples prepared from the 4.0 g/l HA suspension in the mixed ethanol-water solvent (17% water) containing 0.5 g/l chitosan at a current density of 0.1 mA/cm<sup>2</sup> and a deposition time of 20 min.... 137
- Figure 4-47 Tafel plots in Ringer's solution for (a) uncoated Ti substrate, and (b) coated Ti samples prepared from the 4 g/l HA suspension in the mixed ethanol-water solvent (17% water) containing 0.5 g/l chitosan at a current density of 0.1 mA/cm<sup>2</sup> and deposition time of 20 min..... 137
- Figure 4-48 Tafel plots in the Ringer's solution for (a) uncoated and (b, c) the coated 316L stainless-steel samples prepared from the 0.5 g/l chitosan solutions

	containing 3.0 g/l HA, with a deposition time of 3 min: (a,b) without heat treatment, (c) heat treated at 140 °C for 10 h.....	138
Figure 4-49	Tafel plots in the Ringer's solution for the coated 316L stainless-steel samples prepared from the 0.5 g/l chitosan solutions containing 5 g/l HA, with a deposition time of (a,b) 3 min, and (c) 10 min: (a) without heat treatment, (b, c) heat treated at 140 °C for 10 h.....	139
Figure 4-50	Bode plots in the Ringer's solution for (a) uncoated and (b, c) the coated 316L stainless-steel samples prepared from the 0.5 g/l chitosan solutions containing 3.0 g/l HA, with a deposition time of 3 min: (a,b) without heat treatment, (c) heat treated at 140 °C for 10 h.....	140
Figure 4-51	The dependences of the deposit weight on the HA concentration in chitosan solutions for HA-chitosan composite coatings deposited at a constant voltage of 20 V for (a) 3 min and (b) 5 min.....	153
Figure 4-52	TG (a,b,c) and DTA (d,e,f) data for as-prepared HA powders (a,c) and the HA-chitosan composite deposits prepared from the chitosan solution containing 1.0 g/l HA (b,e) and 0.2 g/l HA (c,f).....	155
Figure 4-53	The (a) HA and (b) chitosan content in deposits calculated from TG data versus the HA concentration in chitosan solutions for HA-chitosan composite deposits prepared at a constant voltage of 20 V.....	157
Figure 4-54	The (a) $C_c$ and (b) $\Psi_c$ versus $C_s$ curves for $f=0.6$ .....	158
Figure 4-55	The $C_s/C_c$ versus $C_s$ curves for (a) $f=0.6$ and (b) $f=1.0$ .....	159
Figure 4-56	XRD patterns for (a) as-prepared HA powders, and the deposits prepared from the 0.5 g/l chitosan solutions containing (b, c) 1.0 mM AgNO <sub>3</sub> , (d) 0.5 g/lHA, and (e) 1.0 mM AgNO <sub>3</sub> and 0.5 g/l HA. (c, e) annealed at 300 °C for 1 hr. (▲ — Ag, ● — HA.).....	163
Figure 4-57	(a, b) TG and (c, d) DTA data for the deposits prepared from (a, c) the pure 0.5 g/l chitosan solution, and (b, d) the 0.5 g/l chitosan solution containing 0.5 mM AgNO <sub>3</sub> .....	165
Figure 4-58	(a, b) TG and (c, d) DTA data for the deposits prepared from the solutions containing 0.5 g/l chitosan, 1.0 mM AgNO <sub>3</sub> , and (a, c) 1.0 g/l HA and (b, d) 3.0 g/l HA.....	166

Figure 4-59	EDS spectra for the deposits prepared from the solutions containing 0.5 g/l chitosan, 1.0 mM AgNO <sub>3</sub> , and (a) 0.5 g/l HA, (b) 1.0 g/l HA, and (c) 2.0 g/l HA. ....	167
Figure 4-60	SEM images of the cross-sections of the coatings (A) on a graphite substrate (S) prepared from the 0.5 g/l chitosan solution containing 1.0 mM AgNO <sub>3</sub> for (a) 10 min, and (b) 20 min. ....	168
Figure 4-61	SEM images of the surfaces of the deposits prepared from the 0.5 g/l chitosan solutions containing (a) 1.0 g/l HA, and (b) 1.0 g/l HA and 1.0 mM AgNO <sub>3</sub> . ....	169
Figure 4-62	(a, b) SEM images at different magnifications of the composite coating on a stainless-steel gauze deposited from the 0.5 g/l chitosan solution containing 1.0 mM AgNO <sub>3</sub> and 1.0 g/l HA. ....	170
Figure 4-63	SEM images of the cross-sections of the HA-chitosan (H) /Ag-chitosan (A) bi-layer coatings prepared from the 0.5 g/l chitosan solutions containing 1.0 mM AgNO <sub>3</sub> (A) or 1 g/l HA (H) at deposition times of 15 min for layers A, and (a) 10 min or (b) 20 min for layers H. ....	171
Figure 4-64	(a, b) Multilayer coatings with different numbers of layers, prepared from the 0.5 g/l chitosan solutions containing 1.0 g/l HA (H) or 1.0 mM AgNO <sub>3</sub> (A). ....	172
Figure 4-65	The concentration of released Ag <sup>+</sup> ions as a function of the immersion time for (a) the Ag-chitosan monolayer coating on stainless steel prepared from the 0.5 g/l chitosan solution containing 1.0 mM AgNO <sub>3</sub> , and (b) the HA-chitosan/Ag-chitosan bi-layer coating on stainless steel prepared from the 0.5 g/l chitosan solutions containing 1.0 g/l HA or 1.0 mM AgNO <sub>3</sub> . ....	174
Figure 4-66	The Nyquist plots (a) and Tafel plots (b) for the samples tested in the Ringer's solution: (s) the bare stainless steel substrate, and (c) the stainless steel coated with a HA-chitosan/Ag-chitosan/HA-chitosan three-layer coating, prepared from the 0.5 g/l chitosan solutions containing 1.0 g/l HA or 1.0 mM AgNO <sub>3</sub> . ....	176
Figure 4-67	TG (a,b,c) and DTA(d,e,f) data for (a,d) as-received CaSiO <sub>3</sub> powders and composite deposits prepared from chitosan solutions containing (b,e) 0.5 g/l CaSiO <sub>3</sub> and (c,f) 0.2 g/l CaSiO <sub>3</sub> . ....	179

- Figure 4-68 SEM images of HA-chitosan composite coatings deposited at a constant current of  $0.1 \text{ mA/cm}^2$  for 10 min from the chitosan solutions containing (a) 0.5 g/l HA and (b) 1.0 g/l HA..... 180
- Figure 4-69 SEM images of  $\text{CaSiO}_3$ -chitosan composite coatings deposited at constant current of  $0.1 \text{ mA/cm}^2$  for 10 min from the chitosan solutions containing (a,b) 0.3 g/l  $\text{CaSiO}_3$ , and (c,d) 0.5 g/l  $\text{CaSiO}_3$  at different magnifications..... 181
- Figure 4-70 SEM images at different magnifications (a,b) of HA- $\text{CaSiO}_3$ -chitosan composite coatings deposited at constant  $0.1 \text{ mA/cm}^2$  for 10 min from the chitosan solutions containing 1.0 g/l HA and 0.3 g/l  $\text{CaSiO}_3$ ..... 182
- Figure 4-71 (a,b) SEM images of the cross-sections of the laminate coatings prepared from the pure 0.5 g/l chitosan solution (Ch) or 0.5 g/l chitosan containing 4.0 g/l HA (H)..... 185
- Figure 4-72 SEM image of the cross-section of a  $\text{CaSiO}_3$ -chitosan (C)/HA-chitosan(H)/chitosan(Ch) three-layer coating prepared from the 0.5 g/l chitosan solutions containing 0.3 g/l  $\text{CaSiO}_3$  (C) or 1 g/l HA (H). ..... 186
- Figure 4-73 (a) Tafel and (b) Nyquist plots of (s) the bare stainless steel substrate, and the coated samples with (l) a chitosan/HA-chitosan/chitosan /HA-chitosan 4-layer coating prepared from pure 0.5 g/l chitosan solution or 0.5 g/l chitosan solution containing 4 g/l HA, and (m) a  $\text{CaSiO}_3$ -HA-chitosan monolayer coating prepared from 0.5 g/l chitosan solution containing 1 g/l HA and 0.3 g/l  $\text{CaSiO}_3$ ..... 188

## List of Tables

Table 2-1	Some characteristics of orthopaedic metallic implant materials [Long <i>et al.</i> , 1998].....	6
Table 2-2	The physical and mechanical properties of various bioceramics applied for surgical applications [Kannan <i>et al.</i> , 2002]. .....	9
Table 2-3	Types of implant-tissue response [Hench, 1998].....	10
Table 2-4	Properties of the biologically relevant calcium orthophosphates [Dorozhkin <i>et al.</i> , 2002]. .....	15
Table 2-5	Cystallographic data of calcium phosphates [Dorozhkin <i>et al.</i> , 2002]. .....	16
Table 2-6	Examples of solvents used for electrodeposition.....	38
Table 3-1	List of materials purchased.....	61
Table 4-1	An overview of the coating systems investigated.....	74
Table 4-2	Summary of the experimental results.....	189

## **Chapter 1 Introduction**

Biomaterials are substances that are produced synthetically or biologically for use in the treatment or management of a disease, condition, or injury. The field of biomaterials has been expanding rapidly over the last 30 years such that it is now becoming one of the most intellectually exciting areas of materials science and engineering.

In the past few decades, considerable progress has been made in the improvement and development of orthopaedic devices intended for implantation in the human body. This is due to the active involvement of man in the industrial activities, sports, defence activities, and daily utilization of transporting vehicles. The prime commitments of people in this fast moving world have compelled them to opt for orthopaedic implants for early and speedy recovery to resume their normal life.

Orthopaedic implants are devices mounted on to human's skeletal system for aiding healing, correcting deformities and restoring the lost functions of the original part. They include supporting bone plates, screws, total hip joints, knee joints, elbow joints, shoulder joints, and reattachments for tendons or ligaments. No matter what applications an implant is intended for, it must be compatible with the body. Although many materials have been tested for use in the human body, few have achieved clinical application. This is mainly due to the corrosive saline human body fluid and the complex load and stress situation induced by human's activity. Clinical success

requires a simultaneous achievement of biocompatibility, and a match of the mechanical behavior of the implant with the tissue to be replaced. Only certain materials like metals and alloys, ceramics and polymers are able to meet these requirements.

Among the available materials, metals and alloys are the predominant for load bearing applications (i.e. orthopaedic and dental implants) because of their reasonable biocompatibility and sufficient fatigue strength to endure daily activities such as walking, chewing etc. The limitations of ceramic materials are their low tensile strength and fracture toughness. Their use in bulk form is therefore limited to functions in which only compressive loads are applied. Polymers undergo degradation in the body environment due to biochemical and mechanical factors. This results in tissue irritation and decrease in mechanical properties. Composites combining two or more materials or phases have been developed for biomedical applications. It is important that each constituent of the composite be biocompatible, and that the interface between constituents not be degraded by the body environment. A few composites which are successfully used as implants are low stiffness femoral components for hip joint arthroplasty, radiolucent and biodegradable fracture fixation devices, fracture-resistant bone cements, and wear, creep and fracture-resistant articulation components. However, their degradation under complex states of stress and low mechanical strengths limit their applications. It is also difficult to shape them, and they are yet to attain technical maturity for these applications [Silver, 1994].

Metallic materials have been used for centuries in restoration of anatomical structures because of their excellent mechanical properties. The high modulus and yield point coupled with the ductility of metals make them suitable for load bearing without leading to large deformations and permanent dimensional changes. Implants made of metals and alloys include devices for fracture fixation, partial and total joint replacement, external splints, braces and traction apparatus as well as dental amalgams. Although metals exhibit high strength and toughness, they are susceptible to chemical and electrochemical degradation. Tissue fluid in the human body contains water, dissolved oxygen, proteins, and various ions such as chloride and hydroxide. As a result, the human body presents a very aggressive environment to metals used for implantation. The implant metals may corrode and/or wear, leading to the generation of particulate debris, which may aggravate the body environment and elicit both local and systemic biological responses. Corrosion resistance of a metallic implant material is consequently an important aspect of its biocompatibility.

An effective approach to reduce corrosion and achieve better biocompatibility of a metal or alloy implant is to modify its surface with a functional surface coating. Performance of the metallic substrate can be improved with respect to implant fixation, biocompatibility or bioactivity, corrosion resistance, wear resistance, and antimicrobial property etc. This is a very promising area as it enables the manufacture of advanced biomedical devices or implants with comprehensive functionalities that are otherwise unattainable. The major challenge lies in the utilization of appropriate

coating materials and coating technologies.

The subject of my research thus involves the development of advanced coating materials and deposition techniques for the fabrication of functionalized ceramic and composite coatings on metallic orthopaedic and dental implants.

## **Chapter 2 Literature Review and Research Objectives**

### **2.1 Metals and alloys for orthopaedic and dental implant applications**

Standard metallic orthopaedic materials include stainless steels, cobalt-based alloys, commercially pure titanium (cpTi) and Ti-based alloys, with an increasing number of devices being made of cpTi and Ti alloys. Regarding dental and non-cemented orthopaedic implants, cpTi and Ti alloys are generally preferred to stainless steels and Co-alloys because of their lower modulus, superior biocompatibility and corrosion resistance [Woodman *et al.*, 1984]. Table 2-1 lists some characteristic features of currently used metals and alloys for orthopaedic implant applications. In our research, stainless steels and cpTi will be used as substrates for the investigations of novel ceramic and composite coatings.

#### **2.1.1 Stainless steels**

Stainless steels is still the most used metal for internal fixation devices thanks to a favorable combination of mechanical properties, acceptable biocompatibility and cost effectiveness when compared to other metallic implant materials [Disegi *et al.*, 2000; Schmidt *et al.*, 2001]. It is protected from corrosion by the addition of chromium, which forms a passivated chromium oxide layer on the surface that aids in preventing corrosion. The most common grade of stainless steel used for implants is type 316L. Grade 316 is a standard molybdenum-bearing austenitic stainless steel,

which has excellent toughness given by the austenitic structure. Grade 316L is the low carbon (0.03 %) version of 316, which is immune from sensitisation (grain boundary carbide precipitation). A disadvantage seen for stainless steels is its tendency towards corrosion under physiological conditions causing a release of metal ions such as those of nickel and chromium [Schmidt *et al.*, 2001].

Table 2-1 Some characteristics of orthopaedic metallic implant materials [Long *et al.*, 1998].

	Stainless steels	Cobalt-base alloys	Ti & Ti-base alloys
Designation	ASTM F-138 (‘316 LDVM’)	ASTM F-75 ASTM F-799 ASTM F-1537 (Cast and wrought)	ASTM F-67 (ISO 5832/II) ASTM F-136 (ISO 5832/II) ASTM F-1295 (Cast and wrought)
Principal alloying elements (wt%)	Fe(bal.) Cr(17-20) Ni(12-14) Mo(2-4)	Co(bal.) Cr(19-30) Mo(0-10) Ni(0-37)	Ti(bal.) Al(6) V(4) Nb(7)
Advantages	<ul style="list-style-type: none"> <li>• cost, availability</li> <li>• processing</li> </ul>	<ul style="list-style-type: none"> <li>• wear resistance</li> <li>• corrosion resistance</li> <li>• fatigue strength</li> </ul>	<ul style="list-style-type: none"> <li>• biocompatibility</li> <li>• corrosion resistance</li> <li>• low elastic modulus</li> <li>• fatigue strength</li> </ul>
Disadvantages	<ul style="list-style-type: none"> <li>• Corrosion</li> <li>• high elastic modulus</li> </ul>	<ul style="list-style-type: none"> <li>• high elastic modulus</li> <li>• biocompatibility</li> </ul>	<ul style="list-style-type: none"> <li>• wear resistance</li> <li>• low shear strength</li> </ul>
Primary utilisations	Temporary devices (fracture plates, screws, hip nails) Used for total hip replacement stems in UK (high Nitrogen)	Dentistry castings Prostheses stems Load-bearing components in total joint replacement (wrought alloys)	Used in total hip replacements with modular (CoCrMo or ceramic) femoral heads Long-term, permanent devices (nails, pacemakers)

### 2.1.2 Ti and Ti alloys

Ti and its alloys have been considered the metal of choice for bone implants because of their high osteo-integration properties, suitable modulus of elasticity, low density, improved biocompatibility and magnetic resonance imaging compatibility [Christensen *et al.*, 2000; Wataha *et al.*, 1995; Wataha *et al.*, 1997].

In its elemental form, Ti has a high melting point (1678 °C), exhibiting a hexagonal close packed crystal structure (hcp)  $\alpha$  up to the beta transus (882.5 °C), transforming to a body centered cubic structure (bcc)  $\beta$  above this temperature [Collings, 1984]. Ti alloys may be classified as either  $\alpha$ , near- $\alpha$ ,  $\alpha + \beta$ , metastable  $\beta$  or stable  $\beta$  depending upon their room temperature microstructure [Collings, 1984]. In this regard, alloying elements for Ti fall into three categories:  $\alpha$  -stabilizers, such as Al, O, N, C;  $\beta$  -stabilizers, such as Mo, V, Nb, Ta, (isomorphous), Fe, W, Cr, Si, Ni, Co, Mn, H (eutectoid); and neutral, such as Zr.  $\alpha$  and near- $\alpha$  Ti alloys exhibit superior corrosion resistance with low ambient temperature strength. In contrast,  $\alpha + \beta$  alloys exhibit higher strength due to the presence of both  $\alpha$  and  $\beta$  phases.  $\beta$  alloys (metastable or stable) are Ti alloys with high strength, good formability and superior corrosion resistance. Biocompatibility and corrosion behavior considerations have limited the choice of alloying elements for Ti metal implants. Currently, the most commonly used grades are  $\alpha$  cpTi and  $\alpha + \beta$  (Ti-6Al-4V) alloy.

It is worth noting that the excellent chemical inertness, corrosion resistance, repassivation ability, and biocompatibility of titanium and most other titanium alloys

are thought to result from the chemical stability and structure of the titanium oxide film that is typically only a few nanometers thick [Liu *et al.*, 2004a]. This protective and stable oxide surface layer has been considered responsible for the good biocompatibility with bone and excellent resistance to corrosion processes [Kasemo *et al.*, 1988; Stanford *et al.*, 1991]. It contributes to the formation of apatite and bone-like tissue, thus allowing the onset of favorable cellular reactions [Demri *et al.*, 1997; Geros *et al.*, 1993]. The surface modification of Ti and its alloys to produce a uniform thick TiO<sub>2</sub> layer provides significant improvement in the performance of the metal in the sense of corrosion protection, sinterability, and biocompatibility.

Despite the high corrosion resistance of titanium and alloys currently used for orthopaedic and dental implants, there is increasing evidence showing that titanium is released into and accumulated in the tissue adjacent to the implants [Pan *et al.*, 1997]. The problem of ion release from implant metals is particularly of concern in the case of porous implants due to their large surface area. As the list of potential materials for biomedical applications is somewhat limited because of mechanical strength and biocompatibility requirements, surface protective biocompatible coatings have become the major approach currently used to improve the corrosion resistance of metal implant materials. Biocompatible ceramic and composite ceramic-polymer coatings are of significant interest for the corrosion protection of metallic implants.

## 2.2 Bioceramic materials for orthopaedic and dental implant applications

Ceramics for the repair, reconstruction, and replacement of diseased or damaged part of the body are termed “bioceramics” [Hench, 1998]. Bioceramics have been used very successfully within the human body for many years. They are commonly used in orthopaedic surgery and dentistry. Bioceramics can be polycrystalline (alumina or tricalcium phosphate TCP), bioactive glass, bioactive glass-ceramic (A/W), or bioactive composite (polyethylene-hydroxyapatite). Table 2-2 shows the properties of some typical bioceramic materials.

Table 2-2 The physical and mechanical properties of various bioceramics applied for surgical applications [Kannan *et al.*, 2002].

Material	Density (g/cm <sup>3</sup> )	Young's modulus (GPa)	Compressive strength (MPa)	Tensile strength (MPa)	Flexural strength (MPa)
Carbon (Vitreous)	1.4-1.6	24-28	700	70-200	150-200
Carbon (Vapor deposited)	1.5-1.22	20-21	N/A	N/A	340-700
Hydroxyapatite	2.55-3.07	44-48	310-510	N/A	60-115
β-TCP	3.14	N/A	120	N/A	N/A
Bioglass	2.8	N/A	500	N/A	100-150
Al <sub>2</sub> O <sub>3</sub>	3.93-3.95	380-400	4000-5000	350	400-560
ZrO <sub>2</sub>	4.9-5.66	150-190	1750	N/A	150-700
Human bone	N/A	3-30	130-180	60-160	N/A

When a material is implanted in the body, different types of response are elicited from the host tissue (Table 2-3). Bioceramics may be bioinert (e.g., alumina and zirconia), resorbable (e.g., TCP), bioactive (e.g., hydroxyapatite, bioactive glasses, and glass-ceramics), or porous for tissue ingrowth (e.g., hydroxyapatite-coated metals). Applications of bioceramics include replacements for hips, knees, teeth, tendons, and ligaments and repair for periodontal disease, maxillofacial reconstruction, augmentation and stabilization of the jaw bone, spinal fusion, and bone repair after tumor surgery. Pyrolytic carbon coatings are thromboresistant and are used for prosthetic heart valves.

Table 2-3 Types of implant-tissue response [Hench, 1998].

---

If the material is toxic, the surrounding tissue dies.
If the materials is nontoxic and biologically inactive (almost inert), a fibrous tissue of variable thickness forms.
If the materials is nontoxic and biologically active (bioactive), an interfacial bond forms.
If the material is nontoxic and dissolves, the surrounding tissue replaces it.

---

### 2.2.1 Alumina and zirconia

High-density, high-purity  $\text{Al}_2\text{O}_3$  ( $\alpha$ -alumina) was the first bioceramic widely used clinically. It is used in total hip prosthesis and dental implants because of its combination of excellent corrosion resistance, good biocompatibility, low friction, high wear resistance, and high strength.  $\text{Al}_2\text{O}_3$  with small grains ( $< 4 \mu\text{m}$ ) exhibits

exceptionally low coefficient of friction and minimal wear rates, and thus has been used in orthopaedic surgery for more than 20 years as the articulating surface in total hip prostheses. The primary use of  $\text{Al}_2\text{O}_3$  in the United States is for the ball of the hip joint with the acetabular component being ultrahigh-molecular-weight polyethylene.

Another bioinert polycrystalline bioceramic used in total joint prostheses is zirconia.  $\text{ZrO}_2$  is a well-known polymorph that occurs in three forms: monoclinic, cubic, and tetragonal. Pure  $\text{ZrO}_2$  is monoclinic at room temperature, which is stable up to 1170 °C. Above this temperature it transforms into tetragonal and then into cubic phase at 2370 °C. During cooling, a tetragonal-monoclinic phase transformation takes place with a volume expansion of approximately 3-4%. Stresses generated by the expansion originate cracks in pure  $\text{ZrO}_2$  ceramics. Ruff and coworkers [Ruff *et al.*, 1929] showed the feasibility of the stabilization of cubic phase to room temperature by adding small amounts of CaO. The addition of 'stabilizing' oxides, like CaO, MgO,  $\text{CeO}_2$ ,  $\text{Y}_2\text{O}_3$ , to pure  $\text{ZrO}_2$  allows to generate multiphase materials known as Partially Stabilized Zirconia (PSZ), whose microstructure at room temperature generally consists [Subbarao, 1981] of cubic  $\text{ZrO}_2$  as the major phase, with monoclinic and tetragonal  $\text{ZrO}_2$  precipitates as the minor phase. Compared to  $\text{Al}_2\text{O}_3$ , PSZ has higher fracture toughness and lower Young's modulus, which is better for bone implant [Piconi *et al.*, 1999].

$\text{ZrO}_2$ , in tetragonal form, stabilized by either magnesium or yttrium, has been developed as a medical-grade bioceramic for use in total joint prostheses. The interest

in ZrO<sub>2</sub> derives from its high fracture toughness and tensile strength. These improved properties make it possible to manufacture femoral heads for total hip prostheses that are smaller than the present generation of Al<sub>2</sub>O<sub>3</sub> heads. Most of the ZrO<sub>2</sub> femoral heads in use now consists of 97 mol% ZrO<sub>2</sub> and 3 mol% Y<sub>2</sub>O<sub>3</sub>. It has been reported that over 400,000 ZrO<sub>2</sub> hip joint femoral heads have been implanted since 1985 until 2001 [Cordingley *et al.*, 2003]. Developments are in progress for application of these ceramic materials in other medical devices.

### **2.2.2 Bioglasses and calcium silicates**

Bioactive glasses are a group of surface reactive glass-ceramics that include the original bioactive glass (Bioglass®) first developed by Larry Hench and colleagues [Hench *et al.*, 1971]. Upon implantation, the surface of the materials forms a biologically active hydroxycarbonate apatite layer that provides the bonding interface with bone tissue.

Bonding to bone was first demonstrated for a certain compositional range of bioactive glasses that contained SiO<sub>2</sub>, Na<sub>2</sub>O, CaO, and P<sub>2</sub>O<sub>5</sub> in specific proportions [Hench *et al.*, 1971]. What distinguish these glasses from traditional soda–lime–silica glasses are their compositional features: <60 mol% SiO<sub>2</sub>, high Na<sub>2</sub>O and CaO content, and high CaO:P<sub>2</sub>O<sub>5</sub> ratio. Glasses with substantially larger amounts of P<sub>2</sub>O<sub>5</sub> do not bond to bone. Many bioactive SiO<sub>2</sub> glasses are based upon the so-called 45S5 Bioglass®, which has a composition of 45 wt% SiO<sub>2</sub>, 24.5 wt% CaO, 24.5 wt% NaO<sub>2</sub>,

and 6 wt% P<sub>2</sub>O<sub>5</sub>. Certain amount of B<sub>2</sub>O<sub>3</sub> and CaF<sub>2</sub> can be used to substitute SiO<sub>2</sub> and CaO, respectively, in the 45S5 formula without losing the bioactivity of the material. However, addition of as little as 3 wt% Al<sub>2</sub>O<sub>3</sub> to the 45S5 formula prevents bonding to bone [Hench *et al.*, 1973].

The clinically most important bioactive glass-ceramic is the three-phase silica-phosphate material composed of oxyfluorapatite Ca<sub>10</sub>(PO<sub>4</sub>)<sub>6</sub>(OH,F)<sub>2</sub> and wollastonite (CaSiO<sub>3</sub>) crystals and a residual CaO-SiO<sub>2</sub>-rich glassy matrix, termed A/W glass-ceramic [Nakamura *et al.*, 1985]. A/W glass-ceramic has excellent mechanical properties and forms a bond with bone that has a very high interfacial bond strength [Kitsugi *et al.*, 1989].

Bioglasses and bioactive glass-ceramics have found applications in middle ear, alveolar ridge maintenance implants, and other non-load bearing conditions. Various kinds of bioactive glasses and glass-ceramics with different functions such as high mechanical strength, high machinability and fast setting ability have been developed.

In recent year, calcium silicate ceramics have received increasing attention as candidate materials for orthopaedic and dental implant applications. New studies indicate that some calcium silicates such as CaSiO<sub>3</sub> [Liu *et al.*, 2001; Ni *et al.*, 2006; Ryu *et al.*, 2005] and pseudowollastonite ( $\alpha$ -CaSiO<sub>3</sub>) [Aza *et al.*, 1996] also have excellent bioactivity. Investigations have revealed that dicalcium silicate (Ca<sub>2</sub>SiO<sub>4</sub>) powders [Gou *et al.*, 2004] and plasma sprayed coating [Liu *et al.*, 2003] on titanium alloy substrates exhibited good in vitro bioactivity. Tricalcium silicate (Ca<sub>3</sub>SiO<sub>5</sub>) is

analogous with calcium silicate and dicalcium silicate in component. It has been reported that  $\text{Ca}_3\text{SiO}_5$  exhibits bioactivity and its powders could induce bone-like apatite formation after soaking in simulated body fluid (SBF) [Zhao *et al.*, 2007]. The development of bioactive or biodegradable calcium silicate ceramics may open up new possibilities in the field of bone tissue engineering.

### **2.2.3 Hydroxyapatite and other calcium phosphates**

#### **2.2.3.1 Calcium phosphates**

Calcium phosphate is a family of minerals containing calcium ions ( $\text{Ca}^{2+}$ ) together with orthophosphates ( $\text{PO}_4^{3-}$ ), metaphosphates or pyrophosphates ( $\text{P}_2\text{O}_7^{4-}$ ) and occasionally hydrogen or hydroxide ions. The main mineral component of bone and tooth enamel is made up of hydroxyapatite, a calcium phosphate. It has been known for more than twenty years that ceramics made of calcium phosphates can be used successfully for replacing and augmenting bone tissue. The most widely used calcium phosphate bioceramics are hydroxyapatite and  $\beta$ -tricalcium phosphate. Applications include coatings of orthopaedic and dental implants, alveolar ridge augmentation, maxillofacial surgery, otolaryngology, and scaffolds for bone growth and as powders in total hip and knee surgery.

Table 2-4 presents the known calcium phosphate phases. Abbreviations have been introduced to distinguish between the different compounds. Different phases of calcium phosphate ceramics are used depending on whether a resorbable or bioactive

Table 2-4 Properties of the biologically relevant calcium orthophosphates [Dorozhkin *et al.*, 2002].

Ca/P ratio	Compound	Formula	Solubility at 25 °C, -log(K <sub>sp</sub> )	Solubility at 37 °C, -log(K <sub>sp</sub> )	pH stability range in aqueous solution at 25 °C
0.5	Monocalcium phosphate monohydrate (MCPM)	Ca(H <sub>2</sub> PO <sub>4</sub> ) <sub>2</sub> ·H <sub>2</sub> O	1.14	No data	0.0-2.0
0.5	Monocalcium phosphate anhydrate (MCPA)	Ca(H <sub>2</sub> PO <sub>4</sub> ) <sub>2</sub>	1.14	No data	(d)
1.0	Dicalcium phosphate dihydrate (DCPD, "brushite")	CaHPO <sub>4</sub> ·2H <sub>2</sub> O	6.59	6.63	2.0-6.0
1.0	Dicalcium phosphate anhydrate (DCPA, "monetite")	CaHPO <sub>4</sub>	6.90	7.02	(d)
1.33	Octacalcium phosphate (OCP)	Ca <sub>8</sub> (HPO <sub>4</sub> ) <sub>2</sub> (PO <sub>4</sub> ) <sub>4</sub> ·5H <sub>2</sub> O	96.6	95.9	5.5-7.0
1.5	α-tricalcium phosphate (α-TCP)	α-Ca <sub>3</sub> (PO <sub>4</sub> ) <sub>2</sub>	25.5	25.5	(b)
1.5	β-tricalcium phosphate (β-TCP)	β-Ca <sub>3</sub> (PO <sub>4</sub> ) <sub>2</sub>	28.9	29.5	(b)
1.2-2.2	Amorphous calcium phosphate (ACP)	Ca <sub>x</sub> (PO <sub>4</sub> ) <sub>y</sub> ·nH <sub>2</sub> O	(c)	(c)	(e)
1.5-1.67	Calcium-deficient hydroxyapatite (CDHA)	Ca <sub>10-x</sub> (HPO <sub>4</sub> ) <sub>x</sub> (PO <sub>4</sub> ) <sub>6-x</sub> (OH) <sub>2-x</sub> (0<x<1)	≈ 85.1	≈ 85.1	6.5-9.5
1.67	Hydroxyapatite (HA)	Ca <sub>10</sub> (PO <sub>4</sub> ) <sub>6</sub> (OH) <sub>2</sub>	116.8	117.2	9.5-12
2.0	Tetracalcium phosphate (TTCP)	Ca <sub>4</sub> (PO <sub>4</sub> ) <sub>2</sub> O	38-44	37-42	(b)

(a) The solubility is given as the logarithm of the ion product of the given formulae (excluding hydrate water) with concentrations in mol/l. (b) These compounds cannot be precipitated from aqueous solutions. (c) Cannot be measured precisely. However, the following values were reported: 25.7 ± 0.1 (pH 7.40), 29.9 ± 0.1 (pH 6.00), 32.7 ± 0.1 (pH 5.28). (d) Stable at temperatures above 100 °C. (e) Always metastable. The composition of a precipitate depends on the solution pH value and composition.

Table 2-5 Crystallographic data of calcium phosphates [Dorozhkin *et al.*, 2002].

Compound	Space group	Unit cell parameters <sup>(a)</sup>	Z <sup>(b)</sup>	Density (g/cm <sup>3</sup> )
MCPM	Triclinic P $\bar{1}$	a=5.6261(5), b=11.889(2), c=6.4731(8) $\alpha$ =98.633(6), $\beta$ =118.262(6), $\gamma$ =83.344(6)	2	2.23
MCPA	Triclinic P $\bar{1}$	a=7.5577(5), b=8.2531(6), c=5.5504(3) $\alpha$ =109.87(1), $\beta$ =93.68(1), $\gamma$ =109.15(1)	2	2.58
DCPD	Monoclinic Ia	a=5.812(2), b=15.180(3), c=6.239(2) $\beta$ =116.42(3)	4	2.32
D CPA	Triclinic P $\bar{1}$	a=6.910(1), b=6.627(2), c=6.998(2) $\alpha$ =96.34(2), $\beta$ =103.82(2), $\gamma$ =88.33(2)	4	2.89
OCP	Triclinic P $\bar{1}$	a=19.692(4), b=9.523(2), c=6.835(2) $\alpha$ =90.15(2), $\beta$ =92.54(2), $\gamma$ =108.65(1)	1	2.61
$\alpha$ -TCP	Monoclinic P2 <sub>1</sub> /a	a=12.887(2), b=27.280(4), c=15.219(2) $\beta$ =126.20(1)	24	2.86
$\beta$ -TCP	Rhombohedral R3cH	a=b=10.439(1), c=37.375(6) $\gamma$ =120	21 <sup>(c)</sup>	3.07
HA	Monoclinic P2 <sub>1</sub> /b or hexagonal P6 <sub>3</sub> /m	a=9.84214(8), b=2a, c=6.8814(7) $\gamma$ =120 (monoclinic) a=b=9.4302(5), c=6.8911(2) $\gamma$ =120 (hexagonal)	4 2	3.16
TTCP	Monoclinic P2 <sub>1</sub>	a=7.023(1), b=11.986(4), c=9.473(2) $\beta$ =90.90(1)	4	3.05

(a) a, b, c are given in Å and  $\alpha$ ,  $\beta$ ,  $\gamma$  in °. (b) Number of formula units per unit cell. (c) Per hexagonal unit cell.

material is desired. For the chemically pure compounds, the Ca/P ratio can be between 0.5 - 2.0. In general, the lower the Ca/P ratio, the more acidic and soluble in water the calcium phosphate is. Table 2-5 gives the crystallographic data of these compounds.

The stability of calcium phosphate ceramics is influenced considerably by temperature and the presence of water, either during processing or in the use environment [Groot, 1988]. At body temperature, only two calcium phosphates are stable in contact with aqueous media, such as body fluids: at pH < 4.2, the stable

phase is DCPD, whereas, at  $\text{pH} > 4.2$ , the stable phase is HA. At higher temperatures, other phases, such as TCP and TTCP are present.  $\beta$ -TCP turns into  $\alpha$ -TCP at around  $1200^\circ\text{C}$ . The latter is considered to be stable in the range of  $700$  to  $1200^\circ\text{C}$ .  $\beta$ -TCP is highly soluble in body fluids. When HA and  $\beta$ -TCP are put in contact with living tissues, several interactions occur. As HA and TCP have a lower solubility product than the calcium phosphate ionic product of body fluids, they induce the formation on their surface, of a calcium phosphate apatite from ions present in the fluids. The first stage is the interaction with collagen and later accumulation of proteins and cells on the surface of the material, followed by resorption of the material and bone formation [Thamaraiselvi *et al.*, 2004].

Sintering of calcium phosphate ceramics usually occurs at  $1000^\circ\text{--}1500^\circ\text{C}$  [Groot, 1983]. The phases formed depend on temperature and the partial pressure of water in the sintering atmosphere. When water is present, HA can be formed and is a stable phase up to  $1360^\circ\text{C}$ . When there is no water, TCP and TTCP are the stable phases.

The mechanical behavior of calcium phosphate ceramics strongly influences their application as implants. Tensile and compressive strength and fatigue resistance depend on the total volume of porosity. Porosity can be in the form of micropores ( $<1\ \mu\text{m}$  diameter, due to incomplete sintering) or macropores ( $>100\ \mu\text{m}$  diameter, created to permit bone growth). Due to low reliability under tensile loads, in clinical practice, calcium phosphate bioceramics are used as powders; small, unloaded implants; dental

implants (with reinforcing metal posts); coatings on metal implants; low-loaded porous implants (where bone growth acts as a reinforcing phase); or bioactive phase in a polymer–bioactive ceramic composite.

### 2.2.3.2 Hydroxyapatite

Because of the chemical and crystallographic similarities to bone and teeth mineral, hydroxyapatite (HA) has become the focus of a significant research effort [1994; Ducheyne *et al.*, 1992; Ducheyne *et al.*, 1986; Hench, 1998; Hsieh *et al.*, 2002; Kannan *et al.*, 2005; Koutsopoulos, 2002; Liu *et al.*, 2004b; Moroni *et al.*, 1997; Sousa *et al.*, 1995; Zhitomirsky, 2000b; Zhitomirsky *et al.*, 1997b].

HA is the most stable and least soluble of all calcium orthophosphates. Pure HA crystallizes in the monoclinic space group  $P2_1/b$ . However, at temperatures above 250 °C, there is a monoclinic to hexagonal (space group  $P6_3/m$ ) phase transition in HA [Elliot, 1994]. Some impurities, like partial substitution of hydroxide by fluoride or chloride ions, stabilize the hexagonal structure of HA at ambient temperature. For this reason, natural HA always exhibits a hexagonal space group.

The  $\text{Ca}^{2+}$ ,  $\text{PO}_4^{3-}$ , and  $\text{OH}^-$  ions in HA can be replaced by other ions during processing or in physiological surroundings, forming other apatite phases such as fluorapatite ( $\text{Ca}_{10}(\text{PO}_4)_6(\text{OH})_{2-x}\text{F}_x$ , with  $0 < x < 2$ ) and carbonate apatite ( $\text{Ca}_{10}(\text{PO}_4)_6(\text{OH})_{2-2x}(\text{CO}_3)_x$  or  $\text{Ca}_{10-x+y}(\text{PO}_4)_{6-x}(\text{OH})_{2-x-2y}$ , where  $0 < x < 2$  and  $0 < y < x$ ) [LeGeros *et al.*, 1993]. Fluorapatite is found in dental enamel and hydroxycarbonate

apatite is present in bone.

HA can be prepared in aqueous solutions by mixing exactly stoichiometric quantities of calcium- and phosphate-containing solutions at  $\text{pH} > 9$ , followed by boiling, filtration, and drying. Microcrystalline samples of HA can also be prepared by solid-state reactions of other calcium phosphates (e.g. MCPM, DCPA, DCPD, OCP) with  $\text{CaO}$ ,  $\text{Ca}(\text{OH})_2$ , or  $\text{CaCO}_3$  at temperatures above  $1200\text{ }^\circ\text{C}$ , in an atmosphere of equal volumes of water and nitrogen. Single crystals of HA can be prepared by hydrothermal synthesis.

Unlike the other calcium phosphates, HA does not break down under physiological conditions. In fact, it is thermodynamically stable at physiological pH and forms strong chemical bonds with surrounding bone. Normal bone attaches to HA implants through a thin epitaxial bonding layer. HA has been shown to have a stimulating effect on bone formation, also known as osseo-induction. Pfaff *et al.* reported [Pfaff *et al.*, 1993] that the long-term stability of HA is guaranteed in particular by the phase purity, because a chemical breakdown of the layer is induced by higher solubility of foreign phases.

While its mechanical properties have been found to be unsuitable for load-bearing applications, HA is used as a coating on materials such as titanium and titanium alloys, where it can contribute its 'bioactive' properties, while the metallic component bears the load. A successful example is the bioactive coatings on total hip prosthesis. Synthetic HA ceramic coatings are applied to specific areas of prosthesis to

enhance the bone bonding and biological fixation. The merger of the concepts of biological fixation, enhanced bone formation by a bioactive coating, and optimization of biomechanical stress transfer to the host bone is a major accomplishment of the past 20 years of research and development in orthopaedic total joint replacement [Hench, 1998]. Currently such coatings are applied by plasma spraying, during which thermal decomposition of HA into other soluble calcium phosphates can be induced by the high processing temperatures.

### **2.3 Electrodeposition techniques**

Recently, increasing research interest has been attracted to the fabrication of ceramic and ceramic-polymer composite coatings by means of electrodeposition process [Biest *et al.*, 1999; Chen *et al.*, 1998; Pang *et al.*, 2005a; Redepenning *et al.*, 2003; Zhitomirsky, 2000a, 2002; Zhitomirsky *et al.*, 2003; Zhitomirsky *et al.*, 2001b, 2002a; Zhitomirsky *et al.*, 2002b]. The main reason is that electrodeposition offers a lot of advantages over other surface modification techniques:

- Capability of manufacturing nanostructured multi-component films.
- High purity of deposited materials.
- Applicable to substrates of complex shape.
- Can be used for deposition of ceramics, glasses, polymers, composites.
- Rigid control of the composition and microstructure of deposit.
- Low cost of equipment and materials.

- Easy to be scaled up to industry level.

Electrodeposition of ceramic materials can be performed either by cathodic or anodic methods. However, anodic deposition has limited utility regarding possible materials to be deposited and substrates used for deposition. Cathodic deposition has important advantages for industrial applications. Two processes are commonly used to prepare ceramic coatings by cathodic electrodeposition: electrolytic deposition (ELD) and electrophoretic deposition (EPD). ELD produces colloidal particles in cathodic reactions for subsequent deposition. EPD is achieved via motion of charged particles towards an electrode under an applied electric field. The range of thickness of coating deposited by these techniques is shown in Figure 2-1 [Zhitomirsky, 2002].

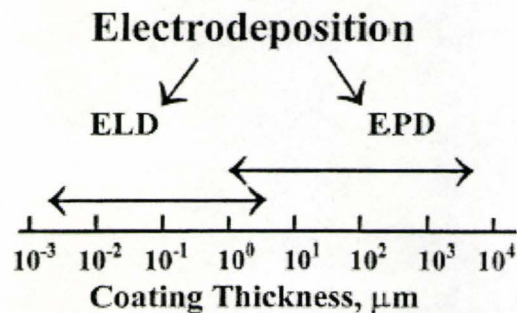


Figure 2-1 Thickness of coatings deposited using ELD and EPD.

Successful applications of cathodic electrodeposition require understanding of the deposition mechanisms. It is important to note that the hydrolysis reactions in ELD and the electrophoretic motion of charged particles in EPD method result in the accumulation of ceramic particles at the electrode. Deposit formation is achieved via

particle coagulation. A thorough understanding of the mechanisms of particle coagulation is crucial for successful electrodeposition and the development of new strategies for the fabrication of advanced ceramic and organoceramic coatings. To better understand the mechanisms of cathodic electrodeposition, the basics of ELD and EPD processes will be discussed in the following part. The topics include the classical Derjaguin-Landau-Verwey-Overbeek (DLVO) theory of colloidal stability, forces between colloidal particles, additives used in bath formulations, and other factors influencing deposit stability and structure formation.

### **2.3.1 Electrolytic deposition**

In cathodic ELD process, the pH in the bulk of solutions is low, whereas the cathodic reactions result in an increase in pH value near the cathode. The hydrolysis of water and some other cathodic reactions, which consume water and produce  $\text{OH}^-$ , result in a significant increase in pH value near the cathode [Zhitomirsky, 2002]. Various cationic species could be hydrolyzed by an electrogenerated base to form colloidal particles of oxides, hydroxides or peroxides [Aries *et al.*, 1998; Chaim *et al.*, 1997; Yen, 2000]. Hydrolysis reactions result in the accumulation of colloidal particles near the electrode. The particle formation kinetics and deposit composition are influenced by solvent, additives, temperature and current density [Chaim *et al.*, 1991; Gal-Or *et al.*, 1991; Pang *et al.*, 2005c; Yen, 2000; Yen, 1999; Zhitomirsky, 1998c, 2000d, 2002]. It was shown [Zhitomirsky, 2000d] that the formation of a

deposit is caused by flocculation introduced by the electrolyte. It is important to note that some pH changes take place, even at open circuit [Hughes *et al.*, 1995], leading to deposit formation.

ELD enables rigid control of film thickness, uniformity and deposition rate. The uniformity of ELD films results from the insulating properties of the deposits and the electric field dependence of the deposition rate. Particle coagulation could be enhanced by Columbic attraction [Sogami *et al.*, 1984], resulting from ion correlation and depletion forces. Cationic surfactants and polyelectrolytes act as electrolytes in compressing the double layer of ceramic particles, resulting in particle flocculation and increasing the deposition process efficiency [Zhitomirsky, 2000a]. As cathodic reactions result in a significant increase in pH value near the cathode, and it is expected that the colloidal particles formed near the cathode could be negatively charged [Zhitomirsky, 2000a]. This may lead to a low adhesion of the deposit on the cathode, which has also negative charges.

### **2.3.2 Electrophoretic deposition**

The mechanisms of EPD have been discussed in numerous publications [Biest *et al.*, 1999; Boccaccini *et al.*, 2002a; Damodaran *et al.*, 1993; Ohshima, 1995; Sridhar *et al.*, 2002; Zhitomirsky, 1998c, 2000a; Zhitomirsky *et al.*, 1997b]. One hypothesis is that charged particles undergo reactions at the electrode, which reduce their surface charge or neutralize them. A difference in pH near electrodes compared with the rest

of the suspension is believed to play a major role in this reduction of charge. The competing forces governing the formation of deposit in the vicinity of the electrode include: the van der Waals' force between particles; the interparticle repulsion of charged particles; the interaction of the deposit forming particles and ions or electrolytes in the suspension; and the pressure exerted by the motion of the charged particles under the influence of applied electric field.

According to Hamaker and Verwey [Hamaker *et al.*, 1940], the formation of a deposit by electrophoresis is similar to the formation of a sediment due to gravitation. The pressure exerted by incoming particles enables particles next to the deposit to overcome the interparticle repulsion. It is important to note that electrophoresis results in the accumulation of charged particles at the electrode surface. The deposit formation is achieved via the particle coagulation, which is influenced by the electrode reactions, solvents, additives and other factors [Biest *et al.*, 1999; Pang *et al.*, 2005a; Zhitomirsky, 2000c, 2002].

In several experiments [Bouyer *et al.*, 1999; Brown *et al.*, 1965; Harbach *et al.*, 1998; Russ *et al.*, 1998a; Zhitomirsky, 1998d] EPD of ceramic particles was performed in the presence of electrolytes and polyelectrolytes. These additives are adsorbed on the particles to create positive charges and stabilize the suspensions. The additives are also important for the deposition of uniform and adherent deposits. EPD of ceramic particles could be associated with ELD of hydroxides or alkoxides, which form an adhesive matrix [Brown *et al.*, 1965; Russ *et al.*, 1998a]. The adhesive

materials promote particle coagulation and bind the particles to the substrate. Therefore, the binder materials may enhance the effect of the van der Waals' force.

EPD of composite materials is an area of intense interest [Boccaccini *et al.*, 1998; Kaya *et al.*, 1999; Limmer *et al.*, 2002; Moreno *et al.*, 2000; Van der Biest *et al.*, 1999; Zhitomirsky, 2002]. Many important advantages of EPD can be cited [Boccaccini *et al.*, 1998; Kaya *et al.*, 1999; Limmer *et al.*, 2002; Moreno *et al.*, 2000; Van der Biest *et al.*, 1999; Zhitomirsky, 2002], which make this technique important for various applications. EPD can be applied to polyelectrolytes and inorganic nanoparticles for the fabrication of advanced composite materials. Moreover, EPD could be combined with other electrochemical strategies [Russ *et al.*, 1998a].

### **2.3.3 Particle interactions and suspension stability**

#### **2.3.3.1 The DLVO theory**

The state of dispersion of particles in suspension can be controlled by careful manipulation of the interparticle forces and their interactions. A quantitative description of the relationship between stability of suspension and energies of interactions between colloidal particles and other surfaces in a liquid has been given by the classical DLVO (Derjaguin-Landau-Verwey-Overbeek) theory [Verwey *et al.*, 1948]. According to this theory, the stability of a colloidal system is determined by the total pair interaction between colloidal particles, which consists of coulombic double-layer repulsion and van der Waals' attraction. The total energy  $V_T$  of

interaction of two isolated, identically charged particles may be defined as:

$$V_T = V_A + V_R \quad (2-1)$$

The attractive energy  $V_A$  of the London-van der Waals' interaction between two spherical particles can be expressed by:

$$V_A = -\frac{A}{6} \left( \frac{2}{s^2 - 4} + \frac{2}{s^2} + \ln \frac{s^2 - 4}{s^2} \right) \quad (2-2)$$

where  $A$  is the Hamaker constant and  $s = 2 + H/a$ , with  $H$  the shortest distance between the two spheres and  $a$  the particle radius. If  $H \ll a$ , Equation (2-2) can be simplified to:

$$V_A = -A \frac{a}{12H} \quad (2-3)$$

The repulsive energy  $V_R$  is:

$$V_R = 2\pi\epsilon\epsilon_0 a \psi^2 \ln[1 + e^{-\kappa H}] \quad (2-4)$$

where  $\epsilon$  is the dielectric constant of the solvent,  $\epsilon_0$  is the vacuum dielectric permittivity,  $\psi$  is the surface potential,  $1/\kappa$  is the Debye length:

$$\kappa = \left( \frac{e^2 \sum n_i z_i^2}{\epsilon\epsilon_0 kT} \right)^{1/2} \quad (2-5)$$

where  $e_0$  is the electron charge,  $k$  is the Boltzmann constant,  $T$  is the absolute

temperature,  $n_i$  is the concentration of ions with valence  $z_i$ . Repulsion between colloidal particles is directly related to the diffuse layer charge on the particles.

The DLVO theory describes the potential energy curve for pair interaction, as shown in Figure 2-2a. When the diffuse-layer repulsion is sufficiently high compared to the van der Waals' attraction, the total energy of particle interaction exhibits a maximum, which makes an energy barrier to particle coagulation.

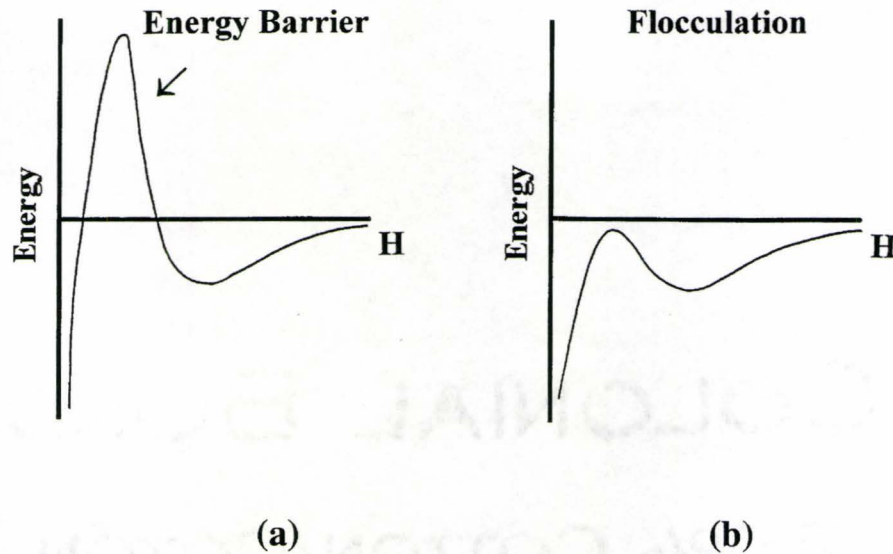


Figure 2-2 Total interaction energy between spherical particles as a function of interparticle separation according to the DLVO theory.

The thickness of the double layer (characterized by the Debye length,  $1/\kappa$ ) is very sensitive to the electrolyte concentration [Verwey *et al.*, 1948]. The DLVO theory explains the existence of a critical electrolyte concentration (flocculation value) for coagulation, decreasing with the valence of the electrolyte ions of a charge

opposite to that of the colloidal particles (rule of Schulze and Hardey [Verwey *et al.*, 1948]). It was demonstrated that the potential energy peak decreases as the electrolyte concentration increases. As the energy barrier disappears, coagulation becomes possible (Figure 2-2b). Flocculation by ions compressing the double layer also follows the Hofmeister series [Verwey *et al.*, 1948]. Within the series of ions of the same charge, the flocculation value increases in the order:

$\text{NH}_4^+$ ,  $\text{K}^+$ ,  $\text{Na}^+$ ,  $\text{Li}^+$ ; and

$\text{Ba}^{2+}$ ,  $\text{Sr}^{2+}$ ,  $\text{Ca}^{2+}$ ,  $\text{Mg}^{2+}$

Therefore, a negatively charged sol is flocculated by large cations at a smaller concentration than by small cations of the same valency. The flocculation value was found to be in the range 20-200 for monovalent ions, 0.3-3 for divalent ions, and 0.003-0.1 for trivalent ions [Verwey *et al.*, 1948]. Flocculation values are affected by sol concentration, temperature, particle size of the colloid, and chemical nature of the sol.

### **2.3.3.2 Other interparticle forces**

In the original DLVO theory, only the van der Waals and electrostatic interactions were considered. Now it has also been identified that in addition to these forces, other physical interactions have to be considered. The attractive ion correlation force between particles could be significant enough to cause aggregation and flocculation of colloidal particles [Chu *et al.*, 1995]. Ions present in ELD and EPD

baths could also influence particle interactions. Electric field-induced aggregation of fine ceramic particles has been observed in the bulk of suspensions during EPD [Zhitomirsky *et al.*, 1997b]. Forces of other origins, such as long-range attractions [Larsen *et al.*, 1997], electrohydrodynamic flows [Trau *et al.*, 1997], polarization interaction [Lavrov *et al.*, 1969], and capillary interactions [Kralchevsky *et al.*, 1994] etc., can also act between the particles.

It is important to note that stabilization of colloidal dispersions may also be influenced by steric stabilization and structural forces. These mechanisms become important when there are macromolecules adsorbed or bounded to the particle surface. Stabilisation is caused by the repulsion between these adsorbed macromolecules. The steric stabilization forces are generally short-range forces ( $< 2$  nm) [Besra *et al.*, 2007]. Presence of these forces can also change the shape of the potential well that controls the particle–substrate interaction.

Caution must be exercised in using sterically stabilized suspension for EPD because the addition of polymers to a colloidal suspension might lead to both attractive and repulsive forces. In other words, polymer adsorption may lead to colloid stability or to particle flocculation. Steric repulsion depends on the thickness of the adsorbed layer, the configuration of the polymer, the firmness with which the polymer is anchored to the surface, and the fraction of molecules adsorbed. Adsorbed polyelectrolytes or neutral polymers may induce flocculation by charge neutralization or bridging flocculation [Ennis *et al.*, 2000; Hoogeveen *et al.*, 1996a]. According to

[Hoogeveen *et al.*, 1996b; Okubo *et al.*, 1999], the attraction between colloidal particles and polyelectrolytes includes electrostatic, hydrophobic, and dipole-dipole interactions. The interaction between two charged surfaces neutralized by grafted polyelectrolytes and counterions has been studied in [Ennis *et al.*, 2000]. In salt-free systems, a long-range repulsion due to free counterions and short-range bridging attraction was considered. It was demonstrated that the addition of salts screens the long-range repulsion. The flocculation or stabilization of colloidal particles may also be induced by non-adsorbing polymers. Addition of non-adsorbing polymer may lead to depletion flocculation or depletion stabilization [Dickinson *et al.*, 1991].

Well dispersed and stable suspensions are very important for the successful deposition. In general, suspensions can be dispersed by electrostatic, steric, or electrosteric stabilization mechanisms. The suspension stability is characterized by settling rate and tendency to undergo or avoid flocculation. Suspensions containing colloidal particles which are 1  $\mu\text{m}$  or less in diameter tend to be stable due to Brownian motion of the particles. Particles larger than 1  $\mu\text{m}$  require continuous hydrodynamic agitation to remain in suspension. Flocculating suspensions settle rapidly and form low density, weakly adhering deposits. It is important to note that deposition will not occur if a suspension is too stable, because the repulsive forces between the particles will not be overcome by the electric field. According to some models for EPD, the suspension should be unstable in the vicinity of the electrodes [Sarkar *et al.*, 1996]. This local instability could be caused by the formation of ions

from electrolysis or discharge of the particles. These ions then cause flocculation close to the electrode surface. Most investigators use zeta ( $\zeta$ ) potential or electrophoretic mobility to characterize a suspension.

#### **2.3.4 Particle charging**

The particles in suspension will electrophoretically move in response to the electric field if they carry a charge. Four mechanisms have been identified by which the charge on the particles can be developed [Heavens, 1990]: (a) selective adsorption of ions onto the solid particle from the liquid, (b) dissociation of ions from the solid phase into the liquid, (c) adsorption or orientation of dipolar molecules at the particles surface, and (d) electron transfer between the solid and liquid phase due to differences in work function.

A charged particle in a suspension is surrounded by ions with an opposite charge in a concentration higher than the bulk concentration of these ions. This is the so-called double-layer (Figure 2-3 [Van der Biest *et al.*, 1999]). When an electric field is applied, these ions and the particle should move in opposite directions. However, the ions are also attracted by the particle, and as a result, a fraction of the ions surrounding the particle will not move in the opposite direction but move along with the particle. Hence, the speed of a particle is not determined by the surface charge but by the net charge enclosed in the liquid sphere, which move along with the particle. The potential at the surface of shear is termed the  $\zeta$  potential or electrokinetic

potential.

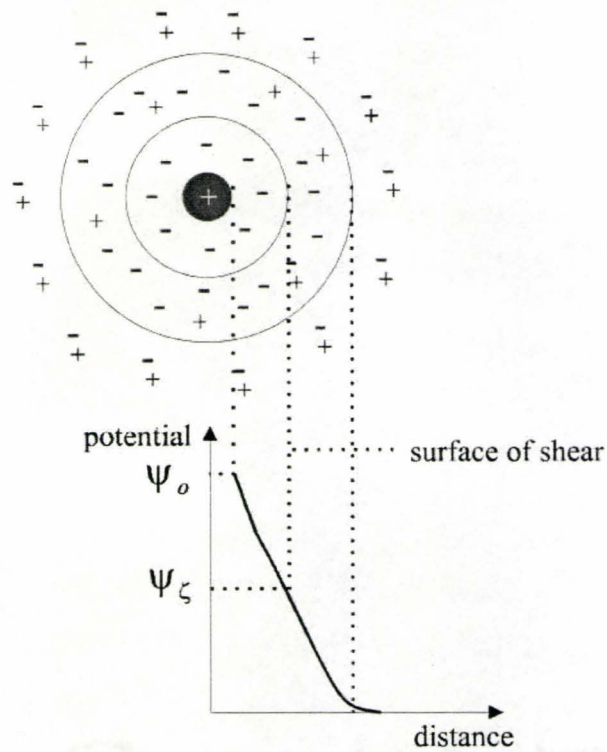


Figure 2-3 Schematic of the double layer surrounding a charged particle and evolution of the electric potential from the surface potential,  $\psi_0$ , to zero far from the particle. The potential at the surface of shear, the limit between the liquid moving with the particle and the liquid, which does not move with the particle, is termed the  $\zeta$  potential ( $\psi_\zeta$ ) and is the main parameter determining the electrokinetic behavior of the particle.

#### 2.3.4.1 Aqueous suspensions

In aqueous media, the charge at the particle-solvent interface could originate from adsorption or desorption of ions, or dissociation of surface groups. Surfaces of oxide particles dispersed in water tend to coordinate water molecules to form hydroxylated surfaces. The surfaces may become positively or negatively charged,

depending on pH:



According to the DLVO theory, colloidal stability is closely related to the  $\zeta$  potential of the colloidal particles. For aqueous suspensions of ceramic powders, especially oxides, the  $\zeta$  potential changes with pH if  $\text{H}^+$  and  $\text{OH}^-$  are potential-determining ions, showing an isoelectric point (IEP) (Figure 2-4). However, in the case of colloidal dispersions coagulated by the addition of hydrolysable metal ions or complexes, more complex behavior was observed. In some cases, no obvious correlation was observed between the  $\zeta$  potential and colloidal stability.

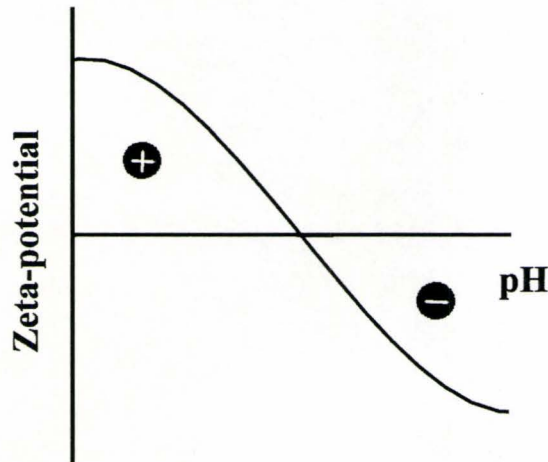


Figure 2-4  $\zeta$  potential of ceramic particles versus pH of suspension.

#### 2.3.4.2 Non-aqueous suspensions

In general, organic liquids are superior to water as a suspension medium for electrophoretic forming. The generally lower dielectric constant of organic liquids limits the charge on the particles as a result of the lower dissociating power. However, much higher field strengths can be used since the problems of electrolytic gas evolution, joule heating and electrochemical attack of the electrodes are greatly reduced.

For non-aqueous media the hydrogen concentration (pH) loses its validity as a general measure for the acidity or alkalinity of a medium. The concept of donor numbers, which expresses the tendency of a solvent to donate electrons, has been developed [Vandepierre *et al.*, 2000]. The relative measure of the alkalinity of a solvent is given by the enthalpy of its reaction with an arbitrarily chosen reference acid. Ranking the relative degree of acidity of media can be performed by using the acceptor number scale, a measure for the tendency of solvents to accept electrons. According to [Labib *et al.*, 1984], particle charging is achieved by electron transfer between the particle and solvent in non-aqueous media. The electron donicity is a measure of the tendency of a molecule to donate electrons in a donor-acceptor reaction. The important finding was that the  $\zeta$  potential of solid particles changes sign for some value of the solvent donicity  $D_{N_0}$ . Solvents having donicity  $D_N > D_{N_0}$  contribute electrons to the solid, resulting in negatively charged particles. Solvents having  $D_N < D_{N_0}$  take electrons from the solids, resulting in positively charged particles.

However, for some materials in the presence of moisture, the charge transfer may involve adsorption or desorption of ions, rather than electron transfer.

The selection of a suitable solvent is of great importance for dispersion and particle charging. The effect of the dielectric constant of the suspending media has been observed [Powers, 1975]. Different solvents may result in different charging modes. Water or organic acids could be used as proton donors [Powers, 1975]. It is important to note that different conditions of powder preparation could result in different surface characteristics of ceramic powders [Schultz *et al.*, 1993]. A good example is that no EPD of fresh HA powders was observed in [Ducheyne *et al.*, 1990], due to the adsorbed water in non-calcined powders. In contrast, nanostructured HA powders precipitated from aqueous solutions were deposited on various cathodic substrates [Zhitomirsky, 2000b; Zhitomirsky *et al.*, 1997b].

#### **2.3.4.3 Additives for particle charging**

A wide variety of additives can be used to control particle charge so as to produce well-dispersed suspensions, such as acids [Damodaran *et al.*, 1993; Harbach *et al.*, 1998], I<sub>2</sub>-H<sub>2</sub>O-acetone [Zhitomirsky, 1998a], NH<sub>4</sub>OH [Kuwabara *et al.*, 1991], and phosphate ester [Paik *et al.*, 1998] etc. Recently, increasing attention has been directed on the utilization of polymer additives to induce steric stabilization, where the organic macromolecules are attached to the particle surface, or depletion stabilization, where the macromolecules are free in suspension. The steric stabilization is effective

in both aqueous and non-aqueous media. Polyelectrolytes are widely used additives that can impart electrostatic and steric stabilization to a colloidal dispersion. The polyelectrolytes can be categorized into two groups: strong polyelectrolytes, for which the degree of ionization is independent of the solution pH, and weak polyelectrolytes, for which the degree of ionization is determined by the solution pH. Poly(ethylenimine) (PEI) is a weak cationic polyelectrolyte. An increase in pH decreases the charge of PEI. In contrast, Poly(diallyldimethylammonium chloride) (PDDA) is a strong polycation because of its quaternary ammonium group, and the degree of dissociation of the ionic groups is nearly pH-independent over a wide pH range. PEI and PDDA were used to stabilize ceramic suspensions, and as additives for particle charging and electrodeposition of various materials [Harbach *et al.*, 1998; Zhitomirsky, 2000a].

### 2.3.5 Solvents

A solvent acts as a vehicle that carries the ceramic particles in suspensions (EPD) or ions in solutions (ELD). The solvent used in electrodeposition must dissolve inorganic salts and organic additives. There are two principal types of solvents used for electrodeposition: water and organic liquids (Table 2-6). ELD needs a sufficient amount of water for base generation in cathodic reactions [Zhitomirsky *et al.*, 1999a]. Non-aqueous solvents prevent the deposit from hydrating. It is known that methanol is capable of extracting non-bridging hydroxo groups and free water [Jones *et al.*, 1988].

Mixed methyl alcohol-water and ethyl alcohol-water solutions were found to be preferable in order to reduce cracking and porosity in the electrolytic deposits [Zhitomirsky, 1998b; Zhitomirsky *et al.*, 1999a]. The addition of alcohols to aqueous solutions reduces the total dielectric constant of the solvent, and thus reduces the solubility of the deposits. It is in this regard that deposition experiments [Zhitomirsky, 1997] performed in mixed methyl alcohol-water solutions indicate a significant enhancement of the deposition rate. Repulsion between colloidal particles formed near the electrode is related to the diffuse-layer charge on the particles. The thickness of the double layer decreases with decreasing dielectric constant of the solvent, promoting particle coagulation. Solvents for EPD should be inert with respect to the powder. Organic liquids are superior to water as a suspension medium for EPD. The use of water-based suspensions causes gas formation from the hydrolysis of water, preventing the deposition of a uniform adherent layer and yielding pinholes. A variety of non-aqueous organic solvents (Table 2-6) are commonly used to prepare suspensions for EPD. The charge on a colloidal particle could originate from solvents. Alcohols are known to behave as proton donors and are important for particle charging. A mixture of solvents may also be useful to achieve particle charging [Yamashita *et al.*, 1997]. The addition of alcohols to aqueous suspensions of titania-containing electrolyte [Kosmulski *et al.*, 1999] resulted in a shift of the IEP towards higher pH values, or the absence of IEP. The experimental results presented in [Kosmulski *et al.*, 1999] indicate that the dielectric constant of the mixed solvent

could be the factor that governs the shift of IEP.

Table 2-6 Examples of solvents used for electrodeposition.

Solvent	Method of deposition	of Deposited material
Water	ELD	Al <sub>2</sub> O <sub>3</sub> -Cr <sub>2</sub> O <sub>3</sub> [Zhitomirsky <i>et al.</i> , 1997a], ZnO [Peulon <i>et al.</i> , 1996]
	EPD	Al <sub>2</sub> O <sub>3</sub> [Hirata <i>et al.</i> , 1991]
Dimethylformamide <sup>a</sup>	ELD	Y <sub>2</sub> O <sub>3</sub> [Matsuda <i>et al.</i> , 1993], TiO <sub>2</sub> [Zhitomirsky <i>et al.</i> , 1995]
Methyl alcohol-water	ELD	TiO <sub>2</sub> [Zhitomirsky <i>et al.</i> , 1999a], RuO <sub>2</sub> -TiO <sub>2</sub> [Zhitomirsky, 1998b]
Ethyl alcohol-water	ELD	CeO <sub>2</sub> [Zhitomirsky <i>et al.</i> , 1999b], SnO <sub>2</sub> [Zhitomirsky, 2000a]
	EPD	CaSiO <sub>3</sub> [Hayashi <i>et al.</i> , 1999]
Isopropyl alcohol	EPD	HA [Ducheyne <i>et al.</i> , 1990; Zhitomirsky, 2000b]
Isopropyl alcohol <sup>a</sup>	ELD	YBa <sub>2</sub> Cu <sub>3</sub> O <sub>7-x</sub> [Abolmaali <i>et al.</i> , 1993]
Ehtyl alcohol-acetylacetone	EPD	MgO, Al <sub>2</sub> O <sub>3</sub> [Yamashita <i>et al.</i> , 1997]
Glacial acetic acid	EPD	Lead Zirconate Titanate [Van Tassel <i>et al.</i> , 1999]
Ethyl alcohol	EPD	Al <sub>2</sub> O <sub>3</sub> , ZrO <sub>3</sub> [Nicholson <i>et al.</i> , 1993]
Dichloromethane	EPD	β-alumina [Foissy <i>et al.</i> , 1982]
Acetone	EPD	Y <sub>2</sub> O <sub>3</sub> -stabilized ZrO <sub>2</sub> [Ishihara <i>et al.</i> , 1996]
Acetylacetone	EPD	Y <sub>2</sub> O <sub>3</sub> -stabilized ZrO <sub>2</sub> [Ishihara <i>et al.</i> , 1996]
Cyclohexanone	EPD	Y <sub>2</sub> O <sub>3</sub> -stabilized ZrO <sub>2</sub> [Ishihara <i>et al.</i> , 1996]
Methyl ethyl ketone	EPD	Al <sub>2</sub> O <sub>3</sub> [Andrews <i>et al.</i> , 1969]
Toluene-ethyl alcohol	EPD	Al <sub>2</sub> O <sub>3</sub> [Andrews <i>et al.</i> , 1969]

<sup>a</sup> Solvent contained a small amount of water.

### 2.3.6 Binders

A binder is added to suspensions or solutions in order to increase the adherence and strength of the deposited material and prevent cracking. EPD of

sub-micrometer particles offers advantages in the fabrication of uniform ceramic coatings with dense packing and good sinterability. However, the use of fine particles initiates deposit cracking, which could be prevented by the use of binder. The optimal amount of binder depends on the particle size and particle surface area.

Many different binders have been used for non-aqueous EPD, including nitrocellulose [Andrews *et al.*, 1969; Mizuguchi *et al.*, 1983], alkyd resin [Andrews *et al.*, 1969], dewaxed shellac [Andrews *et al.*, 1969], and polyvinyl butyral (PVB) [Zhitomirsky, 1998d, 2000a]. It is advantageous to use a binder material, which also acts as a dispersant. Various dispersing aids with an inherent binding effect were used in [Harbach *et al.*, 1998]. Compared with non-aqueous solvents, the variety of water-soluble binders and dispersants is restricted. The low strength of water-soluble binders limits their applicability. Polyvinyl alcohol is an important binder material for aqueous EPD [Moreno *et al.*, 2000].

Polymer binders are common additives in ceramic processing. The most common binders used in EPD are non-ionic-type polymers (polyvinyl alcohol, polyvinyl butyral, ethylcellulose, polyacrylamide, etc.) [Zhitomirsky, 2000a]. The polymer macromolecules adsorb onto the surfaces of ceramic particles. Positively charged ceramic particles provide electrophoretic transport of the polymeric molecules to form deposits on cathodic substrates. Cationic polyelectrolytes with inherent binding properties, such as PDDA or PEI, could be used for particle charging [Zhitomirsky, 2000a] and EPD.

The application of neutral polymers to ELD presents difficulties, as the formation of ceramic particles is achieved near the electrode surface. One important finding was the feasibility of electrochemical intercalation of charged polyelectrolytes into electrolytic deposits [Zhitomirsky, 2000a]. Using cationic polyelectrolytes with inherent binding properties, problems related to cracking in electrolytic deposits could be diminished. Moreover, various organoceramic nanocomposites could be obtained using electrodeposition. The intercalation of polymers is achieved by their adsorption on the surface of colloidal particles, which are produced near the cathode and form a cathodic deposit.

The role of binders in EPD processing is multifunctional. Polymer binders are used to obtain adherent deposits and prevent cracks. In addition, the adsorbed polymer can provide steric stabilization of suspension of ceramic particles and reduce viscosity of the suspension. In EPD processing, charged ceramic particles transport adsorbed polymer to the electrode surface, thus allowing the polymer binder to be included in the deposit. The control of polymer adsorption is of paramount importance. The amount of polymer adsorption depends on polymer concentration in suspension and specific polymer-particle, polymer-solvent, particle-solvent, and particle-dispersant interactions. Good solvents are necessary in order to achieve high polymer concentration in solution. However, the polymer can be adsorbed on the surface of ceramic particles when its solubility in the dispersion medium is low. Adsorption of polymer on ceramic particles in poor solvent can result in bridging flocculation. In

contrast, good solvents are important to achieve steric stabilization. Polymer stabilizing moieties, which extend out from the particle surface must be well solvated in a good solvent. Therefore, for EPD, it could be advantageous to use copolymers of a block or graft type. Indeed, soluble polymers serve to anchor copolymer molecules to the particle surface, whereas chains of soluble polymers enable steric stabilization.

Metal alkoxides and hydroxides have also been used as binder materials [Russ *et al.*, 1998a; Siracuse *et al.*, 1990]. EPD of phosphor particles was performed from a bath containing  $\text{Mg}(\text{NO}_3)_2$ . Metal alkoxides or hydroxides formed on the cathode during deposition and acted as cementing materials to hold the deposit. The type of binder material formed is dependent on the amount of water in the deposition bath [Russ *et al.*, 1998a]. These results show that EPD and ELD could be combined to form advanced deposits.

### **2.3.7 The electrical double layer and electrophoretic mobility**

Most substances acquire surface electric charge when brought in contact with a polar (e.g. aqueous) medium. This surface charge influences the distribution of nearby ions in the polar medium. The ions, which establish the surface charge, are called potential determining ions. These normally include ions of which the solid is composed; hydrogen and hydroxyl ions, ions capable of forming complex or insoluble salts with the solid surface species. Ions of opposite charge (counter-ions) are attracted towards the surface and ions of like charge (co-ions) are repelled away from the

surface. This leads to the formation of a net electrical charge of one sign on one side of the interface and a charge of opposite sign on the other side, giving rise to what is called the electrical double layer. Figure 2-5 shows the schematic of a typical electrical double layer [Weise, 1985]. A widely accepted model for the double layer is the Stern model [Stern, 1924], which was later modified by Graham [Hunter, 1981]. In the modified model, a part of the counter-ion charge is located close to the particle surface (Stern layer) and the remainder is distributed more broadly in the diffuse double layer or lyosphere. The Stern layer is actually a hypothetical plane representing the closest distance of approach of hydrated counter ions to the surface. A schematic representation of the distribution of charge species and the potential drop across the double layer in accordance with the Stern model is also represented in Figure 2-5.

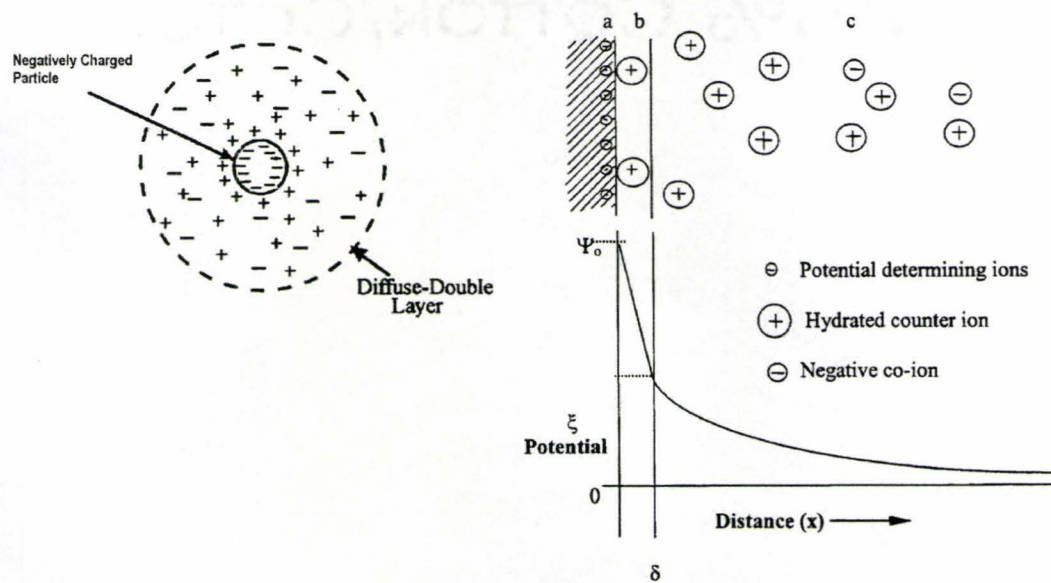


Figure 2-5 Schematic representation of the double layer and potential drop across the double layer: (a) surface charge, (b) Stern layer, (c) diffuse layers of counter-ions.

A major field of investigation in modern colloid and interface science has been the search for a means to predict and determine the exact distribution of electrical charges at or near the solid–liquid interface. The interaction between charged particles is governed predominantly by the overlap of the diffuse layer, and accordingly the potential most relevant to the interaction is the one developed at the boundary between the Stern and diffuse layer ( $\psi_\delta$ ). The potential ( $\psi$ ) at a distance  $x$  from the Stern plane may be represented by the Poisson– Boltzmann expression:

$$\psi = \psi_\delta \exp(-\kappa x) \quad (2-8)$$

where  $\kappa$  is the Debye–Huckle parameter [Stern, 1924] and has the unit of  $(\text{length})^{-1}$ ,  $1/\kappa$  is the distance at which the potential  $\psi$  drops to  $1/e$  of its value at the Stern plane,  $\psi_\delta$ , and this distance is called the double layer thickness or Debye length. The double layer thickness is of great importance in colloid stability because it controls the range of the double layer interaction. The thickness is controlled by the concentration and valence of ions in solution. A high concentration of ions (high ionic strength) in the medium generally results in a decrease in the double layer thickness and consequent decrease in the potential. The thickness is commonly represented in the form of Equation (2-5).

The potential at the slip plane, the  $\zeta$  potential, determines the velocity ( $v$ ) of the particles moving under the influence of an applied electric field ( $E$ ), and the electrophoretic mobility ( $\mu$ ):

$$\mu = \frac{v}{E} \quad (2-9)$$

The motion of particles under the effect of electrophoretic forces has been first addressed by Smoluchowski [Smoluchowski, 1917] and subsequently by many others. Smoluchowski predicted that a rigid spherical particle possessing an electric double layer and embedded in an unbound flow field would be forced to move if subjected to an electrical potential gradient. The mobility of the particle depends linearly on the dielectric constant (or permittivity) of the fluid and the  $\zeta$  potential of the particle, and is inversely proportional to the fluid viscosity. It is given by the following Henry equation:

$$\mu = \frac{2}{3} \frac{\epsilon_0 \epsilon_r \zeta}{\eta} f(\kappa r) \quad (2-10)$$

where  $\epsilon_0$  is the permittivity of vacuum,  $\epsilon_r$  is the relative permittivity of the solvent,  $\eta$  is the solvent viscosity,  $f(\kappa r)$  is the Henry coefficient, which depends on the relation between the thickness of the double layer ( $1/\kappa$ ) and the core radius ( $r$ ) of the particle. The function  $f(\kappa r)$  increases from 1 for  $\kappa r \ll 1$  to 1.5 for  $\kappa r \gg 1$ . For particles that are much smaller than the Debye length, the electrophoretic mobility  $\mu$  is given by Hückel formula:

$$\mu = \frac{2}{3} \frac{\epsilon_0 \epsilon_r \zeta}{\eta} \quad (2-11)$$

For particles that are large compared with  $1/\kappa$  the electrophoretic mobility is given by Smoluchowski equation:

$$\mu = \frac{\varepsilon_0 \varepsilon_r \zeta}{\eta} \quad (2-12)$$

The electrophoretic mobility of a spherical polyelectrolyte, in which fixed charges are distributed at a uniform density  $\rho_{\text{fix}}$ , can be derived from the equation [Ohshima, 1995]:

$$\mu = \frac{\rho_{\text{fix}}}{\eta \lambda^2} \left[ 1 + \frac{2}{3} \left( \frac{\lambda}{\kappa} \right)^2 \frac{1 + \lambda / 2\kappa}{1 + \lambda / \kappa} \right] \quad (2-13)$$

where  $\lambda = (\gamma/\eta)^{1/2}$ , and  $\gamma$  is the frictional coefficient of the polyelectrolyte. In contrast to Equation (2-10) for the electrophoretic mobility of a rigid particle, Equation (2-13) does not include the  $\zeta$  potential. Ohshima [Ohshima, 1994, 1995, 2000] proposed a general electrophoresis theory for the electrophoresis of polyelectrolyte-coated spherical colloidal particles, which combines two different theories: the theory for rigid spheres and that for spherical polyelectrolytes. When a rigid particle is coated by a layer of polyelectrolyte of thickness  $d$ , the general mobility expression is given by:

$$\mu = \frac{\varepsilon \varepsilon_0}{\eta} \frac{\psi_0 / \kappa_m + \psi_{\text{DON}} / \lambda}{1 / \kappa_m + 1 / \lambda} f\left(\frac{d}{r}\right) + \frac{\rho_{\text{fix}}}{\eta \lambda^2} \quad (2-14)$$

where  $d$  is the thickness of polyelectrolyte layer,  $\psi_0$  is the potential at the boundary

between the polyelectrolyte and the surrounding solution, and  $\psi_{DON}$  is the Donnan potential:

$$\psi_0 = \psi_{DON} + \frac{2n^\infty kT}{\rho_{fix}} \left\{ 1 - \left[ \left( \frac{\rho_{fix}}{2ze_0 n^\infty} \right)^2 + 1 \right]^{1/2} \right\} \quad (2-15)$$

$$\psi_{DON} = \frac{kT}{ze_0} \ln \left\{ \frac{\rho_{fix}}{2ze_0 n^\infty} + \left[ \left( \frac{\rho_{fix}}{2ze_0 n^\infty} \right)^2 + 1 \right]^{1/2} \right\} \quad (2-16)$$

where  $k$  is Boltzmann's constant,  $T$  is the absolute temperature,  $e_0$  is the elementary electrical charge, and  $\kappa_m$  is the Debye-Hückel parameter of the polyelectrolyte layer:

$$\kappa_m = \kappa \left[ 1 + \left( \frac{\rho_{fix}}{2ze_0 n^\infty} \right)^2 \right]^{1/4} \quad (2-17)$$

$$f\left(\frac{d}{r}\right) = \frac{2}{3} \left[ 1 + \frac{1}{2(1+d/r)^3} \right] \quad (2-18)$$

The function  $f(d/r)$  tends to 1 as  $d/r$  decreases, whereas it becomes  $2/3$  as  $d/r$  increases [Ohshima, 2000]. In the limit  $\lambda \rightarrow \infty$ , the polyelectrolyte-coated particle behaves like a rigid particle, the surface potential  $\psi_0$  becomes the  $\zeta$  potential and Equation (2-14) tends to the Smoluchowski formula Equation (2-12) for  $d \ll r$ , or the Hückel formula Equation (2-11) for  $d \gg r$ . In the limit  $r \rightarrow 0$ , the particle becomes a spherical polyelectrolyte.

### 2.3.8 Kinetics of electrophoretic deposition

Knowledge of the kinetics of EPD process is necessary in order to (a) control and manipulate deposition rate, and (b) achieve flexibility in microstructural manipulation. Hamaker [Hamaker, 1940] observed a linear dependence of the deposited weight or yield of the EPD with the amount of charge passed, and proposed that the amount deposited (Y) is proportional to the concentration of the suspension  $C_s$ , time of deposition  $t$ , surface area of deposit  $S$ , and the electric field  $E$ :

$$Y = \mu EtSC_s \quad (2-19)$$

where  $\eta$  is the electrophoretic mobility of the particles in the suspension.

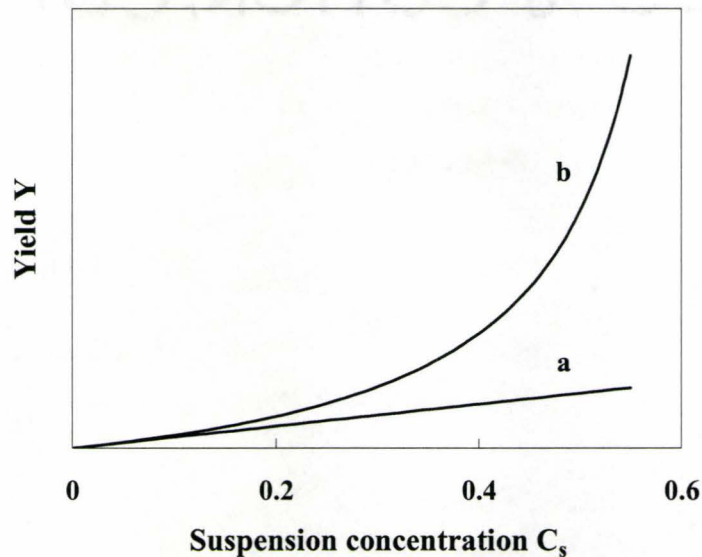


Figure 2-6 Deposition yield as a function of suspension concentration  $C_s$ .

The Hamaker's law for the deposit formation rate in electrophoretic deposition can be derived from a combination of Kynch theory, the equation of continuity for the suspension phase, and the appropriate expression for particle velocity [Biesheuvel *et al.*, 1999]. To arrive at the integral form of Hamaker's law Equation (2-19), it is necessary to assume that, the particle concentration in deposit ( $C_c$ ) remains constant in time, the suspension concentration ( $C_s$ ) is sufficiently low, and at the suspension–deposit interface a sharp discontinuity of the particle concentration develops (i. e. the particle concentration rapidly increases from  $C_s$  to  $C_c$  at the boundary). The Hamaker's law Equation (2-19) also requires a constant particle flux, which requires a constant velocity in suspension and a constant concentration. A constant velocity implies a constant field strength and a constant mobility. This is possible only if charge build up at the electrodes is negligible and the deposit remains sufficiently thin. A constant concentration requires a stagnant (non-stirred) suspension or a low amount of deposited particles compared to the amount present in suspension.

Experiments to determine the influence of suspension concentration on deposit formation rate have been conducted by Biesheuvel *et al.* and a new equation was proposed [Biesheuvel *et al.*, 1999]. Theoretical and experimental data showed a more-than-linear increase in the deposition yield with increasing particle concentration, which is attributed to the movement of the deposit-suspension boundary. It was shown that the deposition yield can be described by the equation [Biesheuvel *et al.*, 1999]:

$$Y = \mu Et S C_s \frac{C_c}{C_c - C_s} \quad (2-20)$$

where  $C_c$  is the particle concentration in the deposit. Hamaker's law Equation (2-19) is obtained if  $C_s$  is appreciably lower than  $C_c$  and, thus, neglected in the denominator in Equation (2-20). Figure 2-6 [Biesheuvel *et al.*, 1999] compares the effect of  $C_s$  on  $Y$  using Equation (2-19) (Figure 2-6 a) and Equation (2-20) (Figure 2-6 b). Equation (2-20) shows that  $Y$  increases more than linearly, with an asymptote at  $C_s = C_c$ . The necessary correction factor  $X$  to Equation (2-19) is obtained by division of Equation (2-20) by Equation (2-19):

$$X = \frac{C_c}{C_c - C_s} \quad (2-21)$$

$X$  is always  $> 1$  and approaches 1 as  $C_s$  approaches zero.

The proposed equation presented a useful starting point for the refinement of the description of deposit formation rates in EPD, however, it only described the EPD from suspensions containing single component (e.g. pure ceramic) particles. For the EPD of organoceramic composite materials, theoretical and experimental investigations on the formation rate of composite deposits from suspensions containing both ceramic particles and polymer macromolecules are needed.

## **2.4 Electrodeposition of bioceramic and composite coatings on implant metals and alloys**

### **2.4.1 Electrolytic deposition of zirconia coatings**

Cathodic ELD is a relatively new technique in ceramic processing that enables the fabrication of nanostructured films. It has been utilized for the formation of nanostructured protective coatings on metals, graphite and carbon fibers [Chaim *et al.*, 1991; Yen, 2000; Zhitomirsky, 1998c]. The electrodeposition of zirconia is under investigation for the fabrication of advanced films for the corrosion protection of metals [Espitia-Cabrera *et al.*, 2003; Yen, 2000; Yen, 1999]. Several investigations have been undertaken on the ELD of zirconia coatings [Aslam *et al.*, 2000; Chaim *et al.*, 1991; Espitia-Cabrera *et al.*, 2003; Gal-Or *et al.*, 1991; Valov *et al.*, 2002; Yen, 2000; Yen, 1999; Zhitomirsky, 1998c; Zhitomirsky *et al.*, 1998]. The high melting point, outstanding thermal and chemical stability, excellent mechanical properties and biocompatibility of  $ZrO_2$  have made this material important for many applications.

Electrolytic  $ZrO_2$  coatings on metal have been verified to improve the corrosion resistance [Yen, 1999; Zhitomirsky *et al.*, 2002a] and wear resistance [Yen *et al.*, 2001] of implant alloys. The ability to deposit uniform zirconia films on substrates of complex shape offers many important opportunities in the application of electrodeposition for the corrosion protection of biomedical implants [Yen, 1999]. Electrodeposition is also being recognized as an effective technique for the fabrication of yttria stabilized zirconia coatings and the composite coatings based on zirconia

[Chaim *et al.*, 1994; Mukherjee *et al.*, 2001; Zhitomirsky *et al.*, 2001a].

However, problems such as deposit cracking and low adhesion of the cathodic deposits are commonly encountered in the electrodeposition of  $\text{ZrO}_2$  via hydroxide precursors [Chaim *et al.*, 1991; Yen, 2000; Yen, 1999]. When the deposit thickness exceeds 0.1–0.2  $\mu\text{m}$  [Zhitomirsky *et al.*, 2000d], the electrolytic zirconium hydroxide films are prone to cracking, which can be attributed to drying shrinkage. Additional shrinkage and cracking result from the subsequent firing process due to the dehydration of the hydroxide precursor.

Film cracking is a common problem of wet chemical deposition methods. The deposition and firing procedures are usually repeated several times to produce a relatively thick film. However, multilayer electrodeposition of zirconia films presents difficulties related to the formation of highly insulating zirconia layers after the dehydration of the hydroxide precursor. Moreover, the cathodic  $\text{ZrO}_2$  deposits are of low adhesion, attributed to the negative charge of the colloidal zirconium hydroxide particles formed in the high pH region at the cathode surface [Zhitomirsky, 2002; Zhitomirsky *et al.*, 2000d]. Therefore, an important task is to deposit thick ELD  $\text{ZrO}_2$  coatings with enhanced adhesion and corrosion protection properties.

Recently, a novel method has emerged for the fabrication of polymer–ceramic composite films. In this method, cathodic electrosynthesis of inorganic particles was combined with EPD of cationic polyelectrolytes. Several electrochemical strategies based on the use of strong, weak and chelating polyelectrolytes are currently under

development [Zhitomirsky, 2002, 2004; Zhitomirsky *et al.*, 2000d]. PDDA is a strong cationic polyelectrolyte, which maintains a positive charge under basic conditions. It was suggested that the deposit formation is driven by the Coulombic attraction between the two charged species: the cationic PDDA and the negatively charged colloidal particles formed at the electrode surface. The use of cationic PDDA with inherent binding properties enables the formation of adherent and crack free composite films [Zhitomirsky, 2002; Zhitomirsky *et al.*, 2000d]. The thickness of the composite films was in the range of 5–10 micrometers, and the composition of the films could be changed by a variation of the PDDA concentration in solutions. It was suggested that the novel approach could be utilized for the fabrication of thick zirconia films. The use of PDDA additive as a binder is important to prevent cracks and improve adhesion of the colloidal zirconia particles formed at the electrode surface. Moreover, in this case the electrostatic repulsion of the PDDA macromolecules can be reduced. The high positive charge of the PDDA macromolecules can be compensated by the negative charge of the colloidal particles formed at the electrode surface.

Presently, substantial attention has been attracted to the fabrication of advanced organic-inorganic composites because of the potential of combining advanced properties of organic and inorganic components [Beecroft *et al.*, 1997; Collins *et al.*, 1999; Gangopadhyay *et al.*, 2000]. Formation of composite coatings based on polyelectrolytes and inorganic nanoparticles has become the subject of

extensive experimental work. Many important studies focused on layer-by-layer assembly [Cassagneau *et al.*, 1998; Cassagneau *et al.*, 2000b; Clark *et al.*, 1998, 2000; Decher, 1997; Decher *et al.*, 1991; Jiang *et al.*, 2000], which utilizes electrostatic interactions between oppositely charged species. This technique offers researchers a strategy for forming a wide variety of advanced organic-inorganic composites [Dante *et al.*, 1999; Dutta *et al.*, 2000b; Kleinfeld *et al.*, 1996; Lvov *et al.*, 1996; Tyan *et al.*, 1999]. Considerable attention has been given to the fabrication of novel composites based on cationic polyelectrolytes such as PDDA, PEI, and poly(allylamine hydrochloride) (PAH). There is a growing interest in the application of composite materials in humidity sensors [Kleinfeld *et al.*, 1995], batteries [Fojas *et al.*, 2002; Zhang *et al.*, 2000], microelectronic devices [Fang *et al.*, 1999a; Fang *et al.*, 1999b; Feldheim *et al.*, 1996], magnetic memory [Liu *et al.*, 1997], and quantum dot devices [Dutta *et al.*, 2000a]. Novel composite materials containing inorganic nanoparticles embedded in a polyelectrolyte matrix [Cassagneau *et al.*, 2000a; Keller *et al.*, 1994; Lvov *et al.*, 2000; Sasaki *et al.*, 2001; Schaak *et al.*, 2000; Wang *et al.*, 2002] are currently under investigation for catalytic, optical, and other applications.

In view of the importance of zirconia coatings and polyelectrolytes for various applications in materials science and surface engineering, it has become an interesting task to explore the possibility of fabricating thick zirconia coatings using polyelectrolyte additives and to develop novel composite coatings based on zirconia and polyelectrolytes. It is suggested that the problem of deposit cracking and low

deposit adhesion can be addressed by the use of burnable polyelectrolyte additives. New deposition strategies are needed to achieve the electrodeposition of composite coatings containing inorganic zirconia nanoparticles in a polyelectrolyte matrix using both strong (i.e. PDDA) and weak cationic polyelectrolytes (i.e. PEI and PAH). The influence of the solvent and polyelectrolytes on the electrosynthesis and crystallization behavior of zirconia, and the deposition mechanisms that control the composition, microstructure, and morphology of the deposited coatings are to be investigated.

#### **2.4.2 Electrophoretic deposition of hydroxyapatite coatings**

HA differs greatly from bone in terms of its properties and microstructure. While HA is a brittle polycrystalline ceramic with a low fracture toughness in the order of  $\sim 0.6\text{-}1.5 \text{ MPa}\cdot\text{m}^{1/2}$  [Yalpani *et al.*, 1992], bone has a complex collagen-fiber-reinforced microstructure and nanostructure, which result in a relatively high fracture toughness, typically  $\sim 2\text{-}12 \text{ MPa}\cdot\text{m}^{1/2}$  for cortical bone [Allan *et al.*, 1979]. Therefore, despite the advantageous bioactivity of HA, its poor mechanical properties have limited its clinical use. One solution to this problem is to use HA to produce bioactive coatings on metal implants. Significant research activity has been associated with the development of HA coatings and composites [Hsieh *et al.*, 2002; Lin *et al.*, 2004; Velayudhan *et al.*, 2004].

Plasma spraying is the current commercial technique to apply HA coatings. However, the high processing temperatures results in thermal decomposition of HA.

At elevated temperature, HA decomposes to other types of calcium phosphates which entail higher sintering temperatures. In addition, they are more soluble than HA in the human body, which is undesirable for an implant. Thus it is very important to get a rigid control of the stoichiometry of synthesized HA particles and HA coatings.

Commercially available HA powders have relatively large particle size. For example, Merck produces HA particles with the diameter in the range of 1-125  $\mu\text{m}$ , whose Ca/P ratio ( $\approx 1.63$ ) is lower than the stoichiometric HA. Therefore, films prepared from commercially available HA powders need to be sintered at temperatures of at least 1200  $^{\circ}\text{C}$ . Such elevated temperatures not only will degrade the mechanical properties of the metal implant, but also will cause decomposition of the HA coating owing to an interfacial reaction with the substrate. These problems can be addressed by using synthesized nanosize HA particles.

The importance of HA coatings for biomedical applications has motivated the development of deposition techniques. The formation of HA coatings using electrochemical methods becomes the subject of intense experimental works. Electrodeposition of HA was performed by EPD [Damodaran *et al.*, 1993; Ducheyne *et al.*, 1990; Ducheyne *et al.*, 1986; Kim *et al.*, 1991; Wei *et al.*, 1999; Zhitomirsky, 1998c] and ELD [Chen *et al.*, 1998; Shirkhazadeh, 1998; Therese *et al.*, 1998; Yen *et al.*, 2002]. ELD produces colloidal HA particles in electrode reactions for subsequent deposition. The small particle size of electrolytic deposits allows increased sinterability of HA at low temperatures. However, ELD can be used for the fabrication

of very thin or porous films. The control of stoichiometry of electrolytic deposits presents difficulties related to the different deposition rate of Ca and P species.

In contrast, thick deposits can be prepared by EPD. Several investigations were focused on the EPD of HA [Wei *et al.*, 1999; Zhitomirsky, 2000b; Zhitomirsky *et al.*, 1997b]. EPD of HA nanoparticles offers good suspension stability and constant deposition rate, and enables the fabrication of ceramic deposits with dense packing and homogeneous microstructure. The main advantage of using EPD is the ability to control the deposit stoichiometry. It offers the possibility to deposit stoichiometric HA coatings in addition to the obvious economic advantages of low cost and simplicity. The degree of stoichiometry of electrophoretic deposits is controlled by the composition of the powder used.

The use of nanostructured HA offers the advantage of improved sinterability at reduced temperatures. However, EPD of HA nanoparticles presents difficulties, related to the cathodic reduction of adsorbed water [Ducheyne *et al.*, 1990]. Recent investigations [Zhitomirsky, 2000b; Zhitomirsky *et al.*, 1997b] have showed the possibility of EPD of HA nanoparticles, and highlighted the importance of the use of nanostructured HA. EPD of HA nanoparticles offers the advantages of good suspension stability and constant deposition rate in the fabrication of ceramic coatings and fibers, with dense particle packing, good sinterability and homogeneous microstructure. However, the fabrication of nanostructured HA coatings on Ti and Ti alloys presents difficulties, related to drying and sintering shrinkage of the coatings

and chemical reactions [Ducheyne *et al.*, 1990] between the HA and substrates during sintering at elevated temperatures.

After deposition the coating must be densified by sintering. The green density of EPD deposits is usually below 60-65 vol %. Dense HA can be obtained by sintering at 1100-1200 °C. The sintering must be performed in a moist atmosphere in order to prevent the decomposition of HA. Such sintering results in significant shrinkage of the coatings, whereas substrate dimensions remain unchanged at the sintering temperature. Therefore, deposit sintering can result in cracking. Additional cracking during cooling can result from the difference in the thermal expansion coefficients of the sintered coating and the substrate.

A difficult task for fabrication of electrophoretic HA deposits on Ti and Ti alloy substrates, is to avoid HA-Ti interfacial reactions and the oxidation of Ti at elevated temperatures. The sintering of HA coating on Ti and its alloys imposed conflicting requirements. The former required high vacuum and temperatures below the  $\alpha+\beta\rightarrow\beta$  transition temperature of Ti-6%Al-4%V (975 °C) [Ducheyne *et al.*, 1981], while the later was best accomplished in a moist atmosphere above 1100 °C [Groot, 1980].

During sintering of HA coatings under oxidizing conditions, titanium is quickly oxidized and the HA is transformed to  $\beta$ -whitlockite because of the reaction of Ti oxide and HA and formation of  $\text{CaTiO}_3$  [Ducheyne *et al.*, 1986]. When HA coating is vacuum sintered on the underlying titanium substrate, it transforms to a

mixture of oxyHA and tetracalcium phosphate [Ducheyne *et al.*, 1990]. The transformation occurs because the underlying titanium substrate easily attracts phosphorus [Raemdonck *et al.*, 1984]. Therefore, preferential diffusion of P to the Ti substrate results in HA decomposition and formation of the calcium phosphate phases with lower chemical stability. These phase transformations can provoke considerable in vitro dissolution of the coating [Kim *et al.*, 1991], and therefore should be avoided.

All the above mentioned problems necessitate the development of new electrochemical strategies for the fabrication of nanostructured HA coatings on implant metals by EPD. Considering the composition and structure of natural bone, which is actually a natural nanocomposite material, an alternative is to fabricate novel bioactive HA-polymer nanocomposite coatings instead of the pure HA coating. All the problems related to the sintering of HA can be eliminated by the fabrication of ceramic-polymer composites.

#### **2.4.3 Electrodeposition of organic-inorganic composite coatings**

Ceramic-polymer composite coating has attracted substantial attention because of the potential of combining advanced properties of organic and inorganic components [Damodaran *et al.*, 1993]. For biomedical implants, metallic substrates provide good mechanical properties for the load-bearing applications, while the composite surface coatings impart other functional properties to the implants including chemical stability, bioactivity, biocompatibility, and antimicrobial

properties.

Electrodeposition offers important advantages for the fabrication of advanced composite coatings for biomedical applications [Boccaccini *et al.*, 2002b; Payne, 2007; Van der Biest *et al.*, 1999; Wu *et al.*, 2005]. Besides its flexibility and simple set-up, the technique enables the formation of homogeneous coatings on substrates of complex shapes, with a good control over the chemical composition, nanostructure/microstructure, thickness, purity, and surface morphology of the deposited materials. It also offers the possibility to include polymers, metals, ceramic nanoparticles, and other functional materials in the composite coating, which is otherwise difficult using techniques such as plasma-spraying and chemical/physical vapour deposition. However, the achievement of codeposition of different materials presents challenging. The formation of a stable solution or suspension containing multiple components for deposition requires a good compatibility among the different materials, as well as the solvent, dispersant, and charging agent etc. Usually, new deposition mechanisms and design of complicated coating structure are needed for the development of a specific coating system.

## **2.5 Research objectives**

- Development of novel electrochemical strategies for the deposition of thick adherent zirconia ceramic and composite coatings using polyelectrolyte additives.

- Development of novel organo-ceramic nanocomposite coatings containing HA nanoparticles with enhanced bioactivity, corrosion protection, and antimicrobial properties.
- Development of new deposition mechanisms for the fabrication of advanced organic-inorganic composite coatings.
- Development of new coating structures for the composite coatings in the form of monolayer, laminates, and functionally graded materials.
- Investigation on the chemical composition, microstructure, corrosion protection, and other functional properties of the developed nanocomposite coatings.

## Chapter 3 Experimental Procedures

### 3.1 Materials

#### 3.1.1 Materials purchased from commercial suppliers

Table 3-1 List of materials purchased.

Material	Supplier	Purity and other specifications
ZrOCl <sub>2</sub> ·8H <sub>2</sub> O	Fluka, Messerschmittstrasse, Germany	Reagent grade
Yttria-stabilized zirconia	Tosoh, Sinnanyo-shi, Japan	TZ-8Y, crystallite size ~22 nm
PDDA*	Aldrich, Milwaukee, WI	M <sub>w</sub> 400,000–500,000
PEI**	Aldrich, Milwaukee, WI	M <sub>w</sub> 70,000 50 wt% solution in water
PAH***	Aldrich, Milwaukee, WI	M <sub>w</sub> 70,000
Ca(NO <sub>3</sub> ) <sub>2</sub> ·4H <sub>2</sub> O	Aldrich, Milwaukee, WI	Reagent grade
(NH <sub>4</sub> ) <sub>2</sub> HPO <sub>4</sub>	Aldrich, Milwaukee, WI	Reagent grade
NH <sub>4</sub> OH	Aldrich, Milwaukee, WI	Reagent grade
AgNO <sub>3</sub>	Aldrich, Milwaukee, WI	Reagent grade
CaSiO <sub>3</sub>	Aldrich, Milwaukee, WI	Reagent grade
NaCl	Caledon Laboratories Ltd., Georgetown, Ontario, Canada	Reagent grade
CaCl <sub>2</sub> ·2H <sub>2</sub> O	Caledon Laboratories Ltd., Georgetown, Ontario, Canada	Reagent grade
KCl	Caledon Laboratories Ltd., Georgetown, Ontario, Canada	Reagent grade
Chitosan	Aldrich, Milwaukee, WI	M <sub>w</sub> 200,000 (from crab shells) Degree of deacetylation ~85 %
Acetic acid	Caledon Laboratories Ltd., Georgetown, Ontario, Canada	Reagent grade
Methanol	Caledon Laboratories Ltd., Georgetown, Ontario, Canada	Reagent grade
Anhydrous Ethyl Alcohol	Commercial Alcohol Inc., Brampton, Ontario, Canada	Reagent grade

\* PDDA – Poly(diallyldimethylammonium chloride)

\*\* PEI – Poly(ethylenimine)

\*\*\* PAH – poly(allylamine hydrochloride)

Table 3-1 gives the materials purchased from commercial sources for the preparation of HA nanoparticles, deposition solutions/suspensions, and electrochemical testing solutions. De-ionized water, methanol, and ethanol were used as solvents. For some of the electrodeposition, a mixed solvent was used as specified in the part 3.2.2.

### **3.1.2 Synthesis of hydroxyapatite nanoparticles**

Stoichiometric HA nanoparticles were synthesized for the development of novel bioactive ceramic and composite coatings. The procedure was based on a wet chemical method described in literature [Zhitomirsky *et al.*, 1997b]. Aqueous solutions of  $\text{Ca}(\text{NO}_3)_2 \cdot 4\text{H}_2\text{O}$  (1.0 M) and  $(\text{NH}_4)_2\text{HPO}_4$  (0.6 M) were used. Precipitation was performed at a temperature of 70 °C by a slow addition of the  $(\text{NH}_4)_2\text{HPO}_4$  solution into the  $\text{Ca}(\text{NO}_3)_2$  solution. The pH of the solutions was adjusted to 11 with  $\text{NH}_4\text{OH}$ . Stirring was performed for 8 hr at 70 °C and 24 hr at room temperature. The precipitate was washed with water and finally with isopropyl alcohol.

## **3.2 Coating by electrodeposition methods**

### **3.2.1 Experimental setups for electrodeposition**

Cathodic electrodeposition was employed for the fabrication of the ceramic and ceramic-polymer composite coatings. A schematic of the setup of the electrochemical cell for deposition is shown in Figure 3-1. The cell included a

cathodic substrate (15-30 cm<sup>2</sup>) centered between two parallel platinum (Pt) counter electrodes. The distance between the electrodes was 15 mm. The volume of the deposition bath was 300 ml. An electrophoresis power supply EPS 601 (Amersham Biosciences) was employed to provide the DC electric field for electrodeposition, either in a constant current density (galvanostatic) or a constant voltage mode.

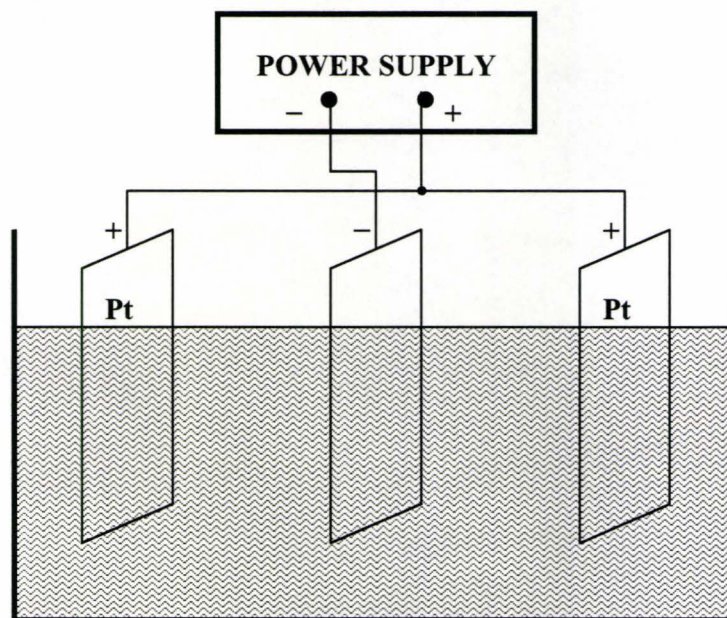


Figure 3-1 A schematic of the setup of the deposition cell.

### 3.2.2 Preparation of solutions and suspensions for electrodeposition

5 mM  $ZrOCl_2$  solutions in a methanol-water (5 vol% water) solvent were prepared for the ELD of  $ZrO_2$  coatings. 0–1.0 g/l PDDA and 0–1.0 g/l PEI were added to the 5 mM  $ZrOCl_2$  solutions for the electrodeposition  $ZrO_2$ -PDDA and  $ZrO_2$ -PEI

composite deposits, respectively. Aqueous 5 mM  $ZrOCl_2$  solutions containing 0-1.5 g/l PAH (pH 2.2-2.4) were used for the electrodeposition of  $ZrO_2$ -PAH composites. Transparent and stable solutions were obtained after the addition of the polymers to the  $ZrOCl_2$  solutions. Electrodeposition was also performed using yttria-stabilized zirconia (YSZ) suspensions. 0-4.0 g/l YSZ particles were dispersed in a 5 mM  $ZrOCl_2$  solution in a methanol-water (5 vol% water) solvent containing 1.0 g/l PEI. The prepared suspensions were relatively stable and allowed the formation of the cathodic deposits.

A biopolymer, chitosan, was utilized for the development of novel bioactive composite coatings containing HA. 3.0 g/l chitosan was dissolved in 1 % acetic acid aqueous solutions, which were then used to prepare 0-0.7 g/l chitosan solutions in a mixed ethanol-water solvent. Deposition experiments were first performed using chitosan solutions in water and the mixed ethanol-water solvent with increasing ethanol content. It was found that the deposit porosity decreased with increasing ethanol content in the mixed ethanol-water solvent. Then, electrodeposition was performed from suspensions of 0-8.0 g/l HA nanoparticles in a mixed ethanol-water solvent (17 vol% water) containing 0-0.7 g/l chitosan. Before the electrodeposition, the solutions were ultrasonicated for 1 hr to achieve a homogeneous dispersion of the HA nanoparticles.

In order to incorporate antimicrobial agent Ag, 0-1 mM  $AgNO_3$  aqueous solutions were added to the chitosan solutions for deposition. Electrodeposition was

performed using 0.5 g/l chitosan solutions containing HA nanoparticles and dissolved  $\text{AgNO}_3$  in a mixed ethanol–water solvent (17 vol% water).

For the development of novel composite coatings with enhanced bioactivity,  $\text{CaSiO}_3$  was introduced into the system. EPD was performed using 0.5 g/l chitosan solutions containing HA and  $\text{CaSiO}_3$  particles in a mixed ethanol–water solvent (17 vol% water). Before the deposition, the solutions were ultrasonicated for 1 hr to achieve a homogeneous dispersion of the HA and  $\text{CaSiO}_3$  particles.

### **3.2.3 Electrodeposition procedures**

Ceramic and organo-ceramic composite deposits were obtained on various conductive cathodic substrates under galvanostatic or constant voltage conditions. The substrates utilized included stainless steel AISI 301 foil (50×50×0.1 mm), stainless steel 316L foil (50×50×0.1 mm), Ti foil (50×50×0.1 mm), Pt foil (50×50×0.1 mm), stainless steel 316L wire (0.125 mm and 0.200 mm diameter), Ti wire (0.127 mm diameter), stainless steel gauze (50 mesh woven from 0.18 mm diameter wire), Ti gauze (50 mesh woven from 0.102 mm diameter wire), carbon fiber and felt (Lydall), and graphite plates (10×50×0.1 mm).

The constant current density employed for the galvanostatic deposition ranged from 0.1 to 5  $\text{mA}/\text{cm}^2$ , and a constant voltage of 0-20 V was used for the constant voltage deposition. The deposition time was varied in the range of 0-20 min to obtain deposits of different thicknesses. Obtained coatings were dried in air at room

temperature.

Laminate coatings were prepared by alternate deposition from different solutions without waiting time after the deposition of individual layers. Obtained dual or multilayer coatings were dried in air at room temperature.

### **3.3 Characterization of the coatings**

#### **3.3.1 Materials characterization methods**

##### **3.3.1.1 Investigation of deposition yield**

The yield or kinetics of an electrodeposition process can be studied by measuring the deposit weight of the deposited coating.

In this work, the deposit weight of a deposited coating was obtained by weighing the foil substrate before and after the deposition, followed by drying at room temperature for 24 hr. A Mettler Toledo AX105 DeltaRange analytical balance, which has a readability of 0.01 mg, was used to measure the weight.

##### **3.3.1.2 X-ray diffraction analysis**

X-ray diffractometry (XRD) is commonly used to determine the phase content in minerals and materials. It is also a very useful tool for the measurement of lattice parameters, internal stresses, crystal size, and crystal orientation etc.

In this work, the phase content of the deposits was determined by XRD with a diffractometer (Nicolet I2), using monochromatized Cu K $\alpha$  radiation at a scanning

speed of 0.5°/min. The studies were performed on films deposited on various substrates and powder samples. For the fabrication of powder samples, the deposits were scraped from the Pt electrodes and dried in air for 24 hr before the XRD analysis. In some cases, sintering was conducted after the drying to allow for crystallization or other phase transformations of the green deposits.

XRD studies were also performed on zirconia films sintered on stainless steel substrates, and as-deposited HA-chitosan composite coatings on stainless steel substrates, to identify the phase content and crystal orientation in the coatings as prepared on the substrate.

The average crystallite size of HA nanoparticles synthesized was calculated by means of X-ray line broadening measurements using a commercially available computer program.

### **3.3.1.3 Thermogravimetric and differential thermal analysis**

Thermogravimetric analysis (TG) is an analytical technique used to determine a material's thermal stability and its fraction of volatile components by monitoring the weight change that occurs as a specimen is heated. The measurement is normally carried out in air or in an inert atmosphere, and the weight is recorded as a function of increasing temperature. In addition to weight changes, some instruments also record the temperature difference between the specimen and one or more reference pans (differential thermal analysis, DTA), which can be used to monitor the energy released

or absorbed via chemical reactions or phase transformations during the heating process.

In this work, TG and DTA were carried out using the deposits that had been scraped from the Pt electrode after deposition and dried at room temperature for 24 hr. The thermoanalyzer (Netzsch STA-409) was operated in air between room temperature and 1200 °C at a heating rate of 5 °C/min. The HA content in HA-chitosan composite coatings was calculated from the weight loss of the deposits at 1000 °C.

#### **3.3.1.4 Scanning and transmission electron microscopy**

The surface morphology and microstructures of the deposited coatings were studied by scanning electron microscopy (SEM) using a Philips 515 scanning electron microscope and a JEOL JSM-7000F scanning electron microscope. The transmission electron microscopy (TEM) investigations on the coatings were performed using a Philips CM12 microscope and a JEOL 2010 FEG high-resolution transmission electron microscope. Dispersion of the HA powders for TEM was accomplished by suspending the powders in water and putting a drop onto a copper grid.

The Ag and HA contents in the HA-Ag-chitosan composite coatings were determined by energy dispersive X-ray spectroscopy (EDS) using coated samples heat treated at 300 °C for 1 hr.

### **3.3.1.5 Atomic force microscopy**

The atomic force microscope (AFM) is a very high-resolution type of scanning probe microscope, with demonstrated resolution of fractions of a nanometer. It can provide a true three-dimensional surface profile of a sample. Additionally, samples viewed by AFM do not require any special treatments that would irreversibly change or damage the sample.

In this work, the surface topography of the composite coatings containing ZrO<sub>2</sub> was studied using a NanoScopeIIIa AFM (Digital Instruments) in tapping mode.

### **3.3.1.6 Inductively coupled plasma spectrometry**

Inductively Coupled Plasma (ICP) spectrometry is an analytical technique used for the detection of trace elements in samples. It is applicable to most elements over a wide range of concentrations. The primary goal of ICP is to get elements to emit characteristic wavelength specific light which can then be measured. Samples have to be dissolved prior to analysis.

In this work, the Ag<sup>+</sup> release rate from the HA-Ag-chitosan composite coatings was tested by soaking coated stainless steel substrates (3×6 cm<sup>2</sup>) in 20 ml high purity water for different time periods. The concentration of Ag<sup>+</sup> ions in the solutions was then determined by inductively coupled plasma optical emission spectroscopy (ICP-OES, Vista-PRO, Varian).

### **3.3.2 Electrochemical methods**

The main advantage of electrochemical techniques for studying corrosion over traditional coupon testing is that it allows the rapid determination of the corrosion rate of a sample without requiring long-term testing. The short-term electrochemical measurements are more than sufficient in many cases, as they allow to compare the performance of inhibitors or to decide that a given metal is corroding too rapidly under those conditions to be a valid candidate for the application.

In this work, the protective properties of the composite coatings were studied by electrochemical methods using a potentiostat (PARSTAT 2273, Princeton Applied Research) controlled by a computer using the PowerSuite electrochemical software package.

#### **3.3.2.1 Corrosion cell setup**

A conventional three-electrode cell (Figure 3-2) was utilized, with a Pt net being the counter electrode and a saturated calomel electrode (SCE) being the reference electrode. The sample to be tested was placed as a working electrode, with a surface area of  $1 \text{ cm}^2$  exposed to the testing solution.  $\text{N}_2$  purging through the solution was started prior to the testing and continued during the whole testing procedure, in order to remove  $\text{O}_2$  from the the solutions.

#### **3.3.2.2 Testing solution**

A simulated body fluid, Ringer's solution ( $\text{NaCl}$  8.6 g/l,  $\text{CaCl}_2 \cdot 2\text{H}_2\text{O}$  0.33 g/l,

KCl 0.30 g/l) [Kannan *et al.*, 2003; Souto *et al.*, 2003; Sridhar *et al.*, 2003], was used for all the electrochemical studies.

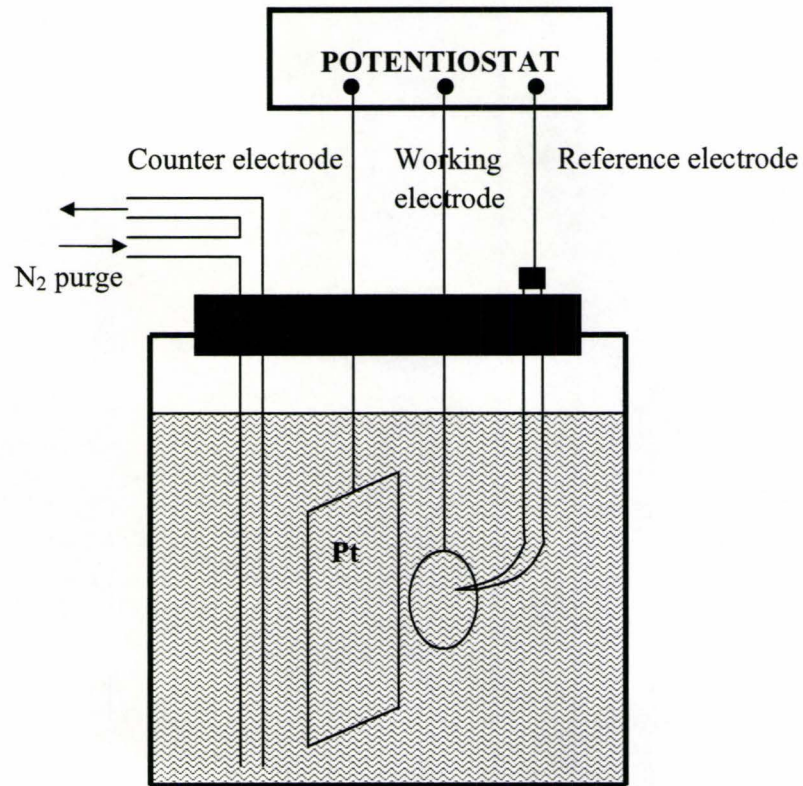


Figure 3-2 A schematic of the corrosion cell setup for the electrochemical measurement.

### 3.3.2.3 Testing methods

#### 3.3.2.3.1 Tafel plot

The Tafel technique provides a fast way of determining the corrosion rate of a specimen. In a typical experiment, a controlled-potential scan was programmed to take place within  $\pm 250$  mV of the corrosion potential of the specimen. The resulting

current is logarithmically plotted versus the potential (log current versus potential).

The corrosion rate can be calculated from the Tafel plot data.

In this work, the Tafel plots were obtained with a scan rate of 1 mV/s.

#### **3.3.2.3.2 *Electrochemical impedance spectroscopy***

Electrochemical impedance spectroscopy (EIS) has been successfully applied to the study of corrosion systems for thirty years and been proven to be a powerful and accurate method for measuring corrosion rates. It is a very versatile electrochemical tool to characterize intrinsic electrical properties of any material and its interface. The basis of EIS is the analysis of the complex impedance of the electrochemical system as a function of the frequency of applied electric field . This analysis provides quantitative information about the conductance, the dielectric constant, the static properties of the interfaces of a system, and its dynamic change due to adsorption or charge-transfer-phenomena. An important advantage of EIS over other laboratory techniques is the possibility of using very small amplitude signals without significantly disturbing the system being investigated. To make an EIS measurement, a small amplitude signal, usually an AC potential between 5 to 10 mV, is applied to an electrochemical cell over a range of frequencies of 0.001 Hz to 100,000 Hz. The real (resistance) and imaginary (capacitance) components of the impedance of the electrochemical system is recorded by measuring the current through the cell. The data can be presented in the form of either Nyquist plot (imaginary part versus real

part of the impedance) or Bode plot (absolute value of the impedance and phase-shift versus signal frequency).

In this work, the corrosion protection properties of the obtained coatings were studied using EIS in the Ringer's solution. The measurements were performed at open circuit potential with a perturbation signal amplitude of 10 mV. The spectra were acquired in a frequency range of 10 mHz–100 kHz.

## Chapter 4 Experimental Results and Discussion

### 4.1 Coating systems investigated

The coating systems that have been investigated in the research are listed in

Table 4-1.

Table 4-1 An overview of the coating systems investigated.

Coating systems	Objectives	Challenges
ZrO <sub>2</sub> coatings	To deposit thick, adherent electrolytic ZrO <sub>2</sub> coatings using weak and strong polyelectrolyte additives	Fabrication of crack-free, thick, adherent ZrO <sub>2</sub> ceramic and composite coatings by ELD; Codeposition of ZrO <sub>2</sub> and the polyelectrolyte; Control over coating composition, nanostructure, and deposition yield.
Functional HA-chitosan composite coatings	To address the problems related to the sintering of HA on surgical metal substrates; To develop novel bioactive composite coatings based on HA ceramic; To achieve a combination of biocompatibility, bioactivity, and other functionalities such as antimicrobial properties in the composite coatings.	Degradation of HA coatings and substrate due to the sintering of HA; Incorporation of polymer and other functional materials into the coatings; Control over the chemical composition, nanostructure, particle orientation, and deposition yield of the coatings; Attainment of corrosion protection of the metallic substrates; Achievement of a combination of biocompatibility, bioactivity, corrosion protection properties and other functionalities.

## **4.2 Cathodic electrodeposition of zirconia coatings**

### **4.2.1 Fabrication of ZrO<sub>2</sub> coatings with weak polyelectrolyte additives**

The experimental results and discussion of this section are produced based on the published paper [Pang *et al.*, 2004].

#### **4.2.1.1 Experimental results**

Electrodeposition experiments performed from the 5 mM ZrOCl<sub>2</sub> solutions containing 0-1.0 g/l PEI or 0-1.5 g/l PAH resulted in the formation of cathodic deposits. Figure 4-1 shows the deposit weight as a function of the deposition time for the 5 mM ZrOCl<sub>2</sub> solutions containing 0.4 g/l PEI. Nearly linear dependence was observed. Similar dependencies were obtained for the solutions containing PAH. These data indicate that the amount of the deposited material can be controlled by a variation of deposition time at a constant current density.

TG data for the deposits prepared from the 5 mM ZrOCl<sub>2</sub> solutions in a methanol-water (5 vol % water) solvent exhibited weight loss that can be attributed to the dehydration of the deposits (Figure 4-2). Two distinct steps in the TG curve are distinguished. A sharp reduction of the sample weight was observed in the range of 20-150 °C. An additional step in the weight loss was recorded in the range of 310-350 °C. At higher temperatures, the weight changed gradually. The total weight loss at 1200 °C was found to be 18.4% of the initial sample weight.

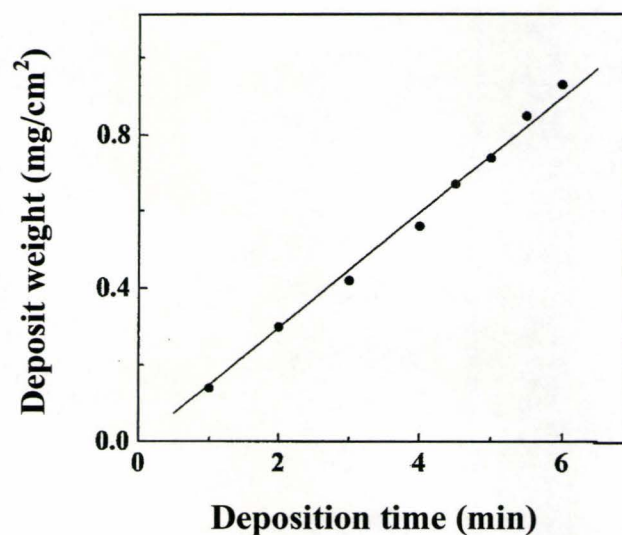


Figure 4-1 Deposit weight versus deposition time for the deposits prepared from the 5mM  $ZrOCl_2$  + 0.4 g/l PEI solutions on a Pt substrate at a current density of 5  $mA/cm^2$ .

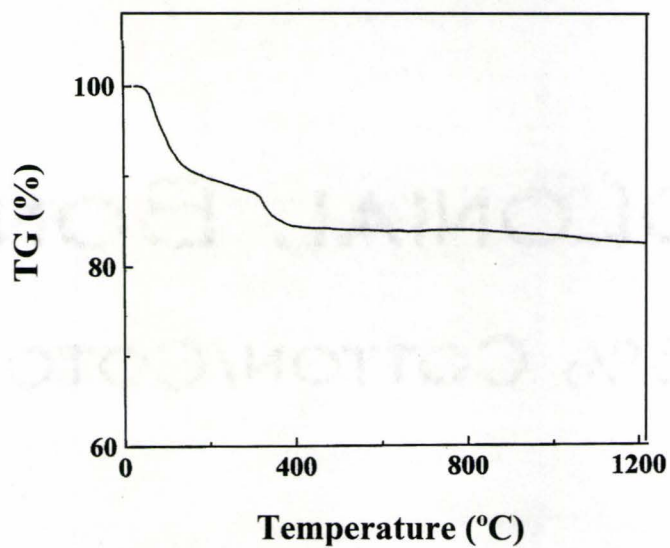


Figure 4-2 TG data for the deposits obtained from the 5 mM  $ZrOCl_2$  solutions at a current density of 5  $mA/cm^2$  (heating rate = 5  $^{\circ}C/min$ ).

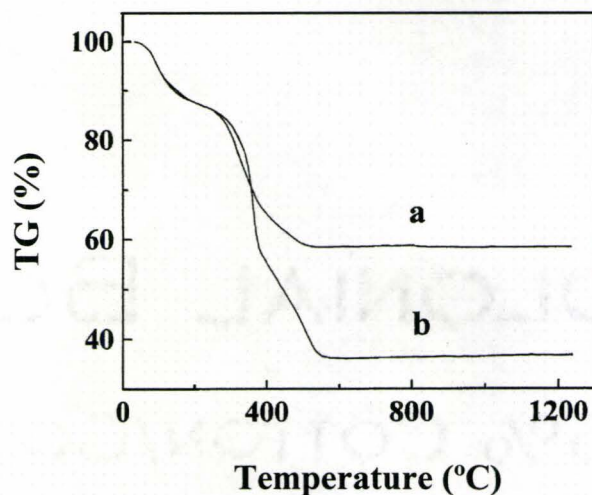


Figure 4-3 TG data for the deposits obtained from the 5 mM  $ZrOCl_2$  solutions containing (a) 0.4 g/l PEI and (b) 1.0 g/l PEI at a current density of  $5 \text{ mA/cm}^2$  (heating rate =  $5 \text{ }^\circ\text{C/min}$ ).

Figure 4-3 compares the results of the TG analysis for deposits obtained from the 5 mM  $ZrOCl_2$  solutions in a methanol-water (5 vol % water) solvent containing different amounts of PEI. The total weight loss at 1200 °C for deposits prepared from the solutions containing 0.4 g/l PEI and 1.0 g/l PEI was found to be 41.8 and 63.7 wt %, respectively. No appreciable weight change was observed at temperatures exceeding 550 °C. These results, coupled with the TG data for deposits prepared from the pure  $ZrOCl_2$  solutions (Figure 4-2), indicate the possibility of electrochemical codeposition of the PEI and zirconium species. The deposits prepared from the solutions containing PEI show weight loss (Figure 4-3), attributed to the dehydration of an inorganic phase, and additional weight loss related to the burning out of an

organic phase. It may be concluded that the deposition process resulted in the formation of the composite coatings containing different amounts of PEI. The increase in the PEI concentration in solutions resulted in a higher PEI content in the deposits. The TG data shown in Figure 4-2 and Figure 4-3 were used to calculate the polymer content in the composite deposits. The content of an organic phase was found to be 28.7 and 55.5 wt % for the deposits prepared from solutions containing 0.4 and 1.0 g/l PEI, respectively.

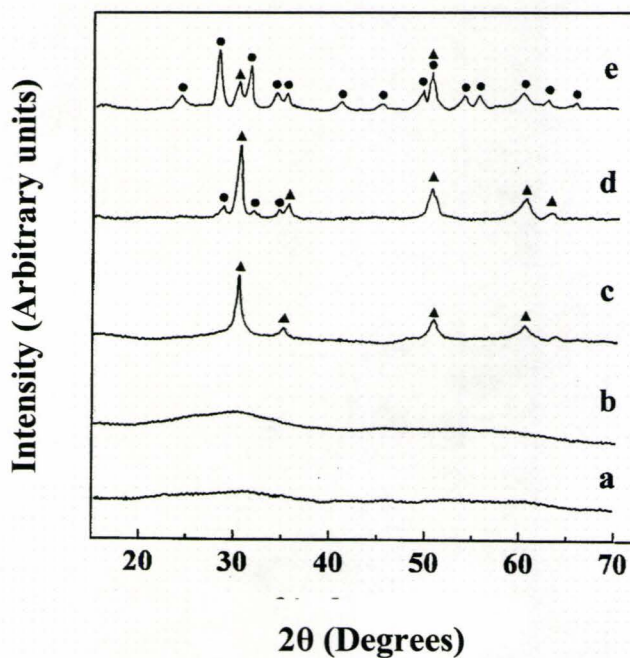


Figure 4-4 XRD patterns for the deposits obtained from the 5 mM  $ZrOCl_2$  solutions containing 0.4 g/l PEI (a) as prepared and after annealing for 1 hr at (b) 200, (c) 400, (d) 600, and (e) 800 °C (▲ = tetragonal zirconia, ● = monoclinic zirconia).

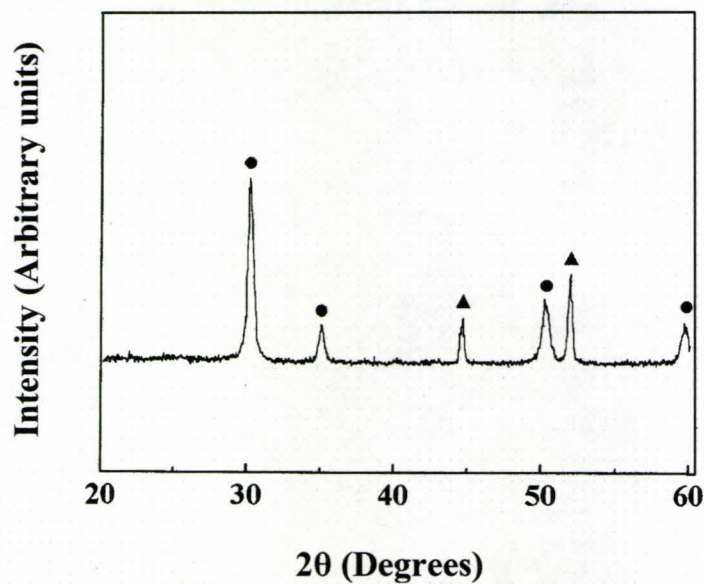


Figure 4-5 XRD pattern of a composite coating prepared from the 5 mM  $ZrOCl_2$  solutions containing 1.0 g/l PEI and 4.0 g/l YSZ (● = YSZ, ▲ = Ni substrate)

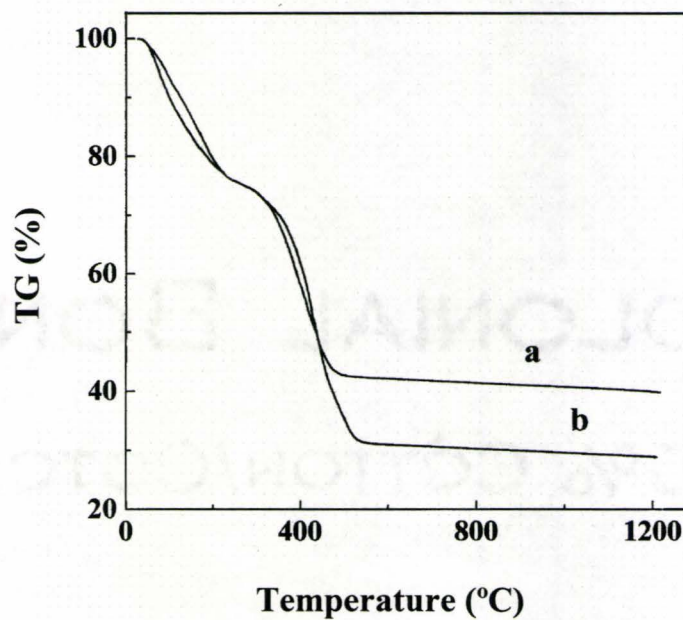


Figure 4-6 TG data for the deposits obtained from the 5 mM  $ZrOCl_2$  solutions containing (a) 0.75 g/l PAH and (b) 1.5 g/l PAH at a current density of 5 mA/cm<sup>2</sup> (heating rate = 5 °C/min).

The deposits were analyzed by XRD both before and after annealing in air at different temperatures. The fresh deposits and those heated at 200 °C were amorphous (Figure 4-4). Further increase of the annealing temperature resulted in the crystallization of tetragonal zirconia, which is the main crystalline phase at 400 and 600 °C. However, it is difficult to distinguish between the cubic and tetragonal zirconia phases owing to peak broadening. Faint peaks of monoclinic zirconia could also be distinguished in the XRD pattern obtained at 600 °C. When the deposits were heated to 800 °C, the XRD pattern displayed peaks of tetragonal and monoclinic zirconia.

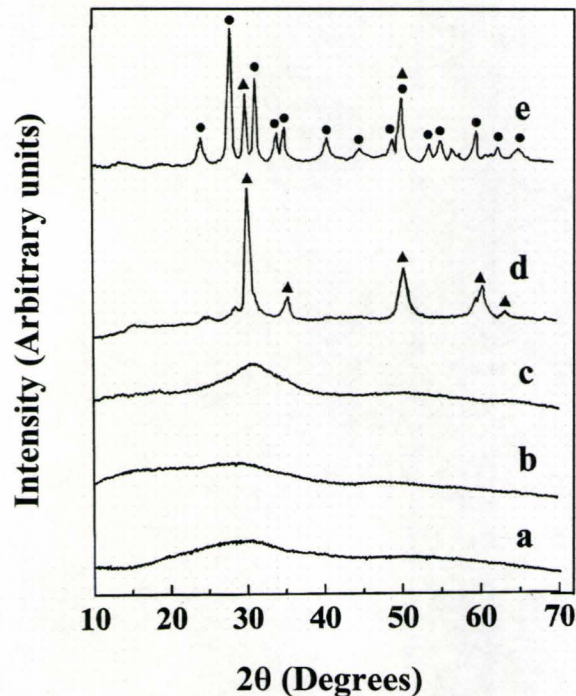


Figure 4-7 XRD patterns for the deposits obtained from the 5 mM  $ZrOCl_2$  solutions containing 0.75 g/l PAH (a) as prepared and after annealing for 1 hr at (b) 200, (c) 400, (d) 600, and (e) 800 °C (▲ = tetragonal zirconia, ● = monoclinic zirconia).

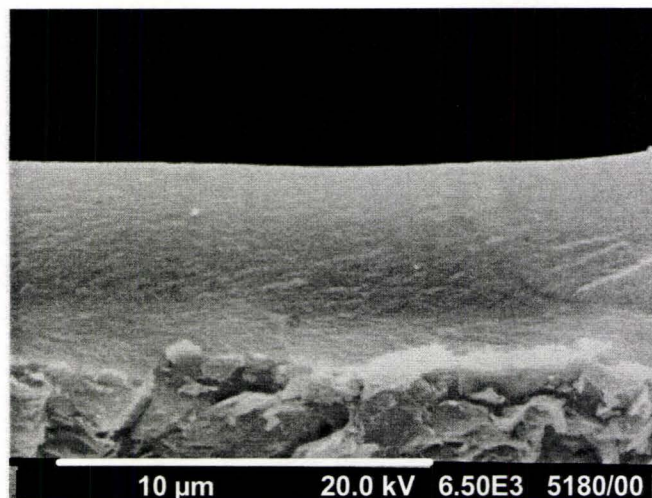


Figure 4-8 SEM picture of the sectioned deposit obtained from a 5 mM  $\text{ZrOCl}_2$  + 0.4 g/l PEI solution on a graphite substrate (bar = 10  $\mu\text{m}$ ).

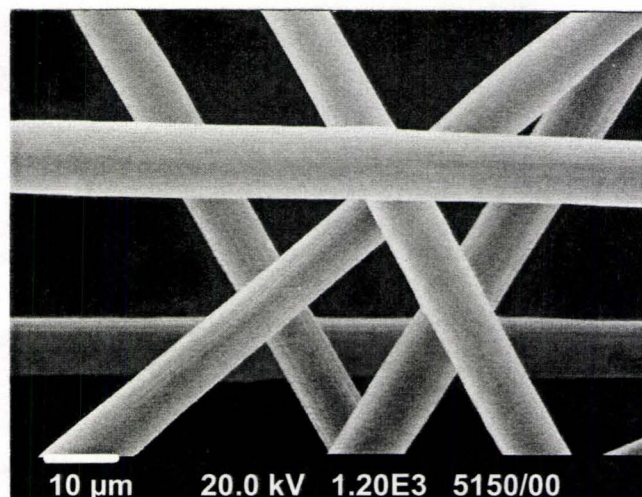


Figure 4-9 SEM picture of the composite deposit prepared from a 5 mM  $\text{ZrOCl}_2$  + 0.4 g/l PEI solution on a carbon felt (bar = 10  $\mu\text{m}$ ).

Electrodeposition was also performed using YSZ suspensions. YSZ particles were dispersed in a solution containing 5 mM  $\text{ZrOCl}_2$  and 1.0 g/l PEI. The prepared suspensions were relatively stable and allowed the formation of the cathodic deposits.

Obtained coatings were characterized by XRD analysis. The X-ray data show peaks of YSZ and indicate the intercalation of the YSZ particles into the composite coatings (Figure 4-5).

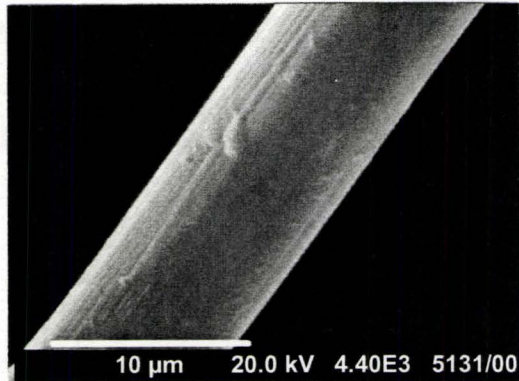
Figure 4-6 shows the TG data for the deposits prepared from the 5 mM  $ZrOCl_2$  aqueous solutions containing different amounts of PAH. The total weight loss at 1200 °C for the deposits prepared from the solutions containing 0.75 and 1.5 g/l PAH was found to be 59.4 and 70.2 wt %, respectively. No appreciable weight change was observed at temperatures exceeding 600 °C. At this point, it is important to note that a weight loss of 32.6% was reported for the deposits obtained from the aqueous  $ZrOCl_2$  solutions [Zhitomirsky *et al.*, 1998]. Therefore, the obtained results, coupled with the TG data for the deposits prepared from the aqueous  $ZrOCl_2$  solutions [Zhitomirsky *et al.*, 1998], indicate the possibility of electrochemical codeposition of the PAH and zirconium species. The deposits prepared from the solutions containing PAH show weight loss (Figure 4-6), attributed to the dehydration of an inorganic phase, and additional weight loss related to the burning out of an organic phase. From the TG data shown in Figure 4-6, it may be concluded that the deposition process resulted in the formation of the composite coatings containing different amounts of PAH. The increase in the PAH concentration in solutions resulted in a higher PAH content in the deposits. Obtained TG data coupled with the TG data for the zirconium species prepared from the aqueous solutions [Zhitomirsky *et al.*, 1998] were used to calculate the polymer content in the composite deposits. The content of an organic phase was

found to be 39.8 and 55.8 wt % for the deposits prepared from the solutions containing 0.75 and 1.5 g/l PAH, respectively.

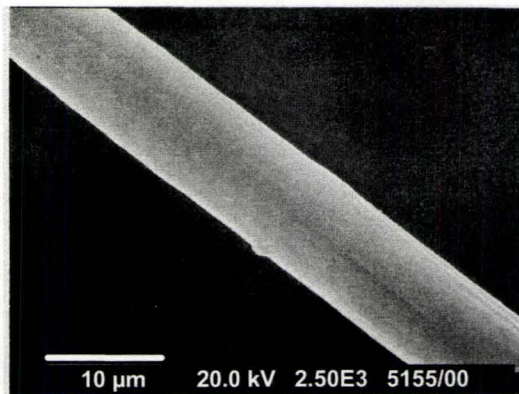
X-ray diffractograms of the fresh deposits prepared from the  $ZrOCl_2$  solutions containing 0.75 g/l PAH exhibited their amorphous nature (Figure 4-7). The deposits thermally treated at 400 °C exhibited a very broad peak near  $2\theta \approx 32^\circ$ , but were essentially amorphous. In Figure 4-7 it can be seen that at 600 °C the deposits exhibited broad peaks, which could be attributed to tetragonal or cubic zirconia. At 800 °C, the transformation to the monoclinic phase was observed.

Composite deposits of various thicknesses in the range of up to several micrometers were obtained on Pt, stainless steel foils, graphite, and carbon-felt substrates.

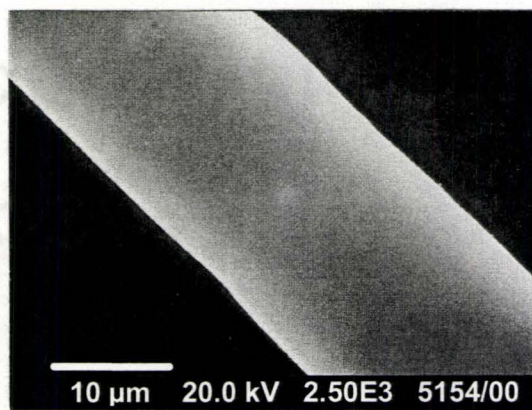
Figure 4-8 shows a SEM picture of a composite coating containing PEI. The obtained coatings adhered strongly to the substrates. Moreover, SEM observations indicate that the method enables coating formation on substrates of complex shape, such as carbon felt (Figure 4-9). It was observed that electrodeposition enabled uniform deposition. Parts a and b of Figure 4-10 show composite deposits on the individual carbon fibers prepared from the solutions containing different amounts of PEI. The deposit thickness was uniform along the fiber length. Deposits of different thicknesses were prepared by the variation of the deposition time (Figure 4-10 b,c). SEM pictures indicate a dense and continuous morphology. The thickness of the deposits on the carbon fibers was in the range of up to 6  $\mu\text{m}$ .



(a)

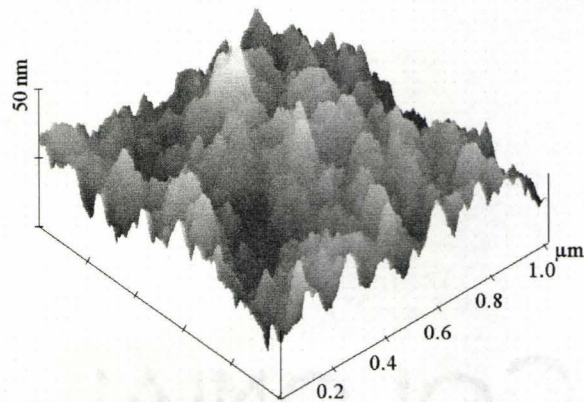


(b)

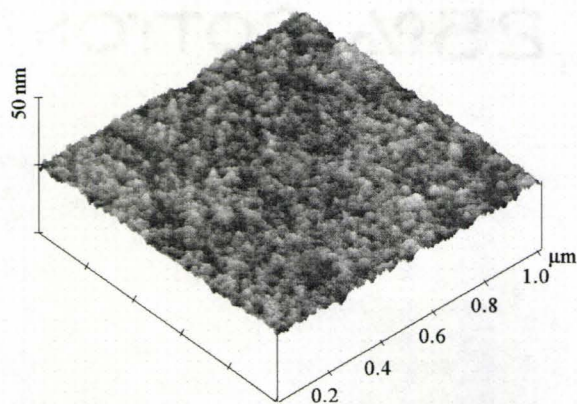


(c)

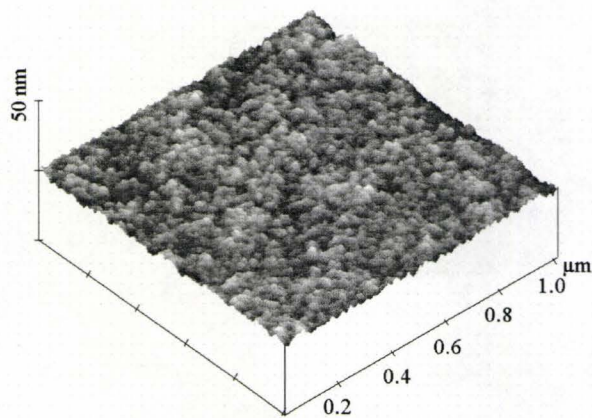
Figure 4-10 SEM pictures of the composite deposits on individual carbon fibres, obtained from the 5 mM  $ZrOCl_2$  solutions containing (a) 0.4 g/l PEI and (b and c) 1.0 g/l PEI (bar=10  $\mu$ m).



(a)



(b)



(c)

Figure 4-11 AFM images of the coatings prepared from the 5 mM  $ZrOCl_2$  solutions containing (a) 0.4 and (b and c) 1.0 g/l PEI at a current density of (a and b) 1.5 and (c) 3 mA/cm<sup>2</sup>, with a deposition time of (a and c) 3 and (b) 5 min.

Figure 4-11 compares the AFM images of the composite coatings on polished stainless steel substrates obtained from the  $ZrOCl_2$  solutions containing PEI. The root-mean-square (rms) surface roughness of the coatings prepared from the solutions containing 0.4 g/l PEI at a current density of  $1.5 \text{ mA/cm}^2$  was found to be 8.1 nm. High surface roughness of the coatings could be attributed to the gas evolution at the cathode surface during deposition. However, it was established that the surface roughness decreased with the increasing polymer content in the deposits. For deposits prepared from solutions containing 1.0 g/l PEI, the rms surface roughness was found to be 0.91 and 0.88 nm for the current densities of 1.5 and  $3 \text{ mA/cm}^2$ , respectively.

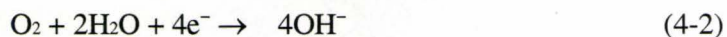
#### 4.2.1.2 Discussion

EPD of the cationic polyelectrolytes has been utilized for the fabrication of the composite coatings on cathodic substrates. The ability to deposit composite materials depends on a thorough knowledge of the factors that control the deposition mechanism and structural evolution of the coatings. Electrophoresis is related to the motion of charged particles or macromolecules toward the electrode and their accumulation at the electrode surface. Deposit formation is achieved as a result of the coagulation of the colloidal particles and polymer macromolecules [Boccaccini *et al.*, 1998; Kaya *et al.*, 1999; Limmer *et al.*, 2002; Moreno *et al.*, 2000; Van der Biest *et al.*, 1999; Zhitomirsky, 2002].

EPD of the polyelectrolytes was combined with electrochemical precipitation

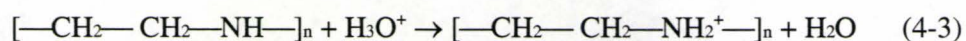
of the colloidal particles, which were produced by the electrogenerated base method.

Cathodic reactions that generate  $\text{OH}^-$  are



These reactions result in basic conditions at the electrode surface. The difference between the solution pH and that in the layer adjacent to the cathode increases with an increasing current density [Kuhn *et al.*, 1983]. It is important to note that the formation of the composite deposits is influenced by the behavior of the polyelectrolytes in basic conditions at the electrode surface.

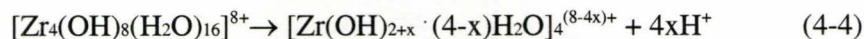
In this work, composite materials were prepared using weak cationic polyelectrolytes, such as PEI and PAH. It is known that the PEI macromolecules can achieve cationicity through protonation of the amine groups in acidic solutions [Baklouti *et al.*, 1997]:



The degree of ionization of PEI depends on the amount of acid added [Baklouti *et al.*, 1997; Zhu *et al.*, 2003]. It was pointed out [Zhu *et al.*, 2003] that the PEI macromolecules had no charge before the titration with acid.

The experimental data presented above indicate codeposition of the polyelectrolytes and zirconium species. In zirconyl chloride solutions, the formation of tetramers  $[\text{Zr}_4(\text{OH})_8(\text{H}_2\text{O})_{16}]^{8+}$  can be expected [Clearfield, 1990]. It is important to

note that the cationic species in solutions show a tendency to release protons [Clearfield, 1990]. Zirconyl chloride solutions are highly acidic, and the following process was considered [Clearfield, 1990]:

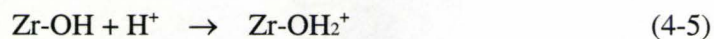


It is suggested that PEI can be partially protonated in acidic zirconyl chloride solutions. As a result, the PEI macromolecules acquire a positive charge.

It is known [Baklouti *et al.*, 1997; Zhu *et al.*, 2003] that protonated PEI has a positive charge over a wide pH range below pH 11. PAH is another weak cationic polyelectrolyte, which is positively charged in acidic solutions [Cassagneau *et al.*, 2000a; Dante *et al.*, 1999; Dutta *et al.*, 2000b; Fang *et al.*, 1999a; Fang *et al.*, 1999b; Feldheim *et al.*, 1996; Keller *et al.*, 1994; Kleinfeld *et al.*, 1996; Lvov *et al.*, 1996; Lvov *et al.*, 2000; Sasaki *et al.*, 2001; Schaak *et al.*, 2000; Shchukin *et al.*, 2003a, b; Tyan *et al.*, 1999; Wang *et al.*, 2002]. It is expected that the electric field provides electrophoretic motion of the charged PEI and PAH macromolecules toward the cathode substrate. The decrease of the polyelectrolyte charge with an increasing pH at the electrode surface reduces the electrostatic repulsion of the polyelectrolyte macromolecules and promotes their deposition. It is important to note that the electrode reactions are not involved in EPD and relatively thick electrophoretic deposits can be obtained [Boccaccini *et al.*, 1998; Kaya *et al.*, 1999; Limmer *et al.*, 2002; Moreno *et al.*, 2000; Van der Biest *et al.*, 1999; Zhitomirsky, 2002] by this

method. On the other hand, cathodic electrosynthesis of the oxide and hydroxide materials is based on the neutralization of the ionic species by the electrogenerated base (Equations (4-1) and (4-2)) to form the colloidal particles at the electrode surface. The formation of an insulating layer prevents electrosynthesis of the zirconium species. As a result, the thickness of the composite monolayers was limited to several micrometers.

Zirconium species can precipitate as zirconium hydroxide or hydrated zirconium oxide [Huang *et al.*, 2001]. The colloidal particles may become positively or negatively charged depending on the pH of the solution



It is important to note that the isoelectric point of hydrous zirconia was reported [Parks, 1965] to be 6.7. Therefore, it is suggested that the colloidal particles formed in basic conditions near the electrode surface are negatively charged. It is suggested that the deposit formation is achieved via heterocoagulation of the colloidal particles and polyelectrolyte macromolecules. The interaction of the polyelectrolytes and colloidal particles could be electrostatic, nonelectrostatic, or a combination of both [Hoogeveen *et al.*, 1996a, b]. This interaction is a complicated phenomenon, influenced by the pH, ionic strength, and electric field. Recent studies indicate that the interaction of zirconia and PEI includes electrostatic attraction and hydrogen bonding [Wang *et al.*, 1999].

Adsorption of protonated PEI on the positively charged zirconia particles was observed at low pHs, below the isoelectric point of  $ZrO_2$ . It was pointed out that this interaction is based on hydrogen bonding. The adsorption increases with an increasing pH. At high pHs, the interaction includes both mechanisms, electrostatic attraction and hydrogen bonding [Wang *et al.*, 1999].

It is known that polyamines form chelating complexes with various heavy-metal ions [Geckeler *et al.*, 1996; Kobayashi *et al.*, 1987; Kobayashi *et al.*, 1985], and metal ions compete with protons to be bound to the polymers. Therefore, we cannot exclude the possibility that the PEI macromolecules may acquire positive charges by way of being bound to the charged zirconium species [Geckeler *et al.*, 1996]. In this case, the electric field provides electrophoretic motion of the PEI macromolecules and bonded cationic zirconium species toward the electrode surface. It is suggested that these species and the free zirconium species, which are not complexed by PEI, participate in cathodic reactions to form hydrated zirconium oxide or zirconium hydroxide.

The electrodeposition of PEI was performed using a mixed methanol-water solvent. Note that the deposition process needs a certain amount of water for base generation in the cathodic reactions (Equations (4-1) and (4-2)). The use of methanol as a solvent is important in order to reduce gas evolution and electrostatic repulsion [Boccaccini *et al.*, 1998; Kaya *et al.*, 1999; Limmer *et al.*, 2002; Moreno *et al.*, 2000; Van der Biest *et al.*, 1999; Zhitomirsky, 2002] of the polymer macromolecules. On the

other hand, the polymer can be adsorbed on the surface of the colloidal particles when its solubility in the dispersion medium is low. It is in this regard that the thickness of the deposited polyelectrolyte multilayers [Dubas *et al.*, 1999] increased with an increasing ethanol content in a mixed water-ethanol solvent. Therefore, another benefit of using a poor solvent is that it promotes the adsorption of the polyelectrolytes on the colloidal particles.

The cathodic precipitation of the zirconium species is influenced by solvent. Indeed, the weight loss for the deposits, prepared from the mixed methanol-water solvent, was found to be 18.4 wt %, compared to the weight loss of 32.6 wt % reported [Zhitomirsky *et al.*, 1998] for deposits prepared from the aqueous solutions. It is in this regard that the precipitation of the zirconium species can result in the formation of hydrated zirconium oxide or zirconium hydroxide, which exhibited weight losses of 21.5 and 32.19 wt %, respectively [Huang *et al.*, 2001]. It is reasonable to expect that the electrosynthesis of the zirconium species is also influenced by the polyelectrolytes. It was observed that the phase content and crystallinity of some materials, prepared by chemical precipitation or electrosynthesis, are influenced by the polyelectrolytes [Shchukin *et al.*, 2003a, b; Zhitomirsky *et al.*, 2003]. On the other hand, some composite materials cannot be considered as a simple mixture of organic and inorganic components.

The method developed for the electrodeposition of the composite materials is a combination of two processes, EPD of polyelectrolytes and electrosynthesis of

inorganic particles. The deposition rate  $W$  in the EPD can be described by the following equation:

$$W = C\mu U/d \quad (4-7)$$

where  $C$  is the concentration of the colloidal particles or polymer macromolecules,  $U=U_{ap}-U_{dep}$ ,  $U_{ap}$  is the applied voltage,  $U_{dep}$  is voltage drop in the deposit,  $d$  is the distance between the electrodes, and  $\mu$  is the electrophoretic mobility of the particles or polyelectrolytes [Boccaccini *et al.*, 1998; Kaya *et al.*, 1999; Limmer *et al.*, 2002; Moreno *et al.*, 2000; Ohshima, 1995; Van der Biest *et al.*, 1999; Zhitomirsky, 2002].

Constant current EPD enables a constant electric field  $U/d$  in solutions and a constant deposition rate. On the other hand, Faraday's law governs the electrosynthesis of inorganic materials. Therefore, at a constant-current mode, EPD and electrosynthesis enable a constant deposition rate. Indeed, the nearly linear deposit weight versus time dependencies were recorded for composite coatings, as shown in Figure 4-1. Equation (4-7) indicates that the increasing polymer concentration in solutions results in an increasing deposition yield. The increasing polymer concentration in solutions at a constant concentration of  $ZrOCl_2$  resulted in an increasing polymer content in the composite deposits (Figure 4-3 and Figure 4-6).

Electrosynthesis enabled the formation of amorphous zirconium species. Crystallization of zirconia was observed after heat treatment at temperatures exceeding 400 °C, as shown in Figure 4-4 and Figure 4-7. On the other hand, the

results indicate the possibility of electrophoretic codeposition of crystalline YSZ and PEI. It is suggested that the adsorption of PEI [Wang *et al.*, 1999] resulted in stable suspensions of positively charged YSZ particles. This strategy paves the way for the fabrication of other ceramic-polymer composites with important functional properties.

The AFM data indicate a relatively high surface roughness of the deposits prepared by the combined electrodeposition method. The uniformity of the electrophoretic deposits results from the insulating properties of the deposited materials and electric field dependence of the deposition rate [Boccaccini *et al.*, 1998; Kaya *et al.*, 1999; Limmer *et al.*, 2002; Moreno *et al.*, 2000; Van der Biest *et al.*, 1999; Zhitomirsky, 2002]. It is suggested that the relatively high surface roughness of the deposits prepared by the combined method, based on EPD of the polyelectrolyte macromolecules and electrosynthesis of the colloidal particles, could be attributed to hydrogen evolution at the cathode surface. Future research may focus on the use of processing additives, which consume  $H^+$  in cathodic reactions and reduce gas evolution.

#### 4.2.2 Fabrication of $ZrO_2$ coatings with a strong polyelectrolyte additive

The experimental results and discussion of this section are produced based on the published paper [Pang *et al.*, 2005c].

##### 4.2.2.1 Experimental results

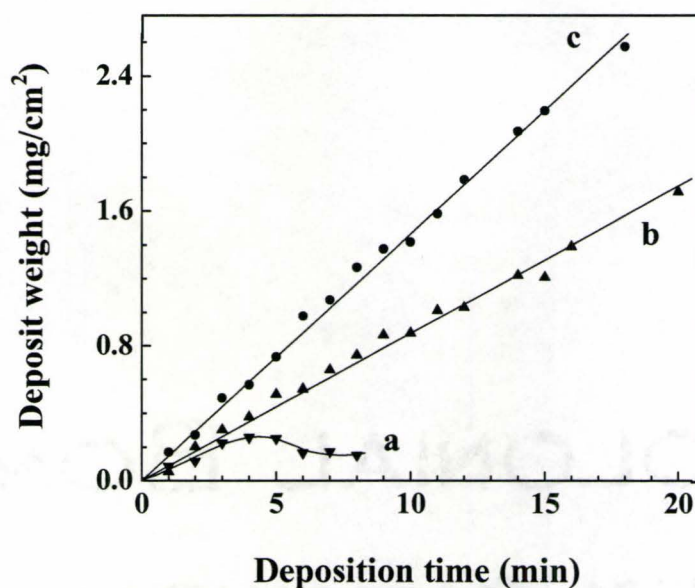


Figure 4-12 Deposit weight versus deposition time for the deposits prepared from the 5 mM  $ZrOCl_2$  solutions (a) without additives, and containing (b) 0.5 g/l and (c) 1.0 g/l PDDA on a stainless steel substrate at a current density of 3 mA/cm<sup>2</sup>.

Electrodeposition experiments performed from the 5 mM  $ZrOCl_2$  solutions containing 0–1.0 g/l PDDA resulted in the formation of cathodic deposits. Figure 4-12 shows the deposit weight as a function of the deposition time for the 5 mM  $ZrOCl_2$  solutions without additives and containing various amounts of PDDA. In the

experiments performed from the pure  $ZrOCl_2$  solutions, a deposit spallation was observed at deposition times exceeding 4 min and no weight gain was obtained at longer deposition durations. The deposit weight versus deposition time dependence showed a maximum at a deposition time of 4 min. The deposits obtained exhibited low adhesion.

In contrast, continuous increase in the deposit weight was observed for the solutions containing 0.5–1.0 g/l PDDA. Nearly linear deposit weight–time dependencies were recorded as shown in Figure 4-12. This implies a possibility of controlling the amount of the deposited material by changing the deposition time at a constant current density. The increase in the PDDA concentration in the solutions resulted in a higher deposition rate (Figure 4-12). The obtained deposits adhered well to the stainless steel and Pt substrates. It should be noted that a continuous increase in the deposit weight was observed for deposition duration of up to 30 min. However, at deposition durations exceeding ~20 min the deposits obtained were porous. TG data for the deposits prepared from the pure  $ZrOCl_2$  solutions exhibited a weight loss that can be attributed to the dehydration of the deposits (Figure 4-13). Two distinct steps in the TG curve can be distinguished. A sharp reduction of the sample weight was observed in the range of 20–150 °C. An additional step in the weight loss was recorded in the range of 310–350 °C. At higher temperatures the weight changed gradually. The total weight loss at 1200 °C was found to be 18.4% of the initial sample weight. TG data for the deposits obtained from the 5 mM  $ZrOCl_2$  solutions

containing different amounts of PDDA are also shown in Figure 4-13. The total weight loss at 1200 °C for the deposits prepared from the solutions containing 0.5 g/l PDDA and 1.0 g/l PDDA was found to be 52.3 and 68.0 wt%, respectively. No appreciable weight change was observed at temperatures exceeding 550 °C.

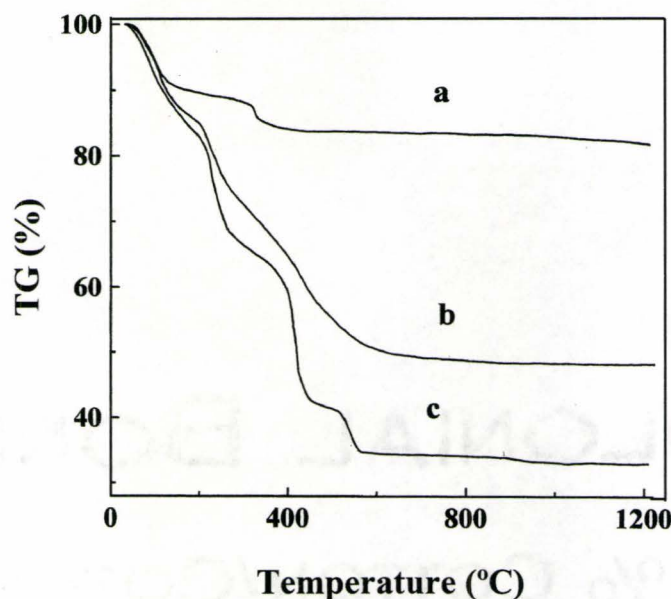


Figure 4-13 TG data for the deposits prepared from the 5 mM  $ZrOCl_2$  solutions (a) without additives and containing (b) 0.5 g/l and (c) 1.0 g/l PDDA.

These results, coupled with the TG data for the deposits prepared from the pure  $ZrOCl_2$  solutions indicate the electrochemical codeposition of the PDDA and zirconium species. The weight loss for the deposits prepared from the solutions containing PDDA is related to the burning out of the organic phase and the dehydration of the inorganic phase. The TG data have been used to calculate the

polymer content in the composite deposits. The amount of PDDA was found to be 41.5 and 60.8 wt% for the deposits prepared from the solutions containing 0.5 and 1.0 g/l PDDA, respectively. This indicates the formation of the composite coatings containing different amounts of PDDA. The increase in the PDDA concentration in the solutions resulted in an increasing PDDA content in the deposits.

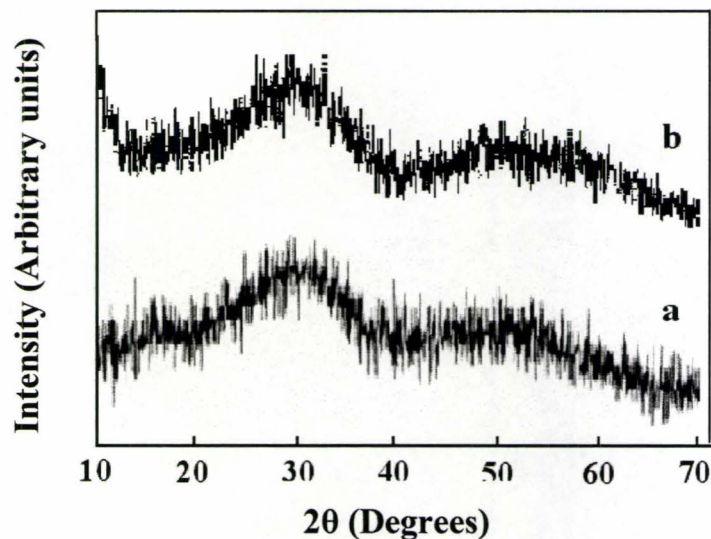


Figure 4-14 XRD patterns of the deposits prepared from the 5 mM  $ZrOCl_2$  solutions (a) without PDDA and (b) containing 0.5 g/l PDDA.

XRD patterns for the fresh deposits exhibited very broad peaks (Figure 4-14), which could be attributed to the small crystal size of zirconia. However, it is suggested that the deposits also contained an amorphous phase.

Figure 4-15 shows the AFM images of the composite coatings on polished stainless steel substrates obtained from the  $ZrOCl_2$  solutions containing 1.0 g/l PDDA.

The root-mean-square (rms) surface roughness was found to be 3.2 nm and 4.2 nm for current densities of 3 and 5 mA/cm<sup>2</sup>, respectively. Relatively high surface roughness of the coatings prepared by the electrodeposition could be attributed to the gas evolution at the cathode surface during deposition. As a result, a higher surface roughness was observed at a higher current density (Figure 4-15).

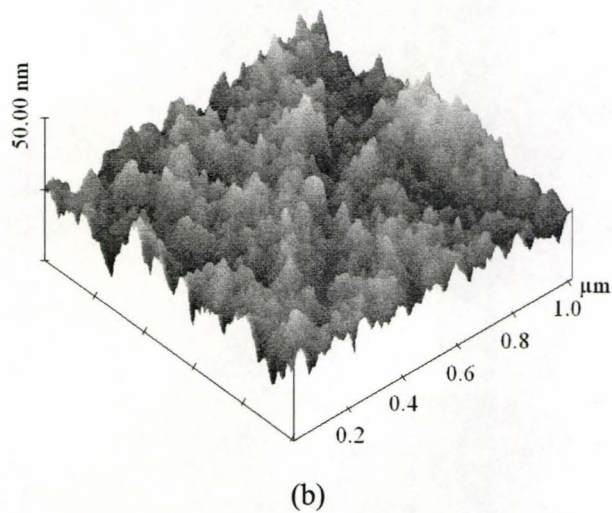
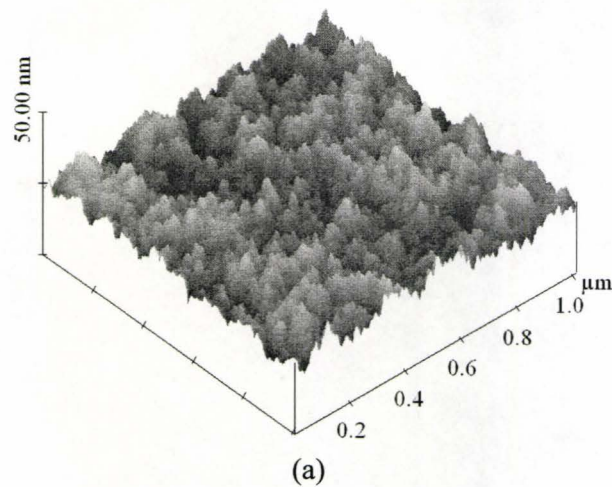


Figure 4-15 AFM images of the composite coatings prepared from the 5 mM ZrOCl<sub>2</sub> + 1.0 g/l PDDA solution at current densities of (a) 3 mA/cm<sup>2</sup> and (b) 5 mA/cm<sup>2</sup>, deposition time 3 min.

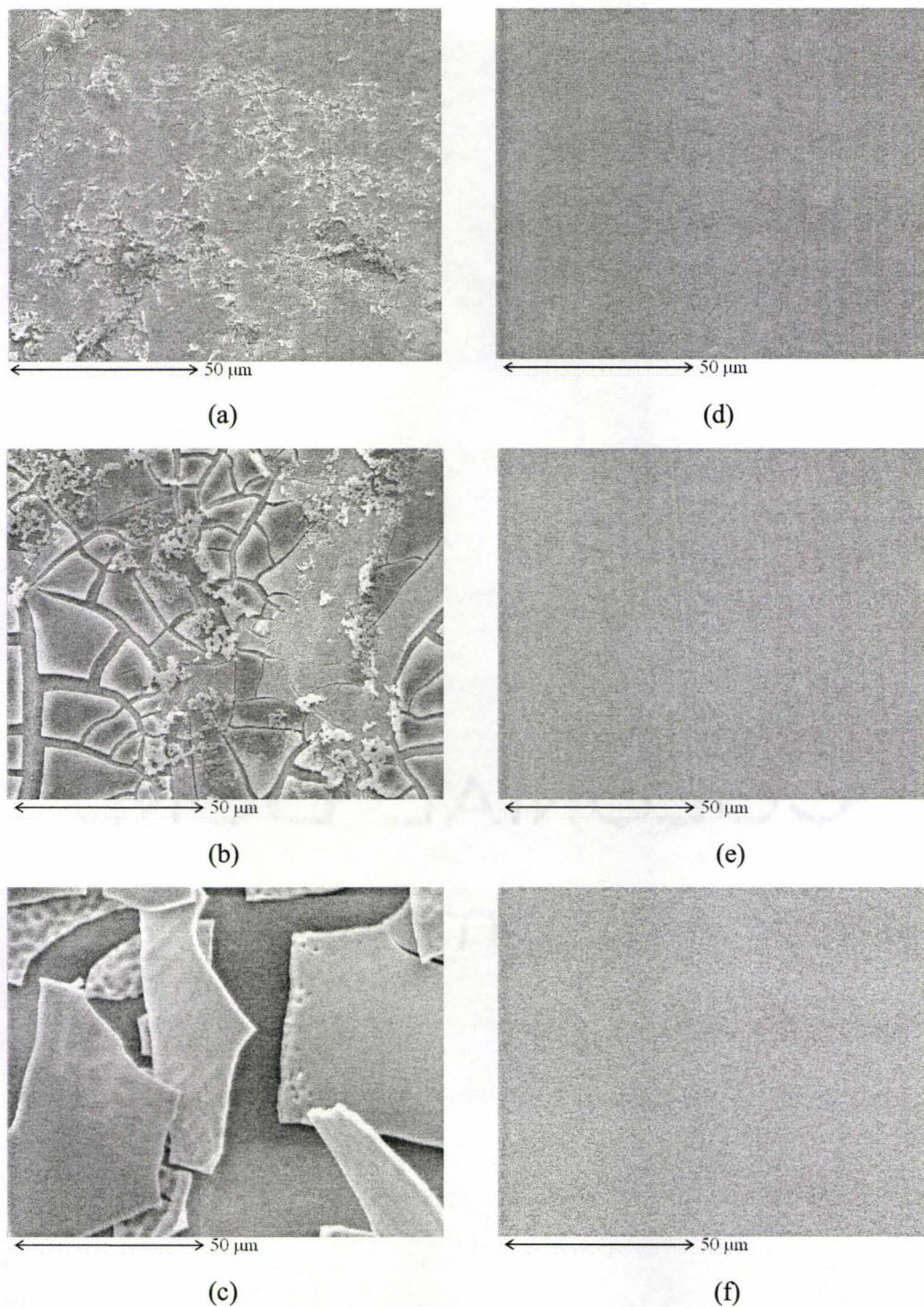


Figure 4-16 SEM pictures of the deposits on stainless steel substrates prepared from the pure 5 mM  $ZrOCl_2$  solution (a,b,c) without additives and (d,e,f) containing 0.5 g/l PDDA: deposition time (a,d) 1, (b,e) 2 and (c,f) 5 min.

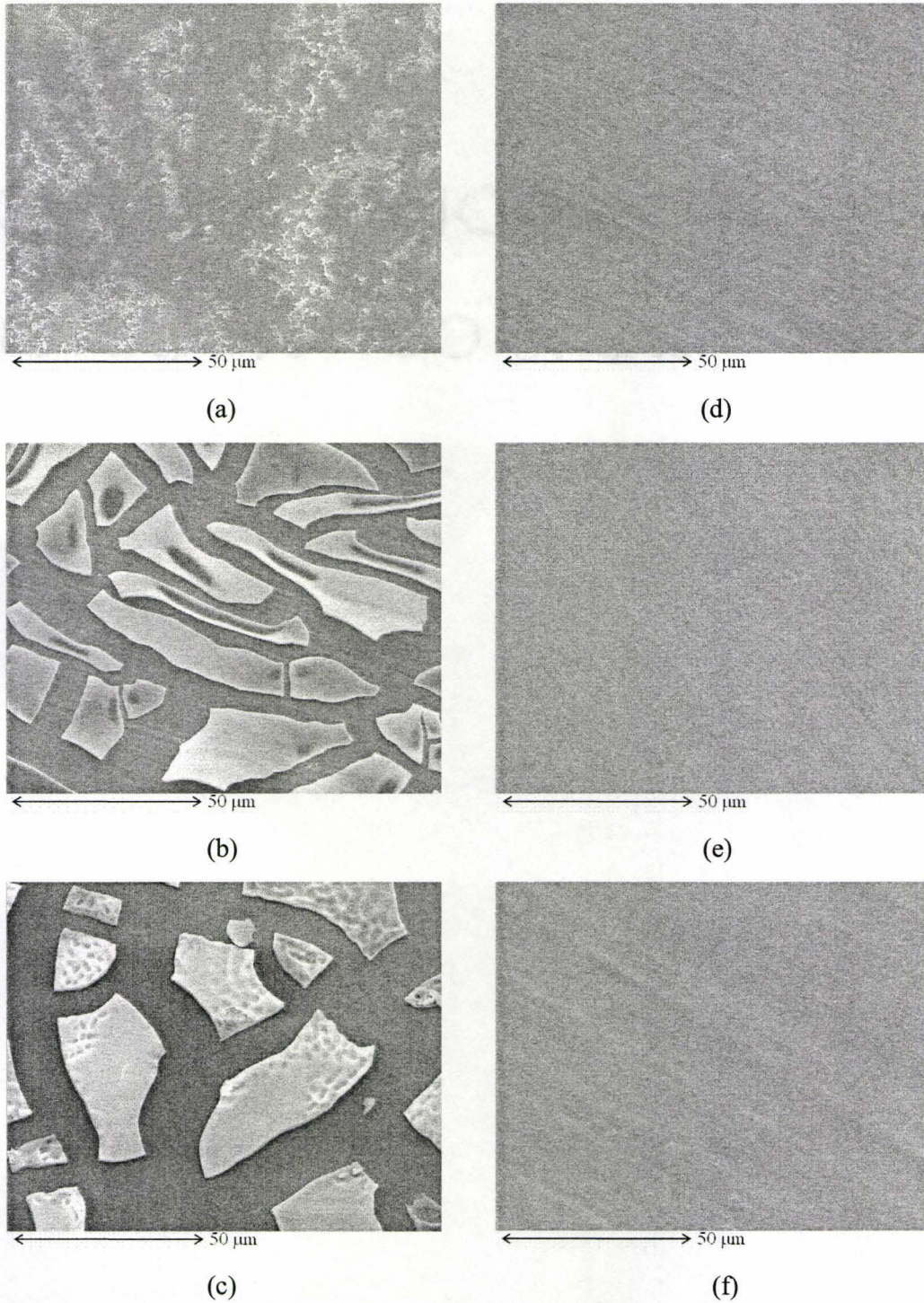


Figure 4-17 SEM pictures of the deposits on stainless steel substrates prepared from the pure 5 mM  $ZrOCl_2$  solution (a,b,c) without additives and (d,e,f) containing 0.5 g/l PDDA: deposition time (a,d) 1, (b,e) 2 and (c,f) 5 min after sintering at 600 °C for 1 hr.

Figure 4-16 compares SEM images of the as prepared coatings for the deposition times of 1, 2 and 5 min. The deposits prepared from the  $ZrOCl_2$  solutions without PDDA exhibited cracking, which increased with the increasing deposition time (Figure 4-16c). Deposits prepared from  $ZrOCl_2$  solutions containing 0.5 g/l PDDA exhibited a crack-free morphology. The deposits containing PDDA adhered well to the substrates.

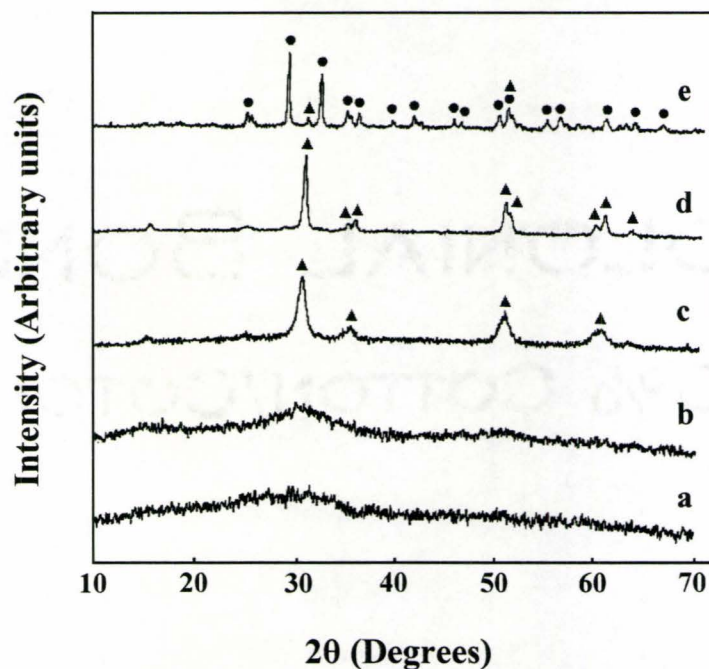


Figure 4-18 XRD patterns for the deposits obtained from the 5 mM  $ZrOCl_2$  solutions, containing 0.5 g/l PDDA: after annealing during 1 hr at (a) 200, (b) 400, (c) 600, (d) 800, and (e) 1000 °C.  $\blacktriangle$  – tetragonal zirconia,  $\bullet$  – monoclinic zirconia.

Figure 4-17 shows the SEM picture of the deposits sintered at 600 °C. The sintering of the deposits prepared from the pure  $ZrOCl_2$  solutions resulted in a

“cracked–mud” appearance [Chaim *et al.*, 1991], as shown in Figure 4-17 (b,c). The deposits exhibited low adhesion and could easily be removed from the substrates. On the other hand, the deposits prepared from the solutions containing PDDA and sintered at the same conditions were crack–free and adherent. The deposit weight–deposition time dependencies shown in Figure 4-12, coupled with the results of TG analysis and SEM investigations of the sintered coatings, indicate that using PDDA as a binder, crack–free and adherent zirconia coatings of various thicknesses in the range of up to 1  $\mu\text{m}$  could be obtained.

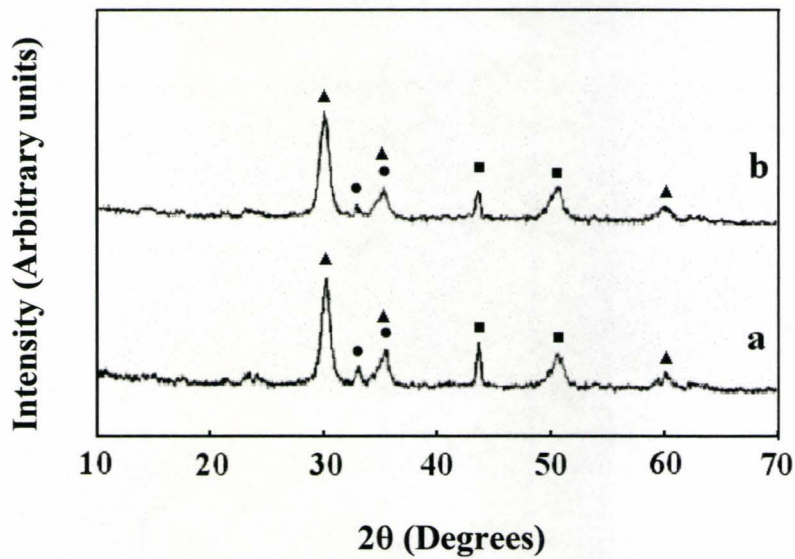


Figure 4-19 XRD patterns for the deposits prepared from the 5 mM  $\text{ZrOCl}_2$  + 0.5 g/l PDDA solution at a current density of 3  $\text{mA}/\text{cm}^2$  after annealing at 600  $^\circ\text{C}$  during 1 hr: deposition time (a) 22 min and (b) 30 min. ▲ – tetragonal zirconia, ● –  $\text{Fe}_2\text{O}_3$ , and ■ – substrate.

Figure 4-18 shows the XRD patterns of the deposits prepared from the 5mM  $ZrOCl_2$  solutions containing 0.5 g/l PDDA and annealed at different temperatures. The XRD patterns at 200 and 400 °C indicate that the deposits mainly contained an amorphous phase. At 600 °C broad peaks were observed which can be attributed to tetragonal or cubic zirconia. At this temperature, it is difficult to distinguish between tetragonal and cubic zirconia owing to the peak broadening. The peaks become sharper at higher temperatures. The XRD pattern at 800 °C displayed peaks of tetragonal zirconia (JCPDS file 17-923). Further increase of annealing temperature resulted in the transformation to monoclinic zirconia (JCPDS file 37-1484) at 1000 °C.

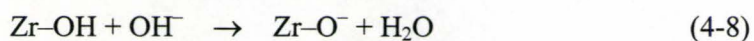
Figure 4-19 shows XRD patterns of zirconia coatings of different thickness sintered on stainless steel substrates. The XRD patterns exhibit peaks of zirconia and the substrates. Small peaks of  $Fe_2O_3$  (JCPDS file 33-664) could be attributed to the partial oxidation of the substrates. The relative intensity of the  $Fe_2O_3$  and substrate peaks decreases with the increasing deposition time and deposit thickness, as shown in Figure 4-19.

#### **4.2.2.2 Discussion**

PDDA is a strong cationic polyelectrolyte, which maintains a positive charge under basic conditions. As a result of the strong electrostatic repulsion of the PDDA macromolecules, no deposit formation was achieved from the aqueous PDDA

solutions [Zhitomirsky *et al.*, 2000a, b, c]. However, codeposition of PDDA and the colloidal particles of metal oxides and hydroxides was observed [Zhitomirsky *et al.*, 2003; Zhitomirsky *et al.*, 2000a, b, c]. It was suggested that the deposit formation is driven by Coulombic attraction between the two charged species: cationic PDDA and the negatively charged colloidal particles formed at the electrode surface.

The mechanism of cathodic electrodeposition of composite zirconium hydroxide – PDDA coatings has been described in the literature [Zhitomirsky, 2002]. The proposed approach is based on two processes: the electrosynthesis of inorganic particles and electrophoresis of PDDA. The cathodic electrosynthesis of the zirconium hydroxide particles is achieved by the electrogenerated base method. In this method, cathodic reduction of water results in high pH conditions at the electrode surface (Equation (4-1)). In zirconyl chloride solutions, formation of tetramers  $[\text{Zr}_4(\text{OH})_8(\text{H}_2\text{O})_{16}]^{8+}$  can be expected [Clearfield, 1990]. The tetramers show a tendency to release protons and form acidic bulk solutions (Equation (4-4)). It is suggested that zirconium species are hydrolyzed by the electrogenerated base to form colloidal particles in the basic conditions at the cathode surface. The following surface reactions occur in aqueous and alcoholic (ROH) suspensions [Yu *et al.*, 2003; Zhitomirsky, 2002] at high pH:



The isoelectric point of hydrous zirconia was reported to be 6.7 [Parks, 1965]. Therefore, it is suggested that the colloidal particles are negatively charged at the cathode surface.

The electric field provides electrophoretic motion of cationic PDDA macromolecules towards the cathode. PDDA macromolecules maintain a high positive charge in acidic and basic conditions. The electrophoresis and electrosynthesis result in the accumulation of the PDDA macromolecules and colloidal particles at the electrode surface. The heterocoagulation of the colloidal particles and the PDDA macromolecules at the electrode surface, results in the deposit formation [Zhitomirsky, 2002]. It is important to note that no deposit formation was observed in the electrodeposition experiments performed from the pure aqueous PDDA solutions [Zhitomirsky, 2002; Zhitomirsky *et al.*, 2000d]. It is suggested that the strong electrostatic repulsion of the PDDA macromolecules at the electrode surface prevents the deposit formation. On the other hand, low adhesion and low Faradaic efficiencies [Gal-Or *et al.*, 1991; Zhitomirsky *et al.*, 1998; Zhitomirsky *et al.*, 2000d] were reported for the deposits prepared from pure aqueous  $ZrOCl_2$  or  $ZrO(NO_3)_2$  solutions. The low adhesion of zirconia deposits could be attributed to the electrostatic repulsion of the negatively charged colloidal particles formed at the electrode surface, the particle–electrode electrostatic interactions and other factors, described in reference [Zhitomirsky, 2002]. However, adherent deposits were obtained from the aqueous  $ZrOCl_2$  solutions containing PDDA.

The attraction of the PDDA macromolecules and colloidal particles could be electrostatic or nonelectrostatic or a combination of both. An important strategy to improve the adsorption of the polymer macromolecules on the colloidal particles is based on the use of a poor solvent [Zhitomirsky, 2002, 2004]. Here the electrodeposition was performed using a mixed methanol–water solvent. Note, that water molecules are necessary for the base generation in Equation (4-1). A polymer can be adsorbed on the surface of the colloidal particles when its solubility in the dispersion medium is low. On the other hand, the lower dielectric constant of the mixed methanol–water solvent results in a reduced dissociation of the ionizable groups and a reduced steric and electrostatic repulsion of the PDDA macromolecules. It is in this regard that the thickness of the deposited polyelectrolyte multilayers [Dubas *et al.*, 1999] increased with the increasing ethanol content in the mixed water–ethanol solvent. Therefore, the methanol–water solvent of a lower dielectric constant could improve the codeposition of the PDDA and inorganic nanoparticles.

The deposition rate in the EPD method [Boccaccini *et al.*, 1998; Boccaccini *et al.*, 2002b; Moreno *et al.*, 2000; Russ *et al.*, 1998b; Van der Biest *et al.*, 1999] can be described by the Equation (4-7). The constant current EPD enables a constant electric field  $U/d$  in the solutions and a constant deposition rate [Boccaccini *et al.*, 2002b; Van der Biest *et al.*, 1999]. On the other hand, Faraday's law governs the electrosynthesis of the inorganic materials. Therefore, a constant deposition rate of the organic and inorganic phases could be expected at a constant current mode of electrodeposition.

Indeed, nearly linear deposit weight–time dependencies were obtained. The increase in the deposition rate with the increasing PDDA concentration in the solutions (Figure 4-12) is in agreement with Equation (4-7).

An important point to be discussed is the influence of the solvent and PDDA on the electrosynthesis of zirconium species. It is known that methanol can remove hydroxyl groups and water from the surface of zirconium hydroxide [Jones *et al.*, 1988]. Zirconium species can precipitate as zirconium hydroxide or hydrated zirconium oxide [Huang *et al.*, 2001]. Clearfield [Clearfield, 1964] prepared monoclinic and cubic hydrous zirconia. A close agreement between the interplanar spacings of the hydrous oxides and those of the calcined products was observed [Clearfield, 1964]. The cubic hydrous zirconia was found to be stable up to 650 °C.

The influence of polyelectrolytes on the chemical precipitation of crystalline inorganic nanoparticles has been reported in several papers [Dutta *et al.*, 2000a; Shchukin *et al.*, 2003b; Shchukin *et al.*, 2003c]. The possibility of low temperature synthesis of crystalline inorganic phases under the influence of organic phases opens novel opportunities for the fabrication of nanomaterials with advanced functional properties [Dutta *et al.*, 2000a; Shchukin *et al.*, 2003b; Shchukin *et al.*, 2003c; Zhitomirsky *et al.*, 2003]. Recent investigations indicate that the phase content and crystallinity of the inorganic nanoparticles prepared by electrosynthesis is influenced by the PDDA additives [Ngankam *et al.*, 2000; Wang *et al.*, 2002; Zhitomirsky *et al.*, 2003]. The cathodic electrodeposition enabled the formation of Fe<sub>3</sub>O<sub>4</sub> nanocrystals in

the PDDA matrix. The obtained coatings exhibited superparamagnetic properties [Zhitomirsky *et al.*, 2003].

The TEM studies of the composite deposits prepared from the  $ZrOCl_2$  solutions containing PDDA [Pang *et al.*, 2005c] revealed the formation of crystalline zirconia particles at room temperature in a polymer matrix. It is suggested that the size and crystallinity of the particles are influenced by the solvent and PDDA. In the cathodic electrodeposition method, zirconia particles were prepared *in-situ* in the PDDA matrix and separated by the polymer. The possibility of the fabrication of zirconia nanoparticles by chemical precipitation in a polymer matrix has also been reported in the literature [Ray *et al.*, 2001]. The method enabled the control of the particle size.

The electrodeposition experiments reported in references [Chaim *et al.*, 1991; Gal-Or *et al.*, 1991; Zhitomirsky *et al.*, 1998] resulted in amorphous deposits. Crystallization of the deposits was observed at temperatures exceeding 400 °C. In contrast, room temperature electrosynthesis of monoclinic zirconia was reported in reference [Aslam *et al.*, 2000], where the crystalline deposits were formed on the self-assembled monolayer (SAM) of pentane-1,5-dithiol on polycrystalline gold substrates. It was shown that the SAM influenced the crystallization behavior of zirconia.

The formation of tetragonal zirconia from amorphous precursors by electrosynthesis method was reported in other investigations [Chaim *et al.*, 1991;

Zhitomirsky *et al.*, 1998]. It was shown that the heat treatment of the precursors at 400–450 °C, resulted in the formation of tetragonal nanocrystallites. The size of the zirconia particles was ~10 nm. Heat treatment at 500–600 °C resulted in the increasing particle size and transformation of tetragonal zirconia to stable monoclinic phase. However, the experimental results of this work showed that the zirconia coatings sintered at 800 °C still exhibited a tetragonal structure (Figure 4-18). It is suggested that the absence of tetragonal–monoclinic phase transformation in the temperature range of 20–800 °C is important to prevent cracking during the sintering of the nanostructured coatings prepared by electrosynthesis. However the kinetics of the transformation to monoclinic phase is influenced by factors such as temperature, particle size and heat treatment duration [Zhitomirsky *et al.*, 1998].

The experimental results also indicate the possibility of electrosynthesis of adherent and thick coatings. The use of PDDA with inherent binding properties is important to prevent cracking attributed to drying shrinkage. However, the increase of the PDDA concentration in the deposits could result in an increasing sintering shrinkage. Therefore, further experiments must be focused on the optimization of the PDDA concentration in the solutions and deposits.

### **4.3 Electrodeposition of hydroxyapatite-chitosan nanocomposite coatings**

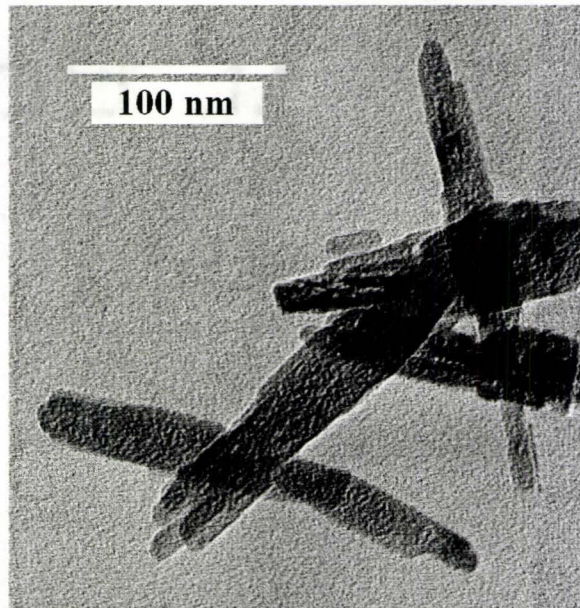
The experimental results and discussion of this section are produced based on the published papers [Pang *et al.*, 2005a, b, 2007; Zhitomirsky *et al.*, 2006].

#### **4.3.1 Experimental results**

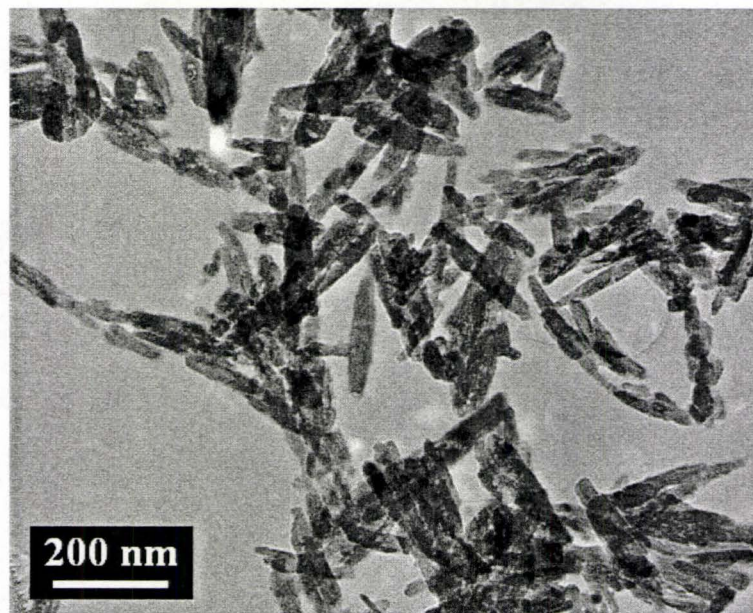
##### **4.3.1.1 TEM studies of the synthesized hydroxyapatite nanoparticles**

Hydroxyapatite nanoparticles prepared by the chemical precipitation method were studied by TEM. Typical TEM micrographs are given in Figure 4-20, showing a needle-like morphology of the HA crystals. The average length of the crystals was about 200 nm and the average aspect ratio was 8. This observation is in a good agreement with the results of other investigations, indicating precipitation of needle-like HA crystals with their long dimension oriented along the *c*-axis of the hexagonal structure [Bouyer *et al.*, 2000; Koutsopoulos, 2002]. It is important to note that TEM observation of HA nanoparticles presents difficulties related to the HA degradation under the electronic beam. Bouyer *et al.* [Bouyer *et al.*, 2000] demonstrated that the periphery of HA nanoparticles becomes amorphous. The thickness of the amorphous layer increased with increasing exposition time. The small size of the HA nanoparticles enabled the formation of well-dispersed suspensions, which were stable against sedimentation for 1–2 days. Electrodeposition performed from the chitosan solutions containing HA resulted in the formation of cathodic

deposits.



(a)



(b)

Figure 4-20 TEM images of the HA nanoparticles.

#### 4.3.1.2 XRD analysis of the hydroxyapatite nanoparticles and chitosan

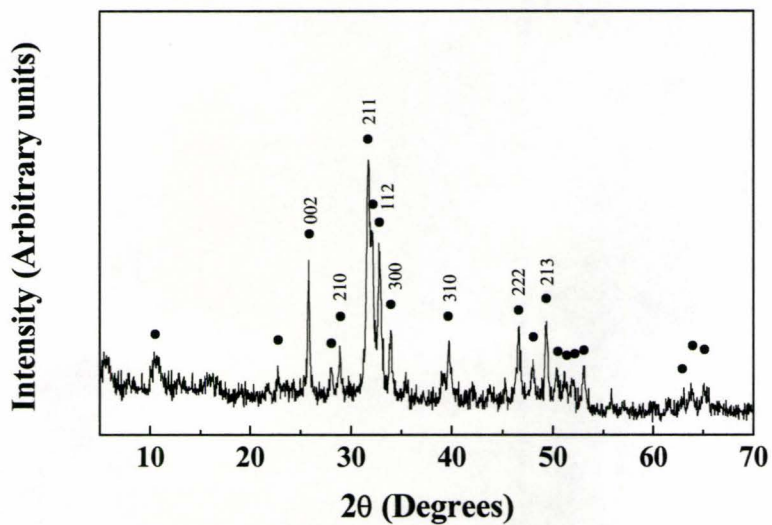


Figure 4-21 XRD pattern of as-prepared HA nanoparticles.

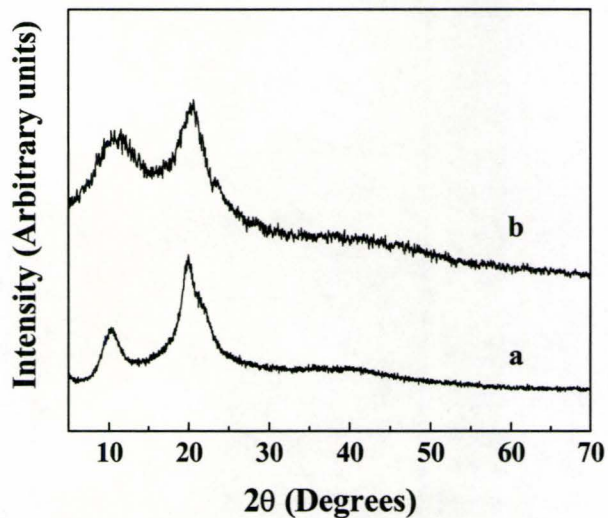


Figure 4-22 XRD pattern of (a) as received chitosan, and (b) the deposit prepared from the 0.5 g/l chitosan solution in the mixed ethanol-water solvent (17% water), deposition time of 20 min.

Figure 4-21 gives the XRD pattern of the synthesized HA nanoparticles. The result showed crystallinity of the as-prepared HA particles. Observed XRD peaks correlated closely with the JCPDS file 09-0432 for HA.

Cathodic deposits were obtained from the chitosan solutions in water and the mixed water-ethanol solvent. The deposition from aqueous solutions was accompanied by significant gas evolution, which resulted in porous coatings. Deposit porosity reduced with increasing ethanol content in the mixed ethanol-water solvent, and with decreasing current density. Uniform and smooth coatings were obtained at low current densities of 0.1-0.2 mA/cm<sup>2</sup>. Figure 4-22 compares XRD patterns of as-received and deposited chitosan. The XRD pattern of as-received chitosan revealed very broad peaks at 2θ of ~10 and ~20°. X-ray studies of the chitosan coatings showed similar peaks at slightly higher diffraction angles.

#### **4.3.1.3 TG/DTA investigations of the hydroxyapatite nanoparticles and chitosan**

TG studies of the as-prepared HA powders (Figure 4-23) showed a total weight loss of 7.5 wt% at 1000 °C, which can be mainly attributed to the liberation of adsorbed water and CO<sub>2</sub>. Essentially most of the weight loss occurred below 300 °C. The DTA curve exhibits a broad endotherm around ~ 90 °C.

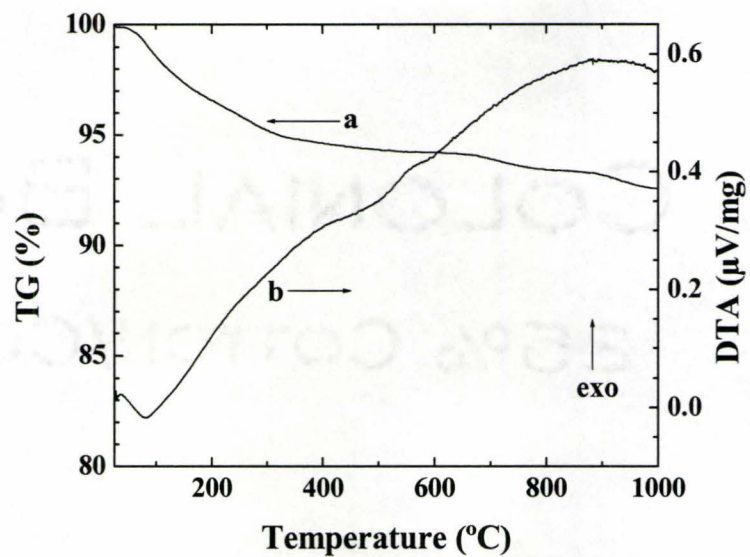


Figure 4-23 (a) TG and (b) DTA data for the HA powders, prepared by the chemical precipitation method.

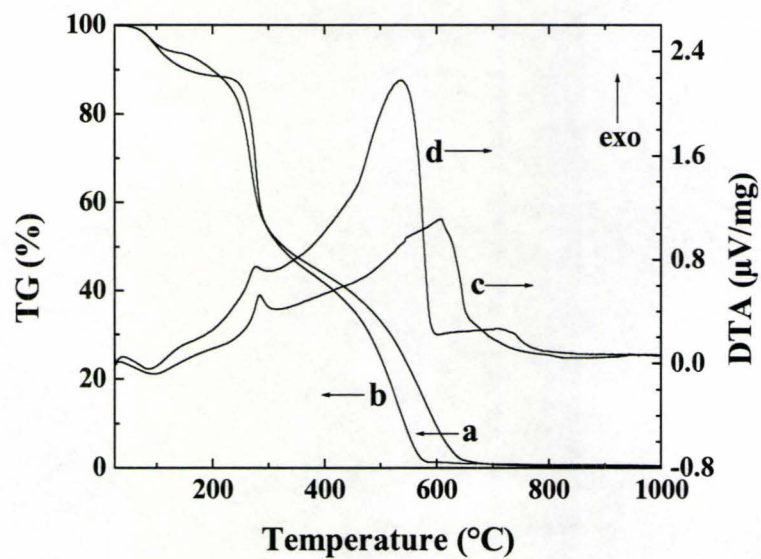


Figure 4-24 (a,b) TG and (c,d) DTA data for (a,c) as-received chitosan powders and (b,d) the pure chitosan deposit obtained from a 0.5 g/l chitosan solution.

Figure 4-24 compares the TG/DTA data for a pure chitosan deposit and as-received chitosan powders. TG studies of the as-received chitosan showed three steps in weight loss. The reduction of the sample weight below 100 °C can be attributed to the liberation of adsorbed water. The two steps in weight loss at 280–300 °C and 500–650 °C can be attributed to the thermal degradation of chitosan, which led to the burning out of the as-received chitosan at 650 °C. The DTA curve for the as-received chitosan exhibited a broad endotherm around 90 °C and exotherms around 280 and 625 °C. It is suggested that the observed endotherm and exotherms correspond to the steps in weight loss. The TG and DTA curves for the chitosan deposit showed similar behavior. However, the burning out of the deposited chitosan was observed at a lower temperature. The DTA curve for the deposited chitosan exhibited exothermic peaks at 275 and 575 °C. The lower thermal degradation temperature of chitosan deposits compared to as-received chitosan powders was also reported in the literature for the chitosan coatings prepared by a casting technique [Nunthanid *et al.*, 2001].

#### **4.3.1.4 TG/DTA investigations of the composite deposits**

The addition of HA powders to chitosan solutions resulted in the codeposition of chitosan and HA. Electrodeposition performed from the 0.5 g/l chitosan solutions containing 0-8.0 g/l HA resulted in the formation of cathodic deposits. The results of TG investigations indicated codeposition of HA and chitosan.

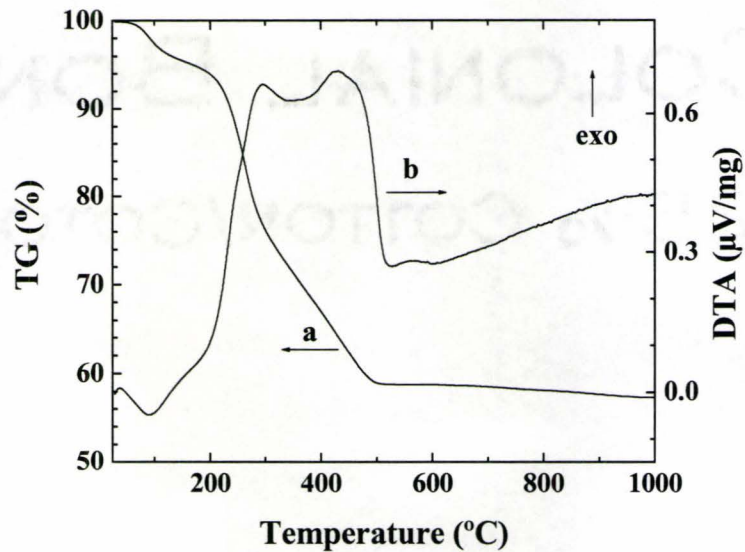


Figure 4-25 (a) TG and (b) DTA data for the composite HA-chitosan deposit prepared from the 1.0 g/l HA suspension in the mixed ethanol-water solvent (17% water) containing 0.5 g/l chitosan, deposition time of 20 min.

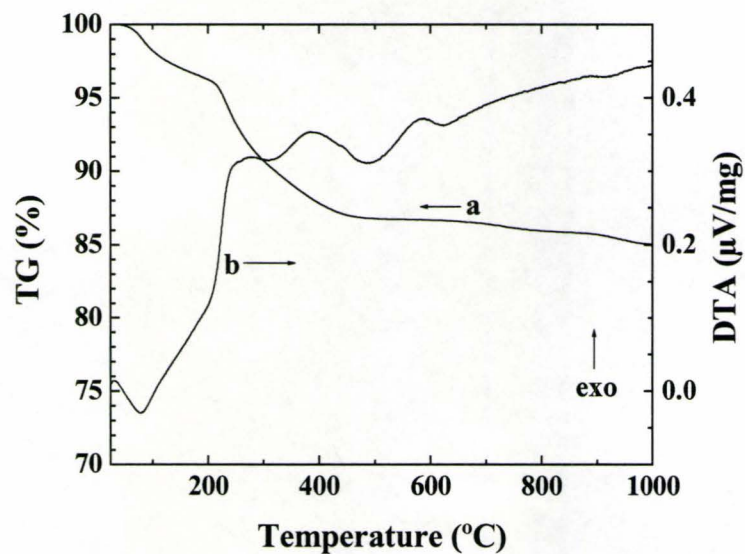


Figure 4-26 (a) TG and (b) DTA data for the composite HA-chitosan deposit prepared from the 8.0 g/l HA suspension in the mixed ethanol-water solvent (17% water) containing 0.5 g/l chitosan, deposition time of 20 min.

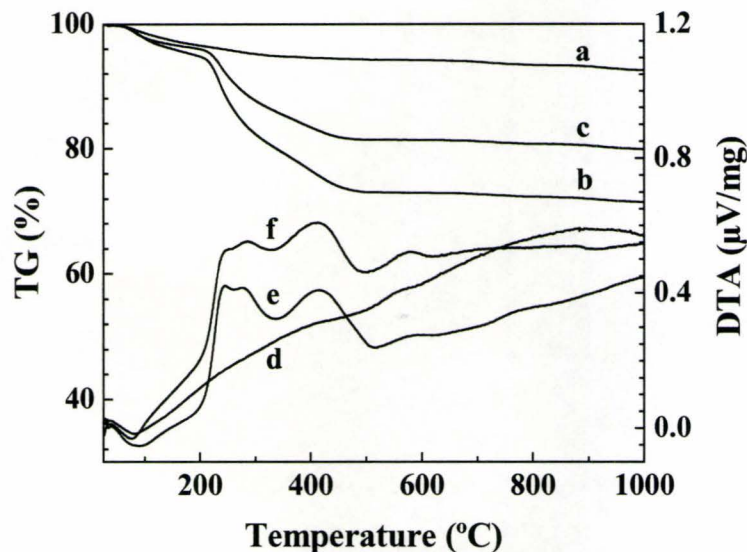


Figure 4-27 TG (a) and DTA (d) data for as-prepared HA powders, compared to (b,c) TG and (e,f) DTA data for the composite HA-chitosan deposits obtained from the (b,e) 2.0 g/l and (c,f) 4.0 g/l HA suspensions in the mixed ethanol-water solvent (17% water) containing 0.5 g/l chitosan at a constant current density of 0.1 mA/cm<sup>2</sup>.

Figure 4-25 and Figure 4-26 show results of TG studies of the coatings prepared from 0.5 g/l chitosan solutions containing 1.0 and 8.0 g/l HA. The total weight loss at 1000 °C was found to be 42.7 and 15.0 wt% for HA concentrations of 1.0 and 8.0 g/l, respectively. The TG data for the composite coatings (Figure 4-25 and Figure 4-26) show an additional weight loss compared to the weight loss for pure HA powders (Figure 4-23), which can be attributed to the burning out of chitosan. The TG data can be used to study the composition of the coatings prepared from the chitosan solutions containing HA. The amount of chitosan was found to be 38.1 and 8.1 wt% for the coatings prepared from the 0.5 g/l chitosan solutions containing 1.0 and 8.0 g/l HA, respectively. DTA data for the composite coatings showed a broad endotherm at

~ 90 °C attributed to the liberation of the adsorbed water, and exotherms in the range of 200-600 °C related to the burning out of chitosan.

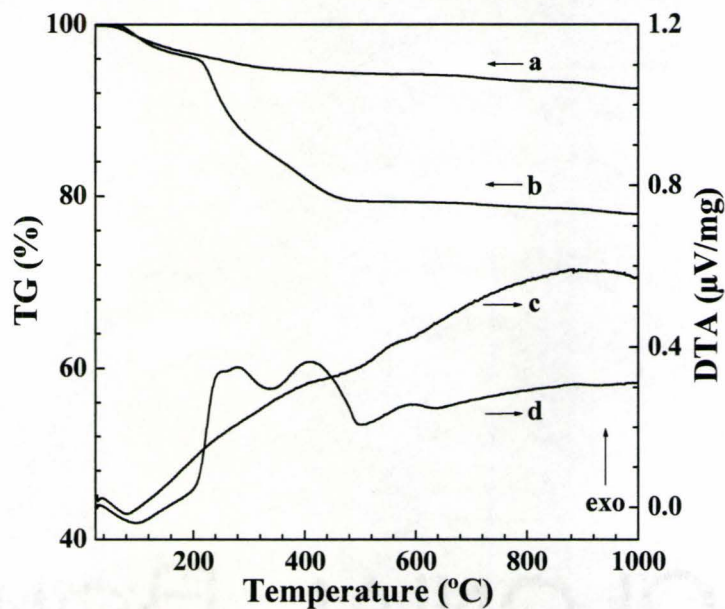


Figure 4-28. (a,b) TG and (c,d) DTA data for (a,c) as-prepared HA powders and (b,d) the composite HA–chitosan deposits obtained from a 0.5 g/l chitosan solution containing 3.0 g/l HA.

Similar TG/DTA data were obtained for the composite deposits prepared from 0.5 g/l chitosan solutions containing different amounts of HA. Figure 4-27 shows TG data for as-prepared HA nanoparticles and composite coatings deposited from 0.5 g/l chitosan solutions containing 2.0 and 4.0 g/l HA. The TG curves for the composite deposits showed an additional step in weight loss in the range of 200-500 °C. The deposits prepared from the solutions, containing 2.0 and 4.0 g/l HA, showed the total

weight loss of 28.5 and 20.1 wt %, respectively. The HA content in the composite coatings prepared from solutions containing 2.0 and 4.0 g/l HA was found to be 71.5 and 79.9 wt%, respectively. The results of TG are in a good agreement with DTA data. DTA data for the composite coatings showed broad endotherms at  $\sim 90$  °C, and exotherms in the range of 200-600 °C related to the burning out of chitosan. Similar exotherms were observed for as-deposited chitosan coating.

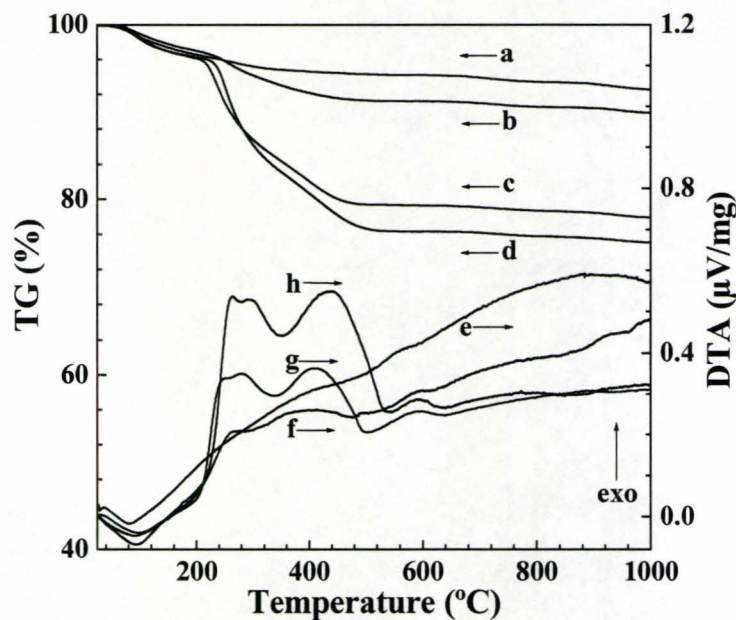


Figure 4-29 (a,b,c,d) TG and (e,f,g,h) DTA data for (a,e) as-prepared HA powders, and the composite HA–chitosan deposits obtained from the 3.0 g/l HA suspensions containing (b,f) 0.1 g/l, (c,g) 0.5 g/l, and (d,h) 0.7 g/l chitosan.

Figure 4-28 compares the TG/DTA data for as-prepared HA nanoparticles and a composite deposit prepared from a 0.5 g/l chitosan solution containing 3.0 g/l HA.

The TG curve of the composite deposit (Figure 4-28 (b)) showed an additional step in the range of 200–500 °C, and the total weight loss was 22.1 wt. %. The HA content in the composite coating was found to be 77.9 wt%. The TG results are consistent with the DTA data.

Figure 4-29 compares the TG/DTA data for as-prepared HA nanoparticles and the composite deposits prepared from 3.0 g/l HA suspensions containing various amounts of chitosan. The TG curves for the composite deposits (Figure 4-29 (b,c,d)) showed an additional step in weight loss in the range of 200–500 °C compared to the TG data for the HA nanoparticles. The composite deposits prepared from the 3.0 g/l HA suspensions containing 0.1, 0.5, and 0.7 g/l chitosan showed the total weight loss of 10.2, 22.1, and 24.9 wt %, respectively. The results of the TG investigations indicate that the composition of the deposits can be changed by a variation of the chitosan concentration in the HA suspensions. The HA content in the composite coatings prepared from the 3.0 g/l HA suspensions containing 0.1, 0.5, and 0.7 g/l chitosan was found to be 89.8, 77.9, and 75.1 wt%, respectively. The TG results are consistent with the DTA data. The DTA data for the composite coatings (Figure 4-29 (f,g,h)) showed broad endotherms at ~90 °C, and exotherms in the range of 200–600 °C related to the burning out of chitosan. Similar exotherms were observed for the as-received and as-deposited chitosan (Figure 4-24 (c,d)).

Figure 4-30 shows the variation of HA content in the composite coatings prepared from 0.5 g/l chitosan solutions containing various amounts of HA. The HA

content was calculated from the TG data for the composite coatings. It was observed that the HA content in the deposited composite coatings increased with the increasing HA concentration in the chitosan solutions. HA–chitosan nanocomposites containing 40.9–85.0 wt% HA were obtained by the variation of the HA concentration in the range of 0.5–8.0 g/l.

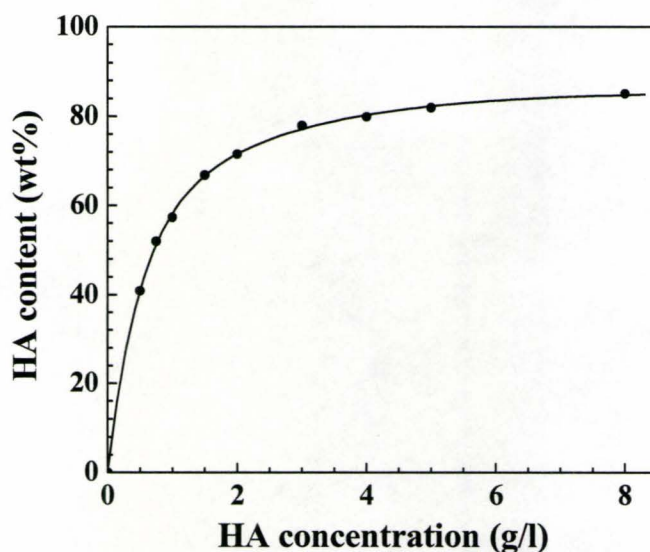


Figure 4-30 The variation of the HA content in the composite coatings as a function of the HA concentration in the 0.5 g/l chitosan solutions used for EPD.

The experimental results presented above indicate the possibility of the fabrication of composite coatings, containing different amounts of chitosan and HA.

#### 4.3.1.5 XRD investigations of the composite deposits

XRD studies of the composite coatings showed peaks of HA (Figure 4-31).

Similar XRD patterns were obtained for other samples prepared from chitosan solutions containing different amounts of HA.

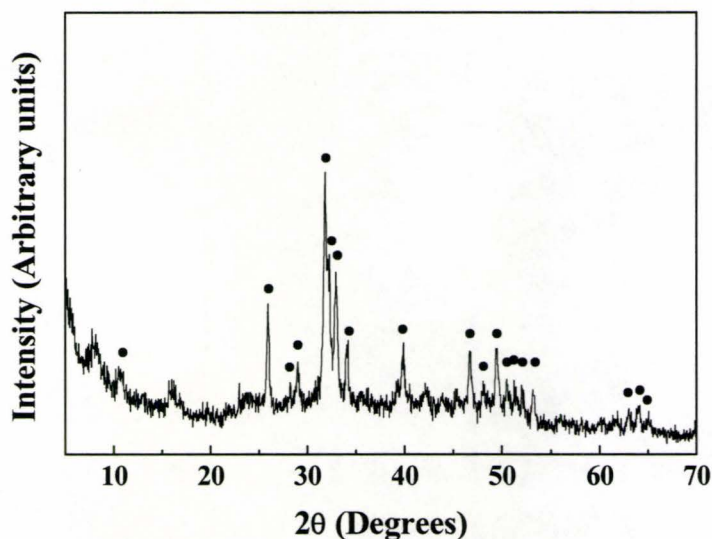


Figure 4-31 XRD pattern of the composite HA-chitosan deposit prepared from the 8.0 g/l HA suspension in the mixed ethanol-water solvent (17% water) containing 0.5 g/l chitosan, deposition time of 20 min. ● – HA (JCPDS 09-0432).

Figure 4-32 compares the XRD patterns of the as-prepared HA nanoparticles and the HA-chitosan composite deposits on a stainless steel substrate. The observed XRD peaks for HA nanoparticles (Figure 4-32 (a)) correlated closely with the JCPDS file 09-0432, with the 211 peak having the highest intensity. A similar XRD pattern was obtained for the as-deposited pure HA coating (Figure 4-32 (b)). The XRD patterns of the composite coatings (Figure 4-32 (c,d,e)) showed an increased intensity of the 300 peak and a suppression of the 002 peak of HA, indicating a preferred orientation of the *c*-axes of the HA crystals parallel to the coating surface. It was

observed that the degree of the orientation of the HA nanocrystals decreased with the increasing HA concentration in the chitosan solutions. However, the composite deposit (Figure 4-32 (e)) scraped from the substrate exhibited a well defined 002 peak and a reduced intensity of the 300 peak (Figure 4-32 (f)), similar to the XRD pattern of the as-prepared HA powders (Figure 4-32 (a)).

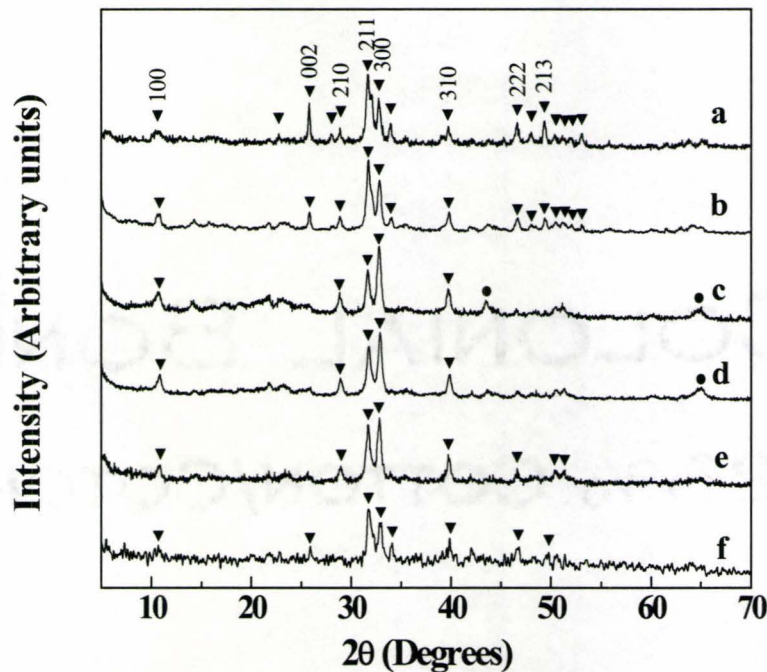


Figure 4-32 XRD patterns for (a) as-prepared HA particles, (b) the pure HA deposit on 316L stainless steel obtained from a 3.0 g/l HA suspension, and the composite deposits on 316L stainless steel prepared from the 0.5 g/l chitosan solutions containing (c) 0.5 g/l, (d) 1.0 g/l, and (e) 3.0 g/l HA, and (f) the same composite deposit as in (e) scraped from the substrate. (▼ — HA ● — substrate).

Figure 4-33 shows the XRD intensity ratio  $I(300)/I(211)$  for the composite coatings versus the HA concentration in the 0.5 g/l chitosan solutions. The

experimental results presented in Figure 4-30 and Figure 4-33 indicate that an increase in the HA concentration in the chitosan solutions would result in an increasing HA content and a decreasing preferred orientation of the HA nanoparticles in the composite coatings.

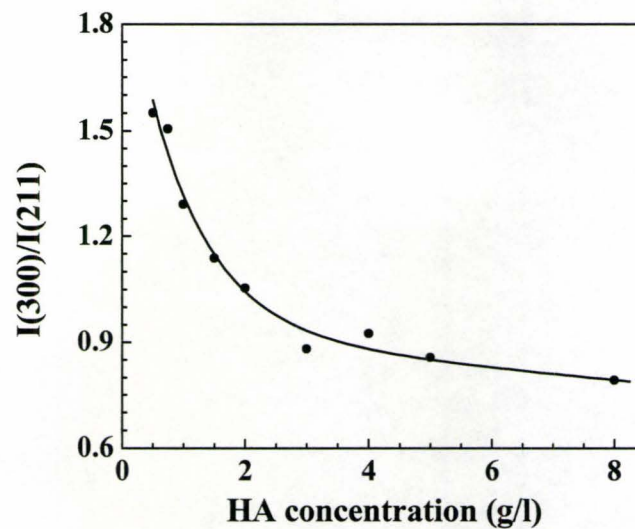


Figure 4-33 The variation of the XRD intensity ratio  $I(300)/I(211)$  of the HA peaks for the same coatings as a function of the HA concentration in the 0.5 g/l chitosan solutions used for EPD.

The X-ray studies of composite coatings on Ti substrate showed similar results (Figure 4-34), indicating the preferred orientation of *c*-axes of the HA crystals in the plane parallel to the coating surface. The XRD pattern presented in Figure 4-34 (b) shows increased intensity of 300 peak. However, the 002 peak was not observed. The same deposit removed from the substrate exhibits well defined 002 peak and reduced intensity of 300 peak. The XRD pattern of the deposit removed from the substrate

(Figure 4-34c) is similar to that of the as-prepared HA.

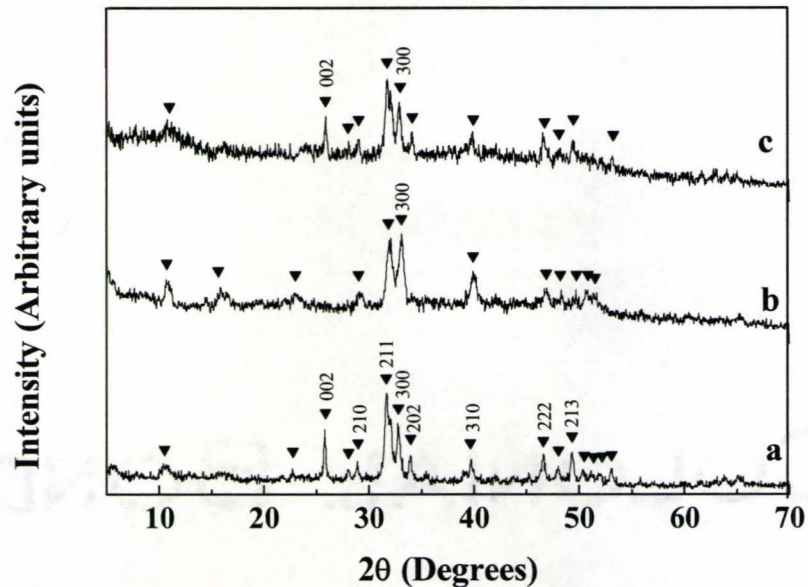


Figure 4-34 XRD patterns for (a) as-prepared HA powders, and a composite deposit (b) on the Ti substrate and (c) scraped from the Ti substrate. The composite deposit was prepared from the 4 g/l HA suspension in the mixed ethanol-water solvent (17% water) containing 0.5 g/l chitosan at a constant current density of 0.1 mA/cm<sup>2</sup> (▼ — HA).

#### 4.3.1.6 Deposition yield

The deposition yield can be changed by the variation of the deposition time at a constant current density. Figure 4-35 shows the deposit weight versus deposition time for the deposits prepared from the 0.5 g/l chitosan solutions containing 4.0 and 8.0 g/l HA. The deposit weight increased with the increasing deposition time. Nearly linear dependence was obtained, which indicates a constant deposition rate.

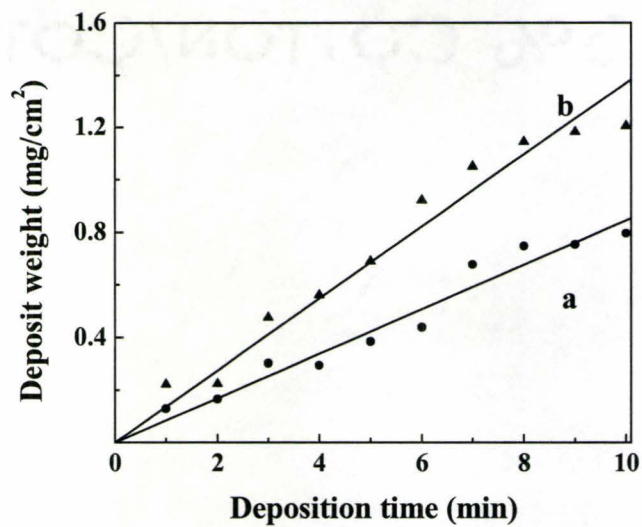


Figure 4-35 Deposit weight versus deposition time for the deposits prepared from the (a) 4.0 g/l HA and (b) 8.0 g/l HA suspensions in the mixed ethanol–water solvent (17 wt% water) containing 0.5 g/l chitosan, at a current density of 0.1 mA/cm<sup>2</sup>.

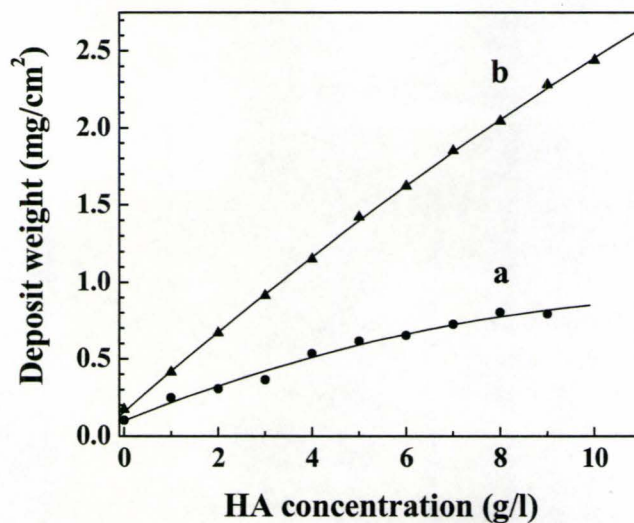


Figure 4-36 Deposit weight versus HA concentration in the suspensions in the mixed ethanol-water solvent (17 % water) containing 0.5 g/l chitosan, at constant current densities of (a) 0.1 and (b) 0.2 mA/cm<sup>2</sup>, and deposition time of 3 min.

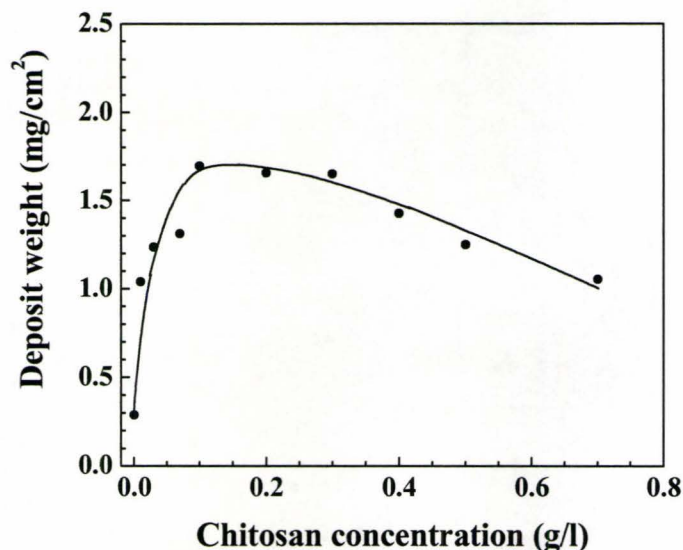


Figure 4-37 Deposit weight versus chitosan concentration in 3.0 g/l HA suspensions, at a current density of 0.1 mA/cm<sup>2</sup> and deposition time of 5 min. The concentration of acetic acid in all the suspensions was 1.9 mM.

Figure 4-36 shows the variation of the deposit weight with the HA concentration in the 0.5 g/l chitosan solutions at different deposition current densities. With the same deposition time, a higher deposit weight was obtained with an increased current density. The increase in HA concentration in the solutions resulted in an increasing deposit weight, which can be attributed to the increasing HA content in the deposited coatings. The experimental data are in agreement with the results of TG investigations.

Figure 4-37 shows the variation of the deposit weight versus the chitosan concentration in solutions containing 3.0 g/l HA. The addition of chitosan to the pure HA suspensions resulted in an increased deposition yield, indicating the codeposition

of HA and chitosan. The highest deposit weight was achieved at 0.1 g/l chitosan. A further increase in the chitosan concentration led to a decreasing deposit weight.

The TG/DTA studies (Figure 4-29) coupled with the results shown in Figure 4-37 indicate that the deposition yield of HA can be increased by an addition of chitosan to the HA suspensions. Indeed, the deposition yield from the pure 3 g/l HA suspension was  $\sim 0.3 \text{ mg/cm}^2$ , whereas the addition of 0.1 g/l chitosan resulted in a  $1.7 \text{ mg/cm}^2$  deposit containing 89.8 wt% HA. The further addition of chitosan resulted in a decreasing deposition yield. However, the TG data in Figure 4-29 indicate that the amount of HA deposited from the 3 g/l HA suspensions containing 0.5 and 0.7 g/l chitosan was still higher than the deposit weight from the pure 3 g/l HA suspension.

#### **4.3.1.7 SEM/TEM investigations of the coatings**

The use of chitosan enabled the formation of dense and adherent coatings at room temperature. Composite coatings were successfully deposited on various conductive substrates. The obtained composite coatings were studied by SEM/TEM.

The deposits obtained at different deposition durations were studied by SEM. Figure 4-38 shows the cross sections of the deposits prepared on graphite substrate. The SEM pictures show relatively uniform deposits of different thicknesses in the range of up to 50  $\mu\text{m}$ . The increase in the deposition time resulted in an increasing coating thickness.

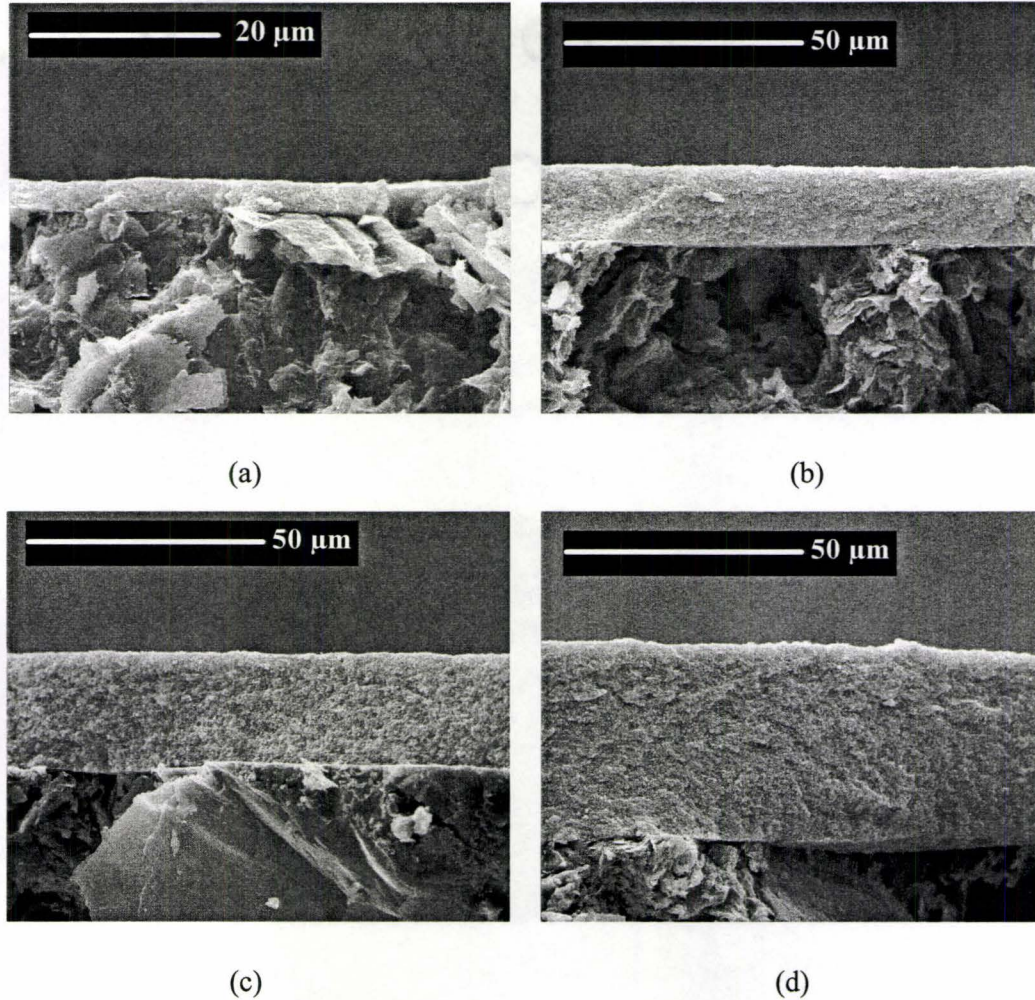


Figure 4-38 SEM pictures of sectioned HA-chitosan composite deposits on graphite substrate obtained from the 8.0 g/l HA suspension in the mixed ethanol-water solvent (17% water) containing 0.5 g/l chitosan at a current density of 0.1 mA/cm<sup>2</sup> and deposition time: (a) 1 min, (b) 3 min, (c) 5 min, and (d) 7 min.

Figure 4-39 shows the increase in the deposit thickness with the increasing deposition time at a constant current density. Nearly linear dependence was obtained, which indicates a constant deposition rate. The galvanostatic deposition offers an advantage [Van der Biest *et al.*, 1999; Zhitomirsky, 1998c, 2002] of constant deposition rate. The increase in the HA concentration in the solutions resulted in an

increase in the coating thickness.

The experimental results presented in Figure 4-35, Figure 4-38, and Figure 4-39 indicate that the amount of the deposited material can be controlled by changing the deposition conditions. The thickness of the coatings can be varied in the range of up to 50  $\mu\text{m}$  by the variation of the deposition time and the HA concentration in the solutions.

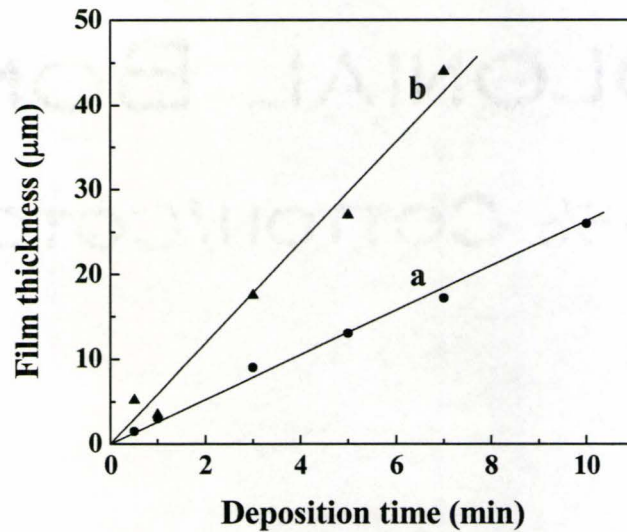


Figure 4-39 The variation of deposit thickness with the deposition time for the HA-chitosan composite deposits prepared from the 0.5 g/l chitosan solutions containing (a) 4 g/l and (b) 8 g/l HA.

Figure 4-40 shows SEM pictures of the composite coating deposited on stainless steel wire. The obtained deposits were relatively dense and adherent to the substrate. Figure 4-41 (a,b) shows the SEM pictures of the composite coatings of different thicknesses on Ti wire. The thickness of the coatings was varied in the range

of up to 50  $\mu\text{m}$  by the variation of the deposition voltage and deposition time. The electrodeposition process resulted in the formation of coatings of uniform thickness. SEM micrographs revealed a smooth, dense and continuous morphology. The uniformity of coatings prepared by electrodeposition results from the insulating properties of the deposits and electric field dependence of the deposition rate [Zhitomirsky, 1998c].

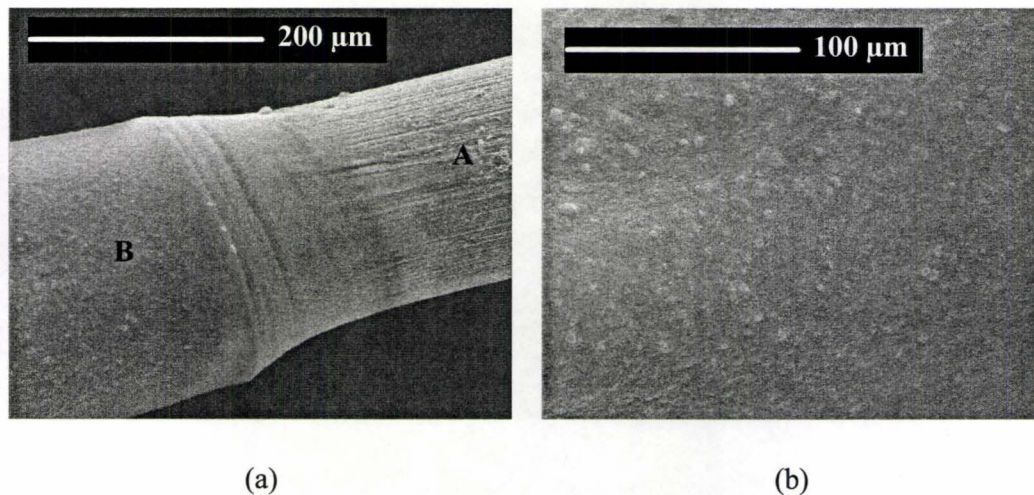


Figure 4-40 SEM pictures of the HA-chitosan composite deposit on stainless steel wire obtained from the 8.0 g/l HA suspension in the mixed ethanol-water solvent (17% water) containing 0.5 g/l chitosan at a current density of 0.1 mA/cm<sup>2</sup> and deposition time 3 min: (a) A — uncoated area, and B — coated area at low magnification; (b) coated area at a higher magnification.

Composite coatings were also deposited on Ti gauze (Figure 4-41 (c,d)). The possibility of deposition of composite coatings on Ti wire and gauze is important for the fabrication of advanced implants for biomedical applications [Ducheyne *et al.*, 1990]. The SEM observations indicate that coatings of different thicknesses can be deposited.

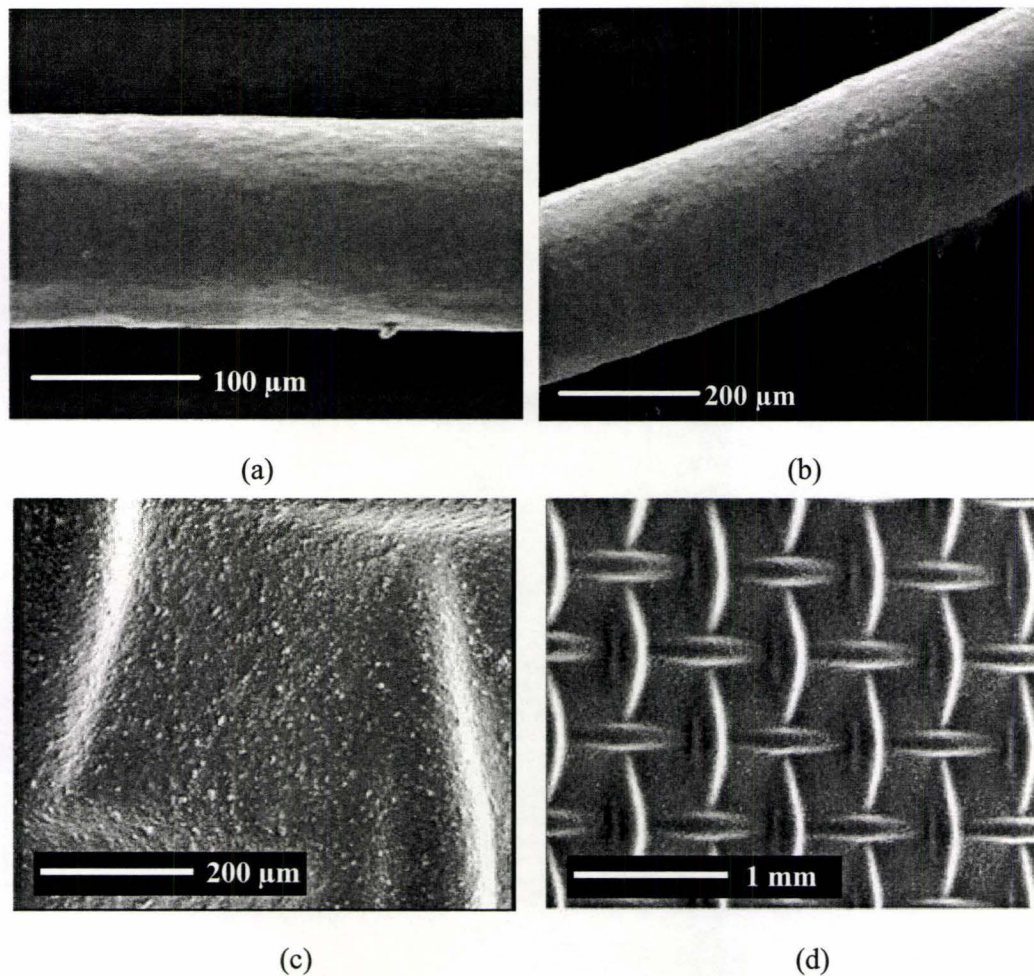


Figure 4-41 SEM pictures of HA-chitosan composite deposits obtained from the 4 g/l HA suspension in the mixed ethanol-water solvent (17% water) containing 0.5 g/l chitosan: on Ti wire substrate, (a) at a constant voltage of 8 V and deposition time of 3 min and (b) at a constant voltage of 12 V and deposition time of 7 min; and on Ti gauze substrate (c,d - different magnifications) at a constant voltage of 12 V and deposition time of 20 min.

Figure 4-42 shows the SEM pictures of the composite coatings of different thicknesses on 316L stainless-steel wire. The thickness of the coatings was varied in the range of up to 60 μm by the variation of the deposition time. SEM micrographs revealed a smooth and continuous morphology. It is suggested that the chitosan with

inherent binding properties enables the formation of adherent composite coatings, resulting in a good bonding between the coatings and the substrates. High-magnification SEM investigations showed that the microstructure of the coatings depends on the coating composition.

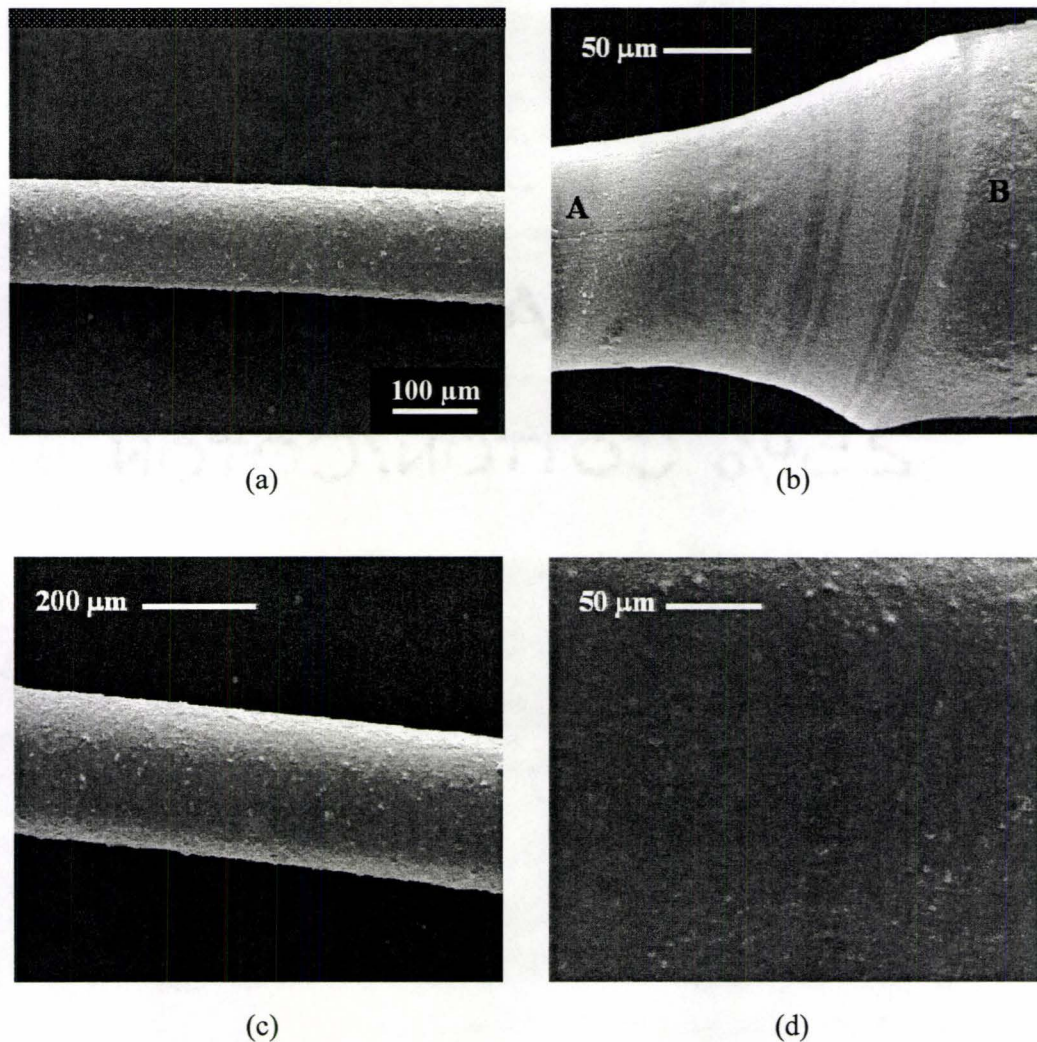


Figure 4-42 SEM images of the HA–chitosan composite deposits on 316L stainless-steel wire prepared from the 0.5 g/l chitosan solutions containing 3.0 g/l HA, with a deposition time of (a) 3 min, (b) 5 min (A — uncoated area, B — coated area), and (c) 10 min. (d) the coated area B at a higher magnification.

SEM pictures of the HA–chitosan composite coatings prepared from the 0.5 g/l chitosan solutions containing 0.5 g/l and 8.0 g/l HA are shown in Figure 4-43. The deposit prepared from the 8.0 g/l HA suspension consisted of HA nanoparticles with adsorbed polymer. The microstructure exhibited significant porosity with a typical pore size of about 100–200 nm. The pore size is comparable with the size of the HA nanoparticles and can be attributed to the packing of the particles. The porosity can also be a result of the hydrogen evolution at the cathode surface during EPD.

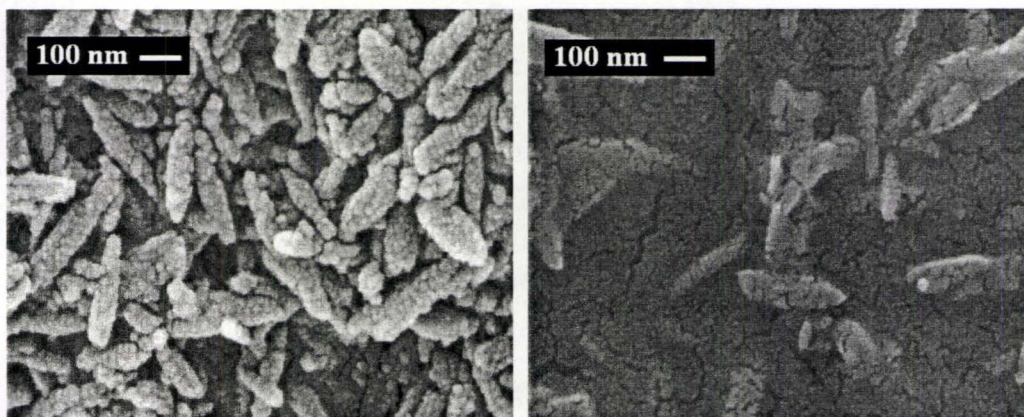


Figure 4-43 SEM pictures of the HA–chitosan composite coatings prepared from the 0.5 g/l chitosan solutions containing (a) 8.0 g/l, and (b) 0.5 g/l HA.

The SEM picture of the deposit prepared from the 0.5 g/l chitosan solution containing 0.5 g/l HA showed that the HA nanoparticles are distributed in a polymer matrix. Figure 4-43 (b) shows small cracks in the chitosan matrix, which can be attributed to drying shrinkage. The SEM results are in a good agreement with the high-resolution TEM investigations. The high-resolution TEM picture (Figure 4-44),

showing the lattice fringes of a HA nanocrystal in an amorphous matrix of chitosan, gives a further evidence of the HA dispersion in a continuous chitosan matrix.

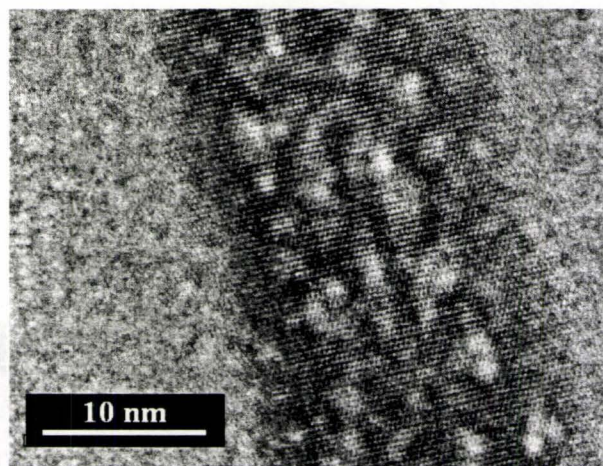


Figure 4-44 High-resolution TEM image of the lattice fringes of a HA crystal in a chitosan matrix for the composite deposit prepared from a 0.5 g/l chitosan solution containing 0.5 g/l HA.

#### 4.3.1.8 Electrochemical characterization of the coatings

Figure 4-45 and Figure 4-46 show the electrochemical behavior of the composite coating on stainless steel in Ringer's solution, in comparison with the uncoated substrate. The impedance spectroscopy data were plotted in the form of the Bode plot of the impedance modulus  $|Z|$  and phase angle  $\phi$  versus frequency (Figure 4-45). It was observed that the impedance values for the coated sample were two orders of magnitude higher than those for the uncoated substrate. This behavior suggests that the deposited composite coating acts as a protective layer against ion diffusion and corrosion. Figure 4-46 shows the obtained Tafel curves for the uncoated

and coated stainless steel. It can be seen that the corrosion current and therefore the rate of corrosion of the coated sample was significantly reduced by the coating. These results indicate that the composite deposit could act as a protective layer and improve the corrosion resistance of the stainless steel substrate in the body fluid environment.

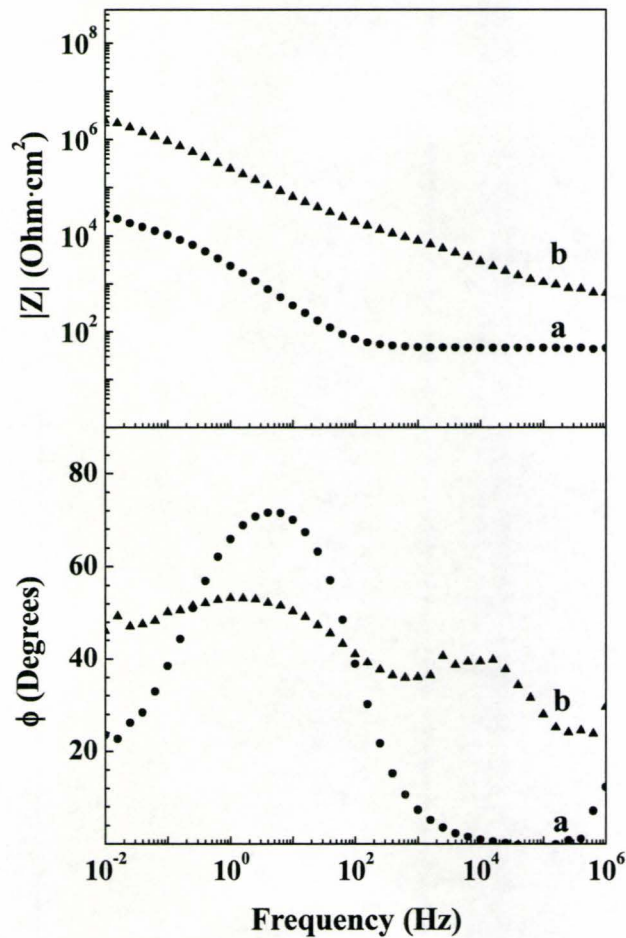


Figure 4-45 Bode plots in Ringer's solution for (a) uncoated stainless steel, and (b) coated stainless steel samples prepared from the 4.0 g/l HA suspension in the mixed ethanol-water solvent (17% water) containing 0.5 g/l chitosan at a current density of 0.1 mA/cm<sup>2</sup> and a deposition time of 20 min.

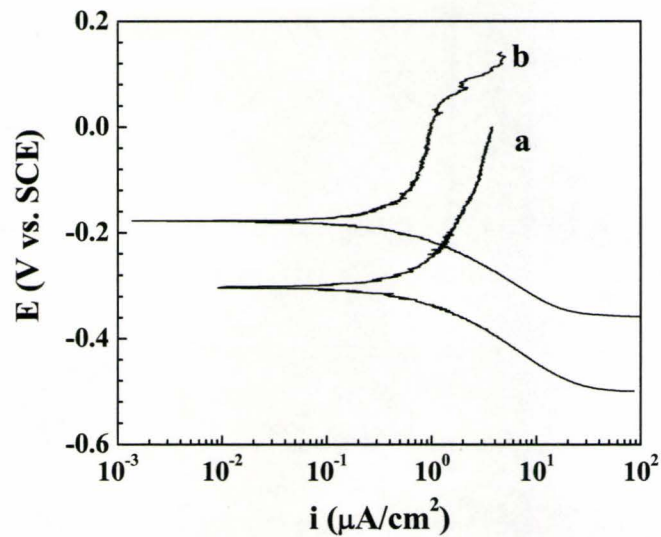


Figure 4-46 Tafel plots in Ringer's solution for (a) uncoated stainless steel, and (b) coated stainless steel samples prepared from the 4.0 g/l HA suspension in the mixed ethanol-water solvent (17% water) containing 0.5 g/l chitosan at a current density of 0.1 mA/cm<sup>2</sup> and a deposition time of 20 min.

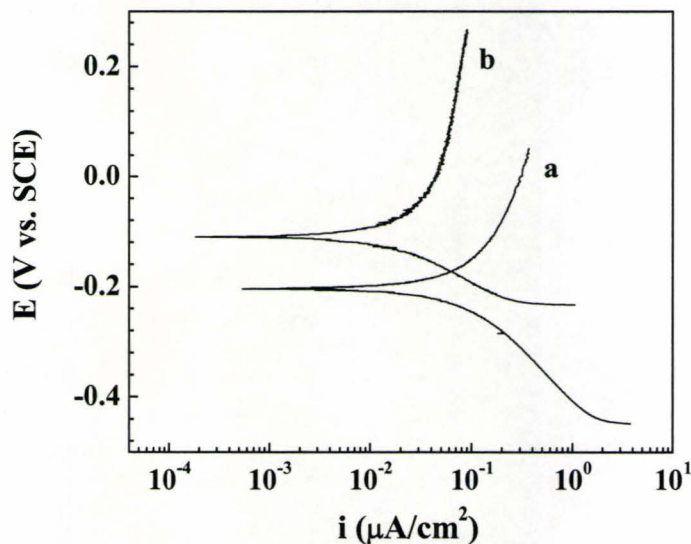


Figure 4-47 Tafel plots in Ringer's solution for (a) uncoated Ti substrate, and (b) coated Ti samples prepared from the 4 g/l HA suspension in the mixed ethanol-water solvent (17% water) containing 0.5 g/l chitosan at a current density of 0.1 mA/cm<sup>2</sup> and deposition time of 20 min.

Similar results were obtained for the composite coating deposited on Ti substrates. Figure 4-47 shows the electrochemical behavior of the coated and uncoated Ti substrates. The comparison of Tafel curves indicates that the composite coating reduced the corrosion current and the rate of corrosion of Ti. Therefore the composite coating can act as a protective layer and improve the corrosion resistance of Ti in the body fluid environment.

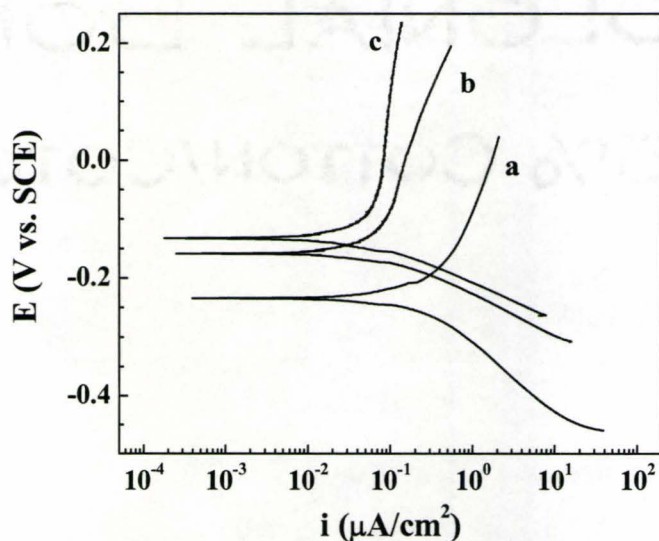


Figure 4-48 Tafel plots in the Ringer's solution for (a) uncoated and (b, c) the coated 316L stainless-steel samples prepared from the 0.5 g/l chitosan solutions containing 3.0 g/l HA, with a deposition time of 3 min: (a,b) without heat treatment, (c) heat treated at 140 °C for 10 h.

Figure 4-48 compares the electrochemical behavior of uncoated and coated 316L stainless steel samples in the Ringer's solution, for another composite coating prepared from the 0.5 g/l chitosan solution containing 3.0 g/l HA. It can be seen from

the Tafel plots that the coated sample showed a smaller corrosion current density. A heat treatment of the coated sample at 140 °C resulted in an additional reduction in the corrosion current density, indicating an improved protection of the substrate. Similar results were obtained for the deposits prepared from the 0.5 g/l chitosan solutions containing 5 g/l HA. The Tafel plots shown in Figure 4-49 indicate that the heat treatment at 140 °C resulted in a smaller corrosion current density and an improved protection of the substrate. The longer deposition time yielded a thicker coating, which provided a better protection of the substrate as indicated by the further reduction in the corrosion current density (Figure 4-49 (c)).

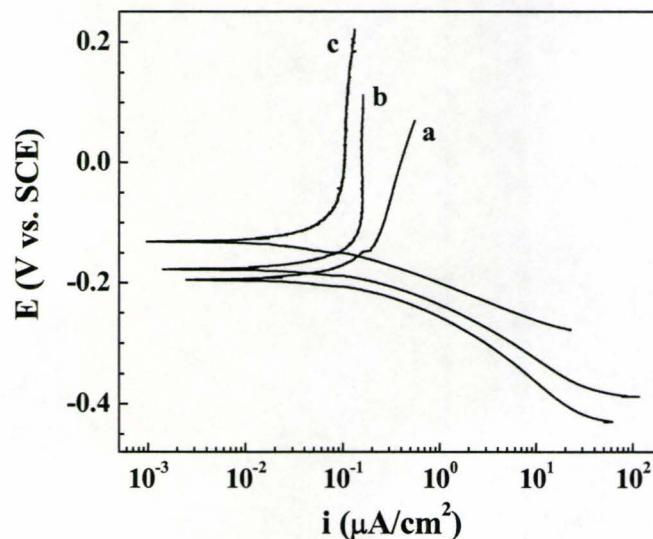


Figure 4-49 Tafel plots in the Ringer's solution for the coated 316L stainless-steel samples prepared from the 0.5 g/l chitosan solutions containing 5 g/l HA, with a deposition time of (a,b) 3 min, and (c) 10 min: (a) without heat treatment, (b, c) heat treated at 140 °C for 10 h.

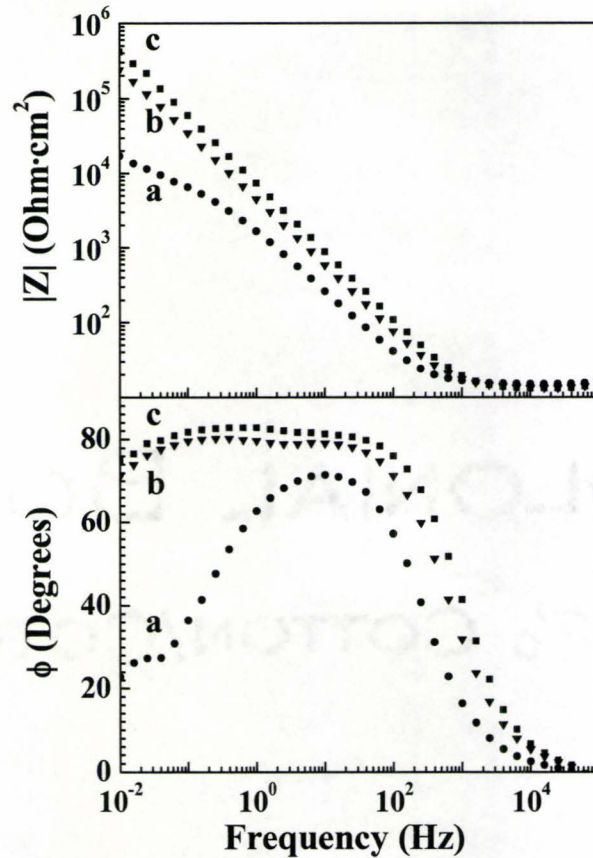


Figure 4-50 Bode plots in the Ringer's solution for (a) uncoated and (b, c) the coated 316L stainless-steel samples prepared from the 0.5 g/l chitosan solutions containing 3.0 g/l HA, with a deposition time of 3 min: (a,b) without heat treatment, (c) heat treated at 140 °C for 10 h.

The obtained coatings were also studied by electrochemical impedance spectroscopy. The results were plotted in the form of Bode plot, giving the impedance modulus  $|Z|$  and phase angle  $\phi$  versus frequency (Figure 4-50). The impedance data are consistent with the experimental results shown in Figure 4-48 and Figure 4-49. The coated samples showed increased impedance values compared to the uncoated sample, and the heat treatment resulted in a further increase in the impedance. This

behavior suggests that the deposited composite coating acts as a protective layer against ion diffusion.

#### **4.3.2 Discussion**

##### **4.3.2.1 Codeposition of hydroxyapatite and chitosan**

As was discussed in the literature review, HA is an important bioceramic widely used in a variety of biomedical applications. Novel composite coatings containing HA thus indicate a possibility to incorporate its bioactivity with the properties of other materials.

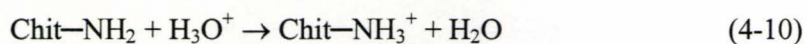
Significant interest has been generated in HA-chitosan composites. Chitosan is a natural cationic polysaccharide that can be produced by alkaline N-deacetylation of chitin. It has a variety of applications in biomedical products, cosmetics, and food processing. Important properties of this material, such as antimicrobial activity, corrosion resistance, biocompatibility, and advanced mechanical properties, have been utilized in biotechnology [Bégin *et al.*, 1999; Janes *et al.*, 2001; Ligler *et al.*, 2001; Ruel-Gariépy *et al.*, 2000]. To enhance the integration of implants and to promote the regeneration of bone, chitosan has been deposited on plasma-sprayed HA coatings on Ti-6Al-4V alloys [Muzzarelli *et al.*, 2001]. In another study [Redepenning *et al.*, 2003], composite coatings were obtained by ELD of brushite ( $\text{CaHPO}_4 \cdot 2\text{H}_2\text{O}$ ) and electrochemical deposition of chitosan. The brushite/chitosan composites were converted to HA/chitosan composites by heating the coatings in aqueous solutions of

sodium hydroxide. However, the control of stoichiometry of the electrolytic HA in the composite deposits is difficult due to the different deposition rate of Ca and P species. A better choice would be the development of a novel method for the fabrication of HA-chitosan composite coatings which combines the EPD of HA and electrochemical deposition of chitosan.

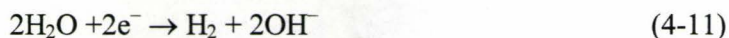
The characteristics of chitosan coatings prepared by different methods varied from one report to another [Lim *et al.*, 1995; Nunthanid *et al.*, 2001; Sorlier *et al.*, 2001]. Obtained coatings exhibited different crystallinity and thermal stability. This was attributed to the difference in the sources of chitin used to produce chitosan, types of solvent used, methods of coating preparation, and other factors [Lim *et al.*, 1995; Nunthanid *et al.*, 2001; Sorlier *et al.*, 2001].

XRD results of this work indicate the crystallinity of the chitosan coatings prepared by electrodeposition from the mixed ethanol-water solvent. TG studies showed that thermal degradation of the chitosan deposit starts at 280-300 °C. This result is in agreement with the literature data, according to which the thermal degradation temperature of chitosan is about 280-300 °C [Nunthanid *et al.*, 2001].

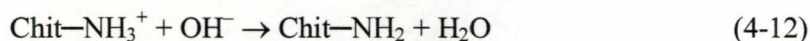
Chitosan is soluble in water only when protonated in acidic solutions [Bartkowiak *et al.*, 1999; Yi *et al.*, 2004]. At low pH, chitosan becomes a cationic polyelectrolyte [Wang *et al.*, 2004]:



Electric field provides electrophoretic motion of the charged chitosan macromolecules towards the cathode surface. It is suggested that the cathodic reaction



results in an increasing pH at the electrode surface. At pH 6.5, chitosan's primary amines become deprotonated [Bartkowiak *et al.*, 1999; Wang *et al.*, 2004; Yi *et al.*, 2004]. Therefore, the chitosan loses its charge and forms an insoluble deposit on the cathode surface:



The experimental results in this work demonstrate the possibility of the fabrication of composite coatings using a combined deposition method based on the EPD of HA and electrochemical deposition of chitosan. It is suggested that positive charges of HA particles can result from the particle-solution exchange interactions of dissolution and ion exchange [Ducheyne *et al.*, 1992]. Ducheyne *et al.* [Ducheyne *et al.*, 1992] reported positive  $\zeta$  potentials of stoichiometric HA particles in the pH range of 3-10. The positive  $\zeta$  potentials, in both acidic and alkaline solutions, were due to the specific presence of  $\text{Ca}^+$ ,  $\text{CaOH}^+$ , and  $\text{CaH}_2\text{PO}_4^+$  on the particle surface. It was shown that the electrokinetic properties of HA are influenced by the ionic strength of the solution, the pH, the concentration of particles in solution, the particle size and shape, and other factors. However, adsorbed water interferes with electrophoretic transport and the EPD of as-precipitated HA powders was not achieved [Ducheyne *et*

*al.*, 1990]. This problem was addressed in the literature [Zhitomirsky *et al.*, 1997b]. A procedure has been developed for the fabrication of HA nanoparticles and the EPD of as-precipitated HA from suspensions in isopropanol [Zhitomirsky *et al.*, 1997b].

It is important to note that electrophoresis results in the accumulation of charged particles at the electrode surface. The deposit formation is achieved via the particle coagulation, which is influenced by the electrode reactions, solvents, additives and other factors [Zhitomirsky, 2002]. The addition of HA to the chitosan solutions enabled the codeposition of HA and chitosan. The results indicate that chitosan promotes the EPD of HA. The formation of composite coatings is achieved via the heterocoagulation of HA nanoparticles and chitosan macromolecules at the electrode surface. We cannot exclude the possibility that the electrokinetic properties of the HA nanoparticles are influenced by the adsorbed chitosan. It is known that the charge on a colloidal particle can originate from the adsorbed polyelectrolyte [Zhitomirsky, 2002]. In several experiments, EPD of ceramic particles was performed in the presence of polyelectrolytes [Van der Biest *et al.*, 1999; Zhitomirsky, 2002]. The polyelectrolyte adsorption on the ceramic particles resulted in the particle charging. Moreover, polyelectrolytes are widely used additives that can impart electrostatic and steric stabilization to a colloidal dispersion.

The HA suspensions without chitosan were unstable and showed rapid sedimentation when stirring was interrupted. In contrast, the addition of chitosan resulted in the formation of stable suspensions of charged HA particles, which were

used for EPD. The use of chitosan enabled the formation of dense and adherent coatings at room temperature. Therefore, problems related to the sintering of electrophoretic HA deposits can be eliminated. In addition, chitosan can impart other important properties to the nanocomposites. The use of chitosan with inherent binding properties and excellent film forming ability enables the formation of adherent and dense deposits. It is suggested that the use of chitosan results in reduced microporosity and enhanced corrosion protection. Of particular importance are the biocompatibility and antimicrobial properties of chitosan, which offer important opportunities in the fabrication of advanced nanocomposite coatings on implants.

#### **4.3.2.2 Chemical composition of the composite coatings**

An important task is to obtain HA–chitosan composite coatings of various compositions and optimize the properties of the nanocomposites. A nanocomposite can be used as a bioactive material when its HA content is higher than 40 wt% [Wei *et al.*, 2003]. It is in this regard that natural bone is considered an organic–inorganic nanocomposite containing ~70 wt% of HA [Wei *et al.*, 2001]. Therefore, it is critical to explore the possibility of fabricating HA-chitosan nanocomposite coatings with various HA contents on Ti and 316L stainless steel.

The results of this work demonstrate the possibility of variation of HA content in the composite coatings. HA is a bioactive ceramic having excellent biocompatibility and ability to bond directly to bone. The HA-chitosan

nanocomposites, containing 70 wt% HA, prepared by a coprecipitation method exhibited a high bioactivity [Zhang *et al.*, 2005]. It is important to note that the nanocomposite can be used as a bioactive medical material when the HA content is higher than 40 wt% [Wei *et al.*, 2003]. In order to obtain bioactive coatings, HA-chitosan nanocomposites with HA content of 71.5 and 79.9 wt% were prepared.

It has been shown that the composition of the deposits is influenced by the HA concentration in the solutions [Pang *et al.*, 2005a, b]. Detailed TG investigations have been performed on the nanocomposites prepared from chitosan solutions containing various amounts of HA. The results indicate that the HA content in the deposits can be changed from 40.9 to 85.0 wt% by the variation of the HA concentration in the 0.5 g/l chitosan solutions. Moreover, it has also been shown that the HA content can be changed in the range of 75.1–89.8 wt% by the variation of the chitosan concentration at a constant HA concentration in the deposition bath. It is known that bioactive nanocomposites can be obtained when the HA content in the materials is higher than 40 wt% [Wei *et al.*, 2003; Wei *et al.*, 2001]. As pointed out above, the HA content in natural bones is about 70 wt%. Therefore, the results of this investigation have offered a possibility for the fabrication of bioactive nanocomposite materials. The capability to change the HA content in the nanocomposites is important for the optimization of the microstructure and properties of the material.

#### 4.3.2.3 Microstructure of the composite coatings

A further development of the coating would be the exploration of the possibility to design and control the nanostructure and preferred orientation of the HA nanoparticles in a matrix of the polymer chitosan, so that the obtained novel HA–chitosan nanocomposite coatings mimics the structure and properties of natural bone.

The microstructure of the deposits depends on the content of HA nanoparticles in the chitosan matrix. X-ray studies showed that the *c*-axes of the HA nanocrystals in the nanocomposite coating were preferentially oriented parallel to the coating surface. The orientation of the HA nanoparticles could be influenced by the electric field [Ueshima *et al.*, 2002] or chitosan [Yamaguchi *et al.*, 2003]. The experimental results indicate that the degree of the preferred orientation of the HA nanoparticles decreases with the increasing HA content in the deposits. Therefore, the orientation of the HA in the nanocomposites prepared by the electrodeposition can be mainly attributed to the interactions between HA and chitosan. When the HA content in the deposit is relatively high, the deposit consists of HA nanoparticles with adsorbed chitosan (Figure 4-43 (a)) and the deposit microstructure is influenced by the interactions and packing of the nanoparticles. In contrast, with a low HA content in the nanocomposite, the HA nanoparticles are separated and oriented in a polymer matrix (Figure 4-43 (b)). The ability to control the orientation of the nanoparticles is important for the fabrication of advanced nanocomposites. It is known that the preferred orientation of

HA nanocrystals plays an important role in the mechanical and other properties of bones [Cui *et al.*, 1996; Kikuchi *et al.*, 2004; Zhang *et al.*, 2003].

#### 4.3.2.4 Deposition yield

In the proposed method, the amount of the deposited material can be controlled by the variation of the deposition time. Coatings of various thicknesses in the range of up to 60  $\mu\text{m}$  were obtained on various conductive substrates.

The formation of cathodic deposits from the pure HA suspensions without chitosan indicated that the HA nanoparticles were positively charged. The addition of chitosan to the HA suspensions resulted in an increased deposition rate of the HA. It is suggested that the chitosan was absorbed on the HA nanoparticles. The adsorption of the charged chitosan macromolecules could result in an electrosteric stabilization of the HA nanoparticles, increase the particle charge, and increase the deposition rate. The amount of adsorbed polymer depends on the polymer concentration in solutions and the specific polymer–particle, polymer–solvent, and particle–solvent interactions [Damodaran *et al.*, 1993; Zhitomirsky, 2002]. Therefore, the choice of the dispersion medium is important for the deposition process [Zhitomirsky, 2002]. A polymer can be adsorbed on the surface of colloidal particles when its solubility in the dispersion medium is low. Note that chitosan can be dissolved in acidic aqueous solutions and water molecules are necessary for the base generation in the Equation (4-11). However, in order to reduce the quality of the solvent and promote the chitosan

adsorption on HA nanoparticles, the mixed ethanol–water solvent was used for the electrodeposition.

The deposition rate  $w$  in EPD process can be described by the relation:

$$w=C\mu U/d \quad (4-13)$$

where  $C$  and  $\mu$  are the particle concentration and mobility, respectively;  $U=U_{ap}-U_{dep}$ , where  $U_{ap}$  is the applied voltage and  $U_{dep}$  is the voltage drop in the deposit; and  $d$  is the distance between the electrodes. When the particle radius is large compared with the Debye length  $1/\kappa$ , the electrophoretic mobility is given by Smoluchowski's formula [Zhitomirsky, 2002]:

$$\mu = \varepsilon\varepsilon_0\zeta/\eta \quad (4-14)$$

where  $\zeta$  is the zeta-potential,  $\eta$  and  $\varepsilon$  are, respectively, the viscosity and relative permittivity of the liquid, and  $\varepsilon_0$  is the permittivity of the vacuum. For particles that are much smaller than  $1/\kappa$ , the electrophoretic mobility is given by Hückel's formula [Zhitomirsky, 2002]:

$$\mu = 2\varepsilon\varepsilon_0\zeta/3\eta \quad (4-15)$$

The adsorption of chitosan can result in a higher charge and higher  $\zeta$  potential of the HA nanoparticles, which in turn leads to a higher electrophoretic mobility and higher deposition rate according to the Equation (4-13). The application of electric field to the suspension of fine particles can result in the particle agglomeration,

sedimentation, decreasing concentration  $C$  of the nanoparticles in the suspension, and decreasing deposition yield [Zhitomirsky *et al.*, 1997b]. Therefore, it is expected that the electrosteric stabilization of the HA nanoparticles by the adsorbed chitosan can provide an increased suspension stability during EPD and yield an increased deposition rate.

However, the experimental results shown in Figure 4-37 indicate that the deposition rate decreases with the increasing chitosan concentration in solutions in the range of 0.1–0.7 g/l. It is suggested that the increase in the polymer concentration in the solutions containing HA nanoparticles can result in an increasing suspension viscosity, decreasing electrophoretic mobility, and thus decreasing deposition yield of the chitosan and HA (Equations (4-13), (4-14) and (4-15)).

#### **4.3.2.5 Corrosion protection properties of the composite coatings**

Testing results indicate that the obtained coating provide the corrosion protection of the 316L stainless steel and Ti substrates. 316L stainless steel and Ti are important implant materials. However, corrosion of these materials in the human body environment remains a serious clinical concern [Kannan *et al.*, 2003; Zielinski *et al.*, 2008]. HA coatings are currently under development for the protection of 316L stainless steel [Kannan *et al.*, 2003]. The method developed in this work offers an advantage of room temperature deposition of protective coatings. A heat treatment of the composite coatings at 140 °C resulted in an improved corrosion protection, which

can be attributed to the increased water resistance of the chitosan [Lim *et al.*, 1995]. It is known that the heat treatment of chitosan coatings at temperatures exceeding 90 °C can result in the formation of cross-links in the coatings and improve their water resistance [Lim *et al.*, 1995]. Further optimization of the deposit composition, deposition procedure, and drying conditions is necessary for the improvement in the protective properties of the coatings, and the prevention of cracks and other defects in the coatings.

#### **4.3.3 Modelling of the formation of the composite deposits**

With the increase in the deposit thickness, the voltage drop in deposit increases, causing a decrease in the effective voltage for electrodeposition according to Equation (4-13). However, when the electrodeposition is conducted under a constant voltage and with short deposition time (i.e. thin deposit), the electric field strength over the deposition bath can be considered constant.

Figure 4-51 shows the deposit weight of the HA-chitosan versus the HA concentration in the chitosan solutions for coatings prepared at a constant voltage of 20 V. A higher deposit weight was observed for the deposition time of 5 min (Figure 4-51 (b)) compared to that for the deposition time of 3 min (Figure 4-51 (a)). The increase in the HA concentration in the suspensions resulted in an increasing deposit weight.

The experimental data in the Figure 4-51 indicate that the increase in deposit

weight with the particle concentration is non-linear. Hamaker equation [Hamaker, 1940] predicts a linear increase in the deposit mass  $M$  with increasing particle concentration  $C_s$  in dilute suspensions:

$$M = \mu Et S C_s \quad (4-16)$$

where  $\mu$  is the particle mobility in an electric field  $E$ ,  $t$  is the deposition time, and  $S$  is the electrode area. However, theoretical and experimental data reported in the literature showed more-than-linear increase in the deposition yield with increasing particle concentration [Biesheuvel *et al.*, 1999], which was attributed to the movement of the deposit-suspension boundary. It was shown that the deposition yield can be described by the equation:

$$M = \mu Et S C_s \frac{C_c}{C_c - C_s} \quad (4-17)$$

where  $C_c$  is the particle concentration in the deposit. Hamaker equation can be obtained when  $C_s$  is appreciably lower than  $C_c$ . Our experimental data (Figure 4-51) also show a more-than-linear increase in the deposit weight with increasing particle concentration. It is important to note that the deposits obtained in this work contain not only HA particles but also chitosan macromolecules. Taking into account that HA and chitosan form a composite deposit and a common deposit-suspension boundary, the deposition yield can be given by the following equation:

$$M = \mu EtSC_s \frac{C_c}{C_c - C_s} + \mu' EtS\Psi_s \frac{\Psi_c}{\Psi_c - \Psi_s} \quad (4-18)$$

where  $\mu'$  is the mobility of chitosan macromolecules,  $\Psi_s$  is the concentration of chitosan in suspension, and  $\Psi_c$  is the concentration of chitosan in deposit. The  $C_c/(C_c - C_s)$  ratio for HA particles and  $\Psi_c/(\Psi_c - \Psi_s)$  ratio for chitosan both depend on  $C_s$  and can be analyzed by the investigation of composition of the HA-chitosan deposits using TG/DTA.

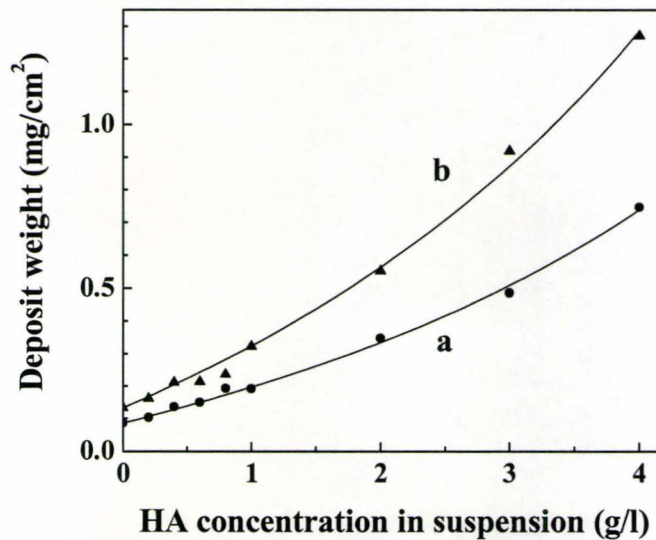


Figure 4-51 The dependences of the deposit weight on the HA concentration in chitosan solutions for HA-chitosan composite coatings deposited at a constant voltage of 20 V for (a) 3 min and (b) 5 min.

The results of TG/DTA studies indicate the composite nature of the deposited films. Figure 4-52 compares the TG/DTA data for HA-chitosan composite coatings

prepared from the 0.5 g/l chitosan solutions containing 0.2 g/l HA and 1.0 g/l HA with those for the as-prepared HA powders. The TG data of the as-prepared HA powders (Figure 4-52 (a)) showed a total weight loss of 7.4 wt% at 1000 °C, which can be mainly attributed to dehydration. The DTA curve exhibits a broad endotherm around ~ 90 °C related to the liberation of adsorbed water. For the composite coatings, the TG data show an additional weight loss compared to the weight loss for pure HA powders, which can be attributed to the burning out of the polymer chitosan. The total weight loss at 1000 °C was found to be 77.6 wt% and 42.7 wt% for the HA concentrations of 0.2 g/l and 1.0 g/l in solutions, respectively. The DTA data for the composite coatings showed a broad endotherm at ~ 90 °C attributed to the liberation of the adsorbed water, and exotherms in the range of 200–550 °C related to the burning out of chitosan. Similar TG/DTA curves were obtained for other composite coatings prepared from the chitosan solutions containing 0.2–4.0 g/l HA. The results of TG/DTA investigations indicate the codeposition of HA and chitosan, and the TG data can be used to study the composition of the composite coating. The HA content in the composite coatings prepared from the 0.5 g/l chitosan solutions containing 0.2 g/l and 1.0 g/l HA was found to be 22.4 wt% and 57.3 wt%, respectively.

Figure 4-53 shows the variation of HA (Figure 4-53 (a)) and chitosan content (Figure 4-53 (b)) in the composite coatings prepared from the 0.5 g/l chitosan solutions containing various amounts of HA. The HA and chitosan contents were calculated from the TG data for the composite coatings. It was observed that the HA

content in the deposited composite coatings increased and in turn the chitosan content decreased with the increasing HA concentration in chitosan solutions. The results are consistent with those of the studies on deposition yield of the composite coating shown in Figure 4-51.

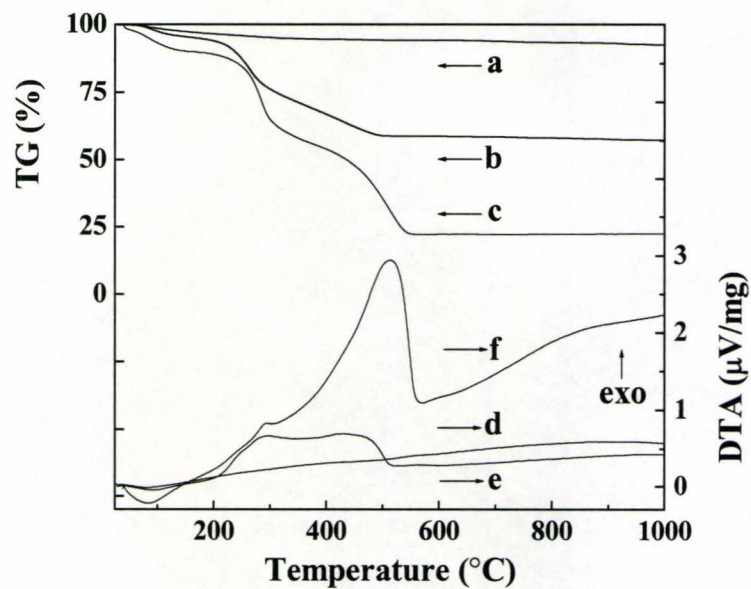


Figure 4-52 TG (a,b,c) and DTA (d,e,f) data for as-prepared HA powders (a,c) and the HA-chitosan composite deposits prepared from the chitosan solution containing 1.0 g/l HA (b,e) and 0.2 g/l HA (c,f).

The data shown in Figure 4-53 were actually weight percentages (g/g) of the HA particles  $\phi_{HA}$  (Figure 4-53 (a)) and chitosan molecules  $\phi_{ch}$  (Figure 4-53 (b)) in the deposits.  $\phi_{HA}$  and  $\phi_{ch}$  are related to the concentration  $C$  (g/l) of HA and chitosan in deposit by:

$$\varphi_{HA} = \frac{C_c}{C_c + \psi_c} \quad \varphi_{ch} = \frac{\Psi_c}{C_c + \Psi_c} \quad (4-19)$$

On the other hand, the mass concentration  $C$  (g/l) and volumetric concentration  $\phi$  (l/l) of the HA and chitosan in deposit are related by their intrinsic density  $\rho$  (g/l):

$$C_c = \phi_{HA} \rho_{HA} \quad \Psi_c = \phi_{ch} \rho_{ch} \quad (4-20)$$

where

$$\phi_{HA} + \phi_{ch} = 1 \quad (4-21)$$

Substituting Equation (4-20) into Equation (4-19) results in:

$$\varphi_{HA} = \frac{\phi_{HA} \rho_{HA}}{\phi_{HA} \rho_{HA} + \phi_{ch} \rho_{ch}} \quad \varphi_{ch} = \frac{\phi_{ch} \rho_{ch}}{\phi_{HA} \rho_{HA} + \phi_{ch} \rho_{ch}} \quad (4-22)$$

Combining Equations (4-21) and (4-22) results in:

$$\phi_{HA} = \frac{1}{1 + \frac{\rho_{HA}}{\rho_{ch}} \left( \frac{1}{\varphi_{HA}} - 1 \right)} \quad \phi_{ch} = \frac{1}{1 + \frac{\rho_{ch}}{\rho_{HA}} \left( \frac{1}{\varphi_{ch}} - 1 \right)} \quad (4-23)$$

$C_c$  and  $\Psi_c$  can be obtained by substituting Equation (4-23) into Equation (4-20):

$$C_c = \frac{\rho_{HA}}{1 + \frac{\rho_{HA}}{\rho_{ch}} \left( \frac{1}{\varphi_{HA}} - 1 \right)} \quad \Psi_c = \frac{\rho_{ch}}{1 + \frac{\rho_{ch}}{\rho_{HA}} \left( \frac{1}{\varphi_{ch}} - 1 \right)} \quad (4-24)$$

Simplifying the equation results in:

$$C_c = \frac{1}{\frac{1}{\rho_{HA}} + \frac{1}{\rho_{ch}} \left( \frac{1}{\varphi_{HA}} - 1 \right)} \quad \Psi_c = \frac{1}{\frac{1}{\rho_{ch}} + \frac{1}{\rho_{HA}} \left( \frac{1}{\varphi_{ch}} - 1 \right)} \quad (4-25)$$

Considering the packing factor  $f$  of the composite deposit, the concentration of HA and chitosan in deposit can be given by:

$$C_c = \frac{f}{\frac{1}{\rho_{HA}} + \frac{1}{\rho_{ch}} \left( \frac{1}{\varphi_{HA}} - 1 \right)} \quad \Psi_c = \frac{f}{\frac{1}{\rho_{ch}} + \frac{1}{\rho_{HA}} \left( \frac{1}{\varphi_{ch}} - 1 \right)} \quad (4-26)$$

where  $f = 1 - \varepsilon$  ( $\varepsilon$ : the deposit porosity).

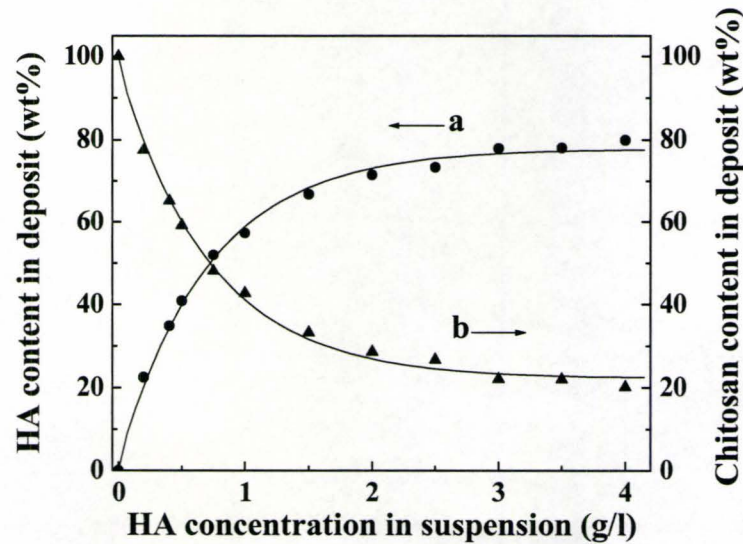


Figure 4-53 The (a) HA and (b) chitosan content in deposits calculated from TG data versus the HA concentration in chitosan solutions for HA-chitosan composite deposits prepared at a constant voltage of 20 V.

Therefore, the dependence of the concentration of HA ( $C_c$ ) and chitosan ( $\Psi_c$ ) in deposit on the HA particle concentration  $C_s$  can be obtained using the Equation (4-26) and experimental data for  $\phi_{HA}$  (Figure 4-53 (a)) and  $\phi_{ch}$  (Figure 4-53 (b)), since  $f$ ,  $\rho_{HA}$ , and  $\rho_{ch}$  are constants independent of  $C_s$  ( $\rho_{HA} = 3153$  g/l [Hoffmann *et al.*, 2003], and  $\rho_{ch} = 300 \sim 600$  g/l).

Figure 4-54 shows the variation of  $C_c$  and  $\Psi_c$  with  $C_s$  for  $f = 0.6$  and  $\rho_{ch} = 300$  g/l. In fact, any value for  $f$  and  $\rho_{ch}$  can be used to calculate  $C_c$  and  $\Psi_c$  using the Equation (4-26), and always the same trend of variation of  $C_c$  and  $\Psi_c$  is obtained. Thus arbitrary units are employed for the y-axis in the Figure 4-54.

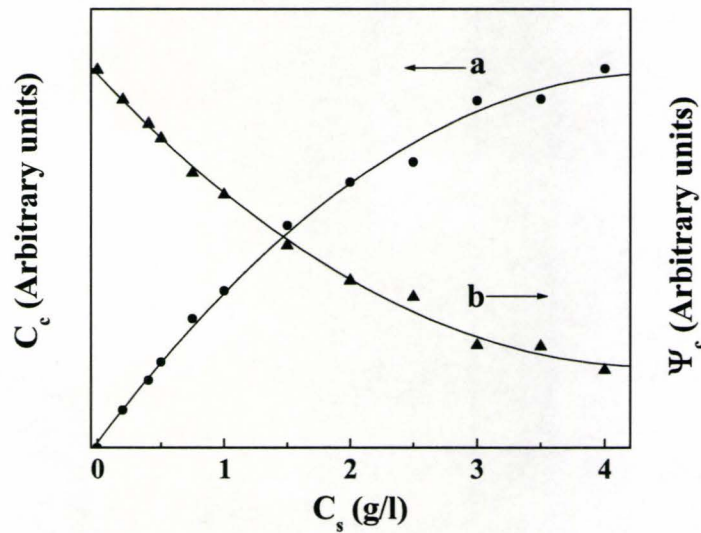


Figure 4-54 The (a)  $C_c$  and (b)  $\Psi_c$  versus  $C_s$  curves for  $f = 0.6$ .

By rearranging Equation (4-18), the deposition yield of the HA-chitosan

composite coating can be given by:

$$M = \mu Et S C_s \left(1 - \frac{C_s}{C_c}\right)^{-1} + \mu' Et S \psi_s \left(1 - \frac{\psi_s}{\psi_c}\right)^{-1} \quad (4-27)$$

The variation of the  $C_s/C_c$  ratio with increasing  $C_s$  can be readily obtained since the dependence of  $C_c$  on  $C_s$  is already known (Figure 4-54 (a)). Figure 4-55 shows the  $C_s/C_c$  ratio versus  $C_s$  curves calculated for different  $f$  values.

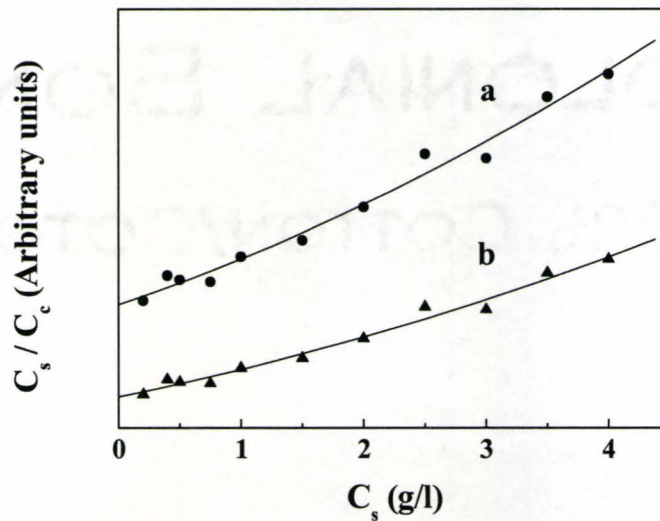


Figure 4-55 The  $C_s/C_c$  versus  $C_s$  curves for (a)  $f=0.6$  and (b)  $f=1.0$ .

Figure 4-55 indicates that the  $C_s/C_c$  ratio shows a more-than-linear increase with  $C_s$ , which leads to a more-than-linear increase in the first term of the Equation (4-27) with the increasing  $C_s$ . Moreover, the second term of the Equation (4-27) provides an addition increase of the deposit yield with  $C_s$ , as  $\Psi_s$  was kept constant at

0.5 g/l and  $\Psi_c$  decreases with the increasing  $C_s$  (Figure 4-54 (b)). The summation of the two terms of the equation leads to a more-than-linear total increase in the HA-chitosan composite deposit yield with the increasing HA particle concentration in suspensions. This is consistent with the experimental data shown in Figure 4-51. The results are in a qualitative agreement with the theory of EPD and experimental data for other materials reported in the literature [Biesheuvel *et al.*, 1999].

#### 4.4 Electrodeposition of hydroxyapatite-Ag-chitosan nanocomposite coatings

There is always a certain risk of bacterial infections caused by metallic or polymer implants. Previous studies have shown that this risk can be reduced by bactericidal silver coatings [Bambauer *et al.*, 1994; Sioshansi, 1994]. However, silver coatings may cause problems on metallic substrate materials, because of low adhesion and due to galvanic corrosion. A better solution is to include Ag in bioactive coatings on implants to yield additional bactericidal properties. It was suggested [Shirkhazadeh *et al.*, 1995] that the potential bone-bonding properties of HA-Ag coatings combined with the potent antibiotic effects of silver may provide an effective means for eradicating the bacterial from the site of infection.

Recently, considerable research interest has been generated in the development of HA composites containing Ag due to the possibility to prevent the implant caused infections using the antimicrobial properties of Ag [Ahearn *et al.*, 1995; Pourrezaei *et al.*, 1994; Simonetti *et al.*, 1992; Yoshida *et al.*, 1999]. Nevertheless, the sintering of HA-Ag composites presents difficulties related to the Ag evaporation and low melting point of Ag [Lee *et al.*, 2006a]. Another approach is based on the use of Ag doped HA. Various methods have been developed for the fabrication of Ag doped HA, including ion-exchange [Feng *et al.*, 1998; Lee *et al.*, 2006b; Shirkhazadeh *et al.*, 1995], wet chemical precipitation [Kim *et al.*, 1998; Oh *et al.*, 2004], and sol-gel methods [Chen *et al.*, 2007; Chung *et al.*, 2006]. However, a

key issue that needs to be addressed in the development of the material is the control of  $\text{Ag}^+$  release rate from it. The low concentration of  $\text{Ag}^+$  ions released from the Ag doped HA can be deficient to render antimicrobial efficacy.

Electrodeposition is a good method to incorporate silver into ceramic or polymer matrix. As was describe before, the use of chitosan enables the room temperature processing of novel HA-chitosan composite coatings, eliminating the problems related to the sintering of HA. In addition, the room temperature processing offers a possibility to codeposit other functional materials such as antimicrobial silver.

The following experimental results and discussion are produced based on the published paper [Pang *et al.*, 2008].

#### **4.4.1 Codeposition of hydroxyapatite, silver, and chitosan**

First, the possibility to codeposit Ag and chitosan, and then Ag, HA and chitosan has been explored. Composite coatings were obtained from the 0.5 g/l chitosan solutions containing 0–1.0 mM  $\text{AgNO}_3$  and 0–3.0 g/l HA. The Ag-chitosan composite deposits prepared from the 0.5 g/l chitosan solutions containing 0.5–1.0 mM  $\text{AgNO}_3$  were amorphous (Figure 4-56 (b)). The XRD pattern of the deposit annealed at 300 °C during 1 h (Figure 4-56 (c)) exhibited broad peaks of Ag, corresponding to the JCPDS file 04-0783. The absence of Ag peaks in the XRD pattern of as-prepared Ag–chitosan composite deposit may be attributed to the formation of Ag–chitosan complexes [Varma *et al.*, 2004]. It is known that pH value

plays an important role in the binding of metal ions since protons and metal ions compete to be bound to amine groups of chitosan. In the acidic chitosan solutions used for the deposition, the amino groups of chitosan become positively charged due to the protonation, making it difficult for  $\text{Ag}^+$  ions to form chelates with chitosan. However, the formation of complexes can be expected in the high pH region at the cathode surface [Zhitomirsky, 2006]. The annealing at 300 °C can result in the decomposition of Ag–chitosan complexes, burning out of chitosan, and formation of metallic Ag. As a result, the XRD studies on the samples annealed at 300 °C for 1 h detected Ag peaks. Further experiments showed that HA–Ag–chitosan nanocomposite coatings can be prepared by cathodic deposition.

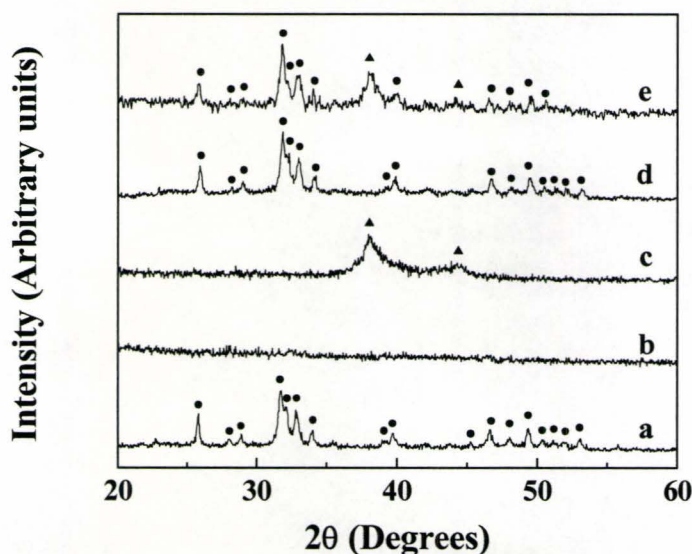


Figure 4-56 XRD patterns for (a) as-prepared HA powders, and the deposits prepared from the 0.5 g/l chitosan solutions containing (b, c) 1.0 mM  $\text{AgNO}_3$ , (d) 0.5 g/lHA, and (e) 1.0 mM  $\text{AgNO}_3$  and 0.5 g/l HA. (c, e) annealed at 300 °C for 1 hr. (▲ — Ag, ● — HA.)

The XRD pattern of a composite coating prepared from the 0.5 g/l chitosan solution containing 0.5 g/l HA (Figure 4-56 (d)) showed reflexes of HA, indicating the codeposition of HA and chitosan. The coatings prepared from the chitosan solutions containing HA nanoparticles and dissolved AgNO<sub>3</sub> showed reflexes of Ag in addition to the reflexes of HA (Figure 4-56 (e)). The results indicate the formation of composite coatings containing HA and Ag in a chitosan matrix. The results of XRD studies are in a good agreement with the results of TG/DTA investigations.

#### 4.4.2 Chemical composition of the composite deposits

Figure 4-57 compares the TG/DTA data for a pure chitosan deposit and a composite deposit prepared from the 0.5 g/l chitosan solution containing 0.5 mM AgNO<sub>3</sub>. The TG data for the pure chitosan deposit showed three steps in weight loss: below 100 °C, and in the ranges of 280–300 °C and 450–570 °C (Figure 4-57 (a)). The DTA curve (Figure 4-57 (c)) exhibited a broad endotherm around 90 °C and exotherms around 275 °C and 550 °C. A reduction in the sample weight below 100 °C can be attributed to the liberation of adsorbed water. The weight loss above 280 °C and corresponding exotherms are related to the burning out of chitosan. For the Ag–chitosan composite deposit, similar steps were observed in the TG curve (Figure 4-57 (b)). The total weight loss of 82.3 wt% for the Ag–chitosan composite at 800 °C indicates the Ag content of 17.7 wt% in the composite coating. Figure 4-57 (a) gives a typical TG graph for the Ag-chitosan coatings prepared from chitosan

solutions containing  $\text{AgNO}_3$ . When the  $\text{AgNO}_3$  concentration was increased, the Ag content in the obtained Ag-chitosan coatings increased up to 45.8 wt% for 1.0 mM  $\text{AgNO}_3$ . The DTA data for the composite coating (Figure 4-57 (d)) showed a broad endotherm at  $\sim 90^\circ\text{C}$ , and exotherms in the range of  $200\text{--}520^\circ\text{C}$  related to the burning out of chitosan.

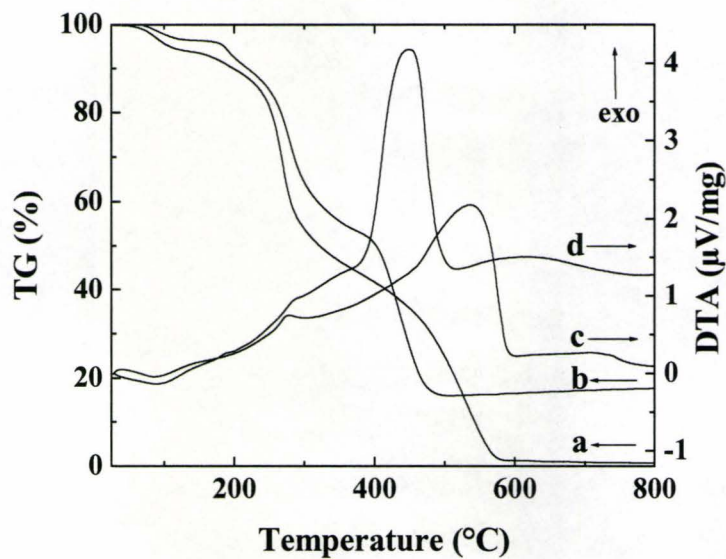


Figure 4-57 (a, b) TG and (c, d) DTA data for the deposits prepared from (a, c) the pure 0.5 g/l chitosan solution, and (b, d) the 0.5 g/l chitosan solution containing 0.5 mM  $\text{AgNO}_3$ .

TG/DTA investigations were also conducted on the HA–Ag–chitosan composite deposits prepared from the chitosan solutions containing both  $\text{AgNO}_3$  and HA (Figure 4-58). The weight losses at  $800^\circ\text{C}$  for the HA–Ag–chitosan composite deposits prepared from the deposition baths containing 1.0 g/l and 3.0 g/l HA are 47.2

wt% and 19.4 wt%, respectively. The total weight loss can be attributed to the deposit dehydration and burning out of chitosan. Taking into account that the concentration of  $\text{AgNO}_3$  in the deposition baths was 1.0 mM for both deposits, the lower weight loss for the deposit prepared from the 3.0 g/l HA suspension can be attributed to a higher HA content in the deposit. These results indicate that the Ag/HA molar ratio in the composite coatings can be varied.

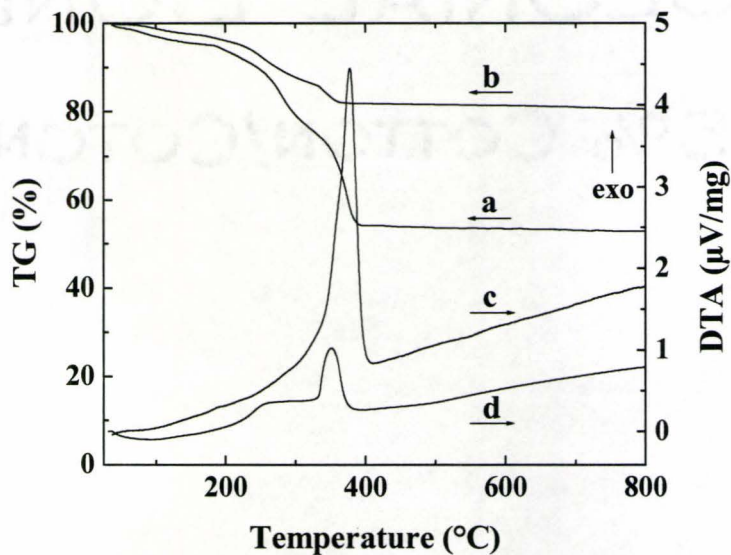


Figure 4-58 (a, b) TG and (c, d) DTA data for the deposits prepared from the solutions containing 0.5 g/l chitosan, 1.0 mM  $\text{AgNO}_3$ , and (a, c) 1.0 g/l HA and (b, d) 3.0 g/l HA.

Indeed, the results of EDS studies (Figure 4-59) showed that the relative intensity of Ca and P peaks corresponding to the deposited HA particles increases compared to the intensity of Ag peaks with an increasing concentration of HA in the suspensions used for the deposition of the composite coatings. The Ag/HA molar ratio

was found to be 1.44, 0.78, and 0.36 for the deposits prepared from the solutions containing 0.5 g/l, 1.0 g/l, and 2.0 g/l HA, respectively. The results of TG and DTA investigations coupled with the EDS data indicate that the composition of the coating can be varied by changing the  $\text{AgNO}_3$  or HA concentration in the chitosan solutions.

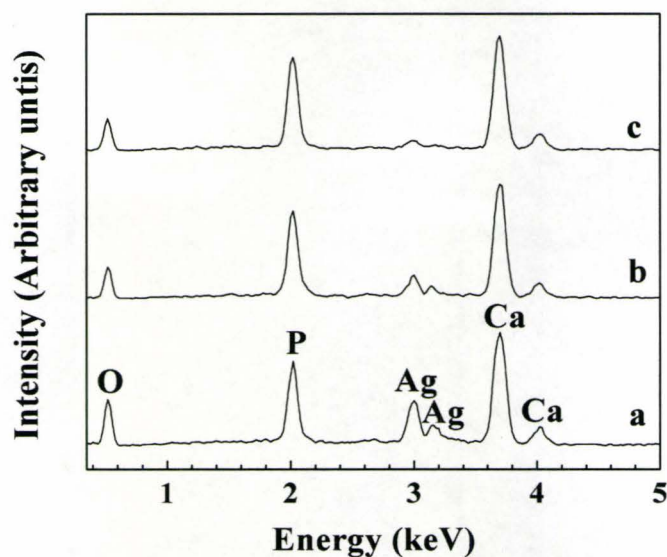
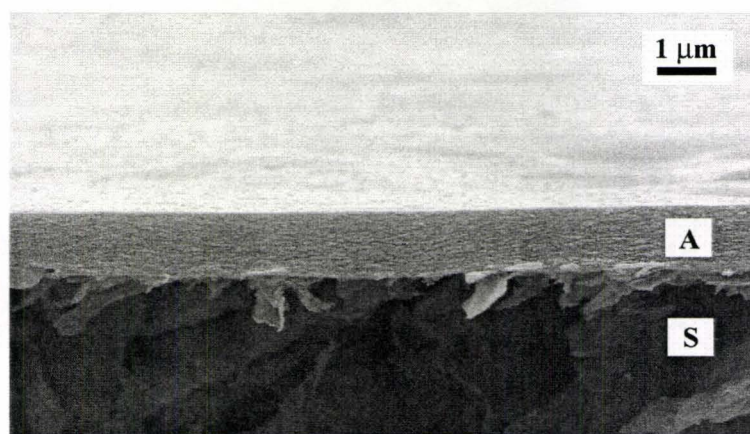


Figure 4-59 EDS spectra for the deposits prepared from the solutions containing 0.5 g/l chitosan, 1.0 mM  $\text{AgNO}_3$ , and (a) 0.5 g/l HA, (b) 1.0 g/l HA, and (c) 2.0 g/l HA.

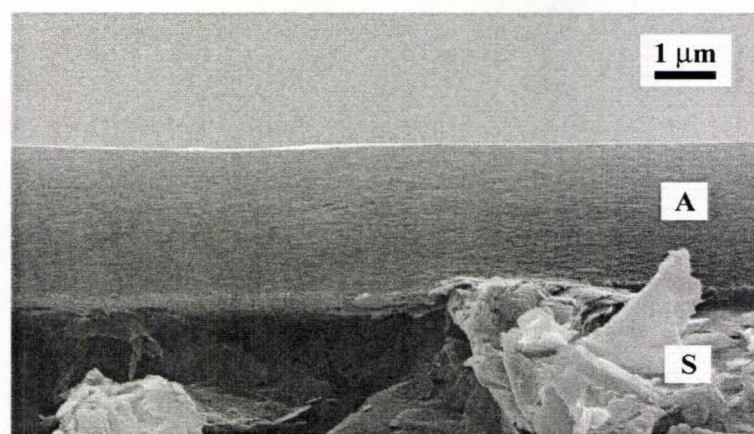
#### 4.4.3 Microstructure of the composite monolayer coatings

It is worth noting that the development of advanced composites includes not only the selection of components but also the materials design. An important task is to design new coating structures for the composite material (e.g. monolayer or functionally graded coating) so that an effectively control of the release rate of  $\text{Ag}^+$  from the coating can be attained. The incorporation of other advance properties and

further functionalization can be expected for the functionally graded or multilayer coatings. In this work, the composite coatings were prepared as HA–Ag–chitosan monolayers, and multilayers containing HA-chitosan and Ag-chitosan layers. The results of SEM studies showed that the use of chitosan enabled the formation of uniform, adherent and crack-free coatings.

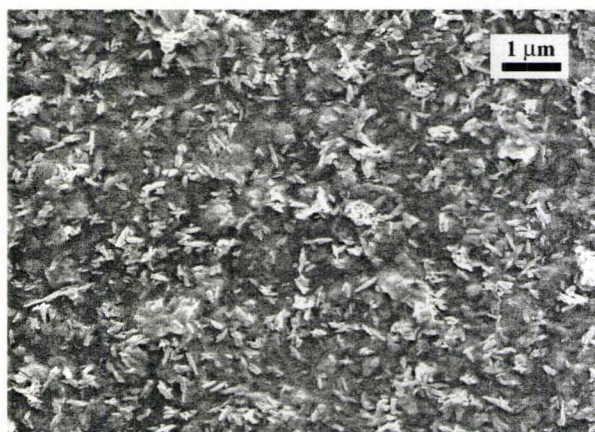


(a)

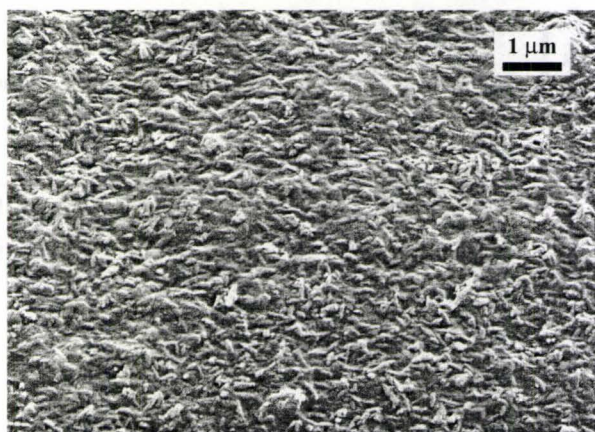


(b)

Figure 4-60 SEM images of the cross-sections of the coatings (A) on a graphite substrate (S) prepared from the 0.5 g/l chitosan solution containing 1.0 mM  $\text{AgNO}_3$  for (a) 10 min, and (b) 20 min.



(a)



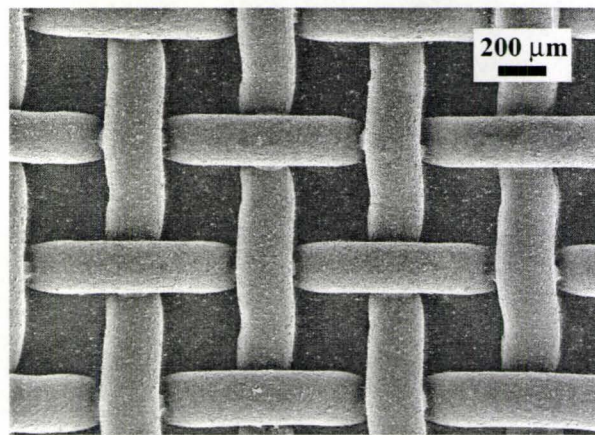
(b)

Figure 4-61 SEM images of the surfaces of the deposits prepared from the 0.5 g/l chitosan solutions containing (a) 1.0 g/l HA, and (b) 1.0 g/l HA and 1.0 mM  $\text{AgNO}_3$ .

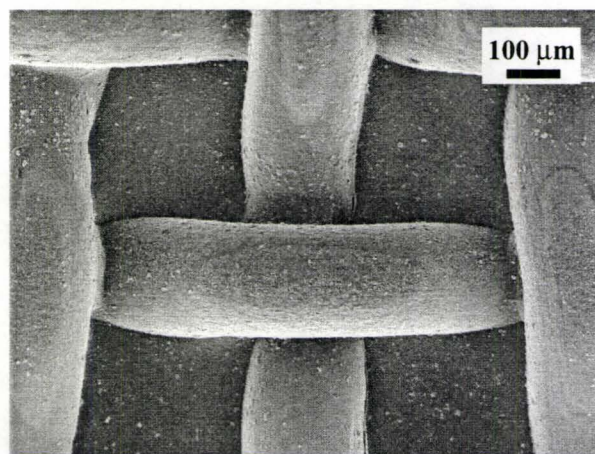
Figure 4-60 shows SEM images of the cross-sections of Ag-chitosan coatings on graphite substrates. The increase in the deposition time resulted in an increasing deposit thickness. The results indicate that the thickness of the coating can be varied in the range of 0–5  $\mu\text{m}$  by changing the deposition time in the range of 0–40 min.

Figure 4-61 shows surfaces of the monolayer composite coatings. The deposits are relatively dense and contain needle-shape HA nanoparticles. The composite

deposits can be obtained on substrates of complex shape. Figure 4-62 shows SEM pictures of the HA-Ag-chitosan monolayer composite coating deposited on a stainless-steel gauze. A comparison of the SEM images of the coated and uncoated gauzes indicates a relatively uniform thickness ( $\sim 20 \mu\text{m}$ ) of the deposits.



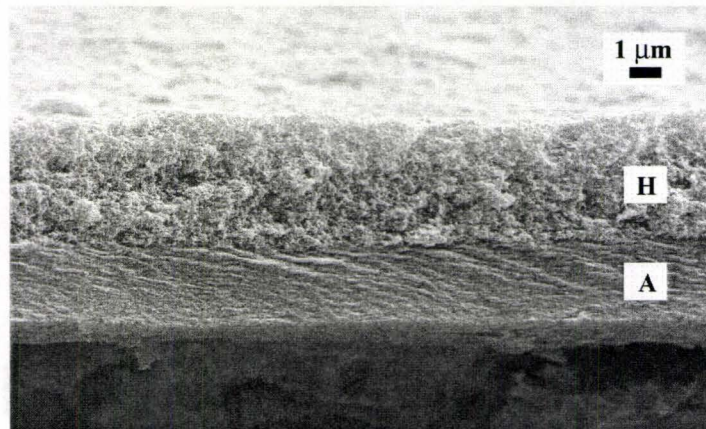
(a)



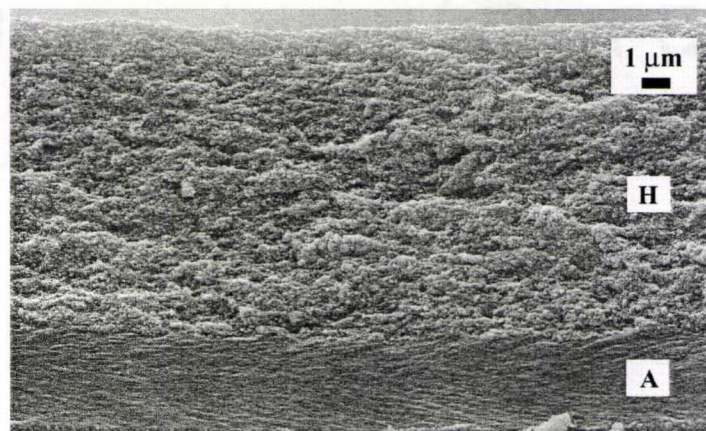
(b)

Figure 4-62 (a, b) SEM images at different magnifications of the composite coating on a stainless-steel gauze deposited from the 0.5 g/l chitosan solution containing 1.0 mM  $\text{AgNO}_3$  and 1.0 g/l HA.

#### 4.4.4 Microstructure of the composite multilayer coatings



(a)

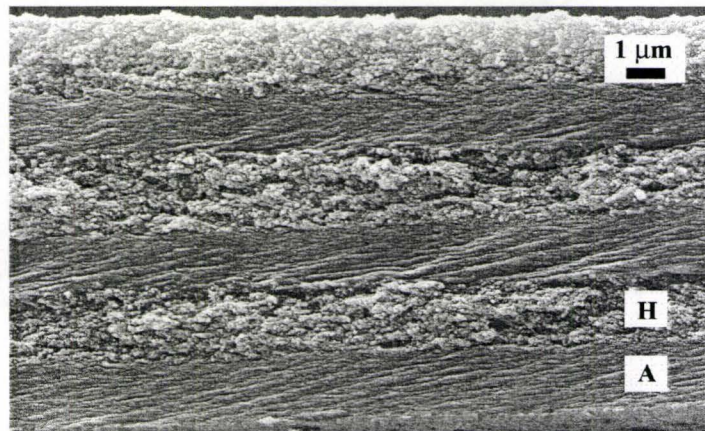


(b)

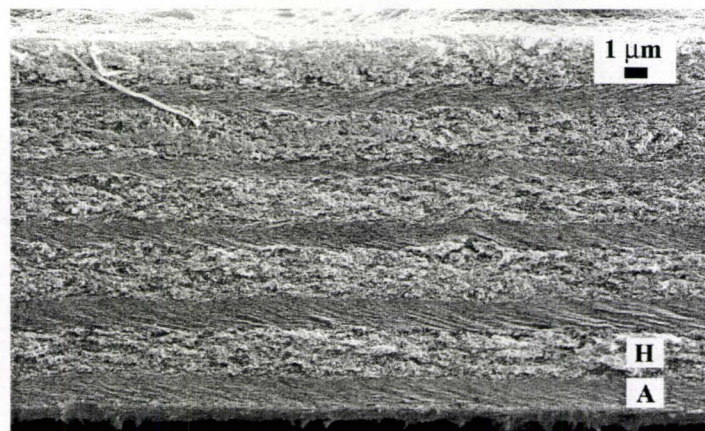
Figure 4-63 SEM images of the cross-sections of the HA-chitosan (H) /Ag-chitosan (A) bi-layer coatings prepared from the 0.5 g/l chitosan solutions containing 1.0 mM AgNO<sub>3</sub> (A) or 1 g/l HA (H) at deposition times of 15 min for layers A, and (a) 10 min or (b) 20 min for layers H.

The examples of a bi-layer coating structures are shown in Figure 4-63. The SEM images of the sectioned HA-chitosan/Ag-chitosan composite coatings indicate that the thickness of the HA-chitosan layer can be changed by the variation of the deposition time. Figure 4-64 shows examples of the multilayer structures containing

different numbers of individual layers. The SEM investigations of the multilayer structure prepared at various experimental conditions showed that the thickness of the coatings can be varied in the range of 0–20  $\mu\text{m}$  by the variation of the deposition time for individual layers or by the variation of the number of layers. The SEM images show a good interfacial bonding between the deposited dense layers of uniform thicknesses.



(a)



(b)

Figure 4-64 (a, b) Multilayer coatings with different numbers of layers, prepared from the 0.5 g/l chitosan solutions containing 1.0 g/l HA (H) or 1.0 mM  $\text{AgNO}_3$  (A).

#### 4.4.5 Ag<sup>+</sup> release rate of the composite coatings

The antimicrobial activity of silver ions has been well established [Slawson *et al.*, 1992]. Silver ions are significant antimicrobials by virtue of their antiseptic properties [Spardaro *et al.*, 1986] with only few bacterial being intrinsically resistant to this metal [Russel *et al.*, 1994]. The antimicrobial activity of silver is dependent on the silver cation Ag<sup>+</sup>, which binds strongly to electron donor groups in biological molecules containing sulphur, oxygen or nitrogen. Hence the silver-based antimicrobial polymers have to release the Ag<sup>+</sup> in order to be effective. The oxidation of the metallic silver to the active species Ag<sup>+</sup> is possible through an interaction of the silver with the water molecules. A steady and prolonged release of the silver biocide in a concentration level (0.1 ppb) capable of rendering an antimicrobial efficacy [Wohrmann *et al.*, 1998] is a key factor for the design of this class of materials. When in excess concentration, Ag<sup>+</sup> has a toxic effect [Yang *et al.*, 2003].

In this work, a layered structure has been designed to control the release of Ag<sup>+</sup> from the composite coating. Turning again to the SEM images of the composite coatings shown in Figure 4-63, it should be noted that the top layer containing HA provides a bioactive surface for the composite coatings and can reduce the Ag<sup>+</sup> release rate from the bottom layer. Moreover, the release rate of antimicrobial Ag species from the bottom layer can be modified by the variation of the thickness and composition of the top layer. As an example, Figure 4-65 compares the kinetics of the release of Ag<sup>+</sup> ions from the Ag-chitosan monolayer and the bi-layer

HA–chitosan/Ag–chitosan composite coating.

A fast release of  $\text{Ag}^+$  ions from the Ag–chitosan monolayer coating was observed during the first 12 hr of immersion, and then the  $\text{Ag}^+$  concentration reached a plateau at about 30 ppm. For the bi-layer composite coating, whose bottom layer was the same as the monolayer coating, the additional top HA–chitosan layer acted as a barrier to prevent the fast release of the  $\text{Ag}^+$  ions from the bottom layer. As a result the release rate of  $\text{Ag}^+$  ions was only 1 ppm during 2 weeks.

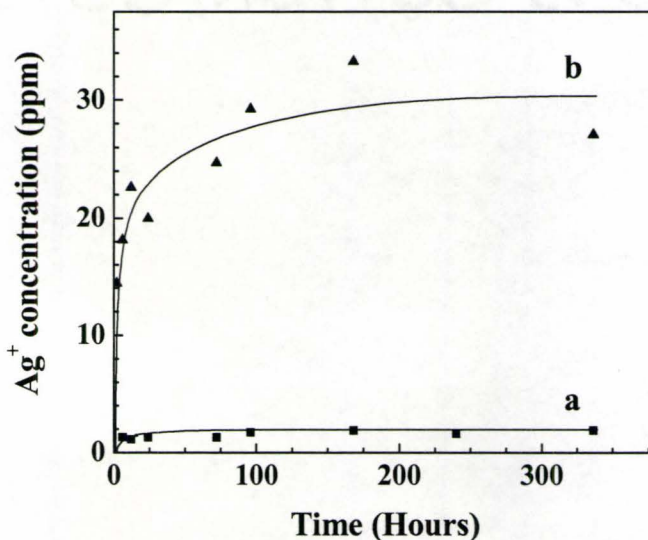
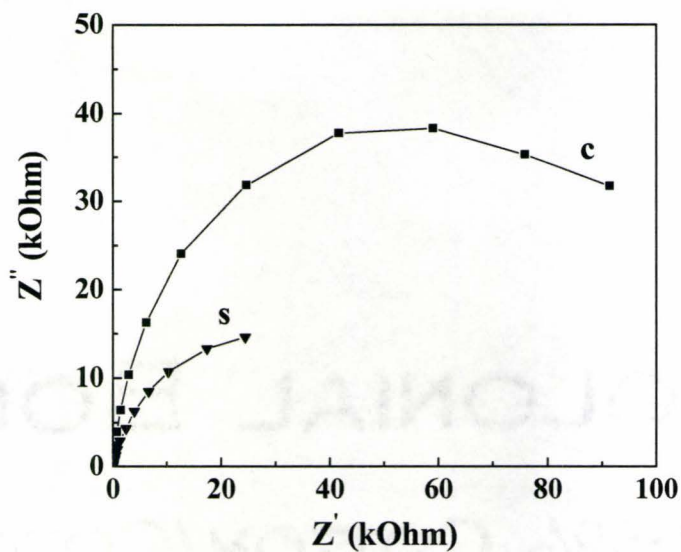


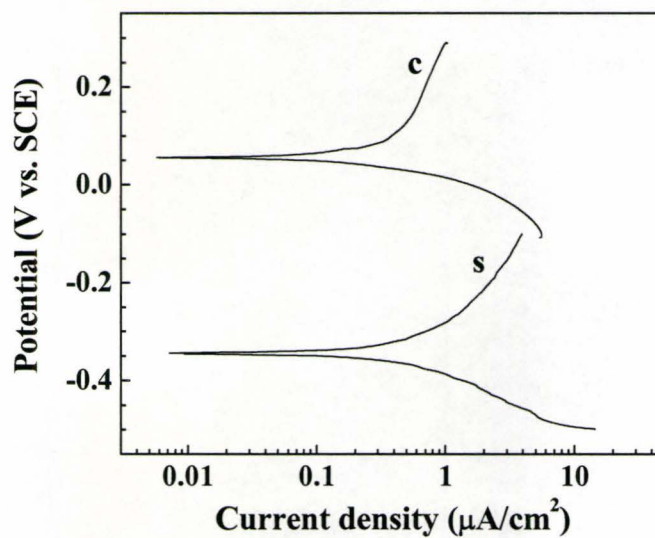
Figure 4-65 The concentration of released  $\text{Ag}^+$  ions as a function of the immersion time for (a) the Ag–chitosan monolayer coating on stainless steel prepared from the 0.5 g/l chitosan solution containing 1.0 mM  $\text{AgNO}_3$ , and (b) the HA–chitosan/Ag–chitosan bi-layer coating on stainless steel prepared from the 0.5 g/l chitosan solutions containing 1.0 g/l HA or 1.0 mM  $\text{AgNO}_3$ .

#### 4.4.6 Corrosion protective properties of the composite coatings

Electrochemical testing results indicate that the layered composite coatings provide corrosion protection of the stainless steel in the Ringer's solutions. Figure 4-66 shows the experimental data for a HA-chitosan/Ag-chitosan/HA-chitosan three-layer coating. The properties of the coated and uncoated samples in the Ringer's solution were compared. The EIS data was presented in the complex impedance diagram (Nyquist plot), where the imaginary component  $Z''$  of the impedance is plotted as a function of the real component  $Z'$  (Figure 4-66 (a)). It was observed that the impedance values for the coated sample were higher than those for the uncoated substrate. This behavior suggests that the deposited composite coating reduces the ion diffusion process and can reduce the corrosion rate of the substrate. This is in a good agreement with the results of potentiodynamic investigations. Figure 4-66 (b) shows the obtained Tafel curves for the uncoated and coated stainless steel samples. It can be seen that the corrosion current and therefore the rate of corrosion of the coated sample was significantly reduced by the coating. These results indicate that the composite deposit can act as a protective layer and improve the corrosion resistance of the stainless steel substrates in the simulated physiological environment.



(a)



(b)

Figure 4-66 The Nyquist plots (a) and Tafel plots (b) for the samples tested in the Ringer's solution: (s) the bare stainless steel substrate, and (c) the stainless steel coated with a HA-chitosan/Ag-chitosan/HA-chitosan three-layer coating, prepared from the 0.5 g/l chitosan solutions containing 1.0 g/l HA or 1.0 mM  $\text{AgNO}_3$ .

## **4.5 Electrodeposition of functionally graded hydroxyapatite-CaSiO<sub>3</sub>-chitosan nanocomposite coatings**

### **4.5.1 Codeposition of hydroxyapatite, CaSiO<sub>3</sub>, and chitosan**

CaSiO<sub>3</sub> materials in crystalline and amorphous forms have generated significant interest for the surface modification of biomedical implants. CaSiO<sub>3</sub> was reported to have a high bioactivity due to the fast formation of an apatite layer on its surface after soaking in simulated body fluid [Hazar, 2007; Ni *et al.*, 2006; Siriphannon *et al.*, 2000]. The silanol groups on the CaSiO<sub>3</sub> surface provided favorable sites for apatite nucleation [Cho *et al.*, 1996; Kokubo *et al.*, 1993]. The addition of CaSiO<sub>3</sub> to biocomposites enabled the formation of advanced materials with enhanced bioactivity. However, the fabrication of CaSiO<sub>3</sub> coatings on metallic substrates presented difficulties attributed to relatively high sintering temperature and brittleness of this material. These problems can be avoided using composite chitosan–CaSiO<sub>3</sub> coatings. It would be of great interest to develop novel HA- CaSiO<sub>3</sub>-chitosan nanocomposite with enhanced bioactivity on implant metals.

The possibility to codeposit CaSiO<sub>3</sub> and chitosan was investigated by adding CaSiO<sub>3</sub> powders to the chitosan solution. Figure 4-67 compares the TG/DTA data for as-received CaSiO<sub>3</sub> powders and the composite deposits prepared from 0.5 g/l chitosan solutions containing 0.2 and 0.5 g/l CaSiO<sub>3</sub>. The TG data for the as-received CaSiO<sub>3</sub> powders (Figure 4-67 (a)) showed a total weight loss of 16.8 wt% at 1000 °C,

which can be attributed to the liberation of adsorbed water. For the  $\text{CaSiO}_3$ -chitosan composite deposits, additional weight loss steps related to the burning out of the polymer chitosan can be seen in the TG curves (Figure 4-67 (b,c)). The total weight loss at 1000 °C for the composite deposits prepared from chitosan solutions containing 0.2 g/l and 0.5 g/l  $\text{CaSiO}_3$  was found to be 70.0 wt% and 81.7 wt%, respectively. The DTA data for the composite coatings showed a broad endotherm at ~ 90 °C attributed to the liberation of the adsorbed water, and exotherms in the range of 200–550 °C related to the burning out of chitosan. The TG/DTA data coupled with the results of XRD studies indicate the possibility of the fabrication of  $\text{CaSiO}_3$ -chitosan composite coating containing different amount of  $\text{CaSiO}_3$ . From the TG data, the  $\text{CaSiO}_3$  content in the composite coatings prepared from the 0.5 g/l chitosan solutions containing 0.2 g/l and 0.5 g/l  $\text{CaSiO}_3$  was found to be 30.0 wt% and 18.3 wt%, respectively. The composition of the composite coating can be varied by the variation of  $\text{CaSiO}_3$  concentration in the chitosan solution.

The formation of cathodic  $\text{CaSiO}_3$ -chitosan deposits indicates that the  $\text{CaSiO}_3$  particles are positively charged in the chitosan solution. The positive charge of the  $\text{CaSiO}_3$  particles can be attributed to the adsorbed chitosan on their surface. The formation of  $\text{CaSiO}_3$ -chitosan composite deposits can be considered as the electrophoretic codeposition of  $\text{CaSiO}_3$  and chitosan. The deposition mechanism is similar to that proposed for the HA-chitosan composite coatings [Pang *et al.*, 2005a, b, 2007]. The chitosan macromolecules adsorbed on the  $\text{CaSiO}_3$  surface provide the

electrosteric stabilization and charging of the  $\text{CaSiO}_3$  particles. Electrophoresis results in the accumulation of the charged  $\text{CaSiO}_3$  particles and chitosan macromolecules towards the cathode surface. At the electrode surface, the cathodic reaction results in an increase in pH. The chitosan loses its charge through deprotonation and forms an insoluble deposit on the cathode surface. The neutralization of the positively charged chitosan macromolecules results in the formation of  $\text{CaSiO}_3$ -chitoan composite deposit.

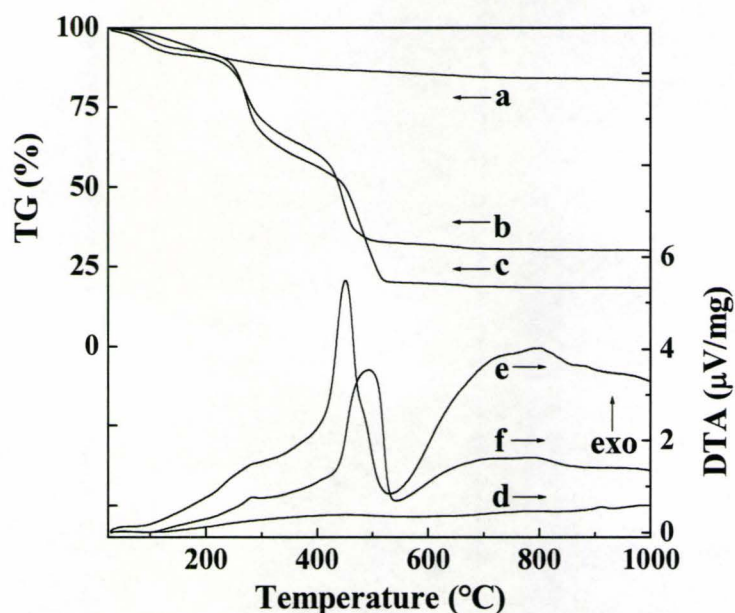


Figure 4-67 TG (a,b,c) and DTA(d,e,f) data for (a,d) as-received  $\text{CaSiO}_3$  powders and composite deposits prepared from chitosan solutions containing (b,e) 0.5 g/l  $\text{CaSiO}_3$  and (c,f) 0.2 g/l  $\text{CaSiO}_3$ .

#### 4.5.2 SEM studies of microstructure of the obtained composite coatings

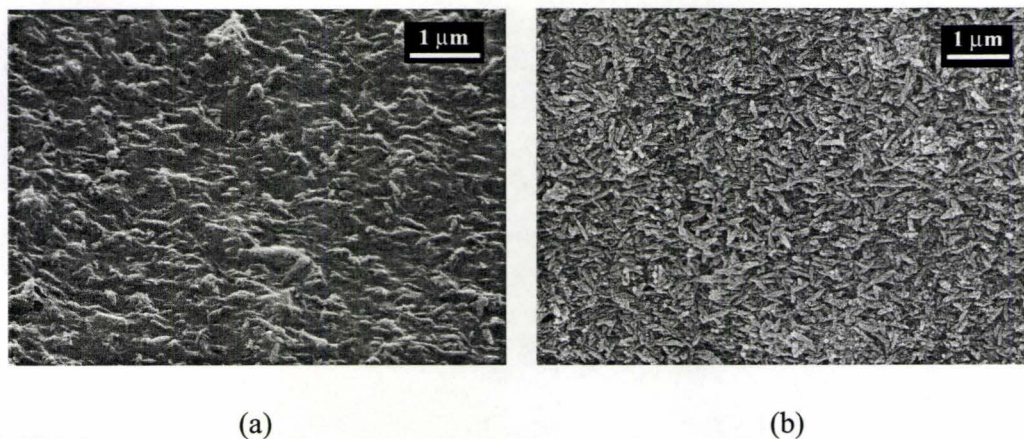


Figure 4-68 SEM images of HA-chitosan composite coatings deposited at a constant current of  $0.1 \text{ mA/cm}^2$  for 10 min from the chitosan solutions containing (a) 0.5 g/l HA and (b) 1.0 g/l HA.

The surface morphology and microstructure of the obtained HA-chitosan and  $\text{CaSiO}_3$ -chitosan composite coatings containing different amounts of HA and  $\text{CaSiO}_3$  were studied by SEM. Figure 4-68 shows the SEM images of the HA-chitosan composite coatings prepared from the chitosan solutions containing 0.5 g/l and 1.0 g/l HA. The surface of the deposits presented the needle-shape HA nanoparticles in a matrix of chitosan. Figure 4-69 gives the SEM images of the  $\text{CaSiO}_3$ -chitosan composite coatings under different magnifications. The deposits showed a higher porosity compared to the HA-chitosan composite deposits (Figure 4-68) due to a larger particle size and agglomeration of particles. The deposits prepared from the chitosan solutions containing 0-1.0 g/l HA and 0-0.5 g/l  $\text{CaSiO}_3$  were smooth, dense,

and adherent to the substrates. A relatively uniform distribution of HA and CaSiO<sub>3</sub> particles in the chitosan matrix was observed. The higher concentration of HA and CaSiO<sub>3</sub> in the chitosan solutions resulted in a higher HA (Figure 4-68 (b)) and CaSiO<sub>3</sub> (Figure 4-69 (c,d)) content in the composite coatings, which is in a good agreement with the TG/DTA results. The obtained results indicate a possibility of codeposition of CaSiO<sub>3</sub> and HA to form composite HA–CaSiO<sub>3</sub>–chitosan coatings.

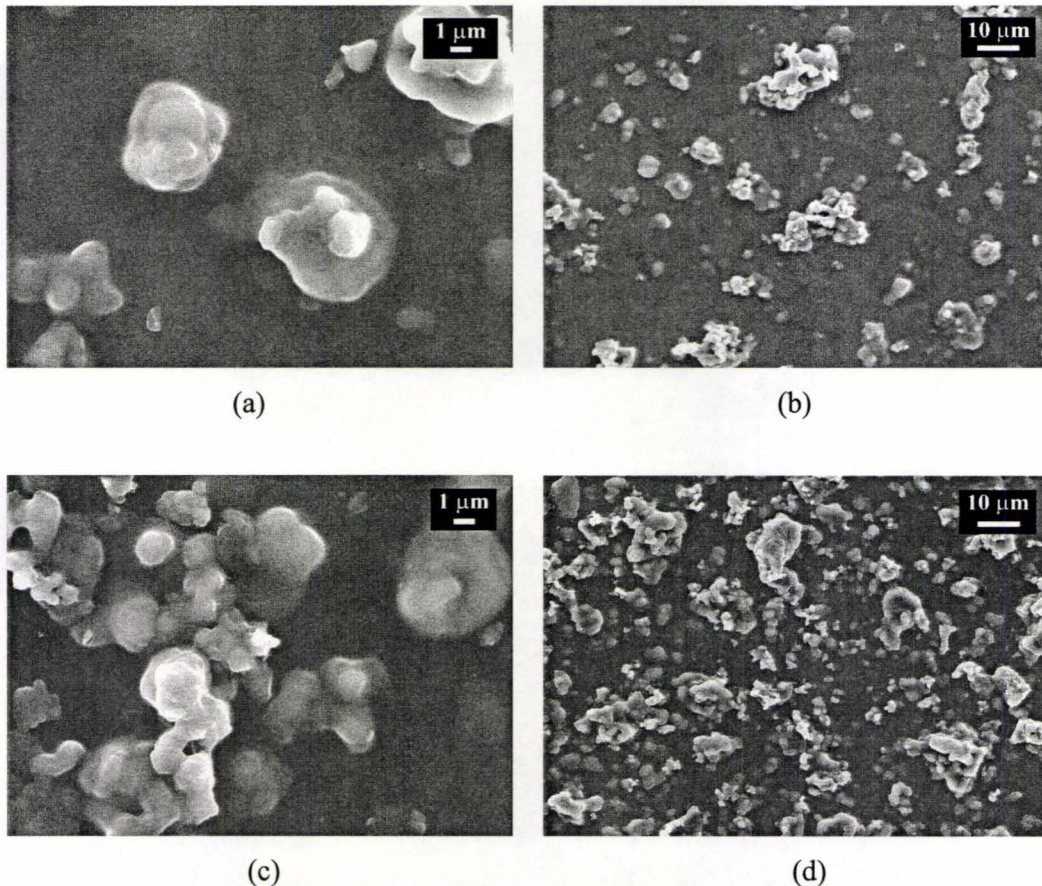
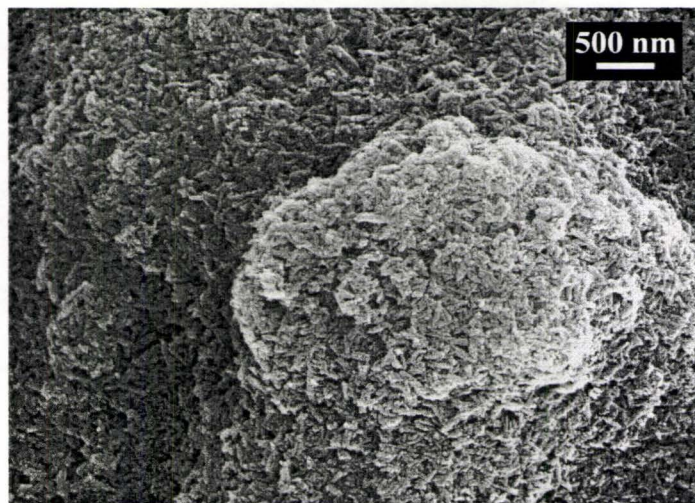


Figure 4-69 SEM images of CaSiO<sub>3</sub>-chitosan composite coatings deposited at constant current of 0.1 mA/cm<sup>2</sup> for 10 min from the chitosan solutions containing (a,b) 0.3 g/l CaSiO<sub>3</sub>, and (c,d) 0.5 g/l CaSiO<sub>3</sub> at different magnifications.



(a)



(b)

Figure 4-70 SEM images at different magnifications (a,b) of HA-CaSiO<sub>3</sub>-chitosan composite coatings deposited at constant 0.1 mA/cm<sup>2</sup> for 10 min from the chitosan solutions containing 1.0 g/l HA and 0.3 g/l CaSiO<sub>3</sub>.

Figure 4-70 shows the SEM images of the HA-CaSiO<sub>3</sub>-chitosan composite deposit prepared from the chitosan solution containing both HA and CaSiO<sub>3</sub> particles. It was observed that the HA nanoparticles and CaSiO<sub>3</sub> powders are uniformly

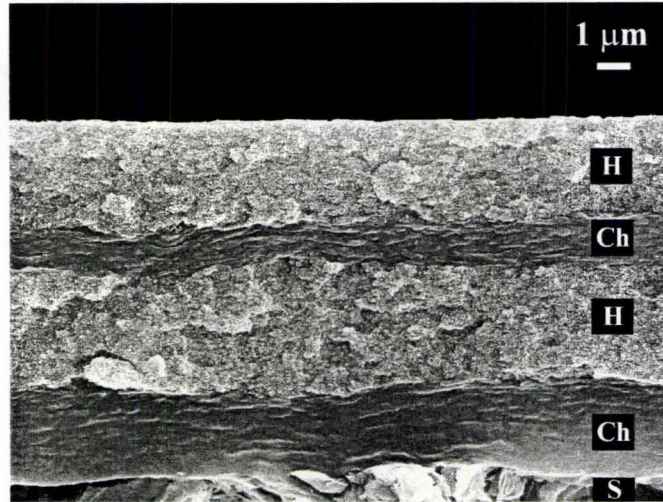
distributed in a polymer matrix. The nano-size HA were distributed between the  $\text{CaSiO}_3$  particles of a larger size (Figure 4-70 (a) and covered the surface (Figure 4-70 (b)) of the  $\text{CaSiO}_3$  particles or agglomerates, resulting in a denser and smoother coating compared to the  $\text{CaSiO}_3$ -chitosan deposit (Figure 4-69).

#### **4.5.3 Preparation of the composite coatings of graded composition and laminate structure**

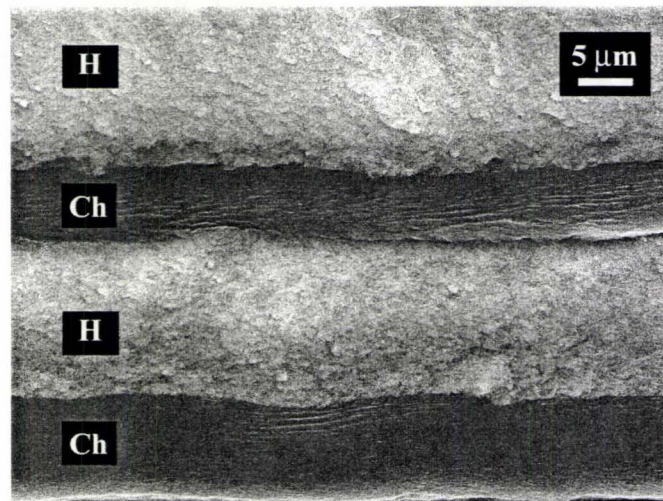
The obtained results pave the way for the fabrication of composite coatings of graded composition and laminate structure. Laminate composite coatings containing individual layers with different HA content were obtained. Figure 4-71 shows an example of the laminate coatings containing alternating pure chitosan and HA-chitosan layers deposited from the chitosan solution containing 4 g/l HA. The pure chitosan layer offers a possibility to improve the adhesion of the composite coating. The HA-chitosan layers has a HA content of ~80 wt%, which is close to that of natural bone. It is expected that the addition of  $\text{CaSiO}_3$  will result in enhanced bioactivity of the composite coatings compared to pure HA. It is worth noting that natural bone is a nanocomposite material that contains laminates of collagen fibrils reinforced with HA nanoparticles. The unique mechanical and other properties of bone are derived from the hierarchical organization of the laminates, i.e., its unique structure of graded composition and porosity.

For the deposition of different materials, it is very important to use appropriate

solvent-binder-dispersant system. Recent studies [Zhitomirsky *et al.*, 2000e] have shown that the use of similar bath compositions and similarly charged particles allows for the deposition of consecutive layers of different ceramics. Well dispersed and stable suspensions of fine particles may be obtained by the use of an effective dispersant. However, the deposit containing fine particles with high surface area is prone to cracking during drying. Binders can be used to increase the adherence and strength of the deposits and prevent the cracking. For a system using different materials as dispersant, binder, and other additives, there are problems related to the competitive adsorption of dispersant, binder, and charging additives on the particle surface and the control of the amount of additives included in the deposit. In this respect, the chitosan used in our work offers important advantages, as it works simultaneously as a dispersant, binder, and charging agent for the EPD. The chitosan adsorbed on the surface of the ceramic particles provides effective electrosteric stabilization of the particles. In the same time, the adsorption of chitosan on the surface of  $\text{CaSiO}_3$  and HA particles provides a positive charge and enables the cathodic electrodeposition of the particles. Moreover, chitosan with inherent binding property can act as an effective binder to enhance the adhesion of the particles to the substrate and prevent cracking. Experimental results show that the chitosan content in the composite deposits can be varied in the range of 0-100 wt% by the variation of chitosan or ceramic particle concentration in the suspensions.



(a)



(b)

Figure 4-71 (a,b) SEM images of the cross-sections of the laminate coatings prepared from the pure 0.5 g/l chitosan solution (Ch) or 0.5 g/l chitosan containing 4.0 g/l HA (H).

The results of our work indicate that EPD enables the fabrication of composite HA-CaSiO<sub>3</sub>-chitosan laminates and materials of graded composition. Figure 4-72 shows an example of the composite coating containing layers of CaSiO<sub>3</sub>-chitosan and

HA-chitosan nanocomposites on top of a chitosan layer. The use of chitosan enables the cathodic EPD of layers of different materials and a good interfacial bonding of layers. The microstructure and composition of the coatings can be varied by the deposition of  $\text{CaSiO}_3$ -chitosan and HA-chitosan layers of different composition and microporosity.

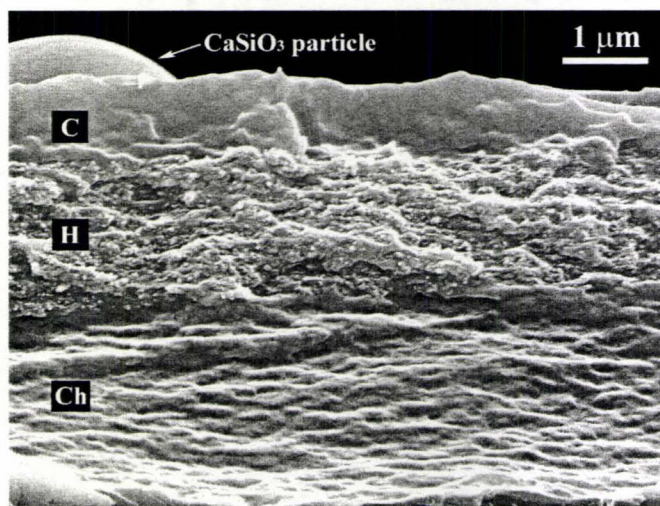


Figure 4-72 SEM image of the cross-section of a  $\text{CaSiO}_3$ -chitosan (C)/HA-chitosan(H)/chitosan(Ch) three-layer coating prepared from the 0.5 g/l chitosan solutions containing 0.3 g/l  $\text{CaSiO}_3$  (C) or 1 g/l HA (H).

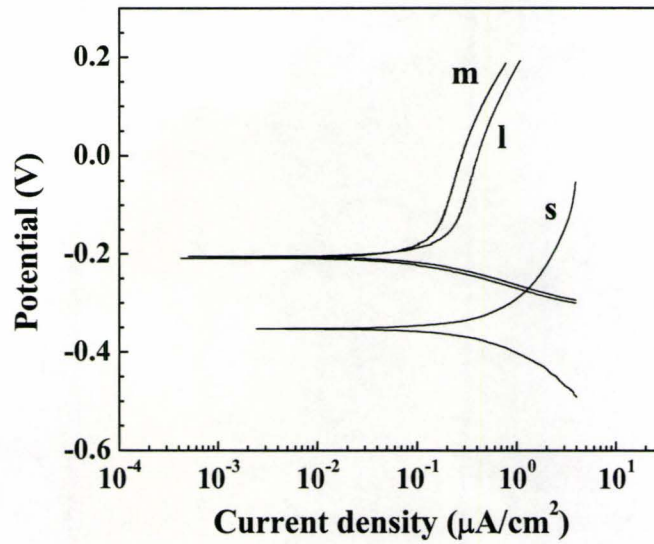
#### 4.5.4 Corrosion protection properties of the composite coatings

The corrosion protection properties of the obtained laminate and monolayer composite coatings have been investigated by electrochemical methods in Ringer's physiological solution. Figure 4-73 show the experimental data for a chitosan/HA-chitosan/chitosan/HA-chitosan four-layer coating and a

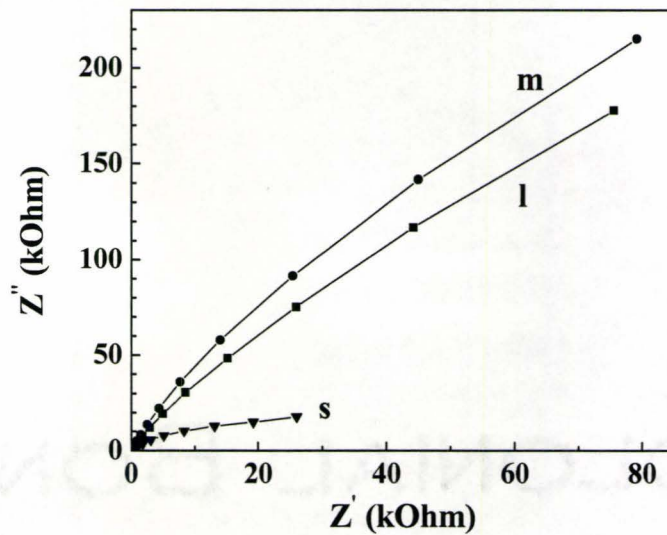
HA-CaSiO<sub>3</sub>-chitosan monolayer coating, compared to those for the uncoated stainless steel substrate. Figure 4-73 (a) shows the obtained Tafel curves for the uncoated and coated stainless steel samples. It can be seen that the corrosion current and therefore the rate of corrosion of the coated samples was significantly reduced by the composite coatings. The monolayer CaSiO<sub>3</sub>-HA-chitosan coating resulted in the lowest corrosion current, indicating slightly better corrosion protection properties than the chitosan/HA-chitosan/chitosan/HA-chitosan four-layer coating. This is in a good agreement with the results of the EIS investigations. The EIS data was presented in the complex impedance diagram (Nyquist plot), where the imaginary component  $Z''$  of the impedance is plotted as a function of the real component  $Z'$  (Figure 4-73 (b)). It was found that the impedance values for the coated sample were higher than those for the uncoated substrate. This behavior suggests that both of the composite coatings impeded the ion diffusion process and reduced the corrosion rate of the substrate. These results indicate that the obtained composite deposits can act as a protective layer and improve the corrosion resistance of the stainless steel substrates in the simulated physiological environment.

The results of this work demonstrate the possibility of the fabrication of advanced composite coatings of graded composition and laminate structure by EPD. An important task for the future research is the investigation of bioactivity, adhesion, mechanical and other properties of the novel coatings and the optimization of the microstructure and properties. The method also exhibits a potential of codeposition of

other materials and further functionalization of the coatings for a variety of applications.



(a)



(b)

Figure 4-73 (a) Tafel and (b) Nyquist plots of (s) the bare stainless steel substrate, and the coated samples with (l) a chitosan/HA-chitosan/chitosan/HA-chitosan 4-layer coating prepared from pure 0.5 g/l chitosan solution or 0.5 g/l chitosan solution containing 4 g/l HA, and (m) a  $\text{CaSiO}_3$ -HA-chitosan monolayer coating prepared from 0.5 g/l chitosan solution containing 1 g/l HA and 0.3 g/l  $\text{CaSiO}_3$ .

#### 4.6 Summary

Two coating systems have been developed in the research. The major outcomes of the investigations are listed in Table 4-2.

Table 4-2 Summary of the experimental results.

Coating systems	Coatings developed	Functional materials used	Outcomes
ZrO <sub>2</sub> coatings	ZrO <sub>2</sub> -PEI	Weak polyelectrolyte additive PEI	Electrochemically codeposition of ZrO <sub>2</sub> and the polyelectrolytes; In-situ synthesis of ZrO <sub>2</sub> nanoparticles;
	ZrO <sub>2</sub> -PAH	Weak polyelectrolyte additive PAH	Formation of composite coatings containing different amounts of polyelectrolytes; Control over the amount of materials deposited;
	ZrO <sub>2</sub> -PDDA	Strong polyelectrolyte additive PDDA	Formation of uniform, dense, adherent, and crack-free coatings of various thicknesses up to several microns on substrates of complex shapes.
Functional HA-chitosan composite coatings	HA-chitosan	Biopolymer chitosan, acting as a binder, dispersant, and charging agent for EPD	Synthesis of HA nanoparticles suitable for EPD; Room temperature processing of novel composite coatings by codeposition of HA and chitosan; Avoiding all problems related to the sintering of HA; Control over the composition, nanostructure, preferred orientation of HA nanoparticles, and deposition yield of the coatings by the variation of deposition conditions;
	HA-Ag-chitosan	Ag with antimicrobial properties;	Formation of dense, adherent bioactive composite coatings of various thicknesses up to 60 μm on substrate of complex shapes; Incorporation of other functional materials (Ag, CaSiO <sub>3</sub> );
	HA-CaSiO <sub>3</sub> -chitosan	CaSiO <sub>3</sub> with excellent bioactivities;	Development of novel coating structures (monolayer, multilayer, and laminates with graded composition), which enabled the controlled release rate of Ag <sup>+</sup> , improved coating adherence to substrate, and enhanced surface bioactivity.

## I. ZrO<sub>2</sub> coatings

Both weak (PEI, PAH) and strong (PDDA) cationic polyelectrolytes can be used for the electrodeposition of thick, adherent ZrO<sub>2</sub> ceramic and composite coatings for biomedical applications. The small amount of the polyelectrolyte additives acting as a binder prevented deposit cracking and increased deposit adhesion. Sintering resulted in the burning out of polymers and formation of zirconia coatings. Coatings up to several microns thick were obtained on various conducting substrates of complex shapes. The proposed electrochemical method combined the EPD of the polyelectrolytes with cathodic electroprecipitation of ZrO<sub>2</sub>. Different mechanisms worked for the charging and formation of deposits of the weak and strong polyelectrolytes. The obtained results are important for the development of new electrodeposition strategies, and pave the way for the fabrication of other ceramic and ceramic-polymer composite coatings based on cationic polyelectrolytes and metal oxides or hydroxides.

## II. Functional HA-chitosan composite coatings

EPD of nanostructured HA coatings on implant metals presents difficulties due to the high-temperature sintering after deposition. The problem can be addressed by the fabrication of ceramic-polymer composite coatings containing HA nanoparticles, for which the densifying sintering process is not needed. On the other hand, the inspiration from bone, a natural nanocomposite material, also suggests the development of HA-polymer nanocomposite coatings instead of pure HA coatings.

In the research, novel electrodeposition strategies have been developed for the fabrication of functional HA-chitosan composite coatings, based on the EPD of chemically precipitated HA nanoparticles and electrochemical deposition of chitosan. The proposed method offers the advantage of room temperature fabrication of the coatings, which enables the incorporation of polymers and other functional materials. Chitosan, acting as a suspension dispersant, charging agent, binder, and polymer component, enabled the codeposition of different materials and formation of composite coatings containing HA nanoparticles and other functional materials. Ag has been electrochemically intercalated into the composite coatings to provide antimicrobial properties.  $\text{CaSiO}_3$  particles have been codeposited with HA and chitosan to enhance bioactivities of the coatings. Further development of the composite coatings resulted in the new designs of coating structures. The composite coatings have been prepared as monolayers, multilayers, or laminates of graded compositions, in attempt to improve the adherence to substrate, control the  $\text{Ag}^+$  release rate, and enhance the surface bioactivity, etc.

To summarize, the two coating systems developed in the research can be used for the fabrication of advanced biomedical implants. The proposed electrochemical methods exhibit a potential of codeposition of other materials and further functionalization of the coatings for a variety of applications.

## **Chapter 5 Conclusions and Future Work**

### **5.1 Conclusions**

The previous chapters have shown that the objectives stated in Chapter 2 have all been achieved. The main conclusions are summarized as follows:

- I. Novel electrochemical strategies, combining the cathodic electrosynthesis of zirconia and electrophoretic deposition of polyelectrolyte additives, have been developed for the deposition of thick adherent zirconia ceramic and composite coatings for biomedical applications.
- II. The method enables uniform deposition of zirconia coatings up to several microns thick on various conducting substrates of complex shapes. The use of the polyelectrolytes with inherent binding properties allowed to reduce cracking attributed to drying shrinkage, and to improve the deposit adhesion. The size and crystallinity of the zirconia nanoparticles in the coatings are influenced by the polymer and solvent used for the electrosynthesis. The amount of the deposited material and the deposit composition could be controlled by a variation of the deposition time and polyelectrolyte concentration in the deposition baths.
- III. New electrophoretic deposition methods have been developed for the fabrication of novel hydroxyapatite-chitosan, hydroxyapatite-Ag-chitosan, and

hydroxyapatite-CaSiO<sub>3</sub>-chitosan nanocomposite coatings for advanced biomedical applications.

- IV. The proposed methods offer the advantage of room temperature fabrication of the composite coatings. The problems related to the sintering of hydroxyapatite on metallic substrates can be avoided. The chitosan acted as dispersant, charging additive, and binder in the deposition of the composite coatings, providing an effective solution to the problems of competitive adsorption of different additives.
- V. The method enabled the formation of dense, adherent and uniform coatings of various thicknesses in the range of up to 60 μm on biomedical implant metals. Bioactive composite coatings containing 40.9–89.8 wt% hydroxyapatite were obtained. The deposit composition of the composite coatings can be tailored by varying the chitosan, hydroxyapatite, and AgNO<sub>3</sub> or CaSiO<sub>3</sub> concentrations in the deposition baths. X-ray studies revealed a preferred orientation of the hydroxyapatite nanoparticles in the hydroxyapatite-chitosan composite coatings with their *c*-axes parallel to the substrate surface. The degree of the preferred orientation increased with a decreasing hydroxyapatite content in the composite coatings.
- VI. The deposition yield of composite coatings can be varied by a variation of the deposition time and the composition of the deposition baths. Under the constant voltage condition, the yield of the hydroxyapatite-chitosan composite

coatings showed a more-than-linear increase with the increasing HA particle concentration in suspension. A mathematical model describing the formation of the hydroxyapatite-chitosan composite deposits has been developed.

- VII. Nanocomposite HA–Ag–chitosan monolayer coatings and multilayer coatings containing individual HA–chitosan and Ag–chitosan layers have been electrochemically deposited on various conductive substrates. The thickness of the multilayer coatings can be varied in the range of 0–20  $\mu\text{m}$  by the variation of the deposition time for individual layers and by the variation of the number of different layers. Elemental analysis revealed that the  $\text{Ag}^+$  release rate from the Ag–chitosan layer in the layered structure can be reduced by the hydroxyapatite–chitosan layer in the structure. The obtained results can be used for the development of biocompatible antimicrobial coatings with controlled  $\text{Ag}^+$  release rate.
- VIII. Novel hydroxyapatite- $\text{CaSiO}_3$ -chitosan nanocomposite coatings with enhanced bioactivity have been electrophoretically deposited as monolayers and laminates. Experimental results demonstrated the possibility of the fabrication of advanced composite coatings of graded composition and laminate structure. The use of chitosan enables the cathodic electrophoretic deposition of layers of different materials and a good interfacial bonding of layers.
- IX. Electrochemical studies have shown that the obtained composite coatings provided corrosion protection of the implant metal substrates in the Ringer's

physiological solutions.

## **5.2 Suggestions for future work**

The research in this work has been focused on the selection/design of new coating materials and structures, and the development of new deposition strategies for the fabrication of the novel coatings. Major efforts have been put on exploring the possibility to codeposit different functional materials, formulating new coating designs, controlling the formation of deposits of excellent qualities, and understanding the deposition mechanisms. Further investigations should be focused on the optimization of deposition conditions and properties of the coatings for their applications on biomedical implants. This may include the investigations on:

- I. The optimum concentrations of the polyelectrolyte additives and deposition conditions for fabrication of the  $ZrO_2$  ceramic and composite coatings with excellent corrosion and wear resistance;
- II. Characterization of the mechanical properties (e.g. adhesion strength) of the developed coatings using ASTM standard testing methods;
- III. In vitro and in vivo characterization of the bioactivities of the functional HA-chitosan composite coatings;
- IV. Optimization of composition and structure of the multilayer coatings and laminates of graded compositions, in terms of adhesion strength, antimicrobial properties, and surface bioactivities.

- V. Development of new coating designs (e.g. dual/multilayer coatings containing a  $ZrO_2$  bottom layer to provide corrosion protection and a HA-chitosan top layer to enhance bioactivities;
- VI. Incorporation of new materials with other functionalities (e.g. proteins for drug delivery) into the developed coatings.

## References

- Abolmaali, S. B. and Talbot, J. B. (1993). "Synthesis of Superconductive Thin Films of  $\text{YBa}_2\text{Cu}_3\text{O}_{7-x}$  by a Nonaqueous Electrodeposition Process." J. Electrochem. Soc. **140** (1): 443-445.
- Ahearn, D. G., May, L. L. and Gabriel, M. M. (1995). "Adherence of organisms to silver-coated surfaces." J. Ind. Microbiol. Biotechnol. **15** (4): 372-376.
- Allan, C. R. and Hadwiger, L. A. (1979). Exp. Mycol **3**: 285.
- Andrews, J. M., Collins, A. H., Cornish, D. C. and Dracass, J. (1969). Proc. Brit. Ceram. Soc. **12**: 211.
- Aries, L., Roy, J., Hajjaji, S. E., Alberich, L., Hernandez, P. V., Costeseque, P. and Aigouy, T. (1998). "Preparation and High-Temperature Behaviour of Electrolytic Alumina Film on Fe-Cr-Al Stainless Steel." J. Mater. Sci. **33**: 429-433.
- Aslam, M., Pethkar, S., Bandyopadhyay, K., Mulla, I. S., Sainkar, S. R., Mandale, A. B. and Vijayamohan, K. (2000). "Preparation, Characterization and Mechanistic Features of Zirconia Films on Bare and Functionalized Gold Surfaces." J. Mater. Chem. **10** (7): 1737-1743.
- Aza, P. N. D., Guitian, F. and Aza, S. D. (1996). "Morphological studies of pseudowollastonite for biomedical application." J. Microsc. **182**: 24-31.
- Baklouti, S., Pagnoux, C., Chartier, T. and Baumard, J. F. (1997). "Processing of Aqueous  $\text{Al}_2\text{O}_3$ ,  $\text{SiO}_2$  and  $\text{SiC}$  Suspensions with Polyelectrolytes." J. Eur. Ceram. Soc. **17**: 1387-1392.
- Bambauer, R., Mestres, P., Pirrung, K. J. and Sioshansi, P. (1994). Artif. Organs **18** (4): 272.
- Bartkowiak, A. and Hunkeler, D. (1999). "Alginate-Oligochitosan Microcapsules: A Mechanistic Study Relating Membrane and Capsule Properties to Reaction Conditions." Chem. Mater. **11**: 2486-2492.
- Beecroft, L. L. and Ober, C. K. (1997). "Nanocomposite Materials for Optical Applications." Chem. Mater. **9** (6): 1302-1317.
- Bégin, A. and Calsteren, M.-R. V. (1999). "Antimicrobial Films Produced from Chitosan." Int. J. Biol. Macromol. **26**: 63-67.
- Besra, L. and Liu, M. (2007). "A review on fundamentals and applications of

- electrophoretic deposition (EPD)." Progress in Materials Science **52**: 1-61.
- Biesheuvel, P. M. and Verweij, H. (1999). "Theory of cast formation in electrophoretic deposition." J. Am. Ceram. Soc. **82** (6): 1451-1455.
- Biest, O. V. d. and Vandeperre, L. J. (1999). "Electrophoretic Deposition of Materials." Annual Review of Materials Science **29**: 327-352.
- Boccaccini, A. R. and Trusty, P. A. (1998). "Electrophoretic Deposition Infiltration of Metallic Fabrics with a Boehmite Sol for the Preparation Ductile-Phase-Toughened Ceramic Composites." J. Mater. Sci. **33** (4): 933-938.
- Boccaccini, A. R. and Zhitomirsky, I. (2002a). "Application of Electrophoretic and Electrolytic Deposition Techniques in Ceramics Processing." Current Opinion in Solid State and Materials Science **6** (3): 251-260.
- Boccaccini, A. R. and Zhitomirsky, I. (2002b). "Application of electrophoretic and electrolytic deposition techniques in ceramics processing." Curr. Opin. Solid State Mater. Sci. **6**: 251-260.
- Bouyer, E., Gitzhofer, F. and Boulos, M. I. (2000). "Morphological study of hydroxyapatite nanocrystal suspension." J. Mater. Sci: Mater. Med. **11** (8): 523-531.
- Bouyer, F. and Foissy, A. (1999). J. Am. Ceram. Soc. **82**: 2001.
- Brown, D. R. and Salt, F. W. (1965). J. Appl. Chem. **15**: 40.
- Brown, P. W. and Constantz, B., Eds. (1994). Hydroxyapatite and Related Materials. Boca Raton, Ann Arbor, London, Tokyo, CRC Press.
- Cassagneau, T. and Fendler, J. H. (1998). "High Density Rechargeable Lithium-Ion Batteries Self-Assembled from Graphite Oxide Nanoplatelets and Polyelectrolytes." Adv. Mater. **10** (11): 877-881.
- Cassagneau, T., Fendler, J. H. and Mallouk, T. E. (2000a). "Optical and Electrical Characterizations of Ultrathin Films Self-Assembled from 11-Aminoundecanoic Acid Capped TiO<sub>2</sub> Nanoparticles and Polyallylamine Hydrochloride." Langmuir **16** (1): 241-246.
- Cassagneau, T., Guérin, F. and Fendler, J. H. (2000b). "Preparation and Characterization of Ultrathin Films Layer-by-Layer Self-Assembled from Graphite Oxide Nanoplatelets and Polymers." Langmuir **16** (18): 7318-7324.
- Chaim, R., Silberman, I. and Gal-Or, L. (1991). "Electrolytic ZrO<sub>2</sub> Coatings II. Microstructural Aspects." J. Electrochem. Soc. **138** (7): 1942-1946.
- Chaim, R., Stark, G., Gal-Or, L. and Bestgen, H. (1994). "Electrochemical ZrO<sub>2</sub> and

Al<sub>2</sub>O<sub>3</sub> Coatings on SiC Substrates." J. Mater. Sci. **29**: 6241-6248.

Chaim, R., Zhitomirsky, I., Gal-Or, L. and Bestgen, H. (1997). "Electrochemical Al<sub>2</sub>O<sub>3</sub>-ZrO<sub>2</sub> Composite Coatings on Non-Oxide Ceramic Substrates." J. Mater. Sci. **32**: 389-400.

Chen, J.-S., Juang, H.-Y. and Hon, M.-H. (1998). "Calcium phosphate coating on titanium substrate by a modified electrocrystallization process." J. Mater. Sci. Mater. Med. **9** (5): 297-300.

Chen, W. C., Bao, C. Y., Jeyachandran, Y. L., Ou, G. M., Fan, H. S., Liao, Y. M. and Zhang, X. D. (2007). "Exploring antibacterial and antiadhesive activities of titanium surface modified with hydroxyapatite sol-gel containing silver." Key Eng. Mater. **330-332 I**: 653-656.

Cho, S.-B., Miyaji, F., Kokubo, T., Nakanishi, K., Soga, N. and Nakamura, T. (1996). "Apatite-forming ability of silicate ion dissolved from silica gels." J. Biomed. Mater. Res. **32** (3): 375-381.

Christensen, F. B., Dalstra, M., Sejling, F., Overgaard, S. and Bunger, C. (2000). "Titanium-alloy enhances bone-pedicle screw fixation: mechanical and histomorphometrical results of titanium-alloy versus stainless steel." Eur. Spine. J. **9** (2): 97-103.

Chu, X. L., Nikolov, A. D. and Wasan, D. T. (1995). "Thin liquid film structure and stability: The role of depletion and surface-induced structural forces." J. Chem. Phys. **103** (15): 6653-6661.

Chung, R.-J., Hsieh, M.-F., Huang, C.-W., Perng, L.-H., Wen, H.-W. and Chin, T.-S. (2006). "Antimicrobial effects and human gingival biocompatibility of hydroxyapatite sol-gel coatings." J. Biomed. Mater. Res. B **76** (1): 169-178.

Clark, S. L. and Hammond, P. T. (1998). "Engineering the Microfabrication of Layer-by-Layer Thin Films." Adv. Mater. **10** (18): 1515-1519.

Clark, S. L. and Hammond, P. T. (2000). "The Role of Secondary Interactions in Selective Electrostatic Multilayer Deposition." Langmuir **16** (26): 10206-10214.

Clearfield, A. (1964). "Crystalline Hydrated Zirconia." Inorg. Chem. **3** (1): 146-148.

Clearfield, A. (1990). "The Mechanism of Hydrolytic Polymerization of Zirconyl Solutions." J. Mater. Res. **5** (1): 161-162.

Collings, E. W. (1984). The physical metallurgy of titanium alloys. Cleveland, Metals Park, OH, American Society for Metals.

Collins, D. E. and Slamovich, E. B. (1999). "Preparation of a Homogeneously

Dispersed BaTiO<sub>3</sub>/Polymer Nanocomposite Thin Film." Chem. Mater. **11** (9): 2319-2321.

Cordingley, R., Kohan, L., Ben-Nissan, B. and Pezzotti, G. (2003). "Zirconia and Partially Stabilised Zirconia as an Orthopaedic Biomaterial - Characteristics, Properties, Performance and Applications." Journal of the Australasian Ceramic Society **39** (1): 20-28.

Cui, F. Z., Wen, H. B. and Su, X. W. (1996). "Microstructures of external periosteal callus of repaired femoral fracture in children." J. Struct. Biol. **117**: 204-208.

Damodaran, R. and Moudgil, B. M. (1993). "Electrophoretic deposition of calcium phosphates from non-aqueous media." Colloid Surf. A **80** (2-3): 191-195.

Dante, S., Hou, Z., Risbud, S. and Stroeve, P. (1999). "Nucleation of Iron Oxy-Hydroxide Nanoparticles by Layer-by-Layer Polyionic Assemblies." Langmuir **15** (6): 2176-2182.

Decher, G. (1997). "Fuzzy Nanoassemblies: Toward Layered Polymeric Multicomposites." Science **277** (8): 1232-1237.

Decher, G. and Hong, J. D. (1991). Macromol. Chem., Macromol. Symp. **46**: 321.

Demri, B., Hage-Ali, M., Moritz, M. and Muster, D. (1997). "Surface Characterization of C/Ti6Al4V Coating Treated with Ion Beam." Biomaterials **18**: 305-310.

Dickinson, E. and Eriksson, L. (1991). "Particle flocculation by adsorbing polymers." Adv. Colloid Interface Sci. **34**: 1-29.

Disegi, J. A. and Eschbach, L. (2000). "Stainless Steel in Bone Surgery." Injury **31** (S4): 4-6.

Dorozhkin, S. V. and Epple, M. (2002). "Biological and medical significance of calcium phosphates." Angew. Chem. Int. Ed. **41**: 3130-3146.

Dubas, S. T. and Schlenoff, J. B. (1999). "Factors Controlling the Growth of Polyelectrolyte Multilayers." Macromolecules **32**: 8153-8160.

Ducheyne, P., Kim, C. S. and Pollack, S. R. (1992). "Effect of phase differences on the time-dependent variation of the zeta potential of hydroxyapatite." J. Biomed. Mater. Res. **26** (2): 147-168.

Ducheyne, P., Martens, M., Meester, P. D. and Mulier, J. C. (1981). Titanium Implants with Porous Structures for Bone Ingrowth: A General Approach. Titanium alloys in surgical implants : a symposium sponsored by ASTM Committee F-4 on Medical and Surgical Materials and Devices and ASTM Committee B-10 on Reactive and Refractory Metals and Alloys, Phoenix, Arizona, Philadelphia, Pa. (1916 Race St.,

Philadelphia, Pa., 19103) : American Society for Testing and Materials, 1983.

Ducheyne, P., Radin, S., Heughebaert, M. and Heughebaert, J. C. (1990). "Calcium Phosphate Ceramic Coatings on Porous Titanium: Effect of Structure and Composition on Electrophoretic Deposition, Vacuum Sintering and in Vitro Dissolution." Biomaterials **11**: 244-254.

Ducheyne, P., Raemdonck, W. V., Heughebaert, J. C. and Heughebaert, M. (1986). "Structural Analysis of Hydroxyapatite Coatings on Titanium." Biomaterials **7**: 97-103.

Dutta, A. K., Ho, T., Zhang, L. and Stroeve, P. (2000a). "Nucleation and Growth of Lead Sulfide Nano- and Microcrystallites in Supramolecular Polymer Assemblies." Chem. Mater. **12** (4): 1042-1048.

Dutta, A. K., Jarero, G., Zhang, L. and Stroeve, P. (2000b). "In-Situ Nucleation and Growth of Gamma-FeOOH Nanocrystallites in Polymeric Supramolecular Assemblies." Chem. Mater. **12** (1): 176-181.

Elliot, J. C. (1994). Structure and Chemistry of the Apatites and Other Calcium Orthophosphates. Amsterdam, Elsevier.

Ennis, J., Sjöström, L., Åkesson, T. and Jönsson, B. (2000). "Surface interactions in the presence of polyelectrolytes. a simple theory." Langmuir **16** (18): 7116-7125.

Espitia-Cabrera, I., Orozco-Hernández, H., Torres-Sánchez, R., Contreras-García, M. E., Bartolo-Pérez, P. and Martínez, L. (2003). "Synthesis of Nanostructured Zirconia Electrodeposited Films on AISI 316L Stainless Steel and Its Behaviour in Corrosion Resistance Assessment." Mater. Lett. **58**: 191-195.

Fang, M., Kim, C. H. and Mallouk, T. E. (1999a). "Dielectric Properties of the Lamellar Niobates and Titanoniobates  $AM_2Nb_3O_{10}$  and  $ATiNbO_5$  (A=H, K, M=Ca, Pb), and Their Condensation Products  $Ca_4Nb_6O_{19}$  and  $Ti_2Nb_2O_9$ ." Chem. Mater. **11** (6): 1519-1525.

Fang, M., Kim, C. H., Saupe, G. B., Kim, H.-N., Waraksa, C. C., Miwa, T., Fujishima, A. and Mallouk, T. E. (1999b). "Layer-by-Layer Growth and Condensation Reactions of Niobate and Titanoniobate Thin Films." Chem. Mater. **11** (6): 1526-1532.

Feldheim, D. L., Grabar, K. C., Natan, M. J. and Mallouk, T. E. (1996). "Electron Transfer in Self-Assembled Inorganic Polyelectrolyte/Metal Nanoparticle Heterostructures." J. Am. Chem. Soc. **118** (32): 7640-7641.

Feng, Q. L., Kim, T. N., Wu, J., Park, E. S., Kim, J. O., Lim, D. Y. and Cui, F. Z. (1998). "Antibacterial Effects of Ag-HAp Thin Films on Alumina Substrates." Thin Solid Films **335**: 214-219.

Foissy, A. A. and Robert, G. (1982). Bull. Am. Ceram. Soc. **61**: 251.

- Fojas, A. M., Murphy, E. and Stroeve, P. (2002). "Layer-by-Layer Polymeric Supramolecular Structures Containing Nickel Hydroxide Nanoparticles and Microcrystallites." Ind. Eng. Chem. Res. **41** (11): 2662-2667.
- Gal-Or, L., Silberman, I. and Chaim, R. (1991). "Electrolytic ZrO<sub>2</sub> Coatings I. Electrochemical Aspects." J. Electrochem. Soc. **138** (7): 1939-1942.
- Gangopadhyay, R. and De, A. (2000). "Conducting Polymer Nanocomposites: A Brief Overview." Chem. Mater. **12** (3): 608-622.
- Geckeler, K. E. and Volchek, K. (1996). "Removal of Hazardous Substances from Water Using Ultrafiltration in Conjunction with Soluble Polymers." Environ. Sci. Technol. **30** (3): 725-733.
- Geros, R. Z. L. and Craig, R. G. (1993). "Strategies to Affect Bone Remodeling: Osteointegration." J. Bone Miner. Res. **8**: S583-596.
- Gou, Z. and Chang, J. (2004). "Synthesis and in vitro bioactivity of dicalcium silicate powders." J. Eur. Ceram. Soc. **24** (1): 93-99.
- Groot, K. d. (1980). "Bioceramics Consisting of Calcium Phosphate Salts." Biomaterials **1**: 47-50.
- Groot, K. d. (1983). Bioceramics of Calcium-Phosphate. Boca Raton, FL, CRC Press.
- Groot, K. d. (1988). Effect of porosity and physicochemical properties on the stability, resorption, and strength of calcium phosphate ceramics. Bioceramics: Materials Characteristics Versus In Vivo Behavior. Ducheyne, P. and Lemons, J. New York, Annals of New York Academy of Science. **523**: 227-234.
- Hamaker, H. C. (1940). "Formation of a deposit by electrophoresis." Trans. Faraday Soc. **36**: 279-283.
- Hamaker, H. C. and Verwey, E. J. W. (1940). Trans. Faraday Soc. **36**: 180.
- Harbach, F. and Nienburg, H. (1998). "Homogeneous functional ceramic components through electrophoretic deposition from stable colloidal suspensions—I. Basic concepts and application to zirconia." J. Eur. Ceram. Soc. **18** (6): 675-683.
- Hayashi, S., Nakagawa, Z.-e., Yasumori, A. and Okada, K. (1999). "Effects of H<sub>2</sub>O in EtOH-H<sub>2</sub>O disperse medium on the electrophoretic deposition of CaSiO<sub>3</sub> fine powder." J. Eur. Ceram. Soc. **19** (1): 75-79.
- Hazar, A. B. Y. (2007). "Preparation and in vitro bioactivity of CaSiO<sub>3</sub> powders." Ceramics International **33** (4): 687-692.

- Heavens, S. N. (1990). Electroforetic Deposition as a Processing Route for Ceramics. Advanced Ceramic Processing and Technology. Binner, J. G. P. Park Ridge, New Jersey, Noyes Publications. **7**: 255-283.
- Hench, L. L. (1998). "Bioceramics." J. Am. Ceram. Soc. **81** (7): 1705-1728.
- Hench, L. L. and Paschall, H. A. (1973). "Direct chemical bonding between bioactive glass-ceramic materials and bone." J. biomed. Mater. Res. Symp. **4**: 25-42.
- Hench, L. L., Splinter, R. J., Allen, W. C. and Greenlee Jr., T. K. (1971). "Bonding mechanisms at the interface of ceramic prosthetic materials." J. Biomed. Mater. Res. **2** (1): 117-141.
- Hirata, Y., Nishimoto, A. and Ishihara, Y. (1991). "Forming of alumina powder by electrophoretic deposition." Nippon Seramikkusu Kyokai Gakujutsu Ronbunshi **99** (2): 108-113.
- Hoffmann, U., Kwait, D. C., Handwerker, J., Chan, R., Lamuraglia, G. and Brady, T. J. (2003). "Vascular Calcification in ex Vivo Carotid Specimens: Precision and Accuracy of Measurements with Multi-Detector Row CT." Radiology **229**: 375-381.
- Hoogeveen, N. G., Stuart, M. A. C. and Fleer, G. J. (1996a). "Polyelectrolyte Adsorption on Oxides I. Kinetics and Adsorbed Amounts." J. Colloid Interface Sci. **182**: 133-145.
- Hoogeveen, N. G., Stuart, M. A. C. and Fleer, G. J. (1996b). "Polyelectrolyte Adsorption on Oxides II. Reversibility and Exchange." J. Colloid Interface Sci. **182**: 146-157.
- Hsieh, M.-F., Perng, L.-H. and Chin, T.-S. (2002). "Hydroxyapatite coating on Ti6Al4V alloy using a sol-gel derived precursor." Mater. Chem. Phys. **74** (3): 245-250.
- Huang, C., Tang, Z. and Zhang, Z. (2001). "Differences between Zirconium Hydroxide ( $Zr(OH)_4 \cdot nH_2O$ ) and Hydrous Zirconia ( $ZrO_2 \cdot nH_2O$ )." J. Am. Chem. Soc. **84** (7): 1637-1638.
- Hughes, A. E., Taylor, R. J., Hinton, B. R. W. and Wilson, L. (1995). Surf. Interface Anal. **23**: 540.
- Hunter, R. J. (1981). Zeta potential in colloid science. London, Academic Press.
- Ishihara, T., Sato, K. and Takita, Y. (1996). "Electrophoretic Deposition of  $Y_2O_3$ -Stabilized  $ZrO_2$  Electrolyte Films in Solid Oxide Fuel Cells." J. Am. Ceram. Soc. **79** (4): 913-919.
- Janes, K. A., Fresneau, M. P., Marazuela, A., Fabra, A. and Alonso, M. J. (2001). "Chitosan Nanoparticles as Delivery Systems for Doxorubicin." J. Controlled Release

73: 255-267.

Jiang, X. and Hammond, P. T. (2000). "Selective Deposition in Layer-by-Layer Assembly: Functional Graft Copolymers as Molecular Templates." Langmuir **16** (22): 8501-8509.

Jones, S. L. and Norman, C. J. (1988). "Dehydration of Hydrous Zirconia with Methanol." Commun. Am. Ceram. Soc. **71** (4): C190-C191.

Kannan, S., Balamurugan, A. and Rajeswari, S. (2003). "Hydroxyapatite coatings on sulfuric acid treated type 316L SS and its electrochemical behaviour in Ringer's solution." Mater. Lett. **57** (16-17): 2382-2389.

Kannan, S., Balamurugan, A. and Rajeswari, S. (2005). "Electrochemical Characterization of Hydroxyapatite Coatings on HNO<sub>3</sub> Passivated 316L SS for Implant Applications." Electrochim. Acta **50**: 2065-2072.

Kannan, S., Balamurugan, A., Rajeswari, S. and Subbaiyan, M. (2002). "Metallic Implants-An Approach for Long Term Applications in Bone Related Defects." Corros. Rev. **20** (4-5): 339-358.

Kasemo, B. and Lausmaa, J. (1988). "Biomaterial and Implant Surfaces: A Surface Science Approach." Int. J. Oral Maxillofac. Implants **3**: 247-259.

Kaya, C., Boccaccini, A. R. and Trusty, P. A. (1999). "Processing and Characterisation of 2-D Woven Metal Fibre-reinforced Multilayer Silica Matrix Composites Using Electrophoretic Deposition and Pressure Filtration." J. Eur. Ceram. Soc. **19**: 2859-2866.

Keller, S. W., Kim, H.-N. and Mallouk, T. E. (1994). "Layer-by-Layer Assembly of Intercalation Compounds and Heterostructures on Surfaces: Toward Molecular "Beaker" Epitaxy." J. Am. Chem. Soc. **116** (19): 8817-8818.

Kikuchi, M., Ikoma, T., Itoh, S., Matsumoto, H. N., Koyama, Y., Takakuda, K., Shinomiya, K. and Tanaka, J. (2004). "Biomimetic synthesis of bone-like nanocomposites using the self-organization mechanism of hydroxyapatite and collagen." Compos. Sci. Technol. **64** (6): 819-825.

Kim, C. S. and Ducheyne, P. (1991). "Compositional Variations in the Surface and Interface of Calcium Phosphate Ceramic Coatings on Ti and Ti-6Al-4V due to Sintering and Immersion." Biomaterials **12** (5): 461-469.

Kim, T. N., Feng, Q. L., Kim, J. O., Wu, J., Wang, H., Chen, G. C. and Cui, F. Z. (1998). "Antimicrobial Effects of Metal Ions (Ag<sup>+</sup>, Cu<sup>2+</sup>, Zn<sup>2+</sup>) in Hydroxyapatite." J. Mater. Sci: Mater. Med. **9**: 129-134.

Kitsugi, T., Yamamuro, T. and Kokubo, T. (1989). "Bonding behavior of a glass-ceramic containing apatite and wollastonite in segmental replacement of the

rabbit tibia under load-bearing conditions." Journal of Bone and Joint Surgery **71A**: 264.

Kleinfeld, E. R. and Ferguson, G. S. (1995). "Rapid, Reversible Sorption of Water from the Vapor by a Multilayered Composite Film: A Nanostructured Humidity Sensor." Chem. Mater. **7** (12): 2327-2331.

Kleinfeld, E. R. and Ferguson, G. S. (1996). "Healing of Defects in the Stepwise Formation of Polymer/Silicate Multilayer Films." Chem. Mater. **8** (8): 1575-1578.

Kobayashi, S., Hiroishi, K., Tokunoh, M. and Saegusa, T. (1987). "Chelating Properties of Linear and Branched Poly(ethylenimines)." Macromolecules **20**: 1496-1500.

Kobayashi, S., Tokunoh, M., Saegusa, T. and Mashio, F. (1985). "Poly(allylamine): Chelating Properties and Resins for Uranium Recovery from Seawater." Macromolecules **18**: 2357-2361.

Kokubo, T., Kushitani, H., Ohtsuki, C., Sakka, S. and Yamamuro, T. (1993). "Effects of ions dissolved from bioactive glass-ceramic on surface apatite formation." J. Mater. Sci: Mater. Med. **4** (1): 1-4.

Kosmulski, M., Durand-Vidal, S., Gustafsson, J. and Rosenholm, J. B. (1999). "Charge interactions in semi-concentrated titania suspensions at very high ionic strengths." Colloid Surf. A **157** (1-3): 245-259.

Koutsopoulos, S. (2002). "Synthesis and Characterization of Hydroxyapatite Crystals: A Review Study on the Analytical Methods." J. Biomed. Mater. Res. **62** (4): 600-612.

Kralchevsky, P. A. and Nagayama, K. (1994). Langmuir **10**: 23.

Kuhn, A. T. and Chan, C. Y. (1983). "PH Changes at Near-Electrode Surfaces." J. Appl. Electrochem. **13**: 189-207.

Kuwabara, K., Sugiyama, K. and Ohno, M. (1991). "All-solid-state electrochromic device. 1. Electrophoretic deposition film of proton conductive solid electrolyte." Solid State Ionics **44** (3-4): 313-318.

Labib, M. E. and Williams, R. (1984). "The use of zeta-potential measurements in organic solvents to determine the donor-acceptor properties of solid surfaces." J. Colloid Interface Sci. **97** (2): 356-366.

Larsen, A. E. and Grier, D. G. (1997). "Like-charge attractions in metastable colloidal crystallites." Nature **385**: 230-233.

Lavrov, I. S. and Smirnov, O. V. (1969). J. Appl. Chem. USSR **42**: 1459.

Lee, B.-T., Shin, N.-Y., Han, J.-K. and Song, H.-Y. (2006a). "Microstructures and

fracture characteristics of spark plasma-sintered HAp-5 vol.% Ag composites." Mater. Sci. Eng. A **429** (1-2): 348-352.

Lee, I.-S., Whang, C.-N., Oh, K.-S., Park, J.-C., Lee, K.-Y., Lee, G.-H., Chung, S.-M. and Sun, X.-D. (2006b). "Formation of silver incorporated calcium phosphate film for medical applications." Nucl. Instrum. Methods Phys. Res. B **242**: 45-47.

LeGeros, R. Z. and LeGeros, J. P. (1993). Dense Hydroxyapatite. An Introduction to Bioceramics. Hench, L. L. and Wilson, J. London, U.K., World Scientific: 139.

Ligler, F. S., Lingerfelt, B. M., Price, R. P. and Schoen, P. E. (2001). "Development of Uniform Chitosan Thin-Film Layers on Silicon Chips." Langmuir **17** (16): 5082-5084.

Lim, L. Y. and Wan, L. S. C. (1995). "Heat Treatment of Chitosan Films." Drug Dev. Ind. Pharm. **21** (7): 839-846.

Limmer, S. J., Seraji, S., Wu, Y., Chou, T. P., Nguyen, C. and Cao, G. (2002). "Template-Based Growth of Various Oxide Nanorods by Sol-Gel Electrophoresis." Adv. Funct. Mater. **12** (1): 59-64.

Lin, F.-H., Hsu, Y.-S., Lin, S.-H. and Chen, T.-M. (2004). "The growth of hydroxyapatite on alkaline treated Ti-6Al-4V soaking in higher temperature with concentrated  $\text{Ca}^{2+}/\text{HPO}_4^{2-}$  simulated body fluid." Mater. Chem. Phys. **87** (1): 24-30.

Liu, X., Chu, P. K. and Ding, C. (2004a). "Surface Modification of Titanium, Titanium Alloys, and Related Materials for Biomedical Applications." Mater. Sci. Eng. R **47**: 49-121.

Liu, X., Ding, C. and Wang, Z. (2001). "Apatite formed on the surface of plasma-sprayed wollastonite coating immersed in simulated body fluid." Biomaterials **22** (14): 2007-2012.

Liu, X., Tao, S. and Ding, C. (2003). "Bioactivity of plasma sprayed dicalcium silicate coatings." Biomaterials **23** (3): 963-968.

Liu, Y., Hou, D. and Wang, G. (2004b). "A simple wet chemical synthesis and characterization of hydroxyapatite nanorods." Mater. Chem. Phys. **86** (1): 69-73.

Liu, Y., Wang, A. and Claus, R. O. (1997). "Layer-by-Layer Electrostatic Self-Assembly of Nanoscale  $\text{Fe}_3\text{O}_4$  Particles and Polyimide Precursor on Silicon and Silica Surfaces." Appl. Phys. Lett. **71** (16): 2265-2267.

Long, M. and Rack, H. J. (1998). "Titanium alloys in total joint replacement - a materials science perspective." Biomaterials **19**: 1621-1639.

Lvov, Y., Ariga, K., Ichinose, I. and Kunitake, T. (1996). "Formation of Ultrathin Multilayer and Hydrated Gel from Montmorillonite and Linear Polycations." Langmuir

12 (12): 3038-3044.

Lvov, Y., Munge, B., Giraldo, O., Ichinose, I., Suib, S. L. and Rusling, J. F. (2000). "Films of Manganese Oxide Nanoparticles with Polycations or Myoglobin from Alternate-Layer Adsorption." Langmuir **16** (23): 8850-8857.

Matsuda, Y., Imahashi, K., Yoshimoto, N., Morita, M. and Haga, M. (1993). "Formation of yttrium oxide by electrodeposition in organic electrolyte." J. Alloys Compd. **193** (1-2): 277-279.

Mizuguchi, J., Sumi, K. and Muchi, T. (1983). "A Highly Stable Nonaqueous Suspension for the Electrophoretic Deposition of Powdered Substances." J. Electrochem. Soc. **130** (9): 1819-1825.

Moreno, R. and Ferrari, B. (2000). "Advanced Ceramics via EPD of Aqueous Slurries." Am. Ceram. Soc. Bull. **79** (1): 44-48.

Moroni, A., Orienti, L., Stea, S., Visentin, M. and Giannini, S. (1997). "Hydroxyapatite Coated Stainless-Steel External Fixation Pins." Mater. Sci. Forum **250**: 231-238.

Mukherjee, A., Harrison, D. and Podlaha, E. J. (2001). "Electrosynthesis of Nanocrystalline Ceria-Zirconia." Electrochem. Solid-State Lett. **4** (9): D5-D7.

Muzzarelli, R. A. A., Biagini, G., DeBenedittis, A., Mengucci, P., Majni, G. and Tosi, G. (2001). "Chitosan-Oxychitin Coatings for Prosthetic Materials." Carbohydr. Polym. **45**: 35-41.

Nakamura, T., Yamamuro, T., Higashi, S., Kokubo, T. and Itoo, S. (1985). "A new glass-ceramic for bone replacement: evaluation of its bonding to bone tissue." J. Biomed. Mater. Res. **19**: 685.

Ngankam, P. A., Lavalley, P., Voegel, J. C., Szyk, L., Decher, G., Schaaf, P. and Cuisinier, F. J. G. (2000). "Influence of Polyelectrolyte Multilayer Films on Calcium Phosphate Nucleation." J. Am. Chem. Soc. **122** (37): 8998-9005.

Ni, S., Chang, J. and Chou, L. (2006). "A novel bioactive porous CaSiO<sub>3</sub> scaffold for bone tissue engineering." Journal of Biomedical Materials Research - Part A **76** (1): 196-205.

Nicholson, P. S., Sarkar, P. and Haung, X. (1993). "Electrophoretic deposition and its use to synthesize ZrO<sub>2</sub>/Al<sub>2</sub>O<sub>3</sub> micro-laminate ceramic/ceramic composites." J. Mater. Sci. **28** (23): 6274-6278.

Nunthanid, J., Puttipipatkachorn, S., Yamamoto, K. and Peck, G. E. (2001). "Physical Properties and Molecular Behavior of Chitosan Films." Drug Dev. Ind. Pharm. **27** (2): 143-157.

Oh, K.-S., Park, S.-H. and Jeong, Y.-K. (2004). "Durability in Antimicrobial Effects of Silver Doped Hydroxyapatite Depending on the Synthesis Route." Mater. Sci. Forum **449-452**: 1233-1236.

Ohshima, H. (1994). "Electrophoretic Mobility of Soft Particles." J. Colloid Interface Sci. **163** (2): 474-483.

Ohshima, H. (1995). "Electrophoretic Mobility of Soft Particles." Colloid Surf. A **103**: 249-255.

Ohshima, H. (2000). "On the General Expression for the Electrophoretic Mobility of a Soft Particle." J. Colloid Interface Sci. **228** (1): 190-193.

Okubo, T. and Suda, M. (1999). "Absorption of polyelectrolytes on colloidal surfaces as studied by electrophoretic and dynamic light-scattering techniques." J. Colloid Interface Sci. **213** (2): 565-571.

Paik, U., Hackley, V. A., Choi, S.-C. and Jung, Y.-G. (1998). "The effect of electrostatic repulsive forces on the stability of BaTiO<sub>3</sub> particles suspended in non-aqueous media." Colloid Surf. A **135** (1-3): 77-88.

Pan, J., Leygraf, C., Thierry, D. and Ektessabi, A. M. (1997). "Corrosion resistance for biomaterial applications of TiO<sub>2</sub> films deposited on titanium and stainless steel by ion-beam-assisted sputtering." J. Biomed. Mater. Res. **35** (3): 309-318.

Pang, X. and Zhitomirsky, I. (2004). "Fabrication of composite films containing zirconia and cationic polyelectrolytes." Langmuir **20** (7): 2921-2927.

Pang, X. and Zhitomirsky, I. (2005a). "Electrodeposition of composite hydroxyapatite-chitosan films." Mater. Chem. Phys. **94** (2-3): 245-251.

Pang, X. and Zhitomirsky, I. (2005b). "Electrodeposition of nanocomposite organic-inorganic coatings for biomedical applications." Int. J. Nanosci. **4** (3): 409-418.

Pang, X. and Zhitomirsky, I. (2007). "Electrophoretic deposition of composite hydroxyapatite-chitosan coatings." Materials Characterization **58** (4): 339-348.

Pang, X. and Zhitomirsky, I. (2008). "Electrodeposition of hydroxyapatite-silver-chitosan nanocomposite coatings." Surf. Coat. Technol. **202**: 3815-3821.

Pang, X., Zhitomirsky, I. and Niewczas, M. (2005c). "Cathodic Electrolytic Deposition of Zirconia." Surf. Coat. Technol. **195**: 138-146.

Parks, G. A. (1965). "The Isoelectric Points of Solid Oxides, Solid Hydroxides, and Aqueous Hydroxo Complex Systems." Chem. Rev. **65**: 177-198.

Payne, G. F. (2007). "Biopolymer-based materials: the nanoscale components and their hierarchical assembly." Current Opinion in Chemical Biology **11**: 214-219.

Peulon, S. and Lincot, D. (1996). "Cathodic electrodeposition from aqueous solution of dense or open-structured zinc oxide films." Adv. Mater. **8** (2): 166-170.

Pfaff, H. G., Willmann, G. and Pothig, R. (1993). Bioceramics. Ducheyne, P. and Christiansen, D. London, Butterworth-Heinemann Ltd. **6**: 421.

Piconi, C. and Maccauro, G. (1999). "Review: Zirconia as a Ceramic Biomaterial." Biomaterials **20**: 1-25.

Pourrezaei, K., Shvets, I., DeLaurentis, M., Boxman, R. L., Beard, R. B., Croitoriu, N., Mukhtar, M., Logan, D. A. and Rastogi, R. (1994). "Development of antimicrobial and antithrombogenic coatings for inside and outside of medical catheters." Surf. Coat. Technol. **68-69**: 669-674.

Powers, R. W. (1975). "The Electrophoretic Forming of Beta-Alumina Ceramic." J. Electrochem. Soc. **122** (4): 490-500.

Raemdonck, W. V., Ducheyne, P. and Meester, P. D. (1984). "Auger Electron Spectroscopic Analysis of Hydroxyapatite Coatings on Titanium." J. Am. Ceram. Soc. **67**: 381-384.

Ray, J. C., Pramanik, P. and Ram, S. (2001). "A Novel Polymer Matrix Method for Synthesizing ZrO<sub>2</sub> Nanocrystals at Moderate Temperature." J. Mater. Sci. Lett. **20** (22): 2017-2019.

Redepenning, J., Venkataraman, G., Chen, J. and Stafford, N. (2003). "Electrochemical preparation of chitosan/hydroxyapatite composite coatings on titanium substrates." J. Biomed. Mater. Res. A **66** (2): 411-416.

Ruel-Gariépy, E., Chenite, A., Chaput, C., Guirguis, S. and Leroux, J.-C. (2000). "Characterization of Thermosensitive Chitosan Gels for the Sustained Delivery of Drugs." Int. J. Pharm. **203**: 89-98.

Ruff, O., Ebert, F. and Stephen, E. (1929). "Contributions to the Ceramics of Highly Refractory Materials: II. System Zirconia-Lime." Z. Anorg. Allg. Chem. **180** (1): 215-224.

Russ, B. E. and Talbot, J. B. (1998a). "An Analysis of the Binder Formation in Electrophoretic Deposition." J. Electrochem. Soc. **145** (4): 1253-1256.

Russ, B. E. and Talbot, J. B. (1998b). "A Study of the Adhesion of Electrophoretically Deposited Phosphors." J. Electrochem. Soc. **145** (4): 1245-1252.

Russel, A. D. and Hugo, W. B. (1994). Antimicrobial Activity and Action of Silver.

Proceedings in Medical Chemistry. Ellis, G. P. and Luscombe, D. K. **31**: 351-70.

Ryu, H.-S., Lee, J. K., Kim, H. and Hong, K. S. (2005). "New type of bioactive materials: Hydroxyapatite/alpha-wollastonite composites." J. Mater. Res. **20** (5): 1154-1163.

Sarkar, P. and Nicholson, P. S. (1996). "Electrophoretic deposition (EPD): mechanisms, kinetics, and application to ceramics." J. Am. Ceram. Soc. **79** (8): 1987-2002.

Sasaki, T., Ebina, Y., Tanaka, T., Harada, M. and Watanabe, M. (2001). "Layer-by-Layer Assembly of Titania Nanosheet/Polycation Composite Films." Chem. Mater. **13** (12): 4661-4667.

Schaak, R. E. and Mallouk, T. E. (2000). "Self-Assembly of Tiled Perovskite Monolayer and Multilayer Thin Films." Chem. Mater. **12** (9): 2513-2516.

Schmidt, C., Ignatius, A. and Claes, L. E. (2001). "Proliferation and Differentiation Parameters of Human Osteoblasts on Titanium and Steel Surfaces." J. Biomed. Mater. Res. **54**: 209-215.

Schultz, M., Grimm, S. and Burckhardt, W. (1993). "The isoelectric point of pure and doped zirconia in relation to the preparation route." Solid State Ionics **63-65**: 18-24.

Shchukin, D. G., Radtchenko, I. L. and Sukhorukov, G. B. (2003a). "Micron-Scale Hollow Polyelectrolyte Capsules with Nanosized Magnetic Fe<sub>3</sub>O<sub>4</sub> Inside." Mater. Lett. **57**: 1743-1747.

Shchukin, D. G., Radtchenko, I. L. and Sukhorukov, G. B. (2003b). "Synthesis of Nanosized Magnetic Ferrite Particles Inside Hollow Polyelectrolyte Capsules." J. Phys. Chem. B **107** (1): 86-90.

Shchukin, D. G., Sukhorukov, G. B. and Möhwald, H. (2003c). "Biomimetic Fabrication of Nanoengineered Hydroxyapatite/Polyelectrolyte Composite Shell." Chem. Mater. **15** (20): 3947-3950.

Shirkhanzadeh, M. (1998). "Direct Formation of Nanophase Hydroxyapatite on Cathodically Polarized Electrodes." J. Mater. Sci: Mater. Med. **9**: 67-72.

Shirkhanzadeh, M., Azadegan, M. and Liu, G. Q. (1995). "Bioactive Delivery Systems for the Slow Release of Antibiotics: Incorporation of Ag<sup>+</sup> Ions into Micro-Porous Hydroxyapatite Coatings." Mater. Lett. **24**: 7-12.

Silver, F. H. (1994). Biomaterials medical devices and tissue engineering: An integrated approach. London, Chapman & Hall.

Simonetti, N., Simonetti, G., Bougnol, F. and Scalzo, M. (1992). "Electrochemical Ag<sup>+</sup> for Preservative Use." Appl. Environ. Microbiol. **58** (12): 3834-3836.

- Sioshansi, P. (1994). Artif. Organs **18** (4): 266.
- Siracuse, J. A., Talbot, J. B., Sluzky, E. and Hesse, K. R. (1990). "The Adhesive Agent in Cataphoretically Coated Phosphor Screens." J. Electrochem. Soc. **137** (1): 346-348.
- Siriphannon, P., Kameshima, Y., Yasumori, A., Okada, K. and Hayashi, S. (2000). "Influence of preparation conditions on the microstructure and bioactivity of  $\alpha$ -CaSiO<sub>3</sub> ceramics: formation of hydroxyapatite in simulated body fluid." J. Biomed. Mater. Res. **52** (1): 30-39.
- Slawson, R. M., Vandyke, M. I., Lee, H. and Trevors, J. T. (1992). "Germanium and Silver Resistance, Accumulation, and Toxicity in Microorganisms." Plasmid **27**: 72-77.
- Smoluchowski, M. v. (1917). "Versuch einer mathematischen Theorie der Koagulationkinetik kolloider Loesungen." Z. Phys. Chem. **92**: 129-132.
- Sogami, I. and Ise, N. (1984). J. Chem. Phys. **81**: 6320.
- Sorlier, P., Denuzière, A., Viton, C. and Domard, A. (2001). "Relation between the Degree of Acetylation and the Electrostatic Properties of Chitin and Chitosan." Biomacromolecules **2** (3): 765-772.
- Sousa, S. R. and Barbosa, M. A. (1995). "The Effect of Hydroxyapatite Thickness on Metal Ion Release from stainless Steel Substrates." J. Mater. Sci. Mater. Med. **6**: 818-823.
- Souto, R. M., Laz, M. M. and Reis, R. L. (2003). "Degradation characteristics of hydroxyapatite coatings on orthopaedic TiAlV in simulated physiological media investigated by electrochemical impedance spectroscopy." Biomaterials **24** (23): 4213-4221.
- Spardaro, J. A., Chase, S. E. and Webster, D. A. (1986). "Bacterial Inhibition by Electrical Activation of Percutaneous Silver Implants." J. Biomed. Mater. Res. **20**: 565-577.
- Sridhar, T. M., Eliaz, N., Mudali, U. K. and Raj, B. (2002). "Electrophoretic Deposition of Hydroxyapatite Coatings and Corrosion Aspects of Metallic Implants." Corros. Rev. **20** (4-5): 255-293.
- Sridhar, T. M., Mudali, U. K. and Subbaiyan, M. (2003). "Sintering Atmosphere and Temperature Effects on Hydroxyapatite Coated Type 316L Stainless Steel." Corros. Sci. **45**: 2337-2359.
- Stanford, C. M. and Keller, J. C. (1991). "Osseointegration and Matrix Production at the Implant Surface." Crit. Rev. Oral. Biol. Med. **2**: 83-101.

- Stern, O. Z. (1924). Elektrochem **30**: 508.
- Subbarao, E. C. (1981). Zirconia-An Overview. Science and Technology of Zirconia. Heuer, A. H. and Hobbs, L. W. Amsterdam, Elsevier. **3**: 1-24.
- Thamaraiselvi, T. V. and Rajeswari, S. (2004). "Biological Evaluation of Bioceramic Materials - A Review." Trends Biomater. Artif. Organs **18** (1): 9-17.
- Therese, G. H. A., Kamath, P. V. and Subbanna, G. N. (1998). "Novel Electrosynthetic Route to Calcium Phosphate Coatings." J. Mater. Chem. **8** (2): 405-408.
- Trau, M., Saville, D. A. and Aksay, I. A. (1997). "Assembly of colloidal crystals at electrode interfaces." Langmuir **13** (24): 6375-6381.
- Tyan, H.-L., Liu, Y.-C. and Wei, K.-H. (1999). "Thermally and Mechanically Enhanced Clay/Polyimide Nanocomposite via Reactive Organoclay." Chem. Mater. **11** (7): 1942-1947.
- Ueshima, M., Nakamura, S., Ohgaki, M. and Yamashita, K. (2002). "Electrovectorial effect of polarized hydroxyapatite on quasi-epitaxial growth at nano-interfaces." Solid State Ionics **151** (1-4): 29-34.
- Valov, I., Stoychev, D. and Marinova, T. (2002). "Study of the Kinetics of Processes during Electrochemical Deposition of Zirconia from nonaqueous Electrolytes." Electrochim. Acta **47** (4419-4431).
- Van der Biest, O. and Vandeperre, L. J. (1999). "Electrophoretic Deposition of Materials." Annu. Rev. Mater. Sci. **29**: 327-352.
- Van Tassel, J. and Randall, C. A. (1999). "Electrophoretic deposition and sintering of thin/Thick PZT films." J. Eur. Ceram. Soc. **19** (6-7): 955-958.
- Vandeperre, L., Zhao, C. and Biest, O. V. d. (2000). Correlation between surface charge of a powder in water and electrophoretic deposition from non-aqueous media. Proceedings of the novel chemistry/processing session of the sixth conference and exhibition of the European Ceramic Society, Brighton, UK, 20-24 June 1999. Binner, J. London, IOM Communications Ltd.: 69-74.
- Varma, A. J., Deshpande, S. V. and Kennedy, J. F. (2004). "Metal complexation by chitosan and its derivatives: a review." Carbohydr. Polym. **55**: 77-93.
- Velayudhan, S., Ramesh, P., Varma, H. K. and Friedrich, K. (2004). "Dynamic Mechanical Properties of Hydroxyapatite-ethylene Vinyl Acetate Copolymer Composites." Mater. Chem. Phys. **89** (2-3): 454-460.
- Verwey, E. J. W. and Overbeek, J. T. G. (1948). Theory of the Stability of Lyophobic Colloids. Amsterdam, New York, Elsevier.

- Wang, J. and Gao, L. (1999). "Surface Properties of Polymer Adsorbed Zirconia Nanoparticles." NanoStruct. Mater. **11** (4): 451-457.
- Wang, T. C., Rubner, M. F. and Cohen, R. E. (2002). "Polyelectrolyte Multilayer Nanoreactors for Preparing Silver Nanoparticle Composites: Controlling Metal Concentration and Nanoparticle Size." Langmuir **18** (8): 3370-3375.
- Wang, X., Du, Y. and Liu, H. (2004). "Preparation, characterization and antimicrobial activity of chitosan-Zn complex." Carbohydr. Polym. **56** (1): 21-26.
- Wataha, J. C., Hanks, C. T. and Sun, Z. L. (1995). "In vitro Reaction of Macrophages to Metal Ions from Dental Biomaterials." Dent. Mater. **11**: 239-245.
- Wataha, J. C., Sun, Z. L., Hanks, C. T. and Fang, D. N. (1997). "Effect of Ni Ions on Expression of Intercellular Adhesion Molecule 1 by Endothelial Cells." J. Biomed. Mater. Res. **36**: 145-151.
- Wei, J., Li, Y., Chen, W. and Zuo, Y. (2003). "A study on nano-composite of hydroxyapatite and polyamide." J. Mater. Sci. **38** (15): 3303-3306.
- Wei, M., Ruys, A. J., Milthorpe, B. K. and Sorrell, C. C. (1999). "Solution ripening of hydroxyapatite nanoparticles: Effects on electrophoretic deposition." J. Biomed. Mater. Res. **45** (1): 11-19.
- Wei, M., Ruys, A. J., Milthorpe, B. K., Sorrell, C. C. and Evans, J. H. (2001). "Electrophoretic deposition of hydroxyapatite coatings on metal substrates: A nanoparticulate dual-coating approach." J. Sol-Gel Sci. Technol. **21** (1-2): 39-48.
- Weise, N. L., Ed. (1985). SME Mineral Processing Handbook. New York, Society of Mining Engineers.
- Wohrmann, R. M. and Munstedt, H. (1998). "Zur bestimmung der freisetzung von silberionen aus silbergefülltem polyurthan." Infection **26**: 49-52.
- Woodman, J. L., Jacobs, J. J., Galante, J. O. and Urban, R. M. (1984). "Metal Ion Release from Titanium-Based Prosthetic Segmental Replacements of Long Bones in Baboons: A long-Term Study." J. Orthop. Res. **1** (4): 421-430.
- Wu, L.-Q., Lee, K., Wang, X., English, D. S., Losert, W. and Payne, G. F. (2005). "Chitosan-mediated and spatially selective electrodeposition of nanoscale particles." Langmuir **21**: 3641-3646.
- Yalpani, M., Johnson, F. and Robinson, L. E. (1992). Advances in Chitin and Chitosan. London, Elsevier Applied Science: 543.
- Yamaguchi, I., Itoh, S., Suzuki, M., Osaka, A. and Tanaka, J. (2003). "The chitosan

prepared from crab tendons: II. The chitosan/apatite composites and their application to nerve regeneration." Biomaterials **24** (19): 3285-3292.

Yamashita, K., Nagai, M. and Umegaki, T. (1997). "Fabrication of green films of single- and multi-component ceramic composites by electrophoretic deposition technique." J. Mater. Sci. **32** (24): 6661-6664.

Yang, H. C. and Pon, L. A. (2003). "Toxicity of metal ions used in dental alloys: a study in the yeast *Saccharomyces cerevisiae*." Drug Chem. Toxicol. **26** (2): 75-85.

Yen, S. K. (1999). "Characterization of Electrolytic ZrO<sub>2</sub> Coating on AISI 316L Stainless Steel." J. Electrochem. Soc. **146** (4): 1392-1396.

Yen, S.-K. (2000). "Mechanism of Electrolytic ZrO<sub>2</sub> Coating on Commercial Pure Titanium." Mater. Chem. Phys. **63**: 256-262.

Yen, S. K., Guo, M. J. and Zhan, H. Z. (2001). Biomaterials **22**: 125-133.

Yen, S. K. and Lin, C. M. (2002). "Cathodic reactions of electrolytic hydroxyapatite coating on pure titanium." Mater. Chem. Phys. **77** (1): 70-76.

Yi, H., Wu, L.-Q., Ghodssi, R., Rubloff, G. W., Payne, G. F. and Bentley, W. E. (2004). "A Robust Technique for Assembly of Nucleic Acid Hybridization Chips Based on Electrochemically Templated Chitosan." Anal. Chem. **76** (2): 365-372.

Yoshida, K., Tanagawa, M. and Atsuta, M. (1999). "Characterization and inhibitory effect of antibacterial dental resin composites incorporating silver-supported materials." J. Biomed. Mater. Res. **47** (4): 516-522.

Yu, J. C., Jiang, Z.-T., Liu, H.-Y. and Yu, J. (2003). "Influence of solvation interactions on the zeta potential of titania powders." J. Colloid Interface Sci. **262**: 97-100.

Zhang, L., Dutta, A. K., Jarero, G. and Stroeve, P. (2000). "Nucleation and Growth of Cobalt Hydroxide Crystallites in Organized Polymeric Multilayers." Langmuir **16** (17): 7095-7100.

Zhang, L., Li, Y., Yang, A., Peng, X., Wang, X. and Zhang, X. (2005). "Preparation and in vitro investigation of chitosan/nano-hydroxyapatite composite used as bone substitute materials." J. Mater. Sci: Mater. Med. **16** (3): 213-219.

Zhang, W., Liao, S. S. and Cui, F. Z. (2003). "Hierarchical Self-Assembly of Nanofibrils in Mineralized Collagen." Chem. Mater. **15**: 3221-3226.

Zhao, W., Chang, J., Wang, J., Zhai, W. and Wang, Z. (2007). "In vitro bioactivity of novel tricalcium silicate ceramics." J. Mater. Sci: Mater. Med. **18** (5): 917-923.

Zhitomirsky, I. (1997). "Cathodic electrosynthesis of titania films and powders."

NanoStruct. Mater. **8** (4): 521-528.

Zhitomirsky, I. (1998a). "Cathodic electrophoretic deposition of diamond particles." Mater. Lett. **37** (1-2): 72-78.

Zhitomirsky, I. (1998b). "Cathodic electrosynthesis of titanium and ruthenium oxides." Mater. Lett. **33** (5-6): 305-310.

Zhitomirsky, I. (1998c). "Electrophoretic and Electrolytic Deposition of Ceramic Coatings on Carbon Fibers." J. Eur. Ceram. Soc. **18** (7): 849-856.

Zhitomirsky, I. (1998d). "Electrophoretic Deposition of Chemically Bonded Ceramics in the System CaO-SiO<sub>2</sub>-P<sub>2</sub>O<sub>5</sub>." J. Mater. Sci. Lett. **17** (24): 2101-2104.

Zhitomirsky, I. (2000a). "Ceramic Films Using Cathodic Electrodeposition." JOM-e **52** (1).

Zhitomirsky, I. (2000b). "Electrophoretic hydroxyapatite coatings and fibers." Mater. Lett. **42** (4): 262-271.

Zhitomirsky, I. (2000c). "Electrophoretic Hydroxyapatite Coatings and Fibers." Materials Letters **42**: 262-271.

Zhitomirsky, I. (2000d). "New Developments in Electrolytic Deposition of Ceramic Films." Am. Ceram. Soc. Bull. **79** (9): 57-63.

Zhitomirsky, I. (2002). "Cathodic Electrodeposition of Ceramic and Organoceramic Materials. Fundamental Aspects." Advances in Colloid and Interface Science **97** (1-3): 279-317.

Zhitomirsky, I. (2004). "Composite Nickel Hydroxide-Polyelectrolyte Films Prepared by Cathodic Electrosynthesis." J. Appl. Electrochem. **34** (2): 235-240.

Zhitomirsky, I. (2006). "Electrophoretic deposition of organic-inorganic nanocomposites." J. Mater. Sci. **41** (24): 8186-8195.

Zhitomirsky, I., Chaim, R., Gal-Or, L. and Bestgen, H. (1997a). "Electrochemical Al<sub>2</sub>O<sub>3</sub>-Cr<sub>2</sub>O<sub>3</sub> Alloy Coatings on Non-Oxide Ceramic Substrates." J. Mater. Sci. **32**: 5203-5213.

Zhitomirsky, I. and Gal-Or, L. (1997b). "Electrophoretic deposition of hydroxyapatite." Journal of Materials Science: Materials in Medicine **8** (4): 213-219.

Zhitomirsky, I. and Gal-Or, L. (1998). "Characterization of zirconium, lanthanum and lead oxide deposits prepared by cathodic electrosynthesis." Journal of Materials Science **33** (3): 699-705.

Zhitomirsky, I. and Gal-Or, L. (1999a). Intermetallic and Ceramic Coatings. Dahotre, N. B. and Sudarshan, T. S. New York, Marcel Dekker Inc.: Chapter 3.

Zhitomirsky, I., Gal-Or, L., Kohn, A. and Hennicke, H. W. (1995). "Electrodeposition of ceramic films from non-aqueous and mixed solutions." J. Mater. Sci. **30** (20): 5307-5312.

Zhitomirsky, I., Niewczas, M. and Petric, A. (2003). "Electrodeposition of Hybrid Organic-Inorganic Films Containing Iron Oxide." Mater. Lett. **57** (5-6): 1045-1050.

Zhitomirsky, I. and Pang, X. (2006). "Fabrication of chitosan-hydroxyapatite coatings for biomedical applications." ECS Trans. **3** (26): 15-22.

Zhitomirsky, I. and Petric, A. (1999b). "Electrolytic and electrophoretic deposition of CeO<sub>2</sub> films." Mater. Lett. **40**: 263-268.

Zhitomirsky, I. and Petric, A. (2000a). "Cathodic Electrodeposition of Polymer Films and Organoceramic Films." Mater. Sci. Eng. B **78** (2-3): 125-130.

Zhitomirsky, I. and Petric, A. (2000b). "Electrochemical Deposition of Yttrium Oxide." J. Mater. Chem. **10** (5): 1215-1218.

Zhitomirsky, I. and Petric, A. (2000c). "Electrolytic Deposition of Gd<sub>2</sub>O<sub>3</sub> and Organoceramic Composite." Mater. Lett. **42** (5): 273-279.

Zhitomirsky, I. and Petric, A. (2000d). "Electrolytic Deposition of Zirconia and Zirconia Organoceramic Composites." Mater. Lett. **46** (1): 1-6.

Zhitomirsky, I. and Petric, A. (2000e). "Electrophoretic deposition of ceramic materials for fuel cell applications." Journal of the European Ceramic Society **20** (12): 2055-2061.

Zhitomirsky, I. and Petric, A. (2001a). "Electrolytic Deposition of ZrO<sub>2</sub>-Y<sub>2</sub>O<sub>3</sub> Films." Mater. Lett. **50** (4): 189-193.

Zhitomirsky, I. and Petric, A. (2001b). "Fabrication of Organoceramic Films by Electrodeposition." Am. Ceram. Soc. Bull. **80** (5): 41-46.

Zhitomirsky, I. and Petric, A. (2002a). "Cathodic Electrodeposition of Ceramic Coatings for Oxidation Protection of Materials at Elevated Temperatures." Can. Metall. Quart. **41** (4): 497-506.

Zhitomirsky, I., Petric, A. and Niewczas, M. (2002b). "Nanostructured Ceramic and Hybrid Materials via Electrodeposition." JOM: The Member Journal of The Minerals, Metals & Materials Society **54** (9): 31-34.

Zhu, X., Tang, F., Suzuki, T. S. and Sakka, Y. (2003). "Role of the Initial Degree of

Ionization of Polyethylenimine in the Dispersion of Silicon Carbide Nanoparticles." J. Am. Chem. Soc. **86** (1): 189-191.

Zielinski, A. and Sobieszczyk, S. (2008). "Corrosion of titanium biomaterials, mechanisms, effects and modelisation." Corros. Rev. **26** (1): 1-22.